

IMPROVING THE UTILITY OF CHERENKOV IMAGING IN THE RADIOTHERAPY CLINIC

A Thesis
Submitted to the Faculty
in partial fulfillment of the requirements for the
degree of

Doctor of Philosophy

by

JACQUELINE MARIE ANDREOZZI

Thayer School of Engineering
Dartmouth College
Hanover, New Hampshire

May 2018

Examining Committee:

Chairman _____
Brian Pogue, Ph.D.

Member _____
David Gladstone, Sc.D.

Member _____
Shudong Jiang, Ph.D.

Member _____
Lesley Jarvis, M.D., Ph.D.

Member _____
Olga Green, Ph.D.

F. Jon Kull, Ph.D.
Dean of Graduate and Advanced Studies

Abstract

More than half of all cancer patients in the United States undergo fractionated, daily radiation therapy as a component of treatment. While radiotherapy is widely regarded as life-saving, errors during delivery can be severe or even fatal, despite their rarity. These incidents may not be noticed immediately, because the treatment beam is not observed directly, and radiation-induced injuries take time to manifest by nature. It is in this context that the goal of the research presented here is to develop new Cherenkov imaging techniques to be used during radiotherapy for quality assurance testing, as well as patient treatment verification.

Cherenkov imaging allows for direct optical visualization of radiation dose deposition as ionizing beams pass through dielectric material via the Cherenkov Effect, by which fast-moving charged particles excite optical emission from media as they relax after rapid polarization. The number of Cherenkov photons produced is proportional to radiation dose delivered for a monoenergetic beam. However, the number of photons that can be detected is governed by efficiency in reaching the detector, which is influenced by variation in tissue optical properties in living subjects. This thesis first focuses on clinical patient imaging requirements, and techniques to improve the correlation between detected Cherenkov light intensity and metrics relating to delivered dose. Patients undergoing whole-breast radiotherapy (WBI), volumetric modulated arc therapy (VMAT), and total skin electron therapy (TSET) are discussed.

Quality assurance imaging is more straightforward, since the optical properties of the irradiated subject can be controlled. The remainder of this thesis employs water tanks

and solid plastics to measure relative dose optically. These methods are adapted to accommodate atypical large field setups for TSET, as well as cutting edge clinical systems combining concurrent magnetic resonance imaging with radiotherapy delivery systems (cobalt-60 and linac based).

Acknowledgements

Navigating the pursuit of a Doctor of Philosophy degree takes a considerable amount of support, guidance, and encouragement. I have been fortunate to have an excess of all of these over the years, from my advisors, research collaborators, friends and family. I would like to thank all of the wonderful people that I have met, worked with, and learned from during my time at Dartmouth College, but in particular, the following individuals:

- Dr. David Gladstone, for constantly inspiring my research with your undeniable aptitude and fascination with medical physics (and intellectual pursuits in general).
- Dr. Lesley Jarvis, for helping me understand that at the end of the day, the reason we are all here is to help our patients, through both science and compassion.
- Dr. Shudong Jiang, for continuously offering me new insight and ways to think about the principles governing the optical physics backbone of my research.
- Dr. Olga Green, for sharing your admirable expertise, and always being willing and excited to collaborate on experiments.
- Dr. Benjamin Williams and Dr. Colleen Fox, for always being there to answer my questions, and teaching me what it means to be a clinical medical physicist.
- Dr. Rongxiao Zhang and Dr. Adam Glaser, for showing me how to be a successful graduate student (and beyond).

- Dr. Petr Bruza, for bringing your new ideas and technical capabilities to the research group, and always providing insightful direction to the research.
- Dr. Karen Mooney, for seeking me out that one fateful day at the AAPM 2015 Annual Meeting; our conversation turned into a collaboration fundamental to my thesis.
- My fellow graduate students at Thayer School of Engineering, who have come and gone over the years as they reached their milestones of success; we learned from each other how to navigate the world and experience of graduate school.

And last, but perhaps most notably:

- Dr. Brian Pogue, for instilling in me the importance of being a researcher contributing to the scientific community, for your patience and understanding as I learned and grew in my capacity as both a scientist and a person, and for always having your door (and inbox) open to provide guidance and reassurance. You taught me how to write papers, how to present at conferences, and how to do good, meaningful science. I will always be grateful for your mentorship, and would not be where I am today without it.

I would finally like to thank the family, who have endured this experience by proxy, and continue to give me the drive to succeed as my career progresses. My parents, siblings, and in-laws have all done this from afar, offering constant encouragement and support when I need it the most. My wonderful husband, Ryan, and our young son Edwin, give me purpose and inspiration each and every day, and I would be lost without them.

Table of Contents

Abstract	ii
Acknowledgements	iv
Table of Contents	vi
List of Figures	xi
List of Tables	xix
List of Acronyms	xx
Chapter 1: Introduction	21
1.1 Problem Statement	21
1.2 Approach to Solving the Problem	22
Chapter 2: Background	24
2.1 Cherenkov Emission Physics	24
2.1.1 <i>Cherenkov Emission Spectra</i>	28
2.1.2 <i>Simulating Cherenkov Emission</i>	30
2.1.3 <i>Detection Approaches</i>	31
2.2 The Radiotherapy Clinic	34
2.2.1 <i>Whole Breast Irradiation</i>	38
2.2.2 <i>Mycosis Fungoides and Total Skin Electron Therapy</i>	39
2.2.3 <i>Magnetic Resonance Imaging Guided Radiotherapy</i>	41
2.2.4 <i>Volumetric Modulated Arc Therapy</i>	43
2.2.5 <i>Cherenkov Imaging During Proton Therapy</i>	44
2.3 Quality Assurance with Cherenkov Imaging	45
2.3.1 <i>Static Beam Analysis in 2D</i>	46
2.3.2 <i>Optical Cone-Beam Tomographic Reconstruction</i>	47
2.3.3 <i>Real-Time Dynamic Plan Visualization</i>	48
2.4 Review of Other Medical Cherenkov Detection Applications	49
2.4.1 <i>Nuclear Medicine</i>	49
2.4.2 <i>Molecular Imaging and Assays</i>	53
Chapter 3: Cherenkov Emission Detector Selection Study	54
3.1 Cameras	55
3.2 Experimental Setup	60
3.3 Image Acquisition and Processing	61

3.4 Metric of Performance	67
3.5 Standalone Detector Results	68
3.6 Intensified Detector Results	69
3.7 Camera Selection Discussion	76
3.8 Camera Selection Conclusion.....	80
Chapter 4: Patient Imaging and Evaluation of <i>in vivo</i> Dose Correlation.....	82
4.1 First Whole Breast Irradiation Clinical Study	82
4.1.1 Methods of Imaging and Data Analysis.....	82
4.1.2 <i>In vivo</i> Data Analysis Results.....	85
4.1.3 Discussion of First Clinical Study Cohort	88
4.1.4 First Clinical Study Cohort Conclusion	91
4.2 Improving the Cherenkov Light-Dose Correlation in Future Patients.....	91
4.2.1 Anthropomorphic Phantom Study Methods	93
4.2.2 Anthropomorphic Phantom Study Results and Discussion	94
4.2.3 Anthropomorphic Phantom Study Conclusion	97
4.3 In Vivo Volumetric Modulated Arc Therapy Imaging	97
4.3.1 VMAT Patient Imaging Methods	98
4.3.2 VMAT Patient Imaging Results	102
4.3.3 VMAT Patient Imaging Discussion	103
4.3.4 VMAT Patient Imaging Conclusion	107
Chapter 5: Optimizing Total Skin Electron Therapy with Cherenkov Imaging.....	108
5.1 Total Skin Election Therapy in the Clinic	108
5.2 Materials and Methods for Initial TSET Optimization Technique	111
5.2.1 Linac and Treatment Setup	111
5.2.2 Cherenkov Imaging System.....	112
5.2.3 Image Processing	113
4.2.4 TSET Optimization with Cherenkov Imaging.....	114
5.2.4 Ionization Chamber Verification	115
5.2.5 Initial Patient Imaging Trials.....	116
5.2.6 Additional Patient Imaging Case Studies	117
5.3 Groundwork Results.....	118
5.3.1 Optimization of TSET	118
5.3.2 Verification of the Optimized Angles	119

5.3.3 Varying Room Geometry.....	122
5.3.4 In vivo Cherenkov TSET imaging	123
5.3.5 Improvements during in vivo Imaging	126
5.4 Discussion of Initial Application of Cherenkov Imaging to TSET	128
5.4.1 Discussion of TSET Geometry Optimization	128
5.4.2 Discussion of TSET Patient Imaging	131
5.5 Initial TSET Imaging Conclusions.....	135
Chapter 6: Floor Scatter during Total Skin Electron Therapy	136
6.1 Materials and Methods of Floor Scatter Study.....	138
6.1.1 TSET Geometry Optimization Experiment Design	139
6.1.2 Floor Scatter Experiment Design.....	141
6.2 Results of Floor Scatter Study.....	143
6.2.1 TSET Geometry Optimization Results.....	143
6.2.2 Floor Scatter Experiment Results	145
6.3 Discussion of Floor Scatter Study	148
6.3.1 TSET Geometry Optimization Discussion	148
6.3.2 Floor Scatter Experiment Discussion	151
6.4 Conclusion of Floor Scatter Study.....	154
Chapter 7: Quality Assurance of MR-IGRT Systems.....	155
7.1 Introduction to the Co-60 MR-IGRT System.....	155
7.2 Materials and Methods with MR-IGRT.....	158
7.2.1 Establishing Measurement Resolution and Acquisition Settings.....	159
7.2.2 Projection Cross Beam Profiles and Projection Percent Depth Dose Curves..	161
7.2.3 System Performance During Active Magnetic Resonance Imaging.....	164
7.2.4 Real-Time Imaging of Commissioning Plan	165
7.3 Results with MR-IGRT	167
7.3.1 Cherenkov-Based Projection Cross Beam Profiles and Projection Percent Depth Dose Curves.....	168
7.3.2 Cherenkov Measurements Concurrent with Magnetic Resonance Imaging.	172
7.3.3 Real-Time Cherenkov Imaging of IMRT Plan	174
7.4 Discussion of Cherenkov Imaging with MR-IGRT	176
7.4.1 Static Beam Quality Assurance Tests.....	176
7.4.2 Magnetic Field Effects on Camera System.....	182

7.4.3 Novel Views of IMRT Plans.....	184
7.5 Conclusion of Cherenkov Imaging with MR-IGRT	186
Chapter 8: Expanding to MR-Linacs.....	188
8.1 Imaging Methods Adapted to an MR-Linac	188
8.2 MR-Linac Dosimetry Results	190
8.2.1 Large Field Dosimetry	190
8.2.2 Small Field Dosimetry.....	192
8.3 MR-Linac Dosimetry Discussion.....	194
8.4 MR-Linac Dosimetry Conclusion	196
Chapter 9: The Electron Return Effect in MR-Linacs.....	197
9.1 Introduction to the Electron Return Effect in MR-Linacs	197
9.2 Materials and Methods.....	198
9.2.1 MR-Linac and TPS.....	198
9.2.2 Phantom Design.....	199
9.2.3 Phantom A: Five Cavity Phantom.....	200
9.2.4 Phantom B: Three Cavity Phantom with Film	200
9.2.5 Phantom C: Two Cavity Water Tank	201
9.2.6 Camera System and Imaging Setup	202
9.2.7 Control Experiment Imaging	203
9.2.8 Image Post Processing	204
9.3 ERE Imaging Results	205
9.3.1 Control Imaging of Phantom A	205
9.3.2 Phantom A Results	207
9.3.3 Phantom B Results	209
9.3.4 Phantom C Results	211
9.4 ERE Imaging Discussion	212
9.5 ERE Imaging Conclusion	215
Chapter 10: Optical Imaging Prototype for MR-RT Alignment.....	216
10.1 Introduction to Alignment Problem	216
10.2 Prototype Phantom and Methods.....	217
10.2.1 Prototype Phantom Design and Optical Imaging Setup	217
10.2.2 Method for Measuring Z-Axis Alignment.....	218
10.2.3 Method for Measuring XY-Alignment	220

10.3 Prototype Phantom Results	222
10.3.1 <i>Results of Z-Axis Alignment Test</i>	222
10.3.2 <i>Results of XY-Alignment Test</i>	224
10.4 Prototype Phantom Discussion	226
10.5 Prototype Phantom Conclusion	228
Chapter 11: Conclusions and Future Directions	229
11.1 <i>In vivo</i> Cherenkov Imaging of Primarily Whole Breast Irradiation	232
11.2 <i>In vivo</i> and Phantom Cherenkov Imaging for Total Skin Electron Therapy	234
11.3 Quality Assurance Optical Imaging for MRI Integrated Radiotherapy Systems	235
11.4 Final Remarks	237
Appendix	239
A.1 <i>Salt-and-Pepper Noise Removal</i>	239
A.2 <i>Shot Noise Removal and Image Smoothing</i>	240
A.3 <i>TSET Optimization Code</i>	241
A.4 <i>Registration of Quality Assurance Curves</i>	246
A.5 <i>Image Registration and Gamma Index Analysis</i>	250
References	252

List of Figures

- Figure 2.1 2D Illustration of the directional Cherenkov photon wavefront, radiating outwards at angle θ_c measured from the path of a charged particle with velocity $\beta c > c$. 25
- Figure 2.2 Spectra of Cherenkov photons emitted after traveling through water (-) and soft tissue (--). 29
- Figure 2.3 Illustration of an intensified CCD or CMOS camera. The input trigger signal controls the voltage supply to the MCP to operate as a fast optical switch. 32
- Figure 2.4 Typical medical linac treatment room; patients must be aligned on the pictured treatment couch exactly as they were aligned on the CT simulation couch for accurate, repeatable, fractionated dose delivery. 36
- Figure 2.5 Patient with mycosis fungoides standing in a patient support structure designed to aid in positioning for the six stances required during the implemented TSET protocol. Skin plaques and lesions are apparent throughout the entire skin surface. 41
- Figure 3.1 a) A top-down view of experimental setup. The gantry was set to 90° , and the radiation beam was incident on the flat solid water phantom positioned vertically on the treatment table. The cameras were placed so as to image the surface of the phantom at an angle without being obstructed by the gantry. b) Example white light image of the phantom taken on the CCD camera while in position. 61
- Figure 3.2. Processed Cherenkov images collected using the CMOS (a-c, top row on the same intensity scale) and CCD (d-f, bottom row on the same intensity scale) cameras with varying exposure times. Room lights were off, since there is no mechanism of fast triggering and gating available with these two camera options. Note the Cherenkov signal was low relative to the background room light. At long exposure times with room lights off a modest contrast is seen. Their utility is feasible, but only at low frame rates (below 1 fps), with noticeable background in the image even after background subtraction. 69
- Figure 3.3 Cherenkov images captured using three types of intensified cameras with room lights on are shown. The HRf ICCD (d-f) outperformed the Unigen 2 ICCD (a-c) because of overall higher intensifier quantum efficiency. However, best performance was demonstrated from an high-gain electron-multiplied CCD (g), which allowed for single-shot imaging, where a high-signal Cherenkov image can be captured from a single radiation pulse from the linac (<0.05 cGy of dose); this image is a constructed from a temporal median filter of multiple frames following the same image processing techniques as with the ICCDs. Minor reshaping was implemented to visually negate the effect of small viewpoint angle changes between systems, but was not used in any quantitative analyses. The Cherenkov spectrum plotted in the graph shown in (h) was generated using Geant4-based simulations of a 6 MV x-ray beam irradiating a light-

skinned tissue volume.⁴⁸ The QE curves were plotted from data supplied by the camera manufacturer. 71

Figure 3.4 Quantitative analysis of a 250 x 150 pixel region shown in (a) for the ICCDs within the incident beam looks at the square of the signal to noise ratio in the region (b) and average Cherenkov intensity in the region (c) versus acquisition frame rate. The yellow vertical line in graph (c) highlights Unigen 2 performance at 4.7 frames per second, which is the basis for performance comparison (above 0.5% of the bit depth, or 327 counts). Intensity values that fall in the orange region of the chart qualify as adequate signal under this defined metric..... 73

Figure 3.5 In vivo Cherenkov images captured during whole-breast irradiation of two patients. The left column shows images captured on the EM-ICCD (a and c), and the right column shows images from the Unigen 2 ICCD (b and d). All images are self normalized. Images a) and b) are presented using an intensity colormap, and research is being done to correlate relative intensity to surface dose. Images c) and d) are the same processed images as a) and b), respectively, only shown in grayscale, where it is easier to visually distinguish the appearance of the blood vessels. 75

Figure 3.6. Decision flow chart for camera selection in Cherenkov imaging. Since clinical imaging requires both fast frame rates and ambient room light for patient safety, an intensified, time-gated solution is required. Other cameras can be used for quality assurance applications with room lights off, over longer acquisition intervals. 77

Figure 4.1 Correlation between average Cherenkov intensity per field and planned monitor units per field on each day of imaging for six patients, comparing 6MV ENTRANCE beams only. The Cherenkov images of each patient are labelled according to their clinical study designation, and arranged in order of ascending planned monitor units. 86

Figure 4.2 Correlation between average Cherenkov intensity per field and planned monitor units per field on each day of imaging for six patients, comparing 6MV EXIT beams only. The Cherenkov images of each patient are labelled according to their clinical study designation, and arranged in order of ascending planned monitor units.. 87

Figure 4.3 (Left) Anthropomorphic silicone breast phantom imaged. (Middle) Tangent beam plan for phantom as seen from a transverse slice of the CT scan in the TPS, with gantry positions for the two beams shown in orange. (Right) Dose cloud for the treatment volume. 93

Figure 4.4 Normalized Cherenkov images of the phantom, with analyzed ROIs drawn on as black boxes, numbered 1-4. The top row shows the images acquired with the TLDs in place measuring the surface dose, and the bottom row shows the same beams being delivered to the phantom without the TLDs. 95

Figure 4.5 Plot of correlation between Cherenkov intensity and measured surface dose.	95
Figure 4.6 Comparison of dose fall-off at the phantom edges for the normal Cherenkov images and the reflectance-corrected Cherenkov images of entrance and exit dose.....	96
Figure 4.7 Timing diagram for Cherenkov frame (left, blue), versus a background frame (right, red). The trigger pulse width and frequency can vary, and the detected light from 25 subsequent pulses add on chip to form each saved frame. The width of the Cherenkov acquisition and the background acquisition was equal.	100
Figure 4.8 Cherenkov camera being placed at the foot of the treatment couch to image VMAT patient treatment.	101
Figure 4.9 Patient #1: (a) Surface dose prediction from TPS for entire treatment fraction. (b) Composite Cherenkov image summation from treatment fraction	102
Figure 4.10 (a) Video of Patient #2 with the camera positioned at the foot of the couch: http://dx.doi.org/10.1117/12.2212844 . (b) Video of Patient #2 with the camera positioned on the side of the couch: http://dx.doi.org/10.1117/12.2212844	103
Figure 5.1 Experimental setup for rapid TSET optimization using Cherenkov imaging.	114
Figure 5.2 (a) Mean Cherenkov intensity (relative surface dose) vs. coefficients of variation for a subset of angle pairs. The historical angle pair used at the institution (255.5° and 284.5°) is labeled by a red square, and the minimum coefficient of variation at a symmetrical angle pair occurred at 252.5° and 287.5°, denoted by the blue star. (b) Calculated coefficients of variation at symmetric angle spreads. The composite Cherenkov images for the original and optimal angles spreads are shown in (c) and (d), respectively, on the same normalization scale; the self-normalized Cherenkov images are shown in (e) and (f). The image in (e) is overlaid with an image of a TSET patient for size scale. The white box in (e) shows the analyzed ROI.	119
Figure 5.3 (a) White light image of the phantom with embedded ionization chamber placed at position 5. (b) Self-normalized, super-imposed, composite Cherenkov image of the phantom irradiated with the two fields historically used for treating patients at our institution (255.5° and 284.5°); approximate locations of a patient’s wrist, back and heel are shown for reference. (c) Cherenkov image of the phantom irradiated with treatment angles producing minimum coefficient of variation (gantry at 252.5° and 288.5°). (d) Mean Cherenkov intensity calculated from the ROIs outlined in black shown in (b, red squares) and (c, blue circles) versus the ionization chamber measurements, at each of the nine positions shown, each normalized to the respective value at position 5 (prescription point). Black square outlines were superimposed on (b) and (c) to illustrate ROI size and placement.....	120

Figure 5.4 (a) Ionization chamber charge measurements for increasing depth of Solid Water between the original treatment angles and the selected optimized treatment angles, demonstrating the decrease in relative dose delivered for the new angles. (b) Normalized percent depth dose between the original treatment angles and the optimized treatment angles..... 121

Figure 5.5 Linear dependence of optimal angle spread on the SSD, using symmetric angle pairs. Images were acquired using 1° increments. 123

Figure 5.6 Composite Cherenkov images for three patients in the six Stanford technique treatment positions. All images are represented on the same color scale. Patients #1 and #2 were treated with angle spread of 29° at SSD=441 cm, and were wearing cloth shorts. Patient #3 was treated with angle spread of 35° at SSD=441 cm, sitting on a bicycle seat for patient stabilization (no cloth shorts). 124

Figure 5.7 (a) Placement of 10 TLDs on Patient #1 (posterior position only). TLDs were also placed on Patient #3 in similar approximate positions. (b) Plot comparing average Cherenkov intensity of ROIs directly on top of the TLD with the measured dose from the TLDs. Each data set is normalized to its respective highest measurement (at the hips). Measurements on opposing wrists and opposing heels are each averaged together for display clarity. Data from Patients #1 and #3 are shown for comparison, although images (a) and (c) correspond to Patient #1 only. (c) The two sets of ten 25x25 pixel regions of interest (ROIs) that were analyzed for average Cherenkov intensity on Patient #1. The white regions are directly on top of the tape affixing the TLDs, and the black regions are offset from the taped regions. There was no statistically significant difference between the mean Cherenkov intensity in the black and white labelled regions; the white labelled regions were used in (b)..... 125

Figure 5.8 Six TSET treatment poses for patients #4 (left, jet) and #5(right, blue)..... 127

Figure 5.9 Case study of legs of TSET Patient #5. a) Coronal plane view of CT scan with adipose segmented in magenta, and muscle segmented in blue. b) Composite Cherenkov image of Patient #7's left leg for the dual-field AP beam. c) Transverse plane of CT scan of patient's legs, at the blue line indicated in a), using the same color designations for adipose and muscle. 127

Figure 5.10 Study of TSET Patient #4, comparing the Cherenkov images of the lower torso and groin area (top row), to body tissue composition from diagnostic CT scans (middle rows), and concurrent surface dosimetry TLD data (2 TLDs per position)..... 128

Figure 6.1 a) Experimental setup. b) Test image from camera: yellow box denotes size and shape of analyzed ROI in floor scatter experiment, and red line designates the height (30cm) of the wooden patient support structure used during TSET. c) PVC test material. d) Steel test material. e) Solid water test material. Each test material in c)-e) was covered with blackout fabric prior to Cherenkov imaging..... 142

Figure 6.2 Composite images of optimized TSET geometry: a) on linac 1, restrained to symmetric gantry angles ($270^{\circ}\pm 20^{\circ}$); b) 90% isodose area of (a); c) on linac 1, asymmetric gantry angles $270^{\circ}+23^{\circ}$ and $270^{\circ}-17^{\circ}$; d) 90% isodose area of (c); e) on linac 2, restrained to symmetric gantry angles ($270^{\circ}\pm 20^{\circ}$); f) 90% isodose area of (e); g) on linac 2, asymmetric gantry angles $270^{\circ}+25^{\circ}$ and $270^{\circ}-17^{\circ}$; h) 90% isodose area of (g). 144

Figure 6.3 Residual images of each test material compared to concrete. The three gantry angles tested are shown in each row of images, with increasing incidence of the primary beam on the floor. The three test materials are grouped into the labeled columns in order of increasing material density (solid water, PVC, steel). 146

Figure 6.4 Box plots showing distributions of the normalized dose differences from the residual images in Figure 3 for: a) gantry angle 270° ; b) gantry angle 253° ; c) gantry angle 240° . The whisker lengths correspond to 1.5 times the interquartile range, and outliers, as the primary points of interest, are marked in red. 147

Figure 6.5 Averaged vertical profile of change in relative dose for gantry angle 240° . . 148

Figure 7.1 Water tank imaging setup with the ICCD looking down the ViewRay bore, set up outside the 5G line..... 159

Figure 7.2 Contrast to noise ratio vs. frame rate evaluated from system calibration Cherenkov images. A power curve fit is shown for each tested exposure. 167

Figure 7.3 Cropped Cherenkov images from one Co-60 source impinging perpendicular to the water surface for square beam sizes: a) 4.2cm; b) 10.5cm; and, c) 14.7cm. The vertical white dotted line in a) designates the location of the Cherenkov pPDD extraction, and the horizontal white dotted line correlates to the Cherenkov pCBP taken at d_{max} . d-f) Cherenkov pCBP curves for the two tested Co-60 sources are compared to projection TPS results at 5 depths. g)-i) Associated Bland-Altman plots to demonstrate measurement agreement after calculating beam widths for each depth. j)-i) Cherenkov pPDD curves are compared to TPS results. m)-o) Associated error plots between the TPS pPDDs and corresponding Cherenkov pPDDs. The green lines delineate the mean value of the differences (δ). The red lines show limits of agreement, two standard deviations above and below the mean ($\delta\pm 2\sigma$). 170

Figure 7.4 a) Simulation comparison from the TPS showing differences between the central axis PDD and the integrated projection PDD for the three square beams tested. b) Ionization chamber PDD acquired along the central axis of a 4.2cm square beam compared to the Cherenkov-based pPDD and Cherenkov-derived PDD, weighted to the ratio of the two 4.2cm curves shown in (a); the residual error difference between the IC and weighted Cherenkov PDD are reported..... 171

Figure 7.5 a) Simulation weighted Cherenkov PDDs compared to central axis ionization chamber measurements for each beam size (4.2cm, 10.5cm, and 14.7cm). b) Beam

widths for three tested beam sizes from one treatment head comparing film central axis (--) and Cherenkov image projection cross beam profile measurements (-).	172
Figure 7.6 a) Checkerboard imaging setup with MRI coils; b) Difference image with and without active MRI imaging.	173
Figure 7.7 Depth-dependent cross-beam profiles from the Cherenkov image of the 14.7-cm square beam illustrating the more pronounced beam asymmetry deeper in the tank.	174
Figure 7.8 Cumulative Cherenkov images of TG-119 C4 IMRT plan in water at 35 second increments during active irradiation (excluding control point interims) until end of plan.	175
Figure 7.9 a) Cumulative dose from TPS; b) Cumulative Cherenkov intensity of TG-119 C4 IMRT plan in water, where black box denotes region of interest used for gamma analysis; c) Gamma index analysis between (a) and (b) with 3mm/3% criteria and 80.5% pass rate. d) Gamma index analysis between (a) and (b) with 4mm/4% criteria and 95.1% pass rate.	175
Figure 8.1 a) Experimental setup, with ICMOS at foot of the couch looking down MR-linac bore; b) TPS projection dose image of 4.98cmx4.98cm beam; c) experimentally acquired Cherenkov image of beam in b); white dashed line denotes extraction of pCBP; d) TPS projection dose image of 14.94cmx14.94cm beam; e) experimentally acquired Cherenkov image of beam in d); dashed white line shows extraction of pPDD.	191
Figure 8.2 a) Projection PDDs of 4.98cm x 4.98cm beam; b) pPDDs of 9.96cm x 9.96cm beam; c) pPDDs of 14.94cm x 14.94cm beam; d)pPDDs of 24.07cm x 27.20cm beam (largest deliverable).	191
Figure 8.3 The pCBPs extracted from the TPS (magenta) and Cherenkov fluorescence images (blue) for the 4.98cmx4.98cm, 9.96cmx9.96cm, 14.94cmx14.94cm, and 24.07cm x 27.20cm beams.	192
Figure 8.4 Experimental Cherenkov-induced fluorescence images of small beams being analyzed to determine the beam size limits of the proposed method; a) 2mm x 4mm beam (smallest possible from machine); b) 8mm x 8mm beam; c)16mm x 16mm 6MV FFF beam from MR-linac.....	193
Figure 8.5 Small field TPS and optical pPDDs for a) 2mm x 4mm, b) 8mm x 8mm, and c) 16mm x 16mm beams.	193
Figure 9.1 a) Phantom A: 5 cavities in acrylic; b) Phantom B: 3 cavities and film in acrylic; c) Phantom C: 2 cavities in water.	199

Figure 9.2 a) Experimental setup with ICMOS at foot of treatment couch, looking down the MR-linac bore to the phantom; b) cropped and scaled resolution and depth of field test target..... 203

Figure 9.3 Top row: Eclipse TPS integrated dose images (Acuros algorithm); Bottom row: optical images for each test case of the control experiment without magnetic field. All images are independently normalized to the dose at d_{max} 205

Figure 9.4 Control experiment line plots for the same sized beam impinging the: a)1cm cavity, b)2cm cavity, c)3cm cavity, and d)the solid area between the 3cm and 2cm cavity. Column 1 presents the pPDDs through the center of each beam. Column 2 shows the pPDDs taken 5mm to the left of each cavity in a)-c), and 1cm to the left of the central axis in d). Column 3 contains the pCBPs at the d_{max} 206

Figure 9.5 Percent error between the optical and TPS pPPDs in Figure 9.4 (d) for depth 3-90mm. 207

Figure 9.6 a) Projection sum images of TPS dose predictions of ERE resulting from 1cm, 2cm, and 3cm cavities in Phantom A, normalized to the dose at d_{max} ; b) associated optical images for each respective cavity irradiation in the presence of the magnetic field, normalized to the dose at d_{max} ; c) pCBPs through the center of each cavity comparing a) and b) for each cavity size; d) cavity-tangent pPDDs, or the vertical dose profiles set to a 2mm lateral shift from the left cavity boundary comparing a) and b); e) central axis pPDDs containing d_{max} comparing a) and b). 208

Figure 9.7 a) TPS planar dose simulation; b) readout of radiochromic film irradiated while within phantom; c) optical dose measurement (film was not inside the phantom at the time of optical acquisition). Dark artifacts in the optical image are the result of the tape (bottom corners) and metal pins used to secure the phantom pieces together... 210

Figure 9.8 PDD and CBP plots comparing the results of the three modalities, optical imaging, TPS dose prediction, and film measurement. a) Registered film (gray) and TPS (green) dose images, with colored line plots designating the physical locations of the subsequent plots (b-f); b) PDDs directly to the right of the metal phantom alignment pin (white line); c) CBPs intersecting all three cavities (blue horizontal line); d) PDDs 2mm to the left of the 3cm cavity (yellow line); e) PDDs 2mm to the left of the 2cm cavity, intersecting the metal pin (magenta line); f) PDDs 2mm to the right of the 1cm cavity (cyan line)..... 210

Figure 9.9 integrated dose image of water tank Phantom C from a) TPS simulation, and b) optical image measurement..... 211

Figure 10.1 CAD drawing of prototype MR-RT alignment phantom. 218

Figure 10.2 a) Imaging setup of prototype phantom on TrueBeam linac with IC MOS camera at foot of treatment couch; b) close up of prototype phantom aligned using treatment room lasers; c) schematic of irradiation scheme for z-axis alignment; d) schematic of irradiation scheme for x-y axes alignment..... 219

Figure 10.3 Integrated optical images of the prototype phantom irradiated by two tangential sheet beams in each tested position for the z-axis alignment test. 223

Figure 10.4 Correlation between optically measured ring diameter and known z translation of the phantom measured using the a) horizontal 1D line profiles, and b) vertical 1D line profiles containing the circle centroid..... 223

Figure 10.5 Integrated optical images of the beamlet arc across the 180° superior portion of the phantom near its front face for x-y localization. The position of the beamlet with respect to the known phantom geometry is shown in d). a) Image at (0mm,10mm); b) image at (0mm,1mm); c) image at (1mm,1mm); e) image at (0mm,0mm); f) image at (1mm,0mm)..... 224

Figure 10.6 Integrated 1D plots of optical image intensity a) along the image rows to measure vertical y displacement, and b) down the image columns to measure lateral x displacement..... 225

List of Tables

Table 2.1 Select publications on pre-clinical CLI using various radionuclides with summarized conclusions in chronological order	52
Table 3.1 Key performance specifications of the five cameras examined as possible detectors for clinical Cherenkov imaging. For the PIMAX cameras the image intensifier is specified as either Unigen2 or HRf in the sensor type.	56
Table 3.2. Selected number of on-chip accumulations and associated readout frame rate for the two ICCD cameras (PIMax3 1024i and PIMax4 1024i) when using full chip acquisition (no binning). The number of analyzed frames was varied to reflect a constant overall time of acquisition.	65
Table 3.3 Average Cherenkov intensity and signal to noise ratio values for the EM-ICCD imaging at 30 frames per second.....	74
Table 4.1 Calculated correlation coefficients between average Cherenkov image intensity within the treatment ROI and prescription or TPS derived quantities.....	88
Table 4.2 Optical absorption and scatter properties of silicone phantom.....	94
Table 6.1 List of properties of floor scatter materials tested.	142
Table 7.1 Measured maximum and average dose differences between normalized Cherenkov and TPS derived pPDDs, at each depth assessed with the TPS simulation..	171
Table 8.1 Statistics calculated from the residual errors between the Cherenkov-based and TPS pPDDs for the four beam sizes shown, omitting the first 3mm of buildup region.	192
Table 8.2 Statistics calculated from the residual errors between the Cherenkov-based and TPS pPDDs for the three small beam sizes shown, omitting the first 3mm of buildup region.	194
Table 9.1 Statistical summary of errors plotted in Figure 9.5.	207
Table 10.1 Known and optically measured shifts in the vertical y direction (left) and lateral x direction (right).	225

List of Acronyms

3-Dimensional External Beam Conformal Radiation Therapy	3D-CRT
Cherenkov Excited Fluorescence	CEF
Contrast to Background Ratio	CBR
Coefficient of Variation	COV
Deep Inspiratory Breath Hold	DIBH
Electronic Portal Imaging Device	EPID
Flattening Filter Free	FFF
Intensified Charge Coupled Device	ICCD
Intensity Modulated Radiation Therapy	IMRT
Magnetic Resonance Imaging Guided Radiotherapy	MR-IGRT
Multi-Leaf Collimator	MLC
Quality Assurance	QA
Radiofrequency	RF
Region of Interest	ROI
Signal to Noise Ratio	SNR
Source to Surface Distance	SSD
Thermoluminescent Dosimeter	TLD
Treatment Planning System	TPS
Total Skin Electron Therapy	TSET
Volumetric Modulated Arc Therapy	VMAT
Whole Breast Irradiation	WBI

Chapter 1: Introduction

The radiotherapy treatment clinic uses invisible, ionizing radiation beams to target and kill disease, predominantly cancer. Because ionizing radiation is indiscriminant between healthy and diseased tissues, it is the responsibility of the clinical team to ensure that patients receive accurate and precise radiation dose delivery. This requires rigorous maintenance of radiation-producing devices, and effectual quality checks of the patient-specific treatment plans prescribed.

1.1 Problem Statement

Clinical systems currently adopted for quality assurance (QA) of radiation therapy plans typically involve either arrays of point measurements, films with lengthy read-out protocols, or geometrically-limited 2D portal images of the radiation beam. These systems inherently impose limited spatial and temporal resolution, as well as detector-size restrictions on the radiation beam assessed. This is especially true for dynamic treatment plans, which make up a substantial fraction of the clinical workflow in the U.S.¹ Therefore, rigorous pre-treatment quality assurance methods are both necessary and time-consuming.

Furthermore, it is not standard of care to physically measure the radiation as it interacts with patient tissue, because *in vivo* dosimetry during all patient treatments is not practically feasible with current tools. Daily patient treatments rely on pre-treatment QA without the patient present, in conjunction with the inherent assumption that the patient is strictly aligned to the same position as the original computed tomography (CT) simulation scan on which the radiation treatment plan is generated. Eliminating this

assumption would require a rapid, real-time, inexpensive, and intuitive radiation beam measurement system on the surface or within the volume of the patient.

1.2 Approach to Solving the Problem

The physical phenomenon known as the Cherenkov Effect has been extensively studied since its discovery in the early 1900s.^{2, 3} It was readily recognized as a distinctive singularity, as the theory of luminescence failed to account for a number of its unusual properties—insensitiveness to the action of quenching agents, anomalous polarization, marked spatial asymmetry, and so on.

The initial applications of Cherenkov radiation naturally fell into the realm of nuclear, particle, and cosmic-ray physics,⁴ with detection of the optical photons being a primary method for measurement of these associated quanta. The Cherenkov Effect has more recently been used in a number of exploratory applications in medical imaging and radiation oncology. With advances in low-light sensors and gated detection, new realms of capability in imaging clinical radiation beams have opened up that utilize optical photons as excitation sources, biochemical indicators, or even dosimeters.

Specifically, advances were initially most prominent in Cherenkov imaging within the field of nuclear medicine. Later applications developed in molecular imaging, novel assays, quality assurance of radiotherapy, and patient treatment imaging during radiotherapy. Each of these is described briefly in this work, but the focus of this thesis is the application of Cherenkov imaging in the radiotherapy clinic.

The research documented herein is intended to explore the benefits and challenges of adopting a Cherenkov imaging system as both a pre-treatment quality

assurance tool, and as an *in vivo* radiation monitoring device. Cherenkov imaging techniques produce temporally resolved 2D images of radiation beams in transparent media and on surfaces such as human tissue. This novel information is intrinsically capable of localizing the position of the radiation beam, and has already been demonstrated for tracking patient setup error.⁵

However, extracting more specific information regarding radiation dose, either relative or absolute, becomes a much more convoluted problem, affected by factors such as detection instrument calibration and precision, variation in optical properties in the irradiated medium, and energy spectra of the radiation source. Therefore, specific methods and approaches are explored to understand and mitigate these factors, and to present directly advantageous applications of Cherenkov imaging techniques in the radiotherapy clinic.

Background regarding the physics of the Cherenkov Effect, the radiotherapy clinic, and applications of Cherenkov imaging are documented in Chapter 2. Chapter 3 presents an in-depth analysis of the camera system requirements for different possible imaging schemes. After establishing the paradigm of the imaging systems used for this work, Chapter 4 describes the clinical experiences of *in vivo* imaging for whole breast irradiation and volumetric modulated arc therapy patients. Chapters 5 and 6 are centered on the application of Cherenkov imaging to total skin electron therapy patients and protocols. Chapters 7 through 10 move into novel techniques that provide benefit to state-of-the-art integrated magnetic resonance imaging guided radiotherapy systems.

Chapter 2: Background

This chapter is largely derived from: J.M. Andreozzi, B.W. Pogue, L.A. Jarvis, and D.J. Gladstone, "Applications of Cherenkov Imaging in Medical Physics," in Adv. Med. Phys. 2016(2016).

2.1 Cherenkov Emission Physics

The physical phenomenon that makes the research documented in this work possible is now known as the Cherenkov (or Čerenkov) Effect, discovered in 1937 by its namesake, Pavel Čerenkov.² The emission of Cherenkov photons occurs when a high-energy charged particle travels through a dielectric medium (such as water or human tissue) at a velocity that exceeds the speed that a light wave phase front can propagate through the same medium; this process is analogous to the sonic boom generated when an object breaks the sound barrier.

The charged particle, often an electron, causes rapid, localized polarization of the medium. As the polarizations of the atoms within the medium relax, a full spectrum of optical photons is emitted as a wavefront, directional with respect to the path of the traveling charged particle; the dielectric medium is itself the source of the light after receiving energy from the traversing charge particle. In relatable terms, the Cherenkov Effect is the soft blue glow of light characteristic to ionizing radiation sources, such as the fuel rods submerged in the cooling pools of nuclear reactors.

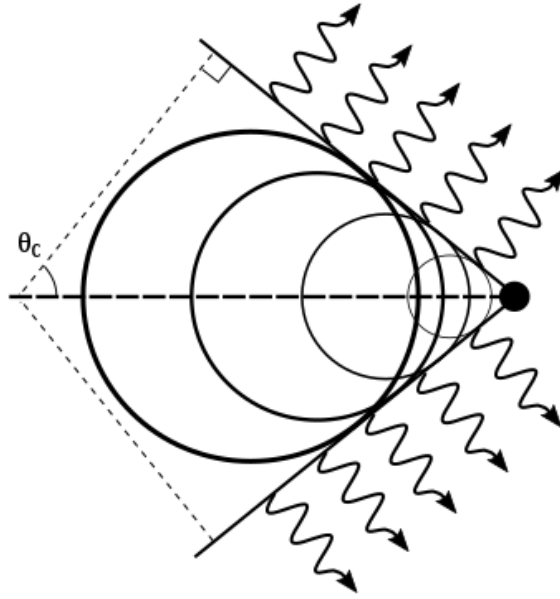


Figure 2.1 2D Illustration of the directional Cherenkov photon wavefront, radiating outwards at angle ϑ_c measured from the path of a charged particle with velocity $\beta c > c$.

Cherenkov emission is known for its directionality, as illustrated in Figure 2.1. This directionality is described by the Cherenkov relation:

$$\cos \theta_c = \frac{1}{\beta n} ,$$

where θ_c is the angle of maximum Cherenkov emission, c is the speed of light in a vacuum, n is the index of refraction of the medium, and the velocity of the charged particle is βc .⁴

Not long after Pavel Cherenkov published the paper that heralded the first official documentation of the phenomenon,⁶ the theoretical interpretation of Cherenkov photon production was published by Ilya Frank and Igor Tamm:

$$\frac{dW}{dl} = \frac{e^2}{c^2} \int_{\beta n > 1} \left(1 - \frac{1}{\beta^2 n^2}\right) \omega d\omega .$$

This equation describes the amount of energy per path length (dW/dl , i.e. a quantification of optical photons) generated by a charged particle traveling faster than the phase velocity of light in a medium of refractive index n at frequency ω (as denoted by $\beta n > 1$, given βc is the velocity of the particle, and c is the speed of light in a vacuum).^{3, 4} It is important to note that the medium through which the charged particle is traveling must be dielectric, because it is the rapid polarization and relaxation of the traversed atoms that results in the eventual release of energy as optical Cherenkov photons.

The Cherenkov Effect is directly related to the radiation dose deposition process. After some consideration in the context of radiation therapy, the so-called Frank-Tamm formula can be used to derive the total number of Cherenkov photons emitted, N_T :

$$N_T = \int \frac{\Phi}{\rho} \left(\frac{dN}{dx} \right) dE$$

where Φ is the poly-energetic electron fluence spectrum of the ionizing beam, ρ is the density of the irradiated medium, dN/dx describes the number of particles emitted per unit path length, and E is the particle energy.⁷

In the case of medical physics applications, the medium of interest is typically soft tissue, which has an index of refraction close to water, leading to Cherenkov emission above energies of approximately 220keV. Work published by Glaser et al.⁷ illustrated the similarities between the Cherenkov emission equation above, and the energy deposited by ionizing radiation per unit mass (dose), D , which can be written as:

$$D = \int \frac{\Phi}{\rho} \left(\frac{-dT}{dx} \right) dE$$

where $-dT/dx$ is the collisional stopping power for an electron in the given medium. Both equations directly depend upon the incident radiation fluence, Φ , and inversely on density.

Monte Carlo simulations in the same paper demonstrated a strong linear correlation between Cherenkov light emission and dose under given conditions. The depth dose curves rise with build-up and decay with attenuation very similarly for dose and Cherenkov light signal, with a small departure in agreement which grows as a function of depth; the percentage disagreement was larger (but still within a few percent) for depths greater than 100mm.

Water imaging of the Cherenkov Effect has been possible with direct imaging from a camera, with a side view of the water tank, orthogonal to the beam direction. Enhancement of the emission signal detection is possible with addition of fluorophore to the water, which absorbs some of the photons and allows isotropic emission of them for superior imaging.⁸

In contrast to water, the emitted photons in tissue undergo an optical elastic scattering from the cellular and biological matrix, which dominates the photon transport. As a result, in tissue, elastically scattered Cherenkov photons are continuously emitted during irradiation from either electron or photon beams, with the emission originating from the primary and/or secondary electrons. The initial directionality of the emission is

lost after a few scattering lengths (300 μm), while the absorption of photons limits the depth of travel to a few millimeters.

Therefore, the signals detected by the exterior, remote camera system originate in the superficial layers of 3-7mm depth with respect to the surface. While the number of optical photons generated is linearly proportional to dose, the number of optical photons that make it to the camera is predominantly governed by the tissue optical properties through which they must travel. When the optical properties of the medium are homogenous, such as the case for phantoms and water tanks, the proportionality is inherently maintained. However, when imaging *in vivo*, this is not a realistic assumption, and variations in tissue optical properties are the primary factor affecting the correlation between deposited dose and detected Cherenkov light intensity.⁹

2.1.1 Cherenkov Emission Spectra

While the sources of Cherenkov radiation are ionizing, Cherenkov radiation itself spans the range of ultraviolet, optical, and near-IR wavelengths. From the Frank-Tamm formula, one can derive the $1/\lambda^2$ dependence of relative Cherenkov emission intensity in a non-scattering medium such as water, where λ is optical photon wavelength.

The correlation between Cherenkov light intensity and surface dose has been established through simulations of simple geometries, and phantom studies with controlled conditions. However, *in vivo* correlations have yet to prove themselves reliable and repeatable. Several factors that have been identified which influence the correlation of data. Heterogeneous tissue optical properties and skin color have the most significant impact on the detected Cherenkov intensity.

Mammalian tissue causes both absorption and scatter at the wavelengths of light generated via the Cherenkov Effect. As a result, the characteristic blue light commonly observed by Cherenkov emissions in nuclear reactor waste pools is not seen. Rather, the blue-green light is heavily absorbed by blood and melanin. The resulting detected Cherenkov spectrum, after passing through tissue, is much different than the raw emission spectrum. Consequently, in human medical applications of Cherenkov imaging, it is prudent to use sensors with high quantum efficiencies at red to near-infrared wavelengths (600-900nm), rather than at ultraviolet to blue wavelengths.¹⁰

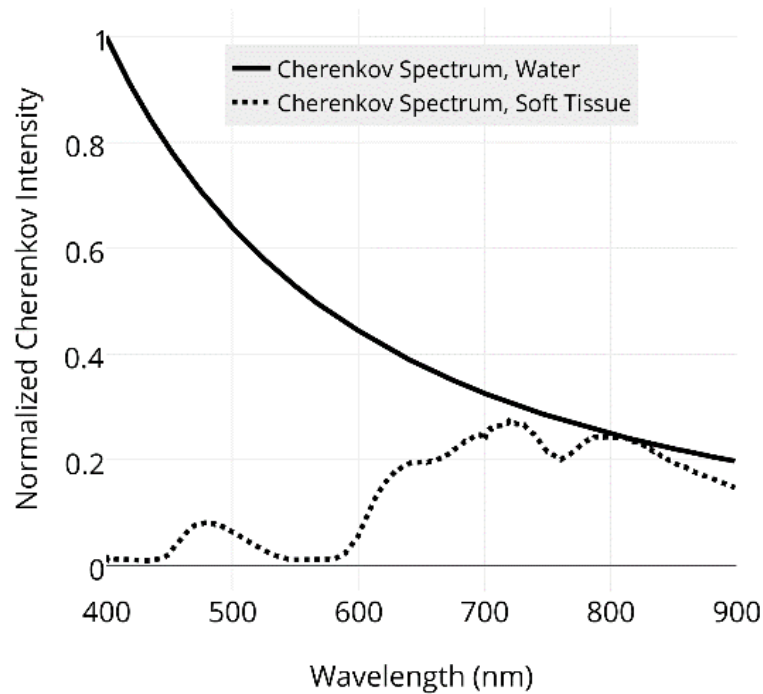


Figure 2.2 Spectra of Cherenkov photons emitted after traveling through water (-) and soft tissue (--).

Figure 2.2 provides the spectra of Cherenkov emission in a transparent, non-absorptive medium (for the given wavelength range), water, as well as in simulated soft

tissue, known to be a heavy absorber of blue light.¹¹ The latter is based on simulation data by Zhang,¹² which used wavelength-dependent values of scattering coefficient, absorption coefficient, and refractive index defined in literature as characteristic of layered human skin and generic tissue.^{11, 13}

In addition to fluctuating tissue properties, simulations have shown that the energy of the incident radiation and the surface curvature contribute most noticeably to variations in detected light intensities. For this reason, it is difficult to compare absolute dosimetry from patient to patient with current techniques. It is interesting to note that the same simulations suggest that variations in extent of curvature (diameters 2.5cm to 20 cm), field size (0.5cm to 20 cm), thickness of slab (2.5cm to 20cm), and source to surface distance (80cm to 120cm) did not significantly impact detected Cherenkov light intensity.⁹

2.1.2 Simulating Cherenkov Emission

A commonly used simulation tool for particle physics is the Geant4 toolkit,¹⁴ which provides a reliable, highly validated simulation means for Cherenkov physics based on advanced Monte Carlo methods in a C++ programming environment. Simulations have been conducted using GEANT4, concluding that there are strong correlations between deposited dose and the number of generated Cherenkov photons for both electron beams and x-ray photon beams.¹⁵

There are easily adapted user interfaces to GEANT4 that are specific to the medical field, such as the Geant4-based Architecture for Medicine-Oriented Simulations (GAMOS),¹⁶ or Geant4 Application for Tomographic Emission (GATE),¹⁷ each of which

provide more user-friendly, modular scripting environments that do not require an in-depth understanding of C++ programming. A GAMOS plug-in was recently produced for simulating radiation-induced Cherenkov light transport in biological media,¹⁸ allowing high energy simulation together with optical photon transport simulation. This was used in Figure 2.2 to generate the Cherenkov photon spectrum escaping tissue, and provides an easily used theoretical method for exploring signal detection strategies in biomedical Cherenkov emission.

2.1.3 Detection Approaches

Since Cherenkov light is an extremely low light emission process, measurement of this requires a detector sensitive to the relevant optical wavelengths, with a high internal or external gain mechanism. The signal levels tend to be at the level of single photon counting, and so the amplification allows significantly faster imaging. Early measurements of Cherenkov light utilized the low noise amplification capabilities of photomultiplier tubes.⁴ Advances in imaging technology have made it possible to detect Cherenkov photons while preserving spatial information using commercial camera pixel densities.

Charge-coupled devices (CCDs) are simple sensors capable of detecting Cherenkov without any additional hardware if it is possible to sustain long exposure times. Similarly, complementary metal-oxide semiconductor (CMOS) sensors can successfully observe Cherenkov emission.^{19, 20} Either of these can be used, but the low light level means that the signals detected are single photon counts, and so creation of a significant signal can require integrating for many seconds to minutes.

Implementing a gain mechanism, such as an external image intensifier, allows for much faster signal acquisition better suited for real-time applications. A phosphor-based intensifier is common, and provides gain in three basic steps. First, it utilizes a photocathode to convert incoming optical photons to electrons. Next, the electrons hit a micro-channel-plate (MCP) photomultiplier tube and multiply through secondary emission while preserving the spatial information of the original photons. The final step of these amplified electrons is conversion from colliding electrons back to optical photons, which is accomplished using a phosphor screen optically coupled to the imaging detection device (CCD or CMOS camera). A basic schematic of this setup is illustrated in Figure 2.3.

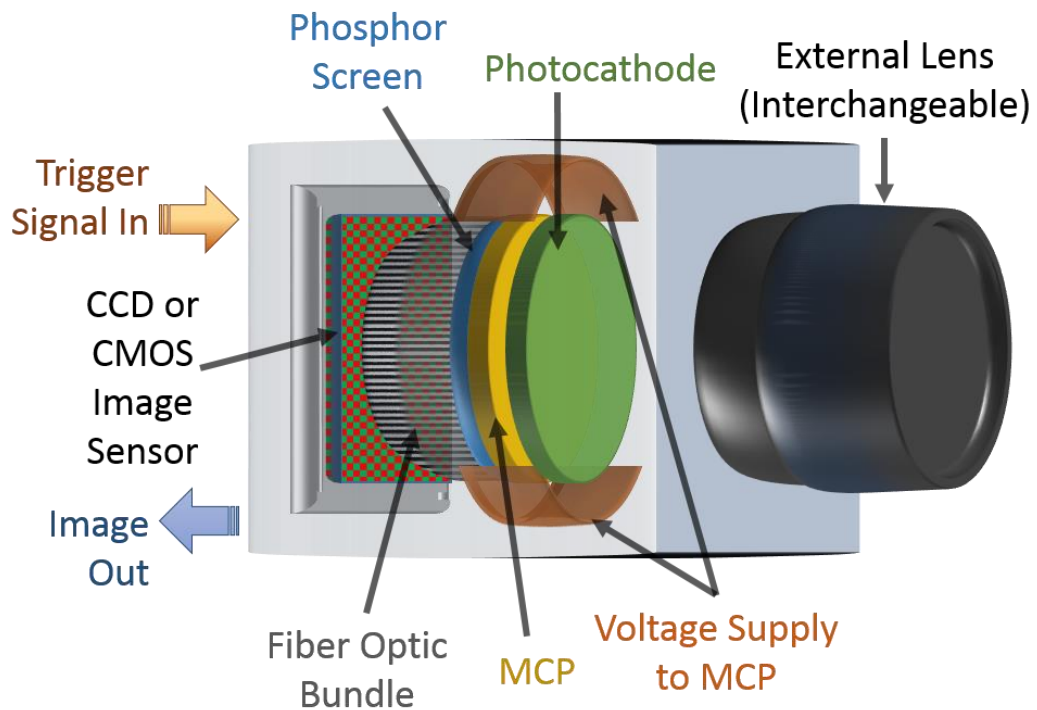


Figure 2.3 Illustration of an intensified CCD or CMOS camera. The input trigger signal controls the voltage supply to the MCP to operate as a fast optical switch.

The benefits of this type of intensifier are that the signal is amplified, and that localization of the signal is still possible, limited only by the spatial resolution of the subsequently impinged camera chip. It also offers the opportunity for nanosecond-level signal gating, since the photocathode can double as an electronic shutter, much faster than any mechanical shuttering system. This concept is important for applications of Cherenkov imaging in which ambient room light is desired, such as *in vivo* patient applications; limiting light capture to only the micro-second windows of active Cherenkov emission eliminates a significant portion of background-light contamination. The drawback of the intensifier is the loss of spectral information from the original signal, which does not generally impede current applications.

The detector choice depends primarily on the requirements of the specific application.¹⁰ The dominating factors of detector-choice are how fast a signal can be detected with acceptable signal-to-noise ratio and signal resolution. Raw light sensitivity, ability to time-gate or control exposure, ability to bin pixels, spectral quantum efficiency, and system gain will all influence the two dominating factors.

As with any imaging modality, a certain level of processing can be expected as necessary to reveal the important underlying information. Much like the detector type depends on the particular application being pursued, the image acquisition settings and processing methods are also dependent on the application. Factors such as gating, exposure time, sensor gain, and pixel binning are chosen at the time of acquisition, and become inherent to the acquired image data. However, processing allows the user to view and analyze the data in dramatically different ways. Typical image processing

techniques that do not generally inhibit the quantitative validity of the data include adjustment of the dynamic range, background image subtraction, and basic noise removal through temporal or spatial median filtering.

2.2 The Radiotherapy Clinic

Radiology primarily capitalizes on the photoelectric effect and transmission properties of ionizing photon beams through tissue to create diagnostic images of internal anatomy while minimizing radiation dose to a gross region. Radiotherapy, on the other hand, uses escalated energies and deliberately heightened doses delivered from medical linear accelerators (linacs) to exploit ionizing radiation to specifically target and kill cancer cells. This occurs largely through hydrolysis of water by the primary ionization event, and subsequent damage of DNA by the generated hydroxyl radicals.²¹

Radiotherapy offers the advantage of being a non-invasive treatment modality capable of de-bulking tumors and eradicating microscopic disease. While the benefits of radiotherapy are many and the associated rates of severe risk are low, radiation is for the most part nonspecific; healthy cells are also damaged, and proper care must be taken to spare their exposure. This means radiotherapy dose prescriptions are limited by the sustained exposure of healthy tissues, within the confines of the accuracy and precision of dose delivery.

Just as is the case with the other two main pillars of modern cancer treatment, chemotherapy and surgery, radiation oncology is a constant battle to balance incurred side effects and possible morbidities with the promise of its curative or palliative potential. It is generally accepted that there are two categories of radiotherapy toxicities:

1) early effects observed within weeks of treatment, such as skin erythema, nausea, wet or dry desquamation, and 2) late effects that manifest after months or years, such as radiation-induced secondary cancers, fibrosis, vascular or neural damage, atrophy, endocrine or growth deficiencies.²²

In most of these cases, the mechanisms by which one patient can become afflicted by these side effects while others are spared are not understood. However, it is accepted that minimizing dose to healthy tissues while maintaining dose levels in diseased areas can help mitigate these effects. The ability to monitor actual dose deposition during treatment would feasibly aid in the capacity to confine and specify distributions of ionizing radiation within the body.

The work of this thesis relates to a common approach to radiation treatment known as external beam radiotherapy, which employs high energy (megavoltage range) x-ray or electron sources from outside of the body. This is most commonly done using a linac, such as the one shown in Figure 2.4. Typical treatment workflow begins with a computed tomography (CT) simulation scan, followed by the creation of a patient-specific treatment plan that uses static or dynamic radiation beams to deliver a prescribed dose to the tumor and minimize dose to healthy tissues.

Fractionated therapy is delivered on a daily basis for up to several weeks; the patient is meticulously positioned on the treatment bed as close to the original CT simulation position as possible. The assumption is that the treatment will be delivered as planned if this alignment is accurate. The radiation oncology team uses many tools to ensure high levels of quality assurance, however, none of these technologies have yet

provided the ability to physically view the beam on the surface of the patient, and thereby eliminate the implied assumption with directly observed evidence of the ionizing radiation.



Figure 2.4 Typical medical linac treatment room; patients must be aligned on the pictured treatment couch exactly as they were aligned on the CT simulation couch for accurate, repeatable, fractionated dose delivery.

Cherenkov imaging has been investigated to enhance current clinical methods of treatment verification, which have the overall goal of achieving precise and accurate dose delivery through pre-treatment quality assurance (QA) and patient alignment protocols. These current methods are assumed to be robust on the grounds that careful QA and alignment provides an implicit direct relationship between the planned treatment and the delivered dose.

Various techniques of *in vivo* dosimetry and treatment verification have been explored to provide on patient verification of delivery, as well as to provide a more dependable means of permanent treatment records.²³ Early approaches of utilizing Cherenkov emission for dosimetry focused on using Cherenkov-based detectors for portal dosimetry,²⁴⁻²⁶ or fiber-based point dosimetry.²⁷⁻³⁰ More recent approaches, like those described in depth in this thesis, utilize a remote camera detector imaging the

radiotherapy beam-induced Cherenkov emission directly from the patient or phantom surface, or water tank volume.

The range of 'on patient' measurement systems varies considerably in technology. Thermoluminescent dosimeters (TLDs) and optically stimulated luminescent detectors (OSLDs) are common forms of *in vivo* dosimeters implemented regularly in the clinic. However, as point measurements that do not give real-time feedback, the usefulness of TLDs and OSLDs is limited to cases where a passive role is suitable, such as in the case of post-treatment dose verification.³¹⁻³⁶

To provide more direct and immediate information, many groups have investigated the use of 2D, 3D, and even 4D Electronic Portal Imaging Device (EPID) reconstructions of dose fluence.³⁷⁻⁴⁶ Major strides have been made with this technology, but routine use in everyday fractionated delivery has not yet occurred.⁴⁷ Given EPIDs can provide a direct measurement of the radiation beam after exiting the patient, they are the most similar competitor to Cherenkov imaging techniques. However, only Cherenkov imaging allows for real-time, 2-dimensional beam measurement directly on the patient surface.

In addition to quality assurance,⁸ Cherenkov imaging is being examined for *in vivo* surface dosimetry and beam tracking for real-time treatment verification.^{7, 48} As a passive monitoring modality, Cherenkov imaging would not require any further dose to the patient, nor interfere with typical treatment protocols. Initial studies on the applications of Cherenkov imaging have shown feasibility of imaging repeatedly, and studies of the potential medical value are ongoing.^{49, 50}

One application of Cherenkov imaging explored in this thesis seeks to fill this gap in the treatment workflow with “on patient” verification, and the possibility of dosimetric imaging. Not only is this intended to mitigate gross errors in delivery, such as treating with incorrect patient setups or beam shapes, but also to pave the way towards more accurate beam targeting. Whole breast irradiation (WBI) and total skin electron therapy (TSET) patients were the primary subjects of this effort. Overviews of the three clinical modalities to which Cherenkov imaging was applied in this work are introduced briefly in sections 2.2.1- 2.2.3 below, and consist of WBI, TSET, and magnetic resonance imaging guided radiotherapy (MR-IGRT).

2.2.1 Whole Breast Irradiation

Radiotherapy can be used in conjunction with both surgery and/or chemotherapy as part of breast cancer treatment, depending on the specific patient diagnosis. The American Society of Clinical Oncology recognizes radiation therapy within one year breast conserving surgery (lumpectomy) as an advantageous clinical care indicator for breast cancer patients under 70 years old.⁵¹ Radiotherapy has been shown to reduce the rate of recurrence by 50-70%, and reduce the death rate by approximately 17% in these cases.⁵²
⁵³ This is because radiotherapy can destroy the microscopic disease left behind after the macroscopic tumor is surgically resected.

WBI is an efficient treatment to study in the case of clinical *in vivo* Cherenkov imaging, because there is, unfortunately as a reality of cancer care, a large throughput of patients from which to draw. While some clinics use intensity modulated radiotherapy

(IMRT) or brachytherapy techniques,⁵⁴ the institution where this research was conducted opts for 3D conformal external beam radiation therapy (3D-CRT).

In 3D-CRT, two tangential gantry angles are selected to appropriately target the whole breast and chest wall, while sparing the lung and heart, with several field-in-field multi-leaf collimator-defined control points. Right breast cases are treated with the patient free-breathing, while left breast patients are treated during deep inspiratory breath hold (DIBH) to maximize the distance between the chest wall and the heart.⁵⁵ Even though each patient treatment is uniquely simulated and planned, the overall similarities and simplicities of the setup provide repeatable imaging scenarios between patients. Following the guidelines of the American Society of Therapeutic Radiation Oncology (ASTRO), patients in the described observational study were prescribed either 50 Gy over 25 fractions in 5 weeks (standard fractionation), or 42.5 Gy over 16 fractions in 3.2 weeks (hypofractionation, Canadian trial schedule).⁵⁶

2.2.2 Mycosis Fungoides and Total Skin Electron Therapy

TSET is an interesting and somewhat unique treatment scenario in the radiotherapy clinic. First, there is no patient-specific treatment planning or simulation imaging; each patient is treated following an established clinical protocol, and the response is clinically managed. Second, the patient is irradiated with large-field beams at an extended source to surface distance (SSD) in six standing configurations. This is opposed to treating at linac isocenter with the patient in a supine position, which is the case for most other treatments (including WBI). Finally, TSET is most commonly a palliative technique for mycosis fungoides, a relatively uncommon affliction (approximately 3000 Americans per

year),⁵⁷ meaning most clinics, if they offer TSET at all, only treat a handful of cases annually.

The name mycosis fungoides is somewhat misleading – fungus is not an etiologic or persistent element of the disease. Rather, it is a low-grade non-Hodgkin’s cutaneous T-cell lymphoma with “mushroom-like” tumors, first described in the early 1800s.⁵⁸ The disease is difficult to cure; it progresses from an erythematous stage, to a plaque stage, then to a tumor stage, manifesting over much of the skin surface with possible involvement of the lymph nodes, with inherent risks of ulceration and secondary infection.⁵⁹

Since the 1950s, electron therapy has been developed and applied as a mode of treatment for mycosis fungoides, with the general aim of delivering a superficial dose of radiation to the entirety of the patient skin surface.^{57, 59–65} A commonly adopted approach is the dual field, six position modified Stanford technique,^{60, 66–68} which was studied in this work. A TSET patient being prepared for irradiation is shown in Figure 2.5.

Following the uniqueness of TSET, a second application of Cherenkov imaging within the radiotherapy clinic that has been documented herein is the use of the technology in TSET setup and treatment. The lack of patient-specific treatment planning makes Cherenkov imaging an appealing treatment verification tool that may be able to enhance the clinical assessment of treatment responsiveness. Additionally, Cherenkov imaging can easily be adapted to observe and measure the very large fields involved in TSET, both *in vivo* or in phantoms to verify the treatment setup. The lack of frequency of

the treatment can understandably lead to inherent inefficiencies with TSET, which can be brought to light via Cherenkov imaging.



Figure 2.5 Patient with mycosis fungoides standing in a patient support structure designed to aid in positioning for the six stances required during the implemented TSET protocol. Skin plaques and lesions are apparent throughout the entire skin surface.

2.2.3Magnetic Resonance Imaging Guided Radiotherapy

An emerging modality of radiotherapy is centered on combining the real-time internal anatomy imaging capabilities of magnetic resonance imaging (MRI) with treatment, known as magnetic resonance imaging guided radiotherapy (MR-IGRT).⁶⁹⁻⁷² Unlike its tomographic-based counterparts, MRI is known for its exceptional soft-tissue contrast, lack of radiation dose, and ability to reconstruct images in any plane of subjects and detectors. Therefore, MR-IGRT systems can be used to monitor internal movement of the target region that results from breathing, the beating heart, gas exchange, or other

subconscious but requisite processes, as it happens, and limit the radiotherapy beam to only deliver dose when the target is within the acceptable beam path.

The very first patient was treated with FDA-cleared MR-IGRT in 2014, on a system that used 3 independent cobalt-60 x-ray photon sources integrated in a gantry within a split-bore 0.35T MRI.^{71, 73} In 2017, the first patients treated with MR-IGRT systems that incorporate MRIs with medical linacs as the radiation sources were documented.^{74, 75} Transitioning from the constant radiation source cobalt-60 to a medical linac was a technical challenge, since the presence of the primary magnetic field of the MRI naturally affects the initial electron beam generation and steering; the engineering accomplishment took substantial magnetic shielding design.

There are other technical challenges that arise from the presence of a strong magnetic field in the vicinity of radiation dose delivery. First, the dosimetric tools typical to the field of radiotherapy are not all MR-compatible.⁷⁶ Second, since the fast free electrons ionized by the incoming x-ray photons are the catalysts of radiation damage within tissue, those electrons become subject to the magnetic field effects themselves.^{72, 77-81} The most severe aberrations occur at tissue-air interfaces, due to the electron return effect.⁸² Fully understanding and accounting for these irregularities (compared to traditional radiotherapy systems) is critical for safe and efficacious patient treatment under this novel modality. In this thesis, applications of Cherenkov imaging as an MR-compatible dosimetry tool are explored.

In spite of the challenges, MR-IGRT systems have shown promising clinical results with improved outcomes for certain diagnoses. The increased precision of radiation

targeting allows for dose escalation while more confidently sparing nearby organs at risk. This has been a critical milestone in the treatment of pancreatic cancer, for which a study has reported clinically significant improved survival outcomes for adaptive MR-IGRT patients.⁸³ Prospective clinical studies are also planned or underway for abdominal and thoracic malignancies.^{84, 85} While long term survival results are not yet available due to the infancy of MR-IGRT in the clinic, the radiotherapy community is optimistic that the technology will continue to grow and provide the required tools to treat areas previously regarded as too risky for therapeutic dose delivery.

2.2.4 Volumetric Modulated Arc Therapy

Linac beams can be intricately shaped to match a target volume via a grid of a few millimeter-wide radiation-blocking leaves called the multi-leaf collimator (MLC); the linac gantry can also rotate 360° about the patient, and new linacs have treatment couches capable of 6 degrees of freedom for positioning. Therefore, if the treatment target is placed at or near the gantry isocenter, it is possible to deliver radiation to the target from multiple angles of entry through the patient, and effectively distribute and minimize radiation to healthy tissue, and maximize radiation to the target volume.

With the advancement of computing algorithms and calculation speeds, this approach has evolved to encompass everything from using numerous shaped beams from various static gantry angle positions (intensity modulated radiation therapy, IMRT), to completely dynamic plans where the radiation beam is modulated in dose rate and in shape by the MLC as the gantry rotates around the patient (volumetric modulated arc therapy, VMAT).⁸⁶

First introduced in 2007, the clinical use of VMAT is still significantly on the rise worldwide.⁸⁷ To guarantee patient safety during treatment, there must be a robust system of checks to ensure that patient treatment falls within established confidence margins. However, none of the currently used procedures allows for observation of the radiation beam interacting with the patient. With this desired capacity in mind, Cherenkov imaging has been used to observe VMAT treatments.⁸⁸ VMAT treatments are, by nature, extremely dynamic, and therefore a high frame rate is necessary, with frequent acquisition of background images.

2.2.5 Cherenkov Imaging During Proton Therapy

Cherenkov imaging application development for electron and photon therapies has been more possible than proton therapy due to easy access to these medical linear accelerators. Most proton studies have focused on the Cherenkov light generated within fibers or plastic scintillators during proton therapy, and not imaging the emission from patient tissue.²⁸ Very preliminary studies on the feasibility of Cherenkov imaging during proton therapy have been conducted using simulations, with only conclusions that it is Cherenkov light that contributes to the glow proton therapy patients report even with eyes closed.⁸⁹

It was shown that even though the primary protons are below the Cherenkov energy threshold for the particle type, liberated secondary electrons are capable of producing Cherenkov photons. However simulations by Glaser et al.⁷, indicate that most of the electrons produced by proton irradiation in the Bragg peak are well below the energy threshold for Cherenkov emission, so there is little signal at the Bragg peak within

tissue or water. Given that the Bragg peak is located at the depth of maximum dose deposition (dependent on proton beam energy), dosimetric information at this location is of crucial interest for any potential QA efforts of proton beams. More study might assess the feasibility of *in vivo* Cherenkov imaging during proton therapy, although at this time the signals are estimated to be significantly less than is observed in traditional photon based therapy.

2.3 Quality Assurance with Cherenkov Imaging

The concept of imaging the Cherenkov emission in water to perform quality assurance (QA) of radiation beams from medical linear accelerators has been developed in our lab over the past several years. These efforts have included 2D static beam analysis,⁷ optical cone-beam tomographic reconstruction for 3D static beam analysis,⁹⁰ as well as 2D temporally resolved IMRT and VMAT dynamic visualization and analysis.⁸ These techniques have been possible because of the inherent linear relationship between deposited radiation dose and the number of generated Cherenkov photons.¹⁸

The basic materials used for these approaches include a water tank that is optically black on all sides (except for the transparent imaging face), and an appropriate camera capable of imaging the low intensity Cherenkov emission (see Section 2.4). Camera selection in this case predominantly affects the speed, efficiency and temporal resolution of data collection. Since there are no inherent dose limits to the water tank, even cameras without intensifiers are possible imaging candidates, however they are generally not ideal sensors.¹⁰

2.3.1 Static Beam Analysis in 2D

An intuitive and original application of water tank Cherenkov imaging has been the simultaneous capture of percent depth dose (PDD) as well as cross-beam profile (CBP) curves. The PDD describes the depth- and energy- dependent dose deposition of an ionizing radiation beam down the central axis of the beam, while the CBP is a lateral plot of the beam flatness and symmetry at a given depth. These are acquired by imaging the flat, transparent, front face of a water-filled tank, with the camera orthogonal to the radiation beam, which is incident on and normal to the water's surface. The camera is aligned such that the water line is in the direct center of the image, so that the surface of the water is not imaged as a plane. There is minimal uncertainty introduced by the meniscus, which can generally be ignored.

In post-processing, the central vertical axis of the beam can be plotted to produce a PDD curve. Taking a horizontal row at the depth of maximum dose, the CBP can be extracted. Test target images are used to calculate the relationship between pixel size and physical measurement in the imaged plane (mm/pixel), so that the data can be easily interpreted and registered with conventional measurement devices.

Previous work by Glaser et al. hypothesized that there are two prime factors that need to be accounted for in order to optimize the correlation between the Cherenkov derived curves and more conventional measurement tools such as ionization chambers or diodes: 1) the inherent directionality of the Cherenkov emission,⁹¹ and 2) the relationship between beam hardening and the energy dependence of the Cherenkov emission intensity.⁸

Cherenkov emission directionality implies that there is an inherent bias in the number of photons that make it to the detector, that is dependent on the geometric relationship of where the photon is generated versus the detector position; it does not affect the theoretic relationship that establishes the linear correlation between how many Cherenkov photons are generated in the medium and the deposited dose. To account for this, Glaser et al. proposed two main correction schemes. The first was to apply an anisotropic phase function, derived from Monte Carlo simulations, as a correction to data knowingly acquired with this bias.⁹¹

While effective for simple, static beam shapes, this approach can become cumbersome with dynamic or irregular beam geometries. The second approach was more experimentally founded: doping the water tank with the fluorophore quinine sulfate, so that the Cherenkov photons are absorbed and re-emitted isotropically as Cherenkov-excited fluorescence (CEF), thereby constraining the effect of the original directional bias.⁹⁰ This latter method has been demonstrated to be both simple and reliable, and has been adopted for all subsequent Cherenkov imaging QA techniques in water tanks described.

2.3.2 Optical Cone-Beam Tomographic Reconstruction

The tomographic reconstruction of static radiation beams was a natural extension of the Cherenkov imaging technique described in Section 2.3.1. Images are acquired at angular increments about the radiation beam, and a cone beam back projection algorithm is applied to reconstruct a 3D surrogate of deposited dose in the tank.⁹⁰ If a telecentric lens

is used to acquire the images, the divergence associated with the cone of acceptance of the lens is severely restricted, and a simpler back-projection algorithm can be employed.⁹²

There are two main approaches to acquiring the images required for the reconstruction: 1) rotate the water tank and camera under the static radiation beam, maintaining orthogonality between the imaging face of the water tank and the optical axis of the camera, and 2) keep the water tank and camera stationary, and rotate the collimator head while holding the multileaf collimator (MLC) and x-y jaw positions. The second option tends to be much faster, because there is no perturbation in the water tank with each angular increment that necessitates a waiting period for the water to resettle.

2.3.3 Real-Time Dynamic Plan Visualization

Perhaps the most unique and novel application of Cherenkov imaging for water tank QA is the capability to provide high spatial resolution data on this dose surrogate as it aggregates in real-time for highly dynamic treatment plans utilizing intensity modulation radiation therapy (IMRT) or volumetric modulated arc therapy (VMAT) techniques.⁸ When using Intensified Charge Coupled Device (ICCD) cameras, frame rates between 2-30 frames per second (fps) have been demonstrated. While imaging the front face of the tank, which is parallel to the plane of gantry rotation, simple addition of the frames provides a real-time view of the location and relative intensity of dose deposited in the water volume.

The benefits of this technique are that it provides a direct view of dose from extremely dynamic plans in real-time, with high spatial resolution, which are only limited by the capabilities of the imaging camera. Viewing dynamic dose from IMRT and VMAT

plans has historically been limited to point measurement array systems such as the ArcCHECK (Sun Nuclear Corp., Melbourne, FL),⁹³ or to portal image views using Electronic Portal Imaging Devices (EPIDs).^{94–96} More advanced techniques using EPIDs have implemented back-projection algorithms, which include estimates of transmission from water-equivalent measurements and/or CT contour data to make them applicable, to an extent, *in vivo*.^{97, 98} A new approach to acquiring transmission measurements for similar back-projection algorithms is currently being explored using Cherenkov imaging.⁹⁹

2.4 Review of Other Medical Cherenkov Detection Applications

2.4.1 Nuclear Medicine

Studies of detection of Cherenkov photons have been carried out in biomedical assays for decades and, starting in 2009, several reports showed *in vivo* detection of these signals was possible.^{100–104} These optical imaging approaches of detecting the emitted Cherenkov photons from nuclear radiation decay, dubbed Cherenkov Luminescence Imaging (CLI), illustrated that experimental nuclear medicine research could be carried out with optical detectors, rather than with single photon emission computed tomography (SPECT) or with positron emission tomography (PET) systems, which are much larger and more expensive. These latter nuclear medicine systems are used widely in molecular imaging, but the methods have high cost, limited availability and throughput, modest spatial resolution and can be time-consuming.¹⁰⁵

As such, optical imaging for radionuclide detection largely solves the mentioned problems of PET and SPECT. In addition, CLI has relatively high sensitivity when the light

is not attenuated by large volumes of tissue. Since 2009, many applications in preclinical studies have been examined both *in vitro* and *in vivo* in small animal models. A representative group of publications is summarized in Table 2.1, to illustrate a wide range of applications, radionuclides, and conclusions about the imaging modality.^{100, 102, 106–114} The results of these studies indicate that the obtained data from Cherenkov radiation detection shows good agreement with PET imaging results for *in vitro* and *in vivo* tests, mostly in small animals, and the potential of CLI in quantitatively assessing radionuclide purity.

All of the preclinical studies cited above used either some version of a commercially available *In Vivo* Imaging System (IVIS), now manufactured by Perkin Elmer, or a simple optical setup with a sensitive charge coupled device (CCD). The IVIS is a phantom or small animal imaging system which typically consists of a heated support for the animal, an anesthesia manifold, lens with interchangeable filters, and a CCD detector, all enclosed in a light tight box. It can also be equipped with optical excitation sources to match the absorption of a particular target. However, in the case of CLI, these are not necessary, because the particle emissions from active radiotracers serve as the excitation source for Cherenkov emission.

Imaging small animals is straightforward with CLI because the Cherenkov light does not have to travel through large lengths of tissue before being detected at the skin surface. However, translating the technique to human studies is challenging as localized signals within organs are quickly attenuated by the more expansive volumes of tissue. Therefore, for CLI to be applicable to human studies, more invasive procedures are

necessary. Early phase human studies have been demonstrated^{115, 116} in the scope of CLI-guided surgery, where the signal only has to be detected within an intraoperative cavity. There is also promise of endoscopic-based CLI, which is minimally invasive, as shown by H. Hu et al. in their study of gastrointestinal disease.¹¹⁷

One of the major drawbacks of CLI is that it is limited to 2-D imaging. Several groups have tried to apply tomographic reconstruction algorithms to CLI to overcome this problem and provide 3-D localization of the Cherenkov light source through Cherenkov Luminescence Tomography (CLT). This was first demonstrated in 2010,¹¹⁹ but at much lower spatial resolution than PET due to the amount of light scattering. Several groups are working towards developing higher resolution reconstruction techniques.^{120, 121}

Table 2.1 Select publications on pre-clinical CLI using various radionuclides with summarized conclusions in chronological order

Publi- cation	Instrument	Radio- nuclide(s)	Emitted Particle(s)	Conclusions
Cho et al. ¹⁰⁰	CCD unit	¹⁸ F	β^+	<ul style="list-style-type: none"> CLI evaluated amount of radioactivity within microfluidic chips (MFCs) Effective tool to test MFCs for failure
Spinelli et al. ¹⁰²	IVIS 200 Xenogen	¹⁸ F	β^+	<ul style="list-style-type: none"> CLI used to image ¹⁸F uptake Localized source depth of Cherenkov Correlated with PET results
Ruggiero et al. ¹⁰⁶	IVIS 200 Xenogen	¹⁸ F, ⁶⁴ Cu, ⁸⁹ Zr, ¹²⁴ I, ¹³¹ I, ²²⁵ Ac	β^+ , β^- , α	<ul style="list-style-type: none"> First use of CLI for quantitative radiotracer uptake <i>in vivo</i> In vitro results correlated with PET
Kim et al. ¹⁰⁷	IVIS Spectrum	¹⁸ F	β^+	<ul style="list-style-type: none"> CLI was used to identify radiolabeled markers for Alzheimer's disease
Aweda et al. ¹⁰⁸	IVIS 100	⁹⁰ Y	β^-	<ul style="list-style-type: none"> CLI was used to visualize a tumor via a particular reporter gene expression in mice
Holland et al. ¹⁰⁹	IVIS 200 Xenogen	⁸⁹ Zr	β^+	<ul style="list-style-type: none"> CLI guided surgical resection is feasible Tumor uptake is quantifiable
Park et al. ¹¹⁰	IVIS 200 Xenogen	⁶⁸ Ga, ³² P, ¹²⁴ I, ¹⁸ F, ¹³¹ I, ⁶⁴ Cu, ¹¹¹ In, ^{99m} Tc, ³⁵ S	β^+ , β^- , electron capture, isomeric transition	<ul style="list-style-type: none"> High energy β^+ and β^- emitters performed well for CLI <i>in vitro</i> CLI can be used for radiochemical purity testing CLI useful in animal/plant sciences
Yang et al. ¹¹¹	IVIS Kinetic	¹³¹ I	β^-	<ul style="list-style-type: none"> CLI performed similarly to γ-camera imaging for determining expression of an miRNA in lung cancer cells
Zhang et al. ¹¹⁸	IVIS Spectrum	¹⁸ F	β^+	<ul style="list-style-type: none"> CLI can be used to localize interscapular brown adipose tissue faster and cheaper than PET
Wang et al. ¹¹³	IVIS Lumina	¹⁹⁸ Au	β^-	<ul style="list-style-type: none"> Radioactive gold nanocages work as a contrast agent in CLI imaging, allowing imaging of whole mice
Natarajan et al. ¹¹⁴	IVIS Spectrum	⁸⁹ Zr	β^+	<ul style="list-style-type: none"> CLI agreed well with PET results in determining targeting of a tracer for bio-marked B cells

2.4.2 Molecular Imaging and Assays

Molecular imaging and molecular sensing assays are now being established with Cherenkov excitation. These emerging areas are new and substantially less developed than the dosimetry approaches, yet could have substantial impact. Cherenkov light excited molecular fluorescence has been demonstrated in a number of nuclear medicine applications, allowing detection of therapeutic doses and even β -emitters which would not otherwise be detected externally to the body.^{122, 123}

Cherenkov-excited optical signals can be used to biochemically sense the environment of the medium that the probes are in. So for example in tissue, sensors for oxygenation or pH are routinely used in experimental studies,^{20, 124, 125} and can now be used in vivo, either coupled to nuclear emission of injected radiation dose, or through external beam irradiation.¹²⁶ Both have been demonstrated in the past few years.

Chapter 3: Cherenkov Emission Detector Selection Study

This chapter is largely derived from: J.M. Andreozzi, R. Zhang, A.K. Glaser, L.A. Jarvis, B.W. Pogue, and D.J. Gladstone, "Camera selection for real-time, in vivo radiation treatment verification systems using Cherenkov imaging," Med. Phys. 42(2), 994–1004 (2015).

Cherenkov emission is a low intensity photon signal spanning the entire optical spectrum, therefore the successful realization of Cherenkov imaging in a clinical setting would require several key criteria be met by the hardware. There are three critical components of the clinical environment in this regard. First, the emission from human tissue is attenuated by absorption and scatter, as compared to water emission, so the camera must have sufficient gain to image a low light level. Second, the system must be able to capture this signal in the midst of ambient room light at levels typically used for patient safety and comfort.

Finally, to be viable as a tool at monitoring and detecting deviations from the planned treatment in real-time, especially in dynamic therapies such as IMRT or VMAT, the rate at which the camera captures and displays the information must approach video frame rates (5-30 frames per second).⁵ By monitoring the beam in real-time, irregular beam deliveries which manifest as abnormal beam shapes (from patient misalignment, multi-leaf collimator malfunction, etc.) or uncharacteristic intensities (improper beam accessories) could be detected. Several camera systems were tested and assessed based on these criteria: i) low light sensitivity, ii) background light suppression, and iii) fast frame rate, in order to identify the best candidates for clinical Cherenkov imaging.

Based on previous experiences, our hypothesis was that real-time clinical Cherenkov imaging of patients for treatment verification would require a detector equipped with both a high gain mechanism, as well as triggered, time-gated acquisition capability. Yet, to be thorough in the evaluation, a set of cameras representing the comprehensive possible choices was used, with no gain, with gain, without gating and with gating. Comparison analysis was completed with average intensity values from images of a standard phantom, using a simple phantom in the same treatment and imaging geometry. Finally, the two high performing choices of cameras were compared directly in images taken during the first clinical trial of Cherenkov imaging during radiotherapy as a standard of comparison for the other imaging systems.

3.1 Cameras

The five cameras listed in Table 3.1 were investigated in this study to determine metrics of performance for Cherenkov imaging under clinically relevant conditions. Each of the four types of cameras represented, charge-coupled device (CCD), complementary metal-oxide-semiconductor (CMOS), intensified charge-coupled device (ICCD), and electron multiplying-intensified charge coupled device (EM-ICCD) have their own inherent strengths and weaknesses. The key factors in the evaluation here were related to: i) low light sensitivity or detective quantum efficiency (DQE) , ii) ambient light rejection, which is solved by gated intensified acquisition typically, and iii) frame rate capability. Of the available options, there are many nuances to the specifications, which will be briefly discussed below. Table 3.1 lists specifications identified as the most meaningful indicators of Cherenkov imaging performance.

Table 3.1 Key performance specifications of the five cameras examined as possible detectors for clinical Cherenkov imaging. For the PIMAX cameras the image intensifier is specified as either Unigen2 or HRf in the sensor type.

Sensor Type	Camera Model	Approx Cost	Chip Size (mm)	Pixel Size (μm)	Sensor Size (pixels)	Gain Factor	Gate Time (ns)	QE of Detector @ 700nm	QE of Intensifier @ 700 nm	Max Frame Rate
CMOS	Canon EOS Rebel T3i	\$600	22.3 x 14.9	4.3	5184 x 3456	1	N/A	\approx 25-40%	N/A	3.7
CCD	Apogee Alta F8300	\$3k	18 x 13.5	5.4	3326 x 2504	1	N/A	42%	N/A	0.1
ICCD (Unigen2)	PIMAX3 1024i	\$55k	13.1 x 13.1	12.8	1024 x 1024	100	2	27%	19%	27
ICCD (HRf)	PIMAX4 1024i	\$60k	13.1 x 13.1	12.8	1024 x 1024	100	2	27%	30%	27
EM-ICCD (HRf)	PIMAX4 512EM	\$85k	8.0 x 8.0	16.0	512 x 512	10,000	2	46%	30%	30

Cost can be a prohibitive factor in realizing any novel modality (imaging or otherwise), and as such, it was deemed necessary to take it into consideration during the evaluation. Low cost was one motivation for including the CMOS and CCD camera options in this study, along with their comparatively high quantum efficiency (QE) values. The monetary values shown in the table reflect figures quoted at the time but could vary by a factor of 2 depending upon manufacturer and specifications. The consequences of overall resolution, and the constituent chip and pixel sizes, were left as qualitative factors to be discussed with reference to the clinical images acquired for this study.

The ability to time gate image acquisition down to 3-5 microsecond intervals is an important ability inherent in the intensified cameras, since the emission of Cherenkov photons is limited to the small time gap immediately after the radiation pulse enters the tissue.¹²⁷ The intensifier itself is able to act as a fast optical switch that activates when

Cherenkov emission is expected. Results from the first two cameras listed in Table 1 will further illustrate the importance of this ability in the next section.

Cherenkov emission has a continuous wavelength spectrum heavily weighted in the blue, but because tissue absorbs light in these spectral regions, the detected Cherenkov emission from the surface of the patient is predominantly in the red and near-infrared region.^{11, 20, 128, 129} The quantum efficiency of the detectors and intensifiers at 700 nm is subsequently valuable in Table 3.1 as a metric for comparing sensitivity to Cherenkov emission from tissue. It is important to point out that mismatch between the Cherenkov emission spectrum and the spectral response (quantum efficiency curve) of the detection hardware will influence the perceived intensity of the imaged Cherenkov light. Success in Cherenkov imaging requires thoughtful hardware selection in this regard.

Two ICCDs were compared to evaluate the effect of the different intensifier characteristics. The intensifiers are the sole gain mechanism of these two cameras. Incoming optical photons are incident on the photocathode, and converted to electrons. These electrons are then accelerated and multiplied in the noise-free vacuum of the micro-channel plate amplifier, and then the amplified electron signal is converted back to optical photons using an output phosphor screen at the back of the intensifier. The photons generated in the phosphor screen are then imaged by the CCD detector as the recorded image.

The gain offered by the intensifier serves to diminish the effect of readout noise and shot noise in the final images, since the latter noise sources become relatively small in comparison to the amplified average signal. One drawback in the proposed application

is the amplification of noise from stray radiation photons can occur, leading to high singular point 'salt-and-pepper noise' in the Cherenkov photon signal. However, the image processing methods of primarily temporal median filtering described in this paper sufficiently remove both natural (CCD, CMOS) and amplified (ICCD, EM-ICCD) salt-and-pepper noise.

Each model intensifier has a wavelength-dependent spectral response (provided from the manufacturer as quantum efficiency curve) based on the sensitivities of the photocathode. Not only does the phosphor screen efficiency vary between tubes, but there is also an efficiency associated with the optical coupling of the components, in addition to each CCD also having its own inherent quantum efficiency spectral response. So, all of these factors multiply together to produce the final signal, and must be taken into consideration when evaluating ICCD performance.

One of the ICCDs was equipped with a Unigen 2 coated filmless Generation 3 intensifier with a P43 output phosphor (Unigen 2) that has peak spectral response varying between 17-19% quantum efficiency in the 500-800 nm range. The Unigen 2 coating extends the spectral response of the intensifier into the UV range, while being transparent and having no effect in the red/infrared regions. The benefit of this coating is limited for imaging Cherenkov in tissue, for the reason described above. The camera design with the Unigen 2 coated intensifier also includes a fiber optic plate, which has a certain loss factor in translating the phosphor image to the CCD.

The Unigen 2 ICCD was the primary imaging system used in the recently concluded first clinical trial of Cherenkov imaging during radiotherapy.⁴⁹ Eleven of the twelve whole-

breast radiotherapy patients in this trial were imaged with this ICCD, and most of the data was acquired at a frame rate of 4.7 frames per second. The average Cherenkov intensity measured from the phantom in this study by the Unigen 2 ICCD at 4.7 frames per second is thus considered the minimum standard for performance comparison.

The second ICCD investigated employed an extended red filmless HRf Generation 3 P43 phosphor intensifier (HRf), which is optimized for a 500-800 nm wavelength range, with a quantum efficiency of over 25% in that region. The higher peak quantum efficiency, coupled with the lack of the fiber optic window between the intensifier and photocathode, promised better signal from the HRf ICCD when compared to the Unigen 2 ICCD. Both cameras have the same CCD chip (Kodak KAI-1003), so overall performance of the HRf camera was expected to exceed that of the Unigen 2 ICCD.

Finally, the EM-ICCD was examined because it presented an attractive prospect for an extremely high-gain system, coupled with the ability to gate the intensifier (also an extended red filmless HRf Generation 3 P43 phosphor intensifier). The EM-ICCD offers two separate gain mechanisms to enhance the incoming signal. First, like the ICCD, the EM-ICCD uses an external intensifier. Second, it has an electron-multiplication mechanism associated with the particular CCD, whereby the already-intensified photon signal is further amplified after optical CCD detection, through a gain register in the detector electronics. Like the ICCD, the EM-ICCD is largely insensitive to read-out noise, since the two gain mechanisms allow the incoming signal to dominate by orders of magnitude.

The tested EM-ICCD was equipped with the HRf Generation 3 P43 phosphor intensifier (same as one of the ICCDs) coupled with a CCD97-00 Front Illuminated 2-Phase Electron Multiplying CCD (e2v inc., Milpitas, CA). The EM-ICCD was used to image one patient in the twelve-patient clinical trial referenced above, in addition to the phantom experiment, to examine the potential for higher frame rate imaging with the enhanced gain.

3.2 Experimental Setup

To construct a fair comparison between the detectors, the five cameras were positioned in similar geometries to image a flat, 1 cm thick square of opaque white Plastic Water phantom (CMNC, Nashville, TN) in front of a 4cm thick block of brown opaque Solid Water phantom (CMNC, Nashville, TN) using the same lens, a Canon EF 135 mm f/2L USM lens (Canon U.S.A., Inc., Melville, NY). The phantom was irradiated by a 6MV, 10cm x 10cm photon beam at a dose rate of 600 monitor units per minute (MUs/min), generated from a Clinac 2100CD linear accelerator (Varian Medical Systems, Palo Alto, CA). As shown in the upper diagram of Figure 3.1, the gantry was set to 90° (given 0° is at the bottom of the rotation facing the ceiling, and 180° is at the top of the arc towards the floor) so that the photon beam was perpendicularly incident on the phantom, which was placed upright on the treatment table.

The cameras were positioned to the side of the gantry to image the full expanse of the phantom with a minimal deviation from the beams eye view to prevent occlusion by the gantry. The white light image in Figure 3.1 was captured on the CCD to record the standard camera scope of view, which includes a partial view of the gantry head in the

right of the frame. A black sheet was placed on the treatment table when imaging with the intensified cameras to eliminate the effect of reflection from the table surface. To monitor data acquisition in real-time, the cameras were controlled via USB or GigE interfaces with a laptop at the treatment console station just outside of the linac room.

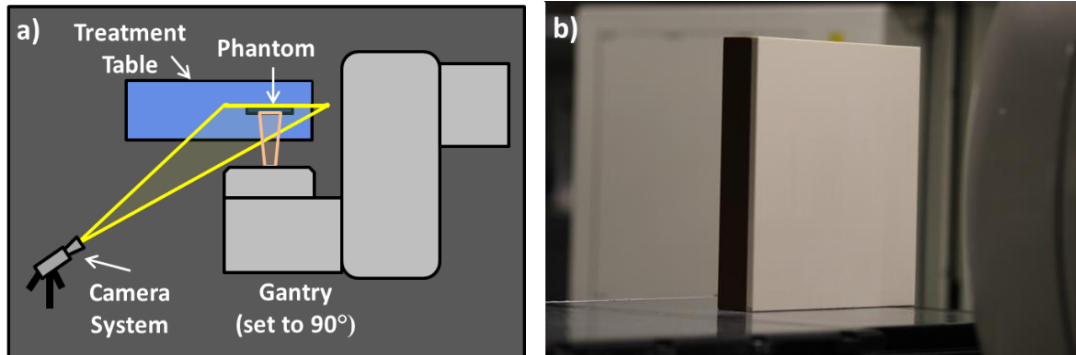


Figure 3.1 a) A top-down view of experimental setup. The gantry was set to 90° , and the radiation beam was incident on the flat solid water phantom positioned vertically on the treatment table. The cameras were placed so as to image the surface of the phantom at an angle without being obstructed by the gantry. b) Example white light image of the phantom taken on the CCD camera while in position.

3.3 Image Acquisition and Processing

The image acquisition process for each of the cameras varied slightly based on the unique proprietary software interfaces and camera settings inherent to each of detection systems; in general, the manufacturer recommended acquisition software was used for each camera. The group of five cameras is naturally separated into two categories: standalone (CMOS, CCD) and intensified (ICCDs, EM-ICCD) detectors. Both categories were processed slightly differently according to this distinction and the general formatting of the native files, but all raw images captured during data acquisition required

post-processing to elucidate the Cherenkov information following the same conventional method.

The characteristic salt and pepper noise observed in the raw images is caused by stray radiation in the imaging environment, and is reliably removed with median filtering. Consequently, general processing consisted of application of a temporal median filter across subsequent images, followed by subtraction of a background image to remove any remaining ambient light contributions, and completed by the application of an 11x11 spatial median filter to remove any remaining stray noise.¹³⁰ This method also effectively diminishes some of the Poisson or shot noise, since the statistical fluctuations from the detector are reduced in much the same way as the more obvious salt and pepper noise from stray radiation. Background subtraction also serves to remove any bias signal from the detector itself. This post-processing was carried out in MATLAB (The MathWorks, Inc., Natick, MA).

The CMOS camera was operated in single-image acquisition picture mode to exploit the full resolution of the camera (5184 x 3456). With all room lights turned off, ten images for each of the three test exposures were acquired with the beam on (Cherenkov frames), and three images were also acquired at the same exposure time but with the beam off to be used as background images, using the software package Canon EOS Utility (Canon U.S.A., Inc., Melville, NY). Three exposure times, 0.1 s, 1.0 s, and 3.2 s, were tested. After conversion from RGB color format to grayscale intensity, the set of thirteen images corresponding to each of the three exposure times were condensed into a single representative grayscale image. The average of the three background frames was

subtracted from the median of the ten Cherenkov frames, and the result was smoothed with an 11x11 spatial median filter, and displayed with an intensity-based colormap for ease of visual interpretation.

In the same manner, a custom LabVIEW (National Instruments Corporation, Austin, TX) program was used to acquire a video stream of ten Cherenkov images and three background images with the radiation beam on and off, respectively, from the CCD. All room lights were turned off when imaging with the CCD, since there is no inherent microsecond-level triggering capability. Exposure time was set to 0.1 s, 1.0 s, and 3.0 s; longer exposure times resulted in partial saturation of the chip. The grayscale CCD data was processed into three descriptive composite images, corresponding to each of the tested exposure times, following the same steps as outlined for the CMOS camera above.

The biggest distinction between acquisition using the two standalone detectors and the three intensified detectors was the ambient room light conditions; the former required all room lights be turned off, while the latter allowed for soft lighting from incandescent bulbs throughout the room. This distinction arises from the triggering and sub-microsecond gating capabilities of the intensifier. A software package called LightField (Princeton Instruments, Trenton, NJ) produced by the manufacturer of the intensified cameras allowed for extensive control of gain, time-gating, and acquisition settings, and was used to acquire all images on the intensified detectors.

Since the linac delivers radiation as a series of pulses at a frequency dependent on the dose rate (for example, approximately 200 Hz at a dose rate of 600 MUs/min), it is possible to both synchronize (trigger) and limit image acquisition to the instant of

Cherenkov emission (time gate) by using the intensifier as a picosecond-capable optical switch or shutter. Current mechanical shutters are not capable of achieving the small time-scale triggering and gating that the intensifier inherently provides and is necessary for this application.

For the photon beam described above, intensified image acquisition is restrained to a window which starts $0.027\ \mu\text{s}$ after the trigger signal is received (the smallest trigger gate delay supported by the tested cameras), and stays open for $3.25\ \mu\text{s}$; these values are specified in the acquisition software LightField, and based on Monte Carlo simulations regarding the duration of Cherenkov photon emission.¹²⁷ The trigger signal originates from the linac as the current on the x-ray target (a roughly 200 Hz signal), which is accessible as a voltage on the linac stand compartment through a bayonet Neill-Concelman (BNC) coaxial cable connection; the trigger threshold in this case was set to $-0.5\ \text{V}$. The trigger voltage threshold can vary based on the make, model and mode of the linac being used.

The triggering and gating of image acquisition allowed the intensified cameras to only capture data in the microsecond windows when Cherenkov photons were being emitted from the surface, as opposed to continuous acquisition as was the case for the standalone detectors. Each linac pulse triggered the image intensifier to turn on for the prescribed gate window, and provided the signal for one accumulation of data on the CCD chip.

Once the set number of accumulations on chip was aggregated on the detector, the image was read-out to software. The readout process took the most time, and it

created the camera-specific limit on maximum supportable frame-rate. In the case of the ICCDs, this was 12.9 fps using the full resolution of the chip. Beyond read-out time, the frame rate of data acquisition was dependent on how many on-chip accumulations were desired for each frame before read-out. The triggering and gating process is described in further detail in previous publications.¹²⁷

Subsequently, instead of varying the exposure time to adjust the frame rate as was the case for the standalone detectors, frame rate for the intensified cameras was more appropriately adjusted by varying the number of on-chip accumulations before the image was read off of the sensor. Table 3.2 outlines the trade-off between on-chip accumulations and frame rate, as exhibited by the two ICCDs tested, without image binning; binning can increase the possible frame rate at the expense of reducing spatial resolution. In the case of relatively low number of on-chip accumulations, the read-out time of the camera (approximately 70 ms with 1024 × 1024 resolution) will limit the frame rate. Because a different sensor with lower resolution (512 × 512) is used in the EM-ICCD, it is able to achieve 30 frames per second at one on-chip accumulation, without binning.

Table 3.2. Selected number of on-chip accumulations and associated readout frame rate for the two ICCD cameras (PIMax3 1024i and PIMax4 1024i) when using full chip acquisition (no binning). The number of analyzed frames was varied to reflect a constant overall time of acquisition.

On-Chip Accumulations	1	5	10	15	20	25	30	35	40	45	50	75	100	200
Frames per Second	12.9	11.3	9.73	8.57	7.66	6.92	6.32	5.81	5.37	5	4.68	3.53	2.83	1.59
Analyzed Frames	100	88	75	66	59	54	49	45	42	39	36	27	22	12

The ICCDs, which vary primarily in the quantum efficiency spectra of their intensifiers (Unigen 2 vs. HRf) and camera generation from the manufacturer (PIMAX3 vs. PIMAX4), acquired 100 Cherenkov images and 10 background images at each of the frame rates listed in Table 3.2, at maximum gain setting of 100. However, while condensing the full data set to a single exemplary image for each setting, the number of frames processed was limited to the number of frames that could be acquired in 7.75 seconds, the time it takes to obtain 100 images at a rate of 12.9 frames per second with the ICCDs; the number of frames was then rounded down to avoid introducing partial frames. This technique was implemented during analysis to ensure that the slower frame rates did not receive any artificial inflation from the benefit of longer aggregate exposure times to the Cherenkov signal. By keeping the acquisition time of each data set constant through coordinating the number of frames analyzed with the frame rate, a better relative comparison of performance was established between the various acquisition settings investigated.

The EM-ICCD was tested using various configurations, however the most pertinent for this study was set up at 1 on-chip accumulation (30 frames per second), at a set gain factor of 10,000 between the intensifier (21.54x) and the electron multiplier (464.16x), which were the manufacturer-provided optimized gain settings. It is worthwhile to note that these optimized settings were established for a different imaging application in a separate laboratory environment, and are not necessarily representative of the most advantageous configuration for Cherenkov imaging.

Processing of the images acquired by the ICCDs and EM-ICCD was carried out in the same fashion as the standalone detectors. The median of the stack of Cherenkov images was calculated (with the stack size being the number of images listed in Table 2 for the ICCDs, and 100 images for the EM-ICCD). The average of the background images was subtracted from the median, and an 11 x 11 spatial median was applied. ¹³⁰

3.4 Metric of Performance

Imaging systems that are used for low signal levels, especially where photon counting is a factor, are typically dominated by Poisson distributed shot noise from the probability of detection leading to a distribution of measured values, where the mean is N , and the standard deviation or noise is $N^{1/2}$. In this situation, the signal to noise ratio is thus simply $N^{1/2}$. Overlaid on this noise are the electronic readout noise, spatial noise and any bias errors from background or background subtraction. In this application, there is the addition of salt-and-pepper noise from the random introduction of individual scatter events causing extremely high values at individual clusters of pixels. The combined removal of salt-and-pepper through temporal median filtering together with background subtraction leads to data from different cameras that must be compared quantitatively.

The ideal comparator for medical systems such as this is typically the detective quantum efficiency (DQE), which is formally defined as the ratio of the quanta signal measured to the quanta signal input. Since the input or output quantum signal is simply measured as the square of the signal to noise ratio (SNR), then the DQE at zero spatial frequency can be expressed as:

$$DQE(0) = N_{OUT} / N_{IN} = (SNR_{OUT})^2 / (SNR_{IN})^2$$

The problem in using this expression to compare Cherenkov signals is that the Cherenkov signal input $(SNR_{IN})^2$ would need to be independently measured by another system. Since the Cherenkov signal is itself very low-fluence with a broadband spectrum, it is a challenge to quantify. Additionally most low sensitivity optical detectors are substantially corrupted in the high radiation environment of a therapy room, so the ability to directly measure N_{IN} is very challenging. However, if cameras are compared with a fixed lens and fixed geometry for imaging, then N_{OUT} measured is directly proportional to the DQE. As such, in this study, we show the results as N_{OUT} or $(SNR_{OUT})^2$ for inter-camera comparisons. In the data processing presented here, the SNR was calculated as the average intensity value of the analyzed region, $\bar{\mu}_{ROI}$, divided by the standard deviation of that region, σ_{ROI} :

$$SNR = \frac{\bar{\mu}_{ROI}}{\sigma_{ROI}}$$

3.5 Standalone Detector Results

Figure 3.2 shows the processed images from the tested CMOS and CCD camera, with varying lengths of image exposure. Processing of all presented images included temporal median filtering, background subtraction, as well as spatial median filtering, as described in Section 3.3 . The CMOS images are represented in double format (with values ranging from 0 to 1), while the CCD images are in 16-bit format (values from 0 to 65535), which

affects the interpretation of the value ranges of their respective colorbars. This distinction arises from the native format of the raw data files.

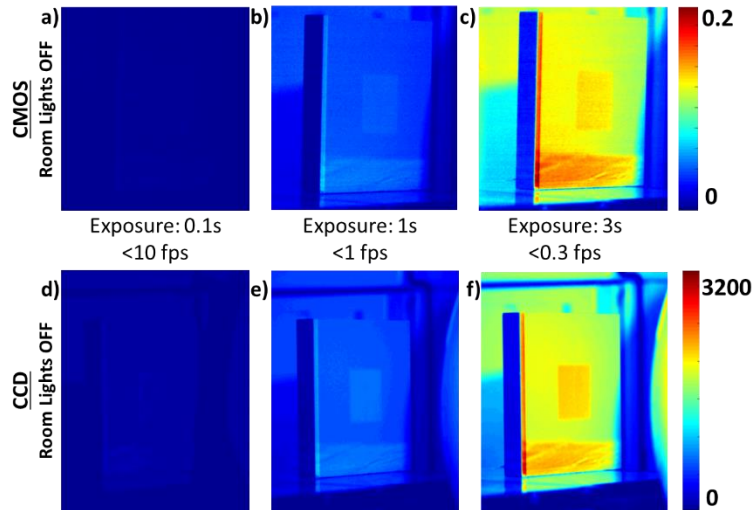


Figure 3.2. Processed Cherenkov images collected using the CMOS (a-c, top row on the same intensity scale) and CCD (d-f, bottom row on the same intensity scale) cameras with varying exposure times. Room lights were off, since there is no mechanism of fast triggering and gating available with these two camera options. Note the Cherenkov signal was low relative to the background room light. At long exposure times with room lights off a modest contrast is seen. Their utility is feasible, but only at low frame rates (below 1 fps), with noticeable background in the image even after background subtraction.

3.6 Intensified Detector Results

Figure 3.3 shows several key imaging results of the three intensified cameras, processed using the methods detailed in Section 3.3. The two columns show three images each that characterize the detected signal at 12.9 (maximum for this detector because of the image readout time from the chip), 9.7 and 4.7 frames per second.

The bulk of the data in the original clinical trial was collected with the Unigen 2 ICCD at 4.7 frames per second. Figure 3.3.c is thus characteristic of the minimum signal desired for an imaging sensor in this application, which is 0.56% of the full 16-bit range

(an average of 369/65536 electron counts per pixel) after processing, including background subtraction. For simplicity, 0.5% was chosen as the average intensity cutoff for adequate Cherenkov signal, which corresponds to a pixel intensity value of 327 as the minimum threshold. The images in Figure 3.3.c-f are from the HRf ICCD for the same frame rates.

Figure 3.3.g shows the image acquired by the EM-ICCD at 30 fps, where each frame is the signal from a single radiation pulse; here, the median of 100 such frames is displayed and analyzed in accordance with the method used for the two ICCDs. This camera is specified to a higher maximum frame rate, because the readout time of the chip is shorter as a result of the lower overall resolution (512x512 versus 1024x1024). The average Cherenkov intensity of the beam region of interest (here only 60 x 100 pixels, again because of the overall decreased resolution of the EM-ICCD to 512 x 512 pixels) was over 20 times the defined minimum threshold for adequate imaging (0.5%, or 327 counts).

Initial visual inspection of these images indicates enhanced performance from the HRf intensifier as compared to the Unigen 2 for the ICCDs. Likewise, the EM-ICCD produced a high-intensity image at the fastest frame rate, due to the increased, dual-faceted amplification capabilities of the hardware. The manufacturer-provided quantum efficiency curves for the intensifiers are reproduced in Figure 2.5.h, alongside the relative number of Cherenkov photons emitted from tissue at each wavelength. The latter curve was generated from a GEANT4-based simulation in GAMOS¹⁶ of a 6MV, 10x10 cm x-ray beam at SSD = 100 cm irradiating a volume with optical properties consistent with those found in literature for a light-skinned sample, as published in previous work.⁴⁸

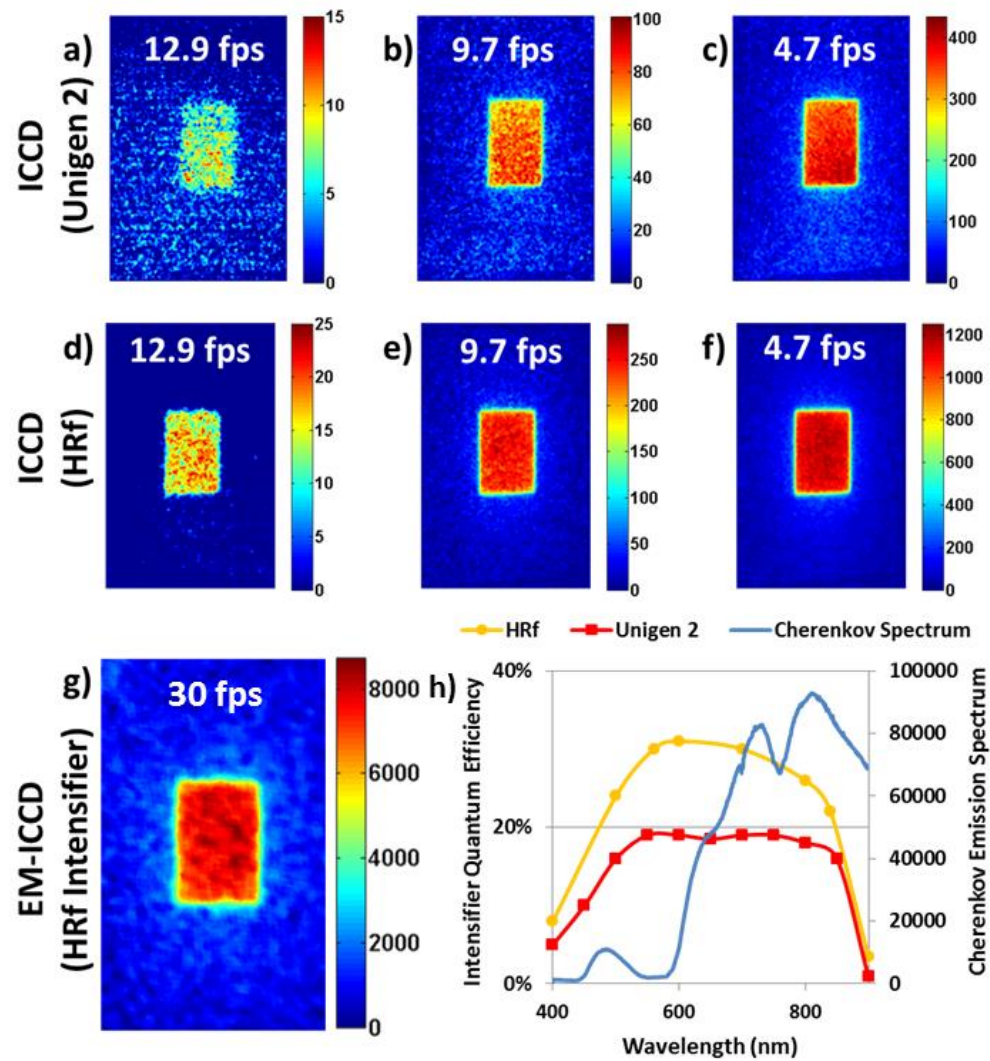


Figure 3.3 Cherenkov images captured using three types of intensified cameras with room lights on are shown. The HRf ICCD (d-f) outperformed the Unigen 2 ICCD (a-c) because of overall higher intensifier quantum efficiency. However, best performance was demonstrated from an high-gain electron-multiplied CCD (g), which allowed for single-shot imaging, where a high-signal Cherenkov image can be captured from a single radiation pulse from the linac (<0.05 cGy of dose); this image is a constructed from a temporal median filter of multiple frames following the same image processing techniques as with the ICCDs. Minor reshaping was implemented to visually negate the effect of small viewpoint angle changes between systems, but was not used in any quantitative analyses. The Cherenkov spectrum plotted in the graph shown in (h) was generated using Geant4-based simulations of a 6 MV x-ray beam irradiating a light-skinned tissue volume.⁴⁸ The QE curves were plotted from data supplied by the camera manufacturer.

The Cherenkov photon count in the y-axis of the spectrum corresponds to delivery of 1 Gy of dose to the entire tissue volume. Quantitative analysis of the treatment regions corroborated the initial qualitative inspections. Figure 3.4 shows the complete set of data points for the two ICCD cameras.

The HRf ICCD SNR² values are shown for each of the tested frame rates, for both lights on and lights off. These surpassed the SNR² of the Unigen 2 ICCD at 4.7 frames per second except in the case of imaging at 12.9 frames per second. All frame rates except for the maximum possible for the Unigen 2 ICCD (12.9 fps) exceeded an SNR of 5, and so were considered acceptable for further analysis in terms of overall useful signal. This threshold is somewhat arbitrary, but provides a decision point to compare camera performance at a reasonable, yet modest SNR value, and is based upon the Rose criterion¹³¹ for the average threshold for visual detection of signals.

The orange highlighted region of the graph in Figure 3.4.c indicates the region of acceptable average Cherenkov intensity values – those at or above the Unigen 2 ICCD detected intensity from the phantom under the same imaging conditions as the first clinical trial (0.5% of the bit depth, or 327 counts). Following this guideline, 8.6 frames per second is the maximum frame rate recommended for clinical Cherenkov image acquisition using the HRf ICCD camera to maintain previously established levels of signal. This graph further illustrates the effectiveness of the imaging and processing technique in eliminating the effects of ambient room lighting. Both cameras exhibit a calculated Pearson correlation coefficient of $r = 0.9999$ when comparing the average intensity values with lights on versus with lights off.

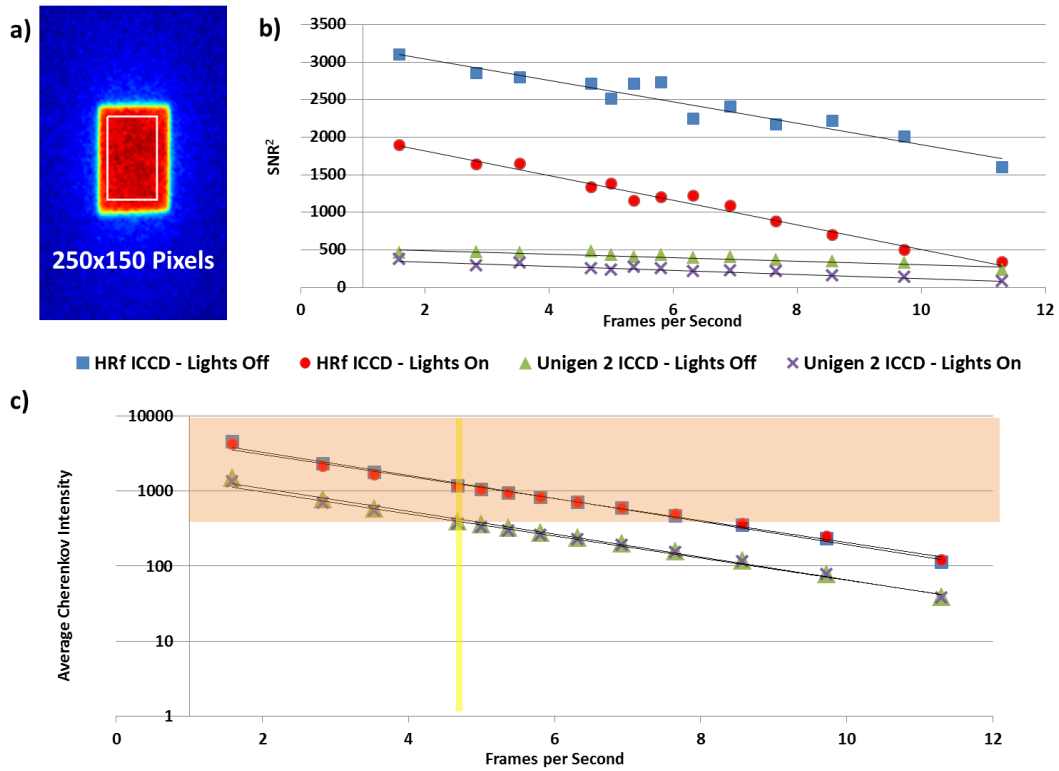


Figure 3.4 Quantitative analysis of a 250 x 150 pixel region shown in (a) for the ICCDs within the incident beam looks at the square of the signal to noise ratio in the region (b) and average Cherenkov intensity in the region (c) versus acquisition frame rate. The yellow vertical line in graph (c) highlights Unigen 2 performance at 4.7 frames per second, which is the basis for performance comparison (above 0.5% of the bit depth, or 327 counts). Intensity values that fall in the orange region of the chart qualify as adequate signal under this defined metric.

The SNR_{IN}^2 and average Cherenkov intensity for the EM-ICCD are not shown on this graph to maintain clarity, since they were measured at over twice the frame rate as the maximum ICCD acquisitions. These values are provided in Table 3.3. Again, the lights in the room did not noticeably affect the measurement. It is critical to note that the average Cherenkov intensity for the EM-ICCD was almost twice the largest measured intensity captured by the HRF ICCD, and five times that of the Unigen 2 ICCD. A metric which would be useful in evaluating camera performance but is not included in this

analysis is Detective Quantum Efficiency (DQE). This quantity is directly proportional to the measured SNR^2 , and so this has been shown in the table.

Table 3.3 Average Cherenkov intensity and signal to noise ratio values for the EM-ICCD imaging at 30 frames per second.

EM-ICCD – 30 Frames per Second					
Lights Off			Lights On		
Average Cherenkov Intensity	SNR	SNR^2	Average Cherenkov Intensity	SNR	SNR^2
7377	35.6	1270	7716	34.5	1190

To more fully evaluate the effect of the resolution limitation of the EM-ICCD, it is useful to reference the clinical patient images acquired with the EM-ICCD and qualitatively compare them to the other images from the clinical trial, which were acquired with the Unigen 2 ICCD. Figure 2.7 depicts these images, which for the EM-ICCD (Figure 5.a and Figure 5.c) were acquired at 30 frames per second (from a single radiation pulse) on patient A, and for the Unigen 2 ICCD (Figure 2.7.b and Figure 2.7.d) were acquired at 4.7 frames per second on patient B. These single, processed images are the composite sum over the course of a single day's treatment for each patient. Because the camera is stationary, both entrance and exit profiles of the beam are imaged on the patients' surface, depending on the gantry angle with respect to the camera position.

When comparing the intensity-mapped images of the EM-ICCD (Figure 3.5.a) and the Unigen 2 ICCD (Figure 3.5.b), it is evident that the latter is much smoother in appearance, simply because the physical pixel sizes are smaller and there are more of them. The lower resolution (512 x 512 as compared to 1024 x 1024) and larger physical

pixel size (16.0 x 16.0 microns as opposed to 12.8 x 12.8 microns) of the EM-ICCD versus the Unigen 2 ICCD contributes to the blockier, less-smooth Cherenkov intensity pattern in Figure 3.5.a. This mismatch in the pixel count between the two cameras was unfortunate and makes it less useful to directly compare them based upon spatial resolution standards, so here we largely focus on the frame rate performance characteristics given the relative gain differences in the two systems.

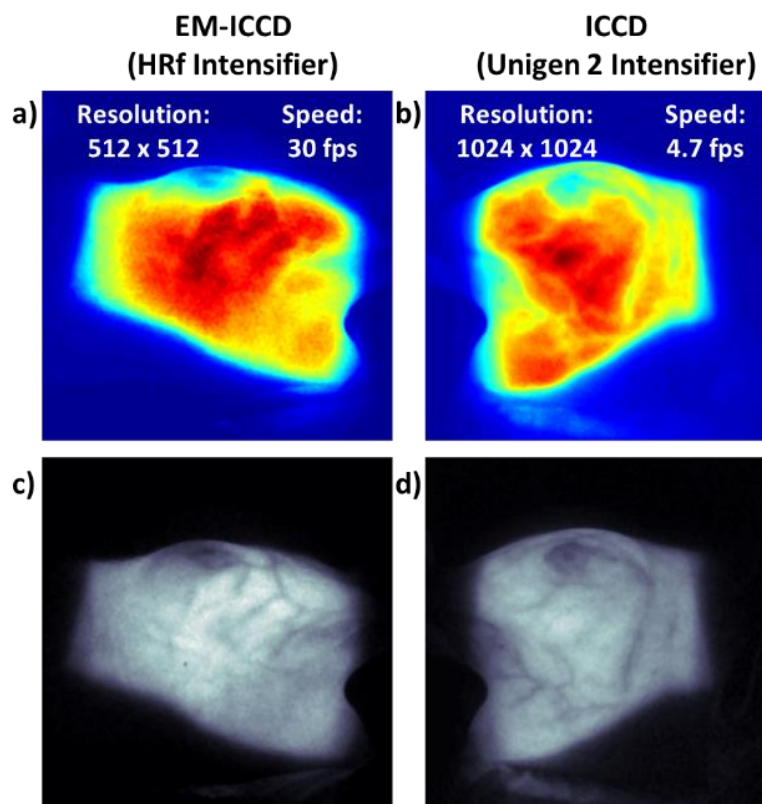


Figure 3.5 In vivo Cherenkov images captured during whole-breast irradiation of two patients. The left column shows images captured on the EM-ICCD (a and c), and the right column shows images from the Unigen 2 ICCD (b and d). All images are self normalized. Images a) and b) are presented using an intensity colormap, and research is being done to correlate relative intensity to surface dose. Images c) and d) are the same processed images as a) and b), respectively, only shown in grayscale, where it is easier to visually distinguish the appearance of the blood vessels.

It is possible to detect the blood vessels in the Cherenkov images, because there is a difference in the attenuation coefficients between the breast tissue and the blood vessels, allowing for observed contrast in the images. After comparing the grayscale images (Figure 3.5.c and Figure 3.5.d), it is visually apparent that the lowered resolution does not hinder the detection of these blood vessels.

3.7 Camera Selection Discussion

Overall, five cameras were investigated in this study to get a better understanding of the hardware requirements of detectors for clinical Cherenkov photon imaging during radiotherapy. The decision of camera type depends on the specific application of Cherenkov imaging (clinical or quality assurance) and the importance of three main criteria to that application: *i) low light sensitivity, ii) background light suppression, and iii) fast frame rate*. The decision process for using different cameras based upon their strengths and limitations is outlined in Figure 2.8.

Video frame rates (>4fps) are required in dynamic therapies, where the beam shape is changing, and in patient scenarios, so that the duration of the treatment is captured. Beyond that criterion, the camera selection will depend upon lighting conditions in the imaging environment. While an electron-multiplying charge coupled device (EMCCD) was not directly tested for this investigation, it has been used by other groups,¹³² and the gain would logically allow for higher frame rates than possible with a standalone camera. However, as it does not have an external hardware intensifier component specifically, it lacks the inherent ability to time-gate on the microsecond level

required for imaging with room lights on, as was demonstrated in this study using two ICCDs and an EM-ICCD.

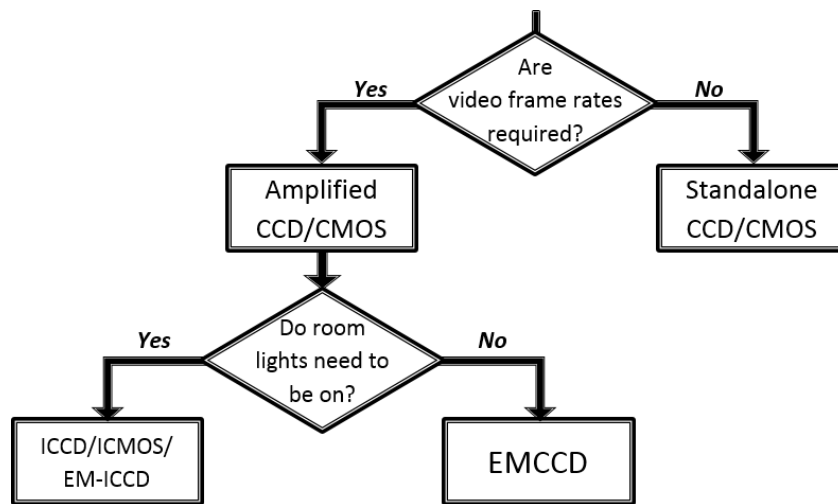


Figure 3.6. Decision flow chart for camera selection in Cherenkov imaging. Since clinical imaging requires both fast frame rates and ambient room light for patient safety, an intensified, time-gated solution is required. Other cameras can be used for quality assurance applications with room lights off, over longer acquisition intervals.

Visual inspection of the processed images from the two standalone detectors (CMOS and CCD), shown in Figure 3.2, clearly demonstrated the ineffectiveness of these cameras for imaging Cherenkov from tissue. Not only are the room lights off for these cases, a condition that is not ideal for patient safety or comfort, but the exposure time required to properly resolve the Cherenkov signal is too large to support real-time imaging, which is the overarching goal of a clinical imaging system.

Since the contrast between the Cherenkov signal and the background (the rest of the phantom surface) is not qualitatively adequate even under what would be considered optimal imaging conditions with the room lights off, it can be concluded that the CMOS and CCD detectors are not adequate for imaging tissue real-time. While it is possible to image optically transparent, less absorptive media such as water or fluorescent molecule

doped water using these types of detectors,⁷ CMOS and CCD cameras are simply not viable as standalone sensors for imaging Cherenkov emission real-time from tissue.

Standalone detectors do not have any means of signal amplification, so there is not currently a simple method of triggering and time gating on the microsecond time scale with them, and absorption of the Cherenkov emission by tissue diminishes the signal to below any reasonable noise floor or resolvable contrast. These cameras still have a place for Cherenkov imaging if speed is not an issue, room lights can be off, and the dielectric medium is transparent to the majority of the Cherenkov spectrum. Notably, they are still suited for quality assurance applications.^{8, 48, 92, 133}

With the standalone detectors sufficiently disproven of viability as real-time Cherenkov imaging cameras of tissue (at least without substantial custom modifications), focus was shifted to the intensified cameras. Between the gain and the ability to trigger, the two ICCD cameras and EM-ICCD were more sensitive to the Cherenkov signal, and could adequately detect the emission from tissue even with ambient room lights.

The superior performance of the HRf ICCD as compared to the Unigen 2 intensifier is attributed to the higher quantum efficiency of the HRf intensifier. It is for this reason that the quantum efficiency of a camera system for incoming photons in the 600-800 nm range must be taken into consideration when determining suitability of a camera system for Cherenkov imaging. It is predominantly these wavelengths that escape the tissue, since tissue preferentially attenuates lower optical wavelengths, and thus absorbs the more widely known “Cherenkov blue” optical emission.

The EM-ICCD definitively outperformed all other cameras examined in this study for performance at clinical Cherenkov imaging in terms of both speed and sensitivity. The increase in gain factor from having two amplification mechanisms instead of just one (i.e. from the intensifier and electron multiplier) allowed the EM-ICCD to demonstrate single-shot imaging. Single-shot imaging is accomplished when the Cherenkov emission from a single radiation pulse (a single on-chip accumulation) is adequate for imaging. The only specification where the EM-ICCD falls behind the others is in resolution (512 x 512 as compared to 1024 x 1024 for the ICCDs).

The implication of single-shot imaging is the potential to measure the treatment region and detect abnormalities from a single radiation pulse, which typically delivers less than 0.05 cGy of dose in the volume for the given beam. For a real-time treatment verification system, finding errors with minimal dose improperly delivered is ideal. If the beam shape or intensity map on the patient can be registered to a gold standard for that treatment, deviations from the intended plan could hypothetically be observed after a single radiation pulse, and alert the clinician to the problem immediately upon starting the treatment or encountering the error.

In the clinical images, both cameras implemented clinically were able to resolve the blood vessels in the breast. We propose these patterns offer patient-specific, unique markings in the Cherenkov images that could be used to more accurately track patient alignment and movement, especially in the non-rigid region of the breast.⁵ The 30 frames per second acquisition rate of the EM-ICCD, where all of the Cherenkov signal per frame is recovered from a single radiation pulse from the linac, provides an advantage over the

slower, 4.7 frame per second acquisition rate of the Unigen 2 ICCD (a sum of 50 radiation pulses); not only is the dose delivered per frame much lower for the EM-ICCD, but the hypothetical time cost of error detection is much shorter.

Since the resolution limitation does not hinder blood vessel detection, the fast frame rate of the EM-ICCD makes it an ideal candidate for research in clinical Cherenkov imaging, if cost is not an obstacle. The HRf ICCD offers an acceptable, lower cost alternative. In general, a camera intended for clinical Cherenkov imaging should have a method of gated acquisition on the microsecond level, and a mechanism of light amplification. Best performance will then be a trade-off in factors of resolution, speed, and contrast.

3.8 Camera Selection Conclusion

All data collected for this study supported the hypothesis that a time-gated, gain equipped system is required for real-time Cherenkov imaging of patients with ambient room lights. Standalone camera systems such as CMOS and CCD cameras, while adequate for quality assurance applications, do not perform fast enough for a real-time system, and are not sensitive enough to the diminished signal from absorptive tissue.

Each of the three intensified cameras tested could successfully image Cherenkov emission from the solid water phantom at video rates. The Unigen 2 ICCD exhibited only basic performance, since the older generation intensifier was in general not as sensitive to the optical Cherenkov spectrum. The HRf ICCD proved to be the mid-grade option, since the wavelength-dependent quantum efficiencies of the intensifier were higher than the Unigen 2 intensifier, and satisfactorily aligned with the Cherenkov emission spectrum

from tissue. The EM-ICCD demonstrated the best performance, and established the viability of imaging from a single pulse of x-rays from the linear accelerator.

Camera selection for both clinical Cherenkov imaging and quality assurance Cherenkov imaging is a non-trivial task, dependent on many factors, and it is a challenge to compare devices from different manufacturers given subtleties of the specifications provided. When looking to implement a system, one needs to determine imaging priorities. However, to accomplish video-rate image acquisition with room lights on for patient comfort and safety, it is necessary to find a gated solution with some form of signal amplification. Gating will ensure Cherenkov photon detection amidst ambient room lighting, and the level of amplification will decrease the overall length of acquisition needed to attain video-rate image streaming.

Chapter 4: Patient Imaging and Evaluation of *in vivo* Dose Correlation

4.1 First Whole Breast Irradiation Clinical Study

Whole-breast external beam radiotherapy has been clinically demonstrated to reduce the risk of disease recurrence. The first *in vivo* observations of the radiation field on the skin of patients using Cherenkov imaging were documented after a pilot clinical trial of 12 patients;^{5,48,49} a second clinical trial of up to 70 patients is currently underway. Cherenkov imaging provides the opportunity for a new treatment verification process that will offer novel information to clinicians about features such as surface dose over the targeted region and precise beam shape, and could ultimately improve patient safety.

The prototype Cherenkov imaging system allows for a completely non-invasive, non-disruptive investigation of factors such as multi-leaf collimator pattern tracking, patient alignment, and correlation between Cherenkov intensity and surface dose for relative quantification and careful monitoring by physicians. While the first two goals are currently being pursued by a spinoff company, DoseOptics LLC (Hanover, NH, USA), the correlation between surface dose and Cherenkov intensity requires careful interpretation and further investigation.

4.1.1 Methods of Imaging and Data Analysis

The data from the first clinical study has been scrutinized to understand the benchmark performance of Cherenkov intensity as a surrogate of surface dose. A PIMAX4 1024i (Princeton Instruments, Trenton, NJ USA) intensified charge-coupled device (ICCD) camera, equipped with a Canon EF 135 mm f/2L USM lens was used to image all of the patients in the group except one, which was imaged using an electron-multiplied ICCD

from the same company; the same EM-ICCD was used in the study described in Chapter 3:. The camera was situated on a tripod, and wheeled into and out of the treatment room for each imaging session, meaning some variation in setup is expected. The camera was placed near the wall to image treatments laterally, approximately 3 meters from treatment isocenter.

As an optical emission, Cherenkov photons are subject to the absorption physics defined by the variations in tissue optical properties over the irradiated anatomy. This means that we expect to detect lower Cherenkov intensities from areas with high blood content, such as blood vessels (blood is a primary absorber of blue light)¹³⁴ when compared to Cherenkov intensities from areas of primarily fat, with low blood content. Therefore a correction factor based on tissue optical properties must be adopted to achieve a strong, spatially robust correlation between detected Cherenkov intensity and simulated surface dose.

Current methods of acquiring and analyzing *in vivo* Cherenkov data allow us only to examine the images on a more macroscopic scale, using global averages of intensity for each treatment beam for comparison. It is important to note that each treatment beam must be analyzed independently, because changes in beam energy and beam geometry (imaging the beam entering or exiting the tissue) significantly affect light intensities. It is also expected that the variations in tissue optical properties between patients (i.e. melanin content/skin color and blood volumes) will create some uncertainties when comparing Cherenkov intensities between individuals.

Because this was an exploratory study aiming to determine the optimal scenario for patient imaging, some patient images had differences in camera settings at the time of data acquisition (such as varying the number of radiation pulses integrated per image) that prevented prudent statistical comparison of the entire group of 12 patients. The cohort of patient data was thus distilled so that only the 6 patients imaged using the same camera acquisition settings and hardware were included.

Post-processing of the patient images was conducted in MATLAB, and consisted of background subtraction, temporal median filtering across 5 frame windows, spatial median filtering with an [11,11] pixel kernel, and finally summing of the image stack into a single composite image. The region of interest (ROI) within the treatment beam was established by thresholding low intensity values based on the first valley from image histogram.

The average Cherenkov intensity values within this ROI were calculated for each treatment session per patient (48 session total, across 6 patients), and compared to the prescribed dose per fraction per field, prescribed monitor units per field, and the average dose calculated within a 7mm superficial volume layer from the volume dose dicom generated by the treatment planning system (TPS). The 7mm depth was chosen to include the entire possible range of generated Cherenkov light capable of exiting the tissue, based on previous Monte Carlo simulation studies (disregarding the variations due to the broadband Cherenkov spectrum).⁹

4.1.2 In vivo Data Analysis Results

The strongest correlations (based on calculated correlation coefficients, R^2) between average Cherenkov intensity per treatment field and metrics of dose quantified by the TPS were observed when associating with the number of planned monitor units per field or total dose per fraction per field, which were virtually indistinguishable. Mean dose per fraction per field at 7mm depth (i.e. surface dose) was also tested, which used the TPS to calculate and sum the dose in a superficial layer at the treatment region, but the correlation coefficient was not as high. These results are summarized in Table 4.1.

The best correlations were also observed when imaging exit beams, attributable to the variabilities introduced in the build-up region of the x-ray photons. The entrance beam correlation plot and respective images are shown in Figure 4.1, and the same for the exit beams is provided in Figure 4.2. Unfortunately only three of the twelve patients imaged were treated with 10MV beams using the standardized imaging setup. This very limited data set achieved $R^2=1$, however, is not statistically significant given the small N. The current hypothesis is that better correlations will be observed in higher energy beams, because more Cherenkov photons are generated in similar sized volumes. Future patient cohorts, with enhanced rigidity in experimental setup (such as mounted cameras) will be necessary to evaluate this hypothesis.

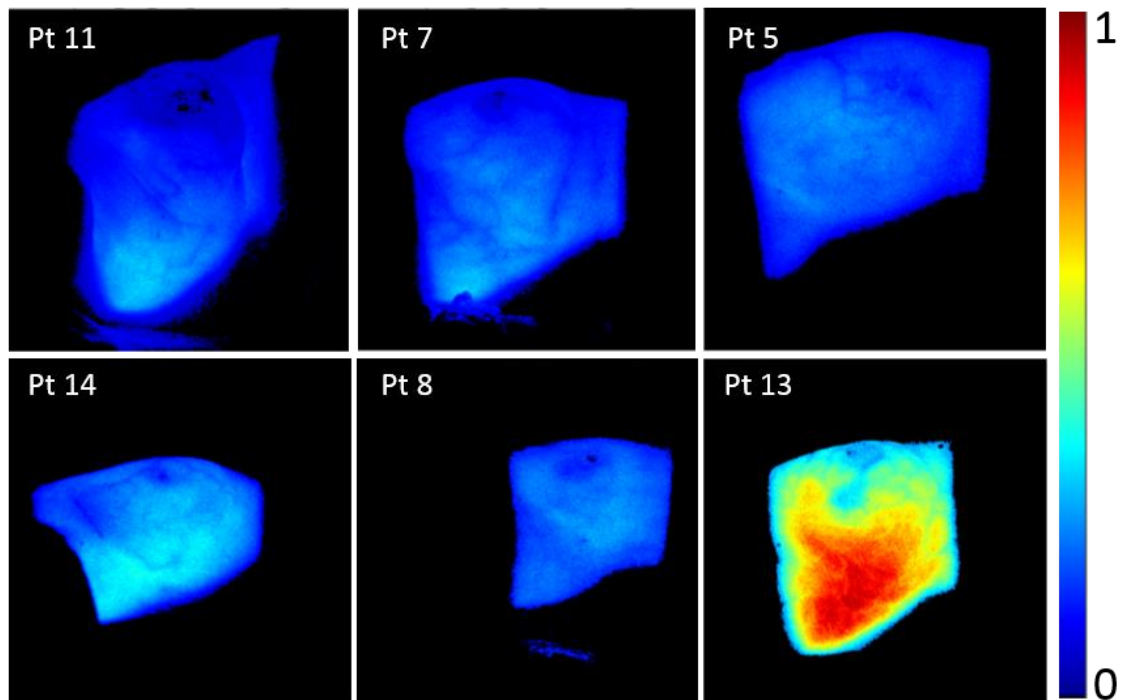
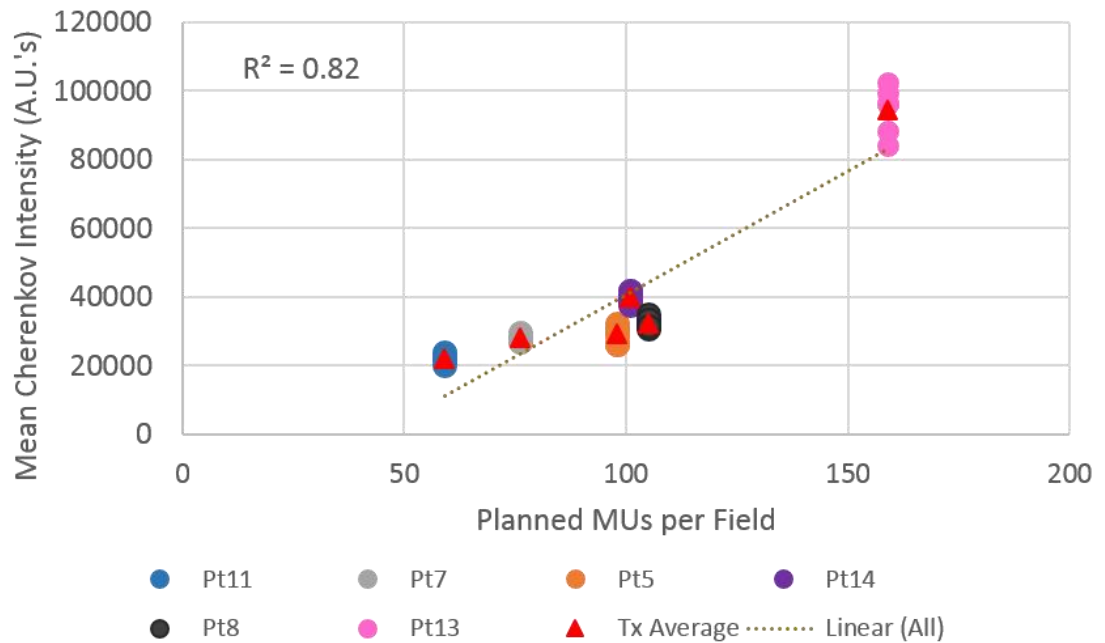


Figure 4.1 Correlation between average Cherenkov intensity per field and planned monitor units per field on each day of imaging for six patients, comparing 6MV ENTRANCE beams only. The Cherenkov images of each patient are labelled according to their clinical study designation, and arranged in order of ascending planned monitor units.

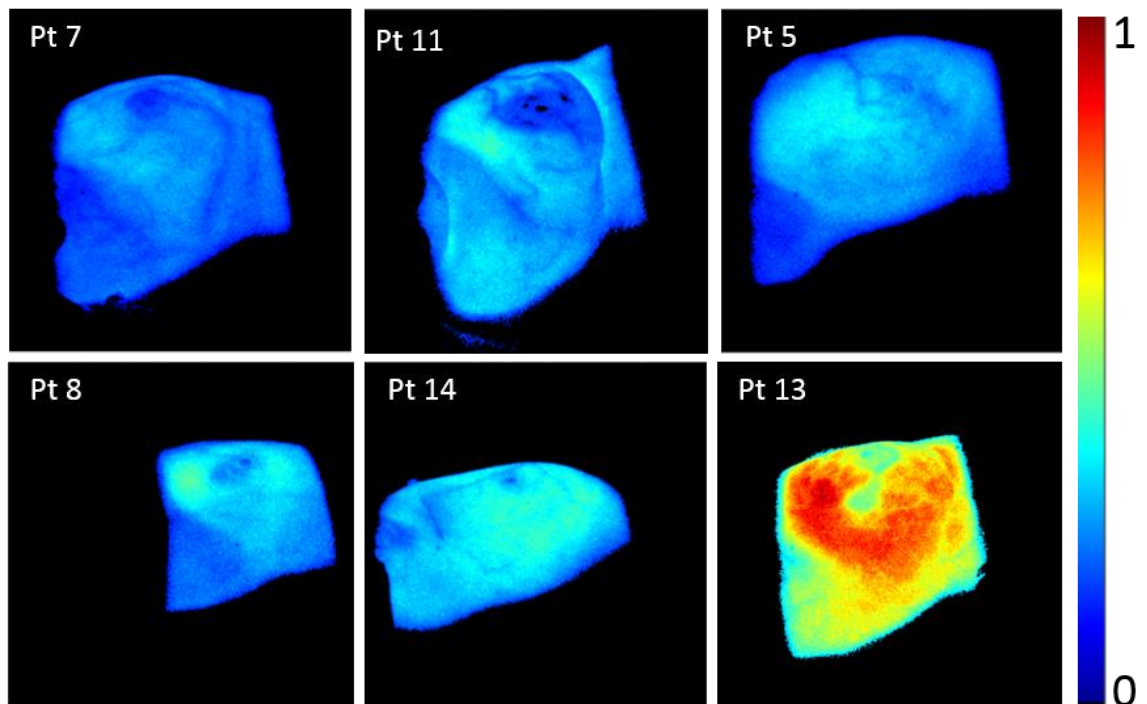
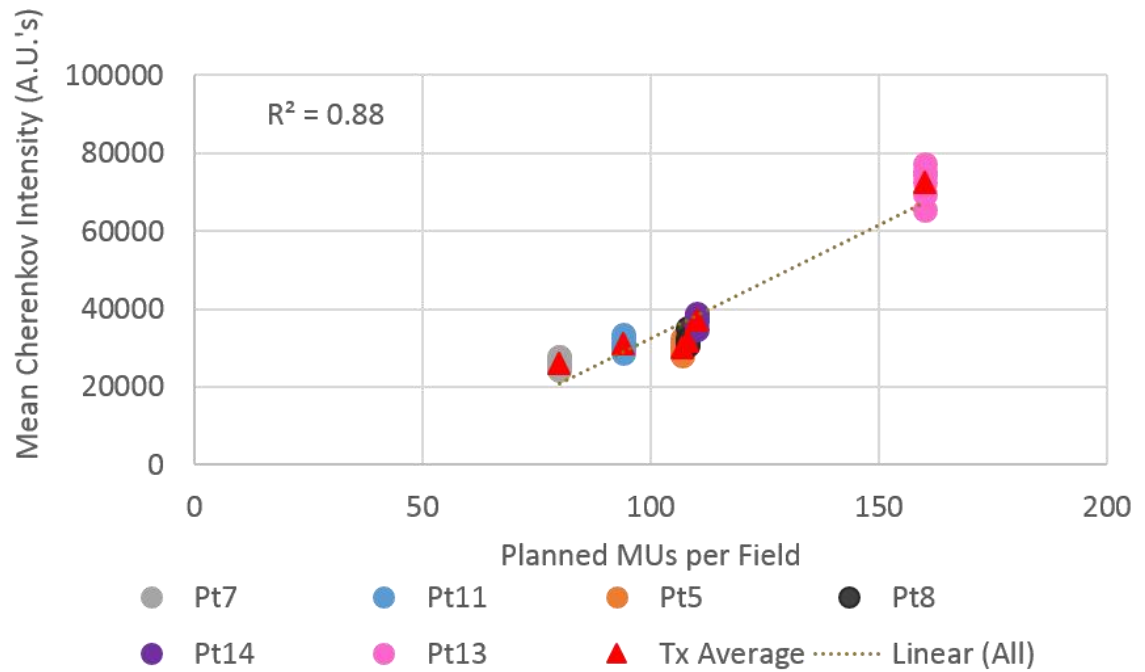


Figure 4.2 Correlation between average Cherenkov intensity per field and planned monitor units per field on each day of imaging for six patients, comparing 6MV EXIT beams only. The Cherenkov images of each patient are labelled according to their clinical study designation, and arranged in order of ascending planned monitor units.

Table 4.1 Calculated correlation coefficients between average Cherenkov image intensity within the treatment ROI and prescription or TPS derived quantities.

N=48 (6 Patients, 6-10 Treatments/Patient) Correlation Tested Against:	Calculated R²	
	Entrance	Exit
Dose per fraction per field	0.83	0.87
Monitor units per field	0.82	0.88
Mean TPS dose per fraction extracted at 7mm	0.74	0.85

4.1.3 Discussion of First Clinical Study Cohort

Many things were learned in imaging the first cohort of 12 patients undergoing WBI. The clinical study established the premise of the technology as a valid treatment tracking and patient positioning tool, with promise to aid in error detection for real-time quality control through the use of novel, video-rate information about the beam position.^{5, 49} This concept has continued to be the subject of much scrutiny, with new algorithms have been developed to verify the day-to-day patient alignment based on the beam-edge visualizations in the Cherenkov images using data from a second patient cohort, imaged under regulated conditions with a ceiling mounted camera.¹³⁵

While information about the beam footprint is relatively straightforward to garner from Cherenkov images, dosimetric data is much more challenging, both within the field of view of a single patient, and well as between patients imaged. In the case of the first patient cohort, there was a relative homogeneity in the patient skin colors due to a lack of diversity in the local patient population. This allowed for basic, gross comparisons to demonstrate a top-level feasibility of such techniques. True dosimetry, whether relative or absolute, will require a method of taking into account tissue optical properties.

There are marked differences in the intensities observed from exit beams versus entrance beams, the latter of which is dimmer due to the build-up region of radiation dose deposition and lower average beam energy.⁹ The exit beams provided clearer delineation of anatomical features such as blood vessels, as seen when comparing Figure 4.2 to Figure 4.1, as well as the higher correlation coefficients, and would be the recommended vantage point if using these anatomical features for patient tracking is desired.

However, because the radiation beam is traveling through various depths of tissue before exiting the body, it also makes sense that localized dosimetry would be affected. Percent depth dose curves (PDDs) of x-ray photons characterize radiation dose fall-off as an exponential curve after reaching the depth of maximum dose (1.5cm for 6MV beams). This exponential attenuation, along with the inverse square law and scattering effects, govern the PDD according to the following equation:

$$P(d, r, f) = 100 \cdot \left(\frac{f+d_m}{f+d} \right)^2 \cdot e^{-\mu(d-d_m)} \cdot K_s \quad ,$$

Where P is the percent depth dose, dependent on the depth d , depth of maximum dose d_m , source to surface distance f , linear attenuation coefficient μ , and a function accounting for scatter dose K_s .¹³⁶ As such, the part of the beam traveling through the much smaller distances near the apex of the breast would not be as attenuated as appreciably as the portion of the beam traveling close to the chest wall, leading to higher Cherenkov intensities in these regions.

The entrance dose side, on the other hand, exposes all of the tissue to the same portion of the PDD, albeit in the less intense, skin-sparing, high-gradient, build-up region.

Future cohorts of larger patient populations should be studied to investigate the hypothesis that entrance field Cherenkov images will provide stronger dose correlations than exit field images, contrary to the results observed here. This is on the premise that entrance fields are more uniformly exposed to a given radiation beam energy spectrum, whereas the exit dose will be spectrally filtered based on patient thickness variation.

These differences also illustrate the importance of taking into account imaging geometry for the purpose of dosimetric analysis. Unlike the first patient cohort, new imaging protocols rely on ceiling-mounted camera systems, which capture both entrance and exit dose in the same frame. This means that the data in the frame must be corrected for both variation in tissue optical properties, as well as entrance versus exit dose, before dosimetry can be accomplished. Feasibly, this can be achieved by mapping the 2D image to the simultaneously acquired 3D patient surface acquired from the patient alignment system (AlignRT, VisionRT Ltd., London, UK), and using ray tracing techniques to determine which pixels in the Cherenkov image correspond to entrance versus exit dose.

Future patient cohorts can also be studied to test the hypothesis that Cherenkov intensity patterns could be used as a predictor of skin reactions in patients.⁴⁹ The first patient cohort does not provide a large enough sample set to definitively evaluate this hypothesis. If it is supported by future research, the Cherenkov images could possibly be used to inform treatment plan adjustments to patients deemed higher risk of desquamation or erythema, and ultimately improve patient comfort.

4.1.4 First Clinical Study Cohort Conclusion

The first clinical study cohort provides a promising glimpse at the potential of *in vivo* Cherenkov imaging for patient alignment, tracking, and possibly surface dosimetry. Without using any corrections for tissue optical properties, reasonable correlation coefficients were calculated establishing the plausible linearity of the inter-patient *in vivo* Cherenkov intensity with the prescribed dose or monitor units prescribed per field. More diverse patient populations with additional variability in skin color will require correction factors for tissue optical properties for adequate comparison.

Intra-fraction dosimetry for each patient will require correction for tissue optical properties, as illustrated by the pronounced patterns of subdermal features, such as blood vessels. Finally, care must be taken to isolate Cherenkov emissions resulting from the entrance of the radiation beam into the tissue, versus the exit of the radiation beam from the tissue.

4.2 Improving the Cherenkov Light-Dose Correlation in Future Patients

This section is largely derived from: J.M. Andreozzi, R. Zhang, D.J. Gladstone, L.A. Jarvis, and B.W. Pogue., "Using a reflectance-based correction on Cherenkov images to strengthen correlation with radiation surface dose in an anthropomorphic breast phantom," in Prog. Biomed. Opt. Imaging - Proc. SPIE 9689 (2016).

The correlation between Cherenkov intensity and dose has been demonstrated in controlled conditions and phantom studies.^{48, 50, 90} However, there has been limited success in observing the correlation *in vivo*.⁴⁹ Monte Carlo simulations have been used to

evaluate the contribution of many factors which have been identified to influence this correlation. The top three contributors, in order of descending influence, are tissue optical properties/skin color, beam energy, and surface curvature.¹²

Establishing the tissue optical properties of an entire patient volume would be cumbersome, however the capturing a near infrared weighted (NIR) reflectance image is hypothetically a straightforward approach and can be accomplished with the Cherenkov imaging camera to reduce registration errors. Preliminary phantom studies have been conducted to evaluate the hypothesis that using an IR-weighted image to normalize the Cherenkov images would improve the correlation between pixel intensity and measured surface dose.¹³⁷

The physical basis for this hypothesis is that 1) NIR wavelengths have the greatest penetration depth in tissue, and 2) the bulk of Cherenkov signal making it out of tissue is weighted in the red-NIR. Therefore, the NIR reflectance image would be an approximation of the Cherenkov light transmission in the tissue, since it is subjected to the effects of the same spatial distribution of tissue optical properties.

This concept was tested by Zhang et al. in biologically-based bovine blood and intralipid phantoms, covered with a top layer of increasing concentrations of melanin. The 5x5 array of samples presented 25 variations of optical properties to simulate an expanse of human skin colors and tissue blood content. The reflectance image normalization method successfully corrected the Cherenkov intensity for the tissue optical property variation in this controlled setup with flat, uniform samples.⁹ An anthropomorphic

homogeneous volume breast phantom, shown in Figure 4.3, was subsequently tested to ensure the method would not be influenced by the effects of curvature.

4.2.1 Anthropomorphic Phantom Study Methods

The right-breast phantom was cast out of a silicone rubber compound (Smooth-On Inc., Macungie, PA USA). Silicone dye was added to the wet silicone to give the phantom a flesh color. A structured light imaging system¹³⁸ was used to measure the optical properties of the phantom on the bottom flat face. These properties are shown in Table 4.2.

A PIMAX4 1024i (Princeton Instruments, Trenton, NJ USA) intensified charge-coupled device (ICCD) camera, equipped with a Canon EF 135 mm f/2L USM lens was used to image the phantom. To acquire cross-polarized reflectance images that reject surface glare, a commercially available flash ring was fitted around the camera lens. A linear polarizing sheet was used to vertically polarize the light output of the flash ring. The front of the camera acquisition lens was fitted with a horizontally polarizing filter. The reflectance images were acquired before irradiation.

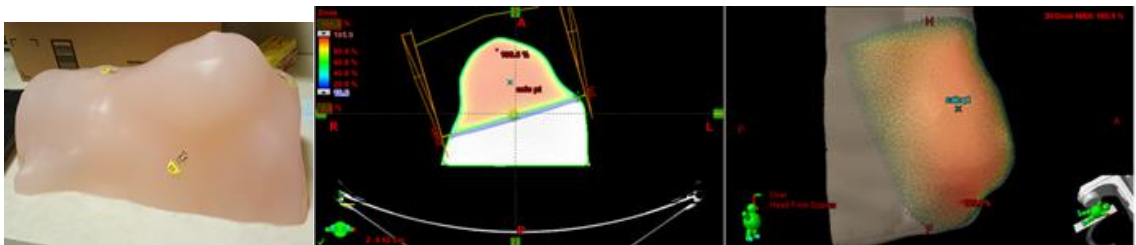


Figure 4.3 (Left) Anthropomorphic silicone breast phantom imaged. (Middle) Tangent beam plan for phantom as seen from a transverse slice of the CT scan in the TPS, with gantry positions for the two beams shown in orange. (Right) Dose cloud for the treatment volume.

Table 4.2 Optical absorption and scatter properties of silicone phantom.

wavelength (nm)	658	730	850	970
μ_a (1/mm)	0.287	0.269	0.233	0.191
μ_s' (1/mm)	0.25	0.35	0.249	0.189

4.2.2 Anthropomorphic Phantom Study Results and Discussion

The purpose of this anthropomorphic phantom study was to investigate a new method for improving the *in vivo* correlation based on a pixel-by-pixel correction from a reference reflectance image, by isolating the issue of curvature from variation in tissue optical properties (the latter of which must be studied separately, as described earlier⁹). The pixel intensities in Cherenkov images of a phantom were correlated with the surface dose measured from thermoluminescent dosimeters (TLDs) placed on the phantom surface, shown in Figure 4.4; the presented Cherenkov images are the sum of each treatment beam.

Because the phantom had homogeneous optical properties, results show no appreciable change in correlation between Cherenkov intensity and surface dose when using the correction method on images of an anthropomorphic solid silicone phantom, as concluded from the plot Figure 4.5. This validates the approach does not unduly alter the Cherenkov intensities, as no change would be expected in a homogeneous phantom. However, the agreement between the Cherenkov and measured dose is not convincingly linear, with R^2 values of 0.58-0.59, which can partially be attributed to the positioning of the TLDs in regions of high gradient dose, as well as tangential with the beam path of TLD position #3 near the apex of the breast phantom.

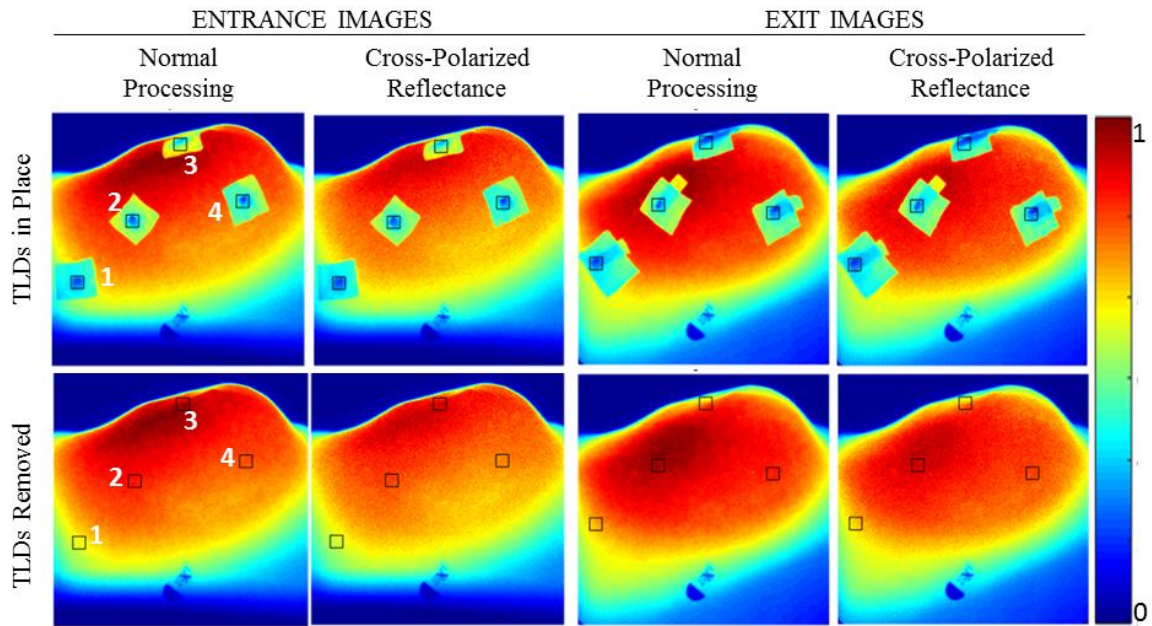


Figure 4.4 Normalized Cherenkov images of the phantom, with analyzed ROIs drawn on as black boxes, numbered 1-4. The top row shows the images acquired with the TLDs in place measuring the surface dose, and the bottom row shows the same beams being delivered to the phantom without the TLDs.

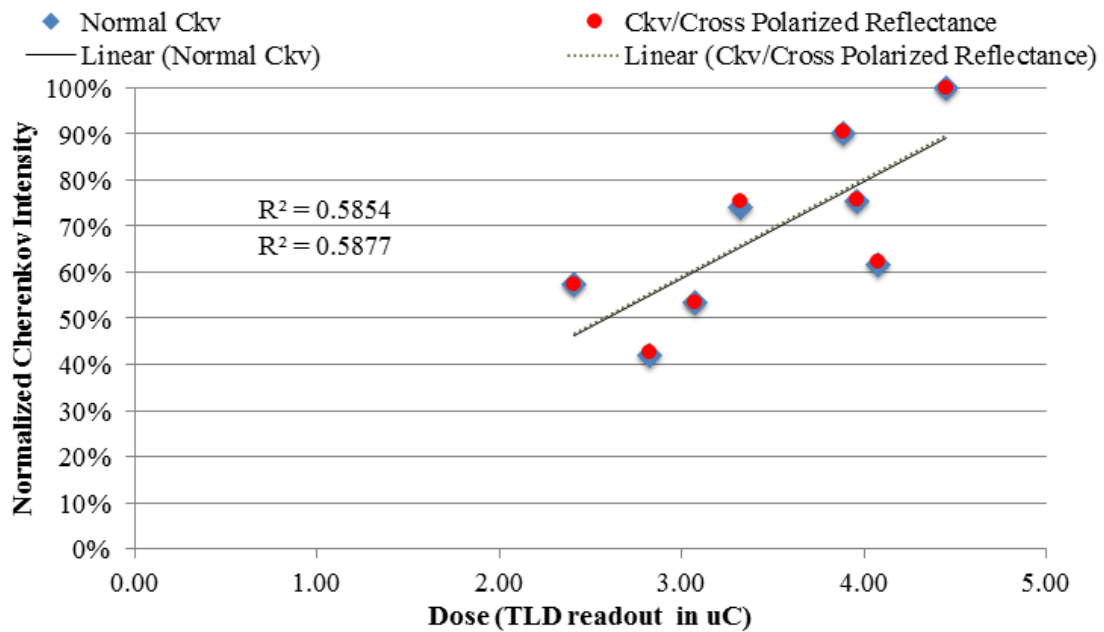


Figure 4.5 Plot of correlation between Cherenkov intensity and measured surface dose.

To ensure that the correction method of normalizing to a reflectance image would not have any undue effects on the edges of the phantom as seen in the 2D Cherenkov images, the line profiles shown in Figure 4.6 were compared. There was no appreciable change in the dose fall-off between the normal Cherenkov image line profiles and the reflectance corrected profiles, for either the entrance or exit dose images. Overall, the cross-polarized reflectance image correction did not have a negative, artifact-inducing impact on the Cherenkov images. More phantom studies need to be conducted to make a definitive statement on its effectiveness to perform the intended correction, given samples of heterogeneous tissue optical properties.

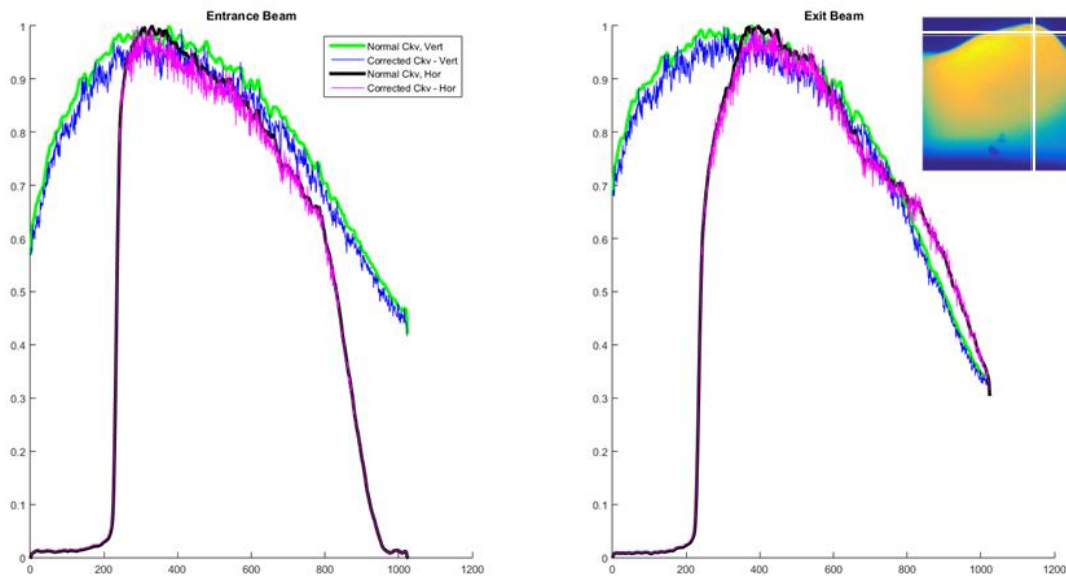


Figure 4.6 Comparison of dose fall-off at the phantom edges for the normal Cherenkov images and the reflectance-corrected Cherenkov images of entrance and exit dose.

4.2.3 Anthropomorphic Phantom Study Conclusion

The primary conclusions from this study validate the approach of using a uniform-illumination, cross-polarized light source and detector to generate a reflectance based correction image for subjects with extensive curvature, such as the case *in vivo*, since the correlation was largely unaffected after normalization.

The problem arises in achieving uniform illumination in a clinical setting, which proves extremely difficult. Skin folds and the less rigid nature of actual human anatomy, compared to the smooth, solid phantom tested here, introduce artifacts in the reflectance images which in turn present in corrected Cherenkov images. These realities limit the translation of this method to the clinic. Instead, modalities that use structured light patterns to measure and fit tissue optical properties, while taking into account surface curvature, are recommended as a future method of obtaining a correction image and general area of study.^{139–141}

4.3 In Vivo Volumetric Modulated Arc Therapy Imaging

This section is largely derived from: J.M. Andreozzi, R. Zhang, D.J. Gladstone, L.A. Jarvis, and B.W. Pogue., "Cherenkov imaging during volumetric modulated arc radiation therapy for real-time beam tracking and treatment response monitoring," in Prog. Biomed. Opt. Imaging - Proc. SPIE 9719 (2016).

The work of Jarvis et al. describes acquisition of clinical Cherenkov images where a background image without Cherenkov emission is acquired before the radiation beam is turned on at each gantry position used for treatment for patients undergoing whole

breast radiotherapy.⁴⁹ This method was effective, since patient movement during breast treatment is typically very minimal and due to breathing, a factor that was in fact evaluated and measured using Cherenkov imaging.⁵

However, the continuous movement of the gantry during VMAT treatment means not only a moving object (the gantry) can be in the frame, but that the shadows cast on the patient from the ambient room light cause fluctuations in light intensity that overwhelm the Cherenkov signal. It is therefore necessary to capture many background images over the course of the entire treatment, so that a background image with similar lighting conditions can be subtracted from the Cherenkov images acquired during a similar instance in time.

4.3.1 VMAT Patient Imaging Methods

All patient treatments analyzed in this research were imaged following an Internal Review Board (IRB)-approved clinical study protocol. The process was designed to have minimal interference with the normal clinical workflow of patient treatment, and no changes to the patient treatment were made for the sake of the study. A TrueBeam (Varian Medical Systems, Palo Alto, CA USA) linac was used to deliver the prescribed 6 MV x-ray VMAT plans to two patients that consented to the observational study.

Patient #1 was treated in the sinus region and restrained to the treatment couch using an open-face mask. The treatment plan used only a single 180° arc over the top of the patient surface, meaning primarily entrance dose was imaged. Patient #2 was treated predominantly in the neck region, and immobilized using a full face mask that ended just below the chin. The VMAT plan utilized two sweeps over the full 360° arc range (once

forward and once back), meaning both entrance and exit dose were imaged depending on the gantry position.

This study used a Canon EF 135 mm f/2L USM lens (Canon U.S.A., Inc., Melville, NY) mounted on a PIMAX4-1024i (Princeton Instruments, Trenton, NJ USA) intensified charge coupled device (ICCD). Images were acquired at full 1024x1024 pixel resolution allowed by the camera, without any binning. The camera was triggered by a voltage signal from the linac signifying the radiation beam is on.

Raw Cherenkov images are encumbered with salt and pepper noise as a result of stray radiation hitting the camera. To remove this noise and minimize the contribution of background light, Cherenkov image processing occurred in three steps. First, a temporal median filter is applied over three or more subsequent frames, since the salt and pepper noise changes from frame to frame. Second, the background image is subtracted from the filtered image. Finally, an 11x11 median filter kernel is used to lightly smooth the image.

Image acquisition was carried out using independently developed LabVIEW (National Instruments, Austin, TX USA) code designed to alternate between Cherenkov images and background images. Cherenkov frames were acquired as 25 subsequent on-chip accumulations of the 3.25 microsecond window immediately following the trigger pulse from the linac. Background frames were acquired as 25 subsequent on-chip accumulations 3 milliseconds after the trigger pulse, when the radiation beam and subsequently the Cherenkov light were no longer present (also 3.25 microsecond window).

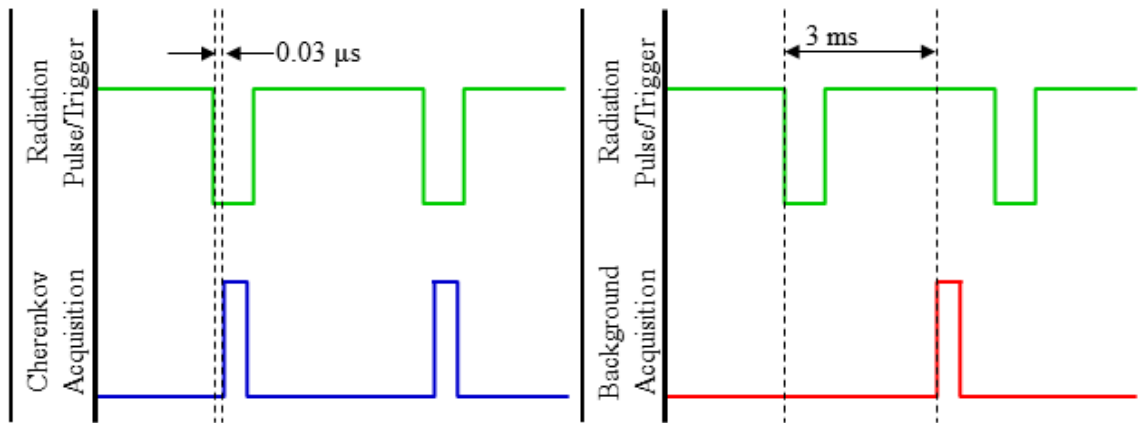


Figure 4.7 Timing diagram for Cherenkov frame (left, blue), versus a background frame (right, red). The trigger pulse width and frequency can vary, and the detected light from 25 subsequent pulses add on chip to form each saved frame. The width of the Cherenkov acquisition and the background acquisition was equal.

Cherenkov image versus background image acquisition followed the repeating pattern of 3 Cherenkov images, followed by one background image. The timing diagram is illustrated in Figure 4.7. Instantaneous frame rates varied between 2-6 frames per second, depending on dose rate.

Placement of the Cherenkov camera is not as obvious as in the case of whole-breast radiotherapy. Logically, having a camera with a beam's-eye view would be ideal for Cherenkov imaging, however the logistics of testing a camera close to the gantry head have impeded such a study. First, the camera would be hit with a lot more stray radiation, causing electronic degradation to an expensive unit. If a cheaper camera was available, or a unit with easily changed CCD chip was developed, this would not be as big of an issue. The second problem is that the patient is not visible if the gantry is irradiating through the treatment couch, and it is the data directly from the patient volume that is most interesting to a user. There would be required validation that linac movement is not

affected by the additional weight of the camera and any shielding materials, however this is not expected to be an issue given clinical implementations of weighted applicators and cones on already massive gantry systems.

Two camera positions were used to observe VMAT treatments. One is the same position used for imaging whole-breast radiotherapy, along the side wall to view a profile of the patient on the table. However, since the gantry obstructs the majority of the entrance Cherenkov image for almost half of the treatment, there is a lot of information lost by using this camera position. The alternate camera position tested was at the foot of the treatment couch, near the ceiling to look down on patient, shown in Figure 4.8. This position was more ideal for Cherenkov imaging during VMAT treatment, because either entrance or exit dose is almost always visible to the camera; a ceiling mounted camera would offer similar advantages.

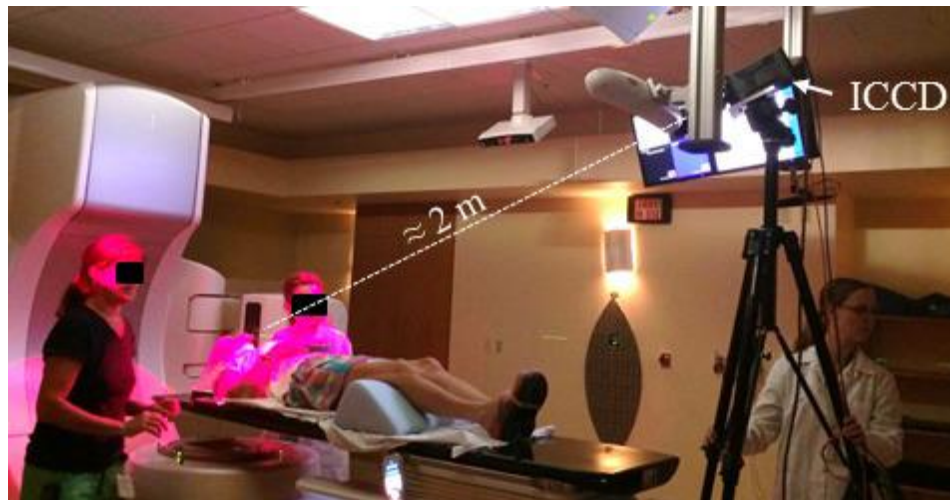


Figure 4.8 Cherenkov camera being placed at the foot of the treatment couch to image VMAT patient treatment.

4.3.2 VMAT Patient Imaging Results

Patient #1 was imaged with the camera placed at the foot of the couch, as shown in Figure 4.8. The processed images from the treatment of Patient #1 were combined into a composite image as the sum of the entire treatment. The clinical treatment planning system (TPS), Eclipse™ (Varian Medical Systems, Palo Alto, CA USA) was also used to generate a predicted map of surface dose from a similar point of view. These images are presented together in Figure 4.9.

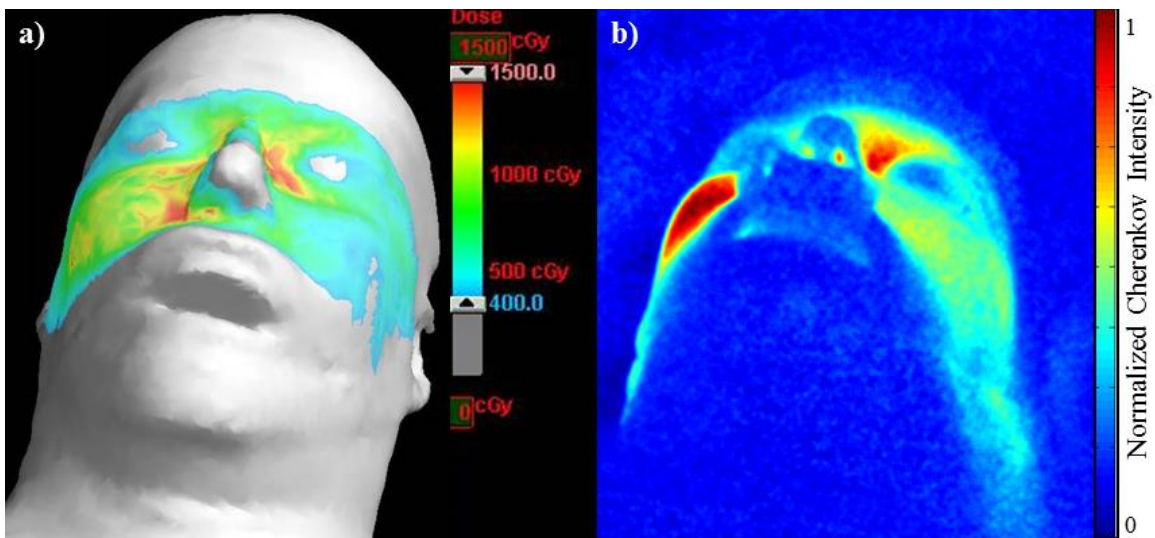


Figure 4.9 Patient #1: (a) Surface dose prediction from TPS for entire treatment fraction. (b) Composite Cherenkov image summation from treatment fraction

Patient #2 was imaged with the camera positioned at both the foot of the couch and the side of the room. Using the time that the treatment beam was on versus the number of Cherenkov images in the processed stack, the videos had an effective frame rate of approximately 4 frames per second (fps). The Cherenkov video was overlaid onto a single white-light reference photo of the patient, taken using the same camera with all

room lights on before the treatment began. Stills from these videos can be seen in Figure 4.10, and the full videos can be viewed following the hyperlinks listed in the caption. Note that for the video in Figure 4.10b, there are segments of the video where little to no Cherenkov can be seen that corresponds to the moments during treatment when the gantry obscured the view of the camera.

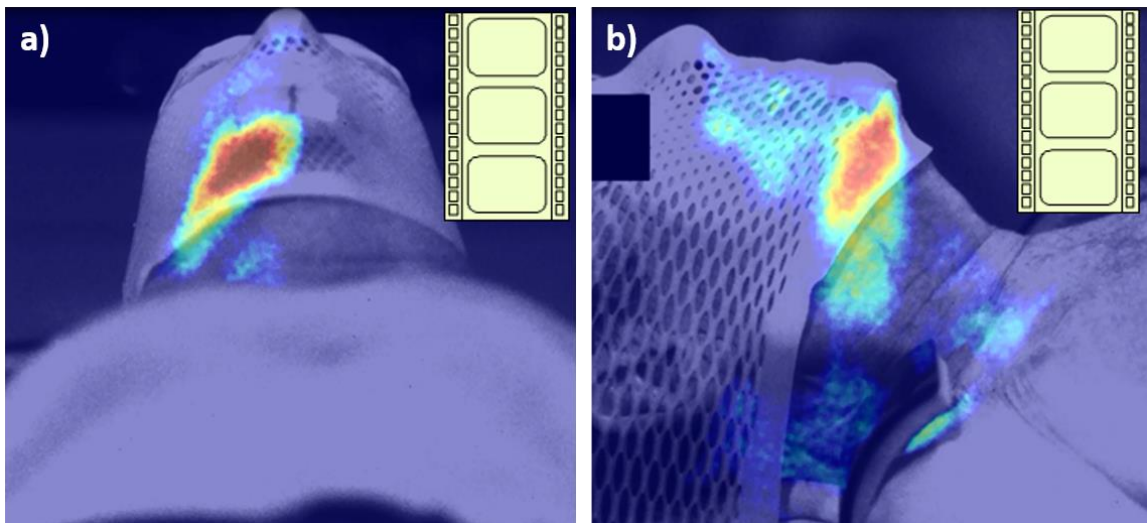


Figure 4.10 (a) Video of Patient #2 with the camera positioned at the foot of the couch: <http://dx.doi.org/10.1117/12.2212844>. (b) Video of Patient #2 with the camera positioned on the side of the couch: <http://dx.doi.org/10.1117/12.2212844>.

4.3.3 VMAT Patient Imaging Discussion

In this study, video-rate (2-6 fps) Cherenkov images were successfully collected for two patients undergoing VMAT radiotherapy from a 6 MV x-ray beam. The quality and function of these images provided a preliminary look at the feasibility of applications for Cherenkov imaging during highly dynamic treatments such as VMAT. In addition, the process afforded further understanding of the influence of imaging setup, and the patient-to-patient differences in treatment on the data.

From the videos in Figure 4.10, it seems reasonable to argue that it would be possible to track the beam directly on the surface of the patient (or on the patient's immobilization mask). The timing of the background subtraction acquisition can be improved with further analysis of the radiation pulse sequence, which in this case was conservatively assumed to be 180Hz. The actual pulse rate is in fact 360Hz, where pulses are dropped from the pulse train periodically to modulate dose rate. A smaller time delay for the background image acquisition needs to be applied in the future to improve quantitative and qualitative imaging results.

With a constant camera position, comparing the day-to-day videos of the tracked beam would provide an additional level of treatment verification to ensure there are no beam-steering or MLC malfunctions occurred. Performing this analysis in real-time or near-real-time would prevent repeated errors, or even errors that could carry over into other treatments.

Furthermore, head and neck tumor sites are known to experience extensive morphological changes over the course of treatment (typically at least 2-4 weeks). It is currently the responsibility of the physician to determine when and if it is appropriate to re-design a treatment plan due to physical changes in the patient, a practice known as adaptive radiotherapy. Analysis of the Cherenkov intensities could provide a quantitative metric that would inform the physician of a necessary re-plan, and further attention is being given to this particular area.

It has been recognized that the camera position in the room will affect the utility of the images. A beam's eye view has the appeal of a constant, unobscured view of the

beam which can be related back to the shape of the MLC at any given point in time, ideal if beam tracking is the primary goal of the imaging. However, the constant change in the “background scene” (i.e. the patient surface) would present a limitation for highly dynamic processes such as VMAT, in that they could not be easily summed to provide a measurement of the entire treatment as a whole in the end. Also, whenever the gantry is rotating below the treatment couch, the surface imaged would be the couch and not the patient.

Regardless, the logistics of attaining beam’s eye view images, with respect to both patient and camera safety, prevented an attempt to capture a treatment in such a fashion. Ultimately, it was decided that the foot of the bed looking down on the patient (Figure 4.8) provided the best static vantage point in this study. This is because this position was never obscured by the gantry during treatment, and provided more frames of meaningful Cherenkov data when compared to the side view.

Another lesson learned in this study was that it is critical to acquire background images periodically through the treatment, because the gantry movement changes the level of background light cast on the patient from the ambient sources. Background subtraction is a cornerstone of Cherenkov image processing that is necessary due to the low nature of the signal. While the background subtraction was performed in post-processing for this proof-of-concept study, it is technically feasible to perform this operation in real-time with more advanced hardware systems.

If a single background image from the beginning of the treatment is used, there is variation in pixel intensity introduced as shadows from ambient room light change on the

surface of the patient as the gantry rotates. Because room lights can fluctuate in intensity over time, reproducibility between daily treatment sessions would be problematic. Subsequently, every fourth image acquired had a delayed acquisition time point from the trigger, so as to serve as a background image. Care had to be taken in post-processing to ensure that the most temporally-appropriate background image was subtracted from each Cherenkov frame.

The two patients imaged illustrate the variation that can occur in treatment plans, depending on the prescription. In Figure 4.9 we see qualitative agreement between the final Cherenkov intensity and the predicted surface dose from the treatment planning system. More work needs to be done to consolidate the coordinate systems of the 2D Cherenkov system with the 3D TPS in order to make a quantitative comparison of the two data sets.

The fact that Patient #1 was treated using gantry angles above the patient provided an interesting case to image, since the camera was able to capture almost exclusively entrance dose. This means that it is more reasonable to take the arithmetic sum of the pixel intensities across the entire treatment arc, without applying any correction factors, to compare to surface dose. The intensity of Cherenkov light observed as entrance or exit dose varies primarily because the entrance side is affected by the build-up region of the x-ray beam, and the exit side is influenced by beam hardening after traveling a certain distance through a medium. Making a meaningful assessment of a composite summation image from the video of Patient #2 would require using complicated correction factors on a frame-by-frame, or even pixel-by-pixel, basis.

Cherenkov intensity has repeatedly been shown to correlate to surface dose in simulations and phantom experiments, but with limited success during in vivo imaging. The task of quantifying Cherenkov intensity in a method that correlates statistically to surface dose was not investigated with this data due to the inherent intricacies of VMAT itself. However, work is being done in more controlled settings with biological phantoms and whole-breast patients to establish the parameters that influence this correlation for in vivo imaging, so that they can be applied to cases such as VMAT in the future.

4.3.4 VMAT Patient Imaging Conclusion

This study successfully imaged the Cherenkov emission from two head and neck VMAT patients during treatment for the first time, as an optical analog for the radiation beam itself. The Cherenkov light illustrated the x-ray beam shape and position on the surface of the patient. With the quality of the images acquired, it is feasible that a rigidly affixed camera could be used to monitor patient treatment on a day-to-day basis to help detect abnormalities in delivery.

Mounting the camera near the ceiling directly above the foot of the treatment couch was found to be the ideal vantage point to eliminate obstruction by the gantry. In select patient treatments where only entrance or exit dose are imaged from the camera position, one can make comparisons between the cumulative Cherenkov intensity for the treatment, and the predicted surface dose from the treatment planning system, without extensive corrections.

Chapter 5: Optimizing Total Skin Electron Therapy with Cherenkov Imaging

This chapter is largely derived from: J.M. Andreozzi et al., “Cherenkov imaging method for rapid optimization of clinical treatment geometry in total skin electron beam therapy,” *Med. Phys.* 43(2), 993–1002 (2016).

5.1 Total Skin Election Therapy in the Clinic

Total skin electron beam therapy (TSET) is an effective treatment for cutaneous lymphomas.^{57, 59, 62, 142, 143} Of the many techniques to deliver TSET,^{144–148} the most common is the modified Stanford technique, which typically uses two electron beams angled approximately 20° above and below the horizontal plane, while the patient holds six different standing positions, at a source to surface distance (SSD) of at least 300 cm.^{31, 60, 145} Regardless of the specific technique selected for TSET, it is recommended that dose be verified with both phantom and *in vivo* dosimetry.⁶⁰

Ionization chambers, diodes, thermoluminescent dosimeters (TLDs) and radiochromic films are common methods for measuring dose on phantoms or on patients,^{31, 149–151} but these are limited to point or small region measurements. Given the complexity of the treatment area in TSET, these verification tools require a large number of measurements, and careful interpretation is critical. In this study, a very practical approach to optimization of the delivery gantry angles was examined with an imaging-based method of dose homogeneity mapping using Cherenkov light imaging.

The main treatment challenge of TSET is the need to deliver a homogenous dose over the entire irregular skin surface, while taking into account unique body shapes and

tolerable positions of each individual patient. The European Organization for Research and Treatment of Cancer (EORTC) consensus report acknowledges that, “the final position of the patient may be a compromise between patient comfort and some of the lesser dosimetry objectives. It is important that compromise be minimized to reduce the risk of relapse and limit the need for top-up treatments,”¹⁵¹ making the coverage more uncertain in each patient on a daily basis.

It is agreed that minimizing dose heterogeneity (+/- 10%) in the patient standing plane is important for TSET. Therefore, an overall goal in this study was to measure this variation by standard techniques, as well as by a newer method utilizing Cherenkov imaging. The modified Stanford technique does not currently take into account the curvature of each individual patient. Measurements of dose in a single plane, before patient treatment, allows clinicians to treat TSET patients in a standardized method. Any variation in dose from patient-to-patient at specific anatomical areas can be adjusted by boosting any under-dosed areas, such as under skin folds, or the bottoms of the feet.

It is currently the physician’s responsibility to monitor radiation treatment response by qualitatively evaluating the condition of the disease on the skin, or by periodic TLD measurements during treatment. It is therefore desirable to have a quick and simple method to analyze patient treatment on a regular basis. Ideally, this would be in the form of an *in vivo* measurement of dose on the entire patient’s surface during treatment. We have begun to explore this possibility using Cherenkov imaging. However, because of the complexities of *in vivo* dose correlation briefly addressed later in this paper, the focus of this article is a more immediately attainable goal: rapidly assess the

x-y or coronal patient plane to attain maximum dose uniformity on a flat surface prior to patient treatment.

Cherenkov imaging has already been applied to develop novel quality assurance protocols in water tanks, to visualize the deposited dose build up real-time inside a 3-dimensional volume.^{8, 90} It has also been used clinically to image whole-breast radiotherapy, to assess beam tracking, breath motion, and explore *in vivo* surface dose correlation.^{5, 48, 50} Applying Cherenkov imaging to unique treatments such as TSET could ensure more homogeneous dose delivery, and provide a new method for TSET protocol commissioning.

According to AAPM Report 23, establishing a TSET technique requires measurements of “electron energy, fluence, depth dose, isodose, and x-ray contamination.”⁶⁰ All of these, except the full 3D volume isodose curves, are generally measured using an ionization chamber or film at the prescription point once the task of selecting the two gantry angles which provide the most uniform dose be completed. It is logical to begin by determining the two gantry angles which provide the least amount of variation in the x-y isodose plane, and then verifying that the rest of the parameters fall within tolerance at the prescription point.

Measurement of isodose in the x-y plane would generally require individual measurements at a large number of points (76 are shown in AAPM Report 23),⁶⁰ with either diodes, TLDs, or ionization chambers. Because Cherenkov imaging provides a complete, real-time, 2D digital dataset, it is possible to eliminate the redundancy of these

measurements and achieve a full assessment with two individual beam images on a flat plane, instead of up to 152 point measurements, for each tested angle pair.

Given the rarity and variety of TSET delivery, it is desirable to optimize the technique in each department, and ideally to verify skin coverage for each daily treatment, in each individual patient given his/her distinctive anatomy and body habitus. With known variability in TLD placement and slight variations in body position, it is particularly challenging to be quantitative about the delivered dose in this treatment. Therefore, there is a need to verify TSET setup geometry for a given treatment room configuration, as well as visualize treatment delivery and skin coverage for individual patients, each day of treatment. In this chapter, the ability of Cherenkov imaging to fill this first role is demonstrated, and continuing research on dosimetrically-valuable *in vivo* Cherenkov imaging of TSET patients is discussed.

5.2 Materials and Methods for Initial TSET Optimization Technique

5.2.1 Linac and Treatment Setup

A Varian Clinac 2100 CD (Varian Medical Systems, Palo Alto, CA, USA) medical linear accelerator commissioned for patient TSET treatment was used for the phantom studies and verification testing presented in this article. The system is capable of operating for TSET at 6MeV electrons only. Because of the energy limitation, patient treatment at our institution is always conducted without an external spoiler. The commissioned treatment follows a modified Stanford technique, whereby the patient is placed in 6 unique bodily configurations: anterior-posterior, posterior-anterior, right anterior obliques, left anterior obliques, right posterior obliques and left posterior obliques.

The patient is irradiated with the prescribed dose using two treatment angles intended to provide uniform coverage in the treatment plane. At our institution, the original treatment angle pair was 284.5° and 255.5° , also written as $\pm 14.5^\circ$ above and below the horizontal, and equivalent to a 29° spread. For clarity, all three angle designations will be given in the article in parentheses whenever a treatment configuration is mentioned, following the format ($\pm 14.5^\circ$, 29° spread, 255.5° and 284.5°).

5.2.2 Cherenkov Imaging System

A PIMAX4 1024i (Princeton Instruments, Trenton, NJ USA) intensified charge-coupled device (ICCD) camera with HRf intensifier was used to acquire all Cherenkov images in this study.¹⁰ The HRf intensifier component utilizes a photocathode to convert incoming light photons to electrons, which are multiplied using a micro-channel plate, then converted once more into photons after striking a phosphor screen. The amplified light is fiber-coupled with the CCD chip, so that low light signals such as Cherenkov emission can be detected. With this particular device, image resolution was 1024x1024 pixels.

A 24mm F/1.8 lens (Sigma Corporation, Ronkonkoma, NY) was used to capture the entire height and width of the patient support structure at the given imaging distance. The camera was mounted on a tripod and placed near the gantry head of the linear accelerator (Varian 2100CD, Varian Medical Systems, Inc., Palo Alto, CA USA), approximately 4 meters from the patient support structure.

The camera was set to maximum intensifier gain, and 500 on-chip accumulations per frame, which produced a frame rate of 1.3 fps. Images were obtained using the

software LightField (Princeton Instruments, Trenton, NJ USA). Room lights were turned off in phantom studies, but left on at a modest level for patient safety and comfort in clinical applications.

Room lights are required to be on in the case of patient imaging so that the treating technicians can maintain a constant visual on the patient through the internal CCTV monitoring system to ensure the patient remains standing in the correct positions. Since the safety concern is not present in the case of the phantom, room lights were turned completely off to reject the most background light possible. In all cases, the room alignment lasers are turned off during imaging to prevent saturation of the camera.

Imaging with room lights on is possible by microsecond-level time gating. Each image exposure is triggered off of a beam pulse from the linear accelerator, and time-gated to the window from 3.0 to 8.0 μs after the trigger pulse. This allows for the synchronization of acquisition with source radiation pulse via signal from the linac high voltage power supply, and subsequently the Cherenkov photon emission.¹²⁷

5.2.3 Image Processing

Post-processing was carried out in MATLAB (The Mathworks, Inc., Natick, MA USA). To eliminate noise from stray radiation, as well as any remaining background light, a sequence of image processing steps was followed, as outlined in previous publications.^{50,}

¹³⁰ This processing incorporated background image subtraction, temporal median filtering over 40-50 frames, and spatial median filtering with an 11x11 kernel. In order to generate a single image representative of a dual-field treatment, composite Cherenkov images

were produced by mathematically summing the noise-removed images of each single treatment beam at two tested gantry angles.

4.2.4 TSET Optimization with Cherenkov Imaging

A 1.2m x 2.2m x 1cm sheet of white polyethylene was placed in the x-y treatment plane at an SSD of 441 cm. This plane coincides with the coronal patient plane in the anterior-posterior treatment position, as established by the placement of the wooden patient support structure flush against the wall in the given room geometry. The ICCD was placed near the gantry head approximately 4m from the phantom, as shown in Figure 5.1. A blackout curtain was adhered to the distal side of the plastic sheet to eliminate variations in reflected light from the support structure. To determine the optimal treatment angles, the white polyethylene phantom was irradiated with the TSET beam at 62 gantry angles, from 239.5° to 300.5°, at 1° increments. Fifty frames were acquired at each gantry angle using the same camera settings and post-processing as described above.

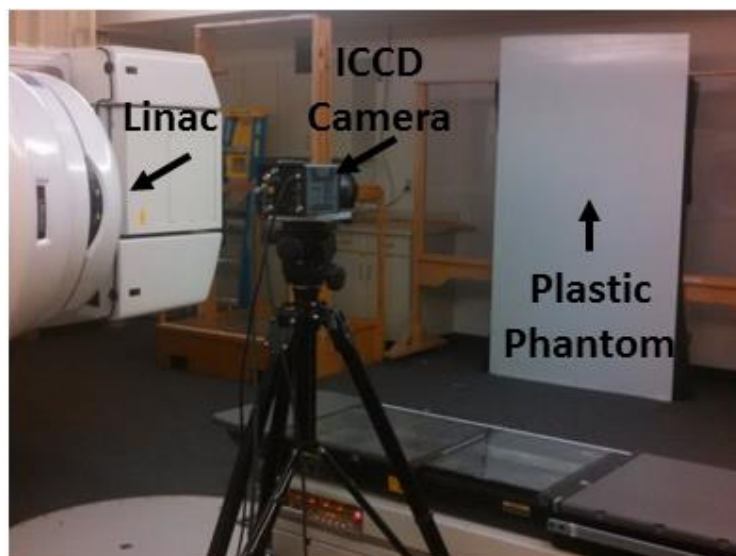


Figure 5.1 Experimental setup for rapid TSET optimization using Cherenkov imaging.

To simulate dual-field treatment, all unique pairs of the 62 images were summed into a composite Cherenkov image, and the resulting 1891 composite images were analyzed. A region of interest (ROI) for analysis was selected through a numerical process using the composite image of the currently prescribed angle pair ($\pm 14.5^\circ$, 29° spread, 255.5° and 284.5°) as the basis.

In this process, a line profile was extracted from the composite image directly at the center line (column number 512 out of 1024). The peak intensity of this line profile was designated the vertical midpoint, and the upper and lower bounds of the ROI were designated as 400 pixels above the peak and 400 pixels below the peak. These quantities ensured the ROI encompassed the 2m height span of the patient support structure. The left and right boundaries of the ROI were determined by calculating the full-width half-maximum of the intensity profile formed by the row of pixel values perpendicular to and including the peak intensity determined from the vertical profile, making the entire ROI roughly 800 x 550 pixels, or approximately 2m x 1.4m.

5.2.4 Ionization Chamber Verification

A 30 x 30 x 5 cm slab of standard Solid Water (CMNC Co., Nashville, TN USA) was milled to fit an Exradin P11 Spokas Parallel Plate Ionization Chamber (Standard Imaging, Middleton, WI USA). With the ionization chamber embedded in the Solid Water, a 30 x 30 x 1 cm slab of white-surface Plastic Water (CMNC Co., Nashville, TN USA) was placed over it, to provide a flat, light-colored and uniform imaging surface. The 1cm thick Plastic Water also ensured that the ionization chamber measured the radiation beam at depth of maximum dose (1.1cm, the last 1mm accounted for by the thickness of the ionization

chamber wall). The flat phantom containing the ionization chamber was physically translated across nine positions constituting a 3x3 matrix in the patient treatment plane to survey the entire height and width of the plane, and irradiated in each position using the original treatment angle pair, as well as the optimized treatment angle pair.

The ionization chamber was also used to verify the percent depth-dose curve remained unchanged with the new treatment angles. With the gantry placed at 270°, the ionization chamber, mounted in the slab of Solid Water, was placed at a source to surface distance (SSD) of 441 cm. The field projection crosshairs of the gantry were used to ensure the ionization chamber was centered at midline.

The charge measurements were recorded after irradiating with 200 MUs of the prescribed treatment beam at the desired angle pairs (the original as well as the optimized). The ionization chamber was translated away from the source, and slabs of Solid Water were placed in front of the instrument to increase the depth of each exposure reading. The depth of solid water in front of the chamber was increased from 0 to 31 mm in this fashion, while the SSD remained constant, for all subsequent exposure measurements. This permitted the acquisition of a percent depth dose (PDD) curve for the TSET setup using the parallel plate ionization chamber embedded in solid water.

5.2.5 Initial Patient Imaging Trials

Three patients were imaged TSET was delivered per standard institutional protocol using a modified Stanford technique, consisting of six patient positions treated with dual fields, a 6 MeV electron beam, without spoiler, open to maximum field size of 36 x 36 cm (at isocenter), and operating at a dose rate of 888 MU/min. The prescribed total dose was

1800 - 3600 cGy, delivered in 200 cGy/cycle, with a cycle delivered over two days. Cherenkov imaging of treatment was performed with local IRB approval and informed patient consent. Measurements of surface dose were carried out during TSET following standard procedures using TLD-100 rods (1mm diameter, 6mm length) secured to the patient's skin.

5.2.6 Additional Patient Imaging Case Studies

Imaging TSET patients presents a unique opportunity to characterize variation in Cherenkov intensities exhibited by different living tissues, which cannot be accurately replicated in phantom studies that lack the dynamics of blood flow and respiration. In that vein, focused case studies were initiated. These experiments aimed to correlate variations in Cherenkov intensity to tissue optical properties, as estimated from inferences of tissue types from the patients' most recent diagnostic CT scans.

Two additional patients (Patient #4 and Patient #5) were imaged during TSET after adopting the optimized treatment geometry at SSD=300cm on a Varian Trilogy linac also commissioned with a dual-field modified Stanford technique. The same camera system and setup was used to acquire Cherenkov images during treatment, with the exception that the camera lens was changed to an 135mm focal length Canon lens during select treatments, to focus the field of view to the torso or the extremities.

Diagnostic CT volumes of the patient were acquired and segmented in the areas of interest for adipose, muscle and bone. The Cherenkov images were qualitatively compared to the segmented CT volumes to evaluate the hypothesis that Cherenkov intensity would be highest in areas corresponding to the thickest superficial layers of

adipose tissue. This is based on the premise that adipose has less blood content than muscle tissue, where blood is the dominant absorber of generated Cherenkov light wavelengths.¹³⁴ TLD measurements were used to validate true surface dose as a benchmark of the variability in the Cherenkov-based measurements.

5.3 Groundwork Results

5.3.1 Optimization of TSET

The coefficient of variation was calculated within the defined ROI of each of the 1,891 unique composite images and plotted against mean Cherenkov intensity. The minimum coefficient of variation occurred at gantry angles 252.5° and 288.5°. However, a symmetric spread ($\pm 17.5^\circ$, 35° spread, 252.5° and 287.5°) was chosen as the optimal angle set for simplicity of delivery, because the coefficient of variation was raised by less than 1.2% between the spread exhibiting the true minimum and the symmetric angle minimum (Figure 5.2a).

Figure 5.2 shows the composite Cherenkov images for treatment delivery on the flat tissue phantom using the original angle pair compared to the optimized angle pair. Increasing the angle spread resulted in more homogenous but decreased dose (Figure 5.2 (c) compared to Figure 5.2 (d)), and therefore more monitor units need to be delivered from each beam of the optimized pair to result in the same prescribed dose. The horizontal line across the bottom of the polyethylene sheet is a piece of medical tape used to mark the height of the bottom platform of the patient support structure.

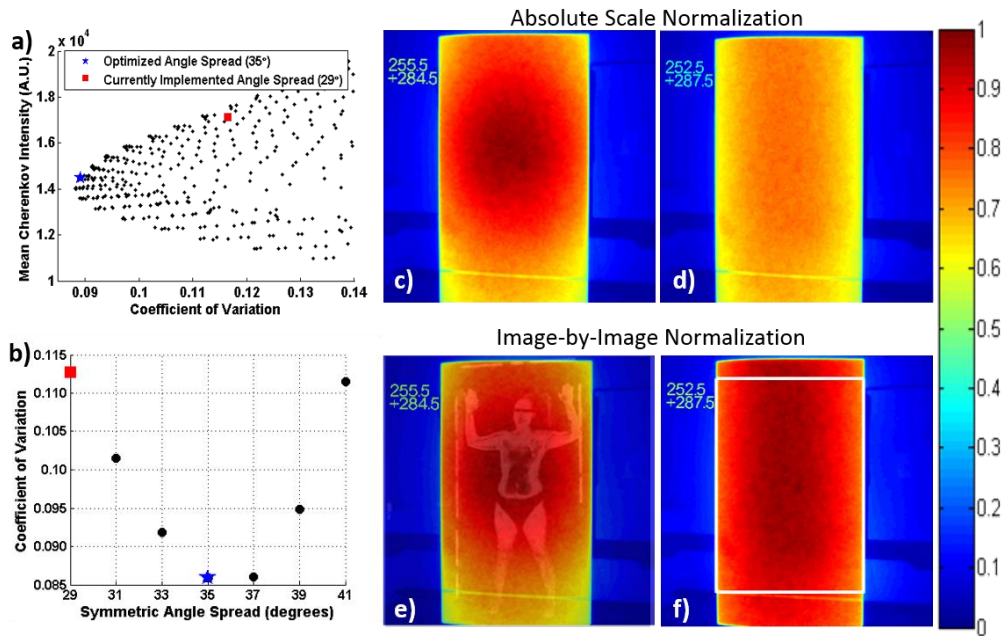


Figure 5.2 (a) Mean Cherenkov intensity (relative surface dose) vs. coefficients of variation for a subset of angle pairs. The historical angle pair used at the institution (255.5° and 284.5°) is labeled by a red square, and the minimum coefficient of variation at a symmetrical angle pair occurred at 252.5° and 287.5°, denoted by the blue star. (b) Calculated coefficients of variation at symmetric angle spreads. The composite Cherenkov images for the original and optimal angles spreads are shown in (c) and (d), respectively, on the same normalization scale; the self-normalized Cherenkov images are shown in (e) and (f). The image in (e) is overlaid with an image of a TSET patient for size scale. The white box in (e) shows the analyzed ROI.

5.3.2 Verification of the Optimized Angles

Cherenkov imaging on a flat tissue phantom was confirmed as an accurate surrogate for delivered dose by correlating Cherenkov intensity with dose measured using an ionization chamber at depth of maximum dose. This produced a coefficient of determination $R^2=0.93$ (Figure 5.3(d)). Additionally, the heterogeneous dose observed through Cherenkov imaging of the flat phantom at the originally prescribed treatment angles (Figure 5.2(c),(e); red squares on Figure 5.3(d)) was confirmed by ionization chamber measurements exhibiting variation from 75.6-100% of prescribed dose (Figure 5.2(b),(d); blue circles on Figure 5.3(d)).

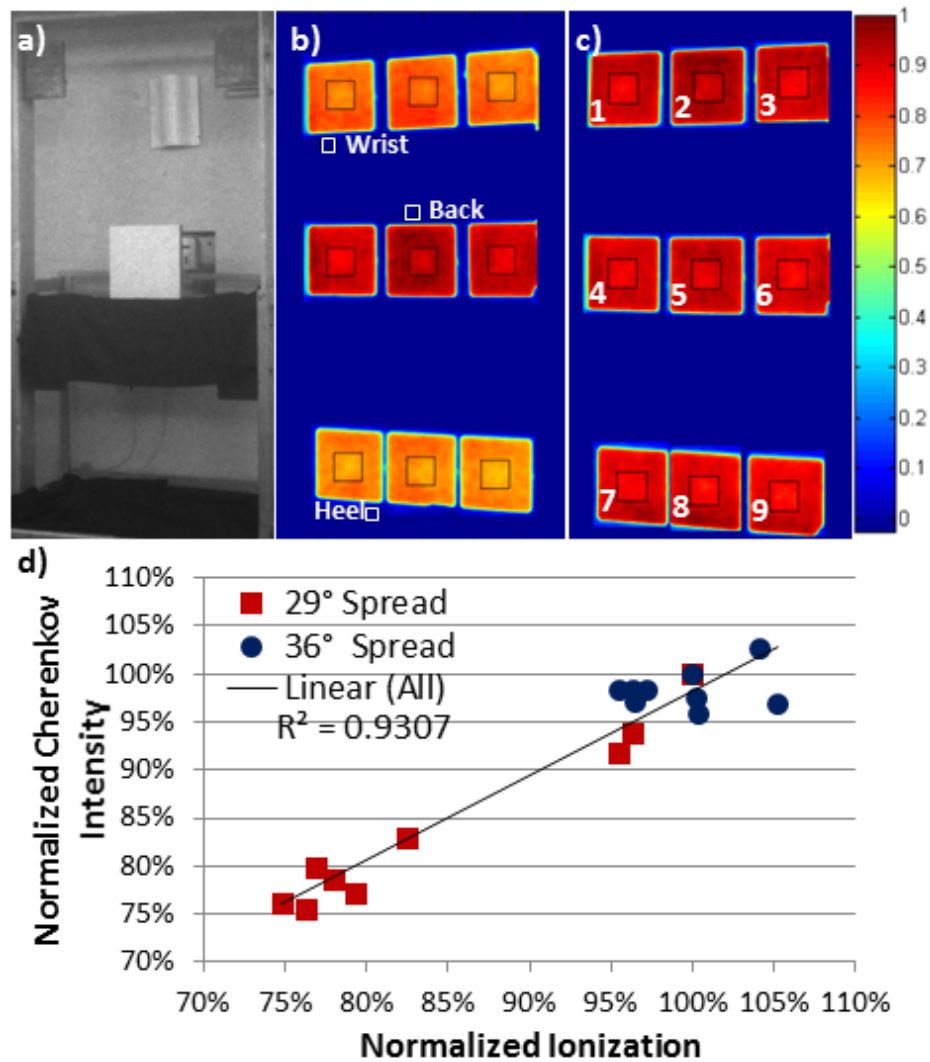


Figure 5.3 (a) White light image of the phantom with embedded ionization chamber placed at position 5. (b) Self-normalized, super-imposed, composite Cherenkov image of the phantom irradiated with the two fields historically used for treating patients at our institution (255.5° and 284.5°); approximate locations of a patient’s wrist, back and heel are shown for reference. (c) Cherenkov image of the phantom irradiated with treatment angles producing minimum coefficient of variation (gantry at 252.5° and 288.5°). (d) Mean Cherenkov intensity calculated from the ROIs outlined in black shown in (b, red squares) and (c, blue circles) versus the ionization chamber measurements, at each of the nine positions shown, each normalized to the respective value at position 5 (prescription point). Black square outlines were superimposed on (b) and (c) to illustrate ROI size and placement.

The dose distribution of the optimized treatment geometry was measured using an ionization chamber concurrently with Cherenkov imaging at nine positions to confirm

improved homogeneity (Figure 5.3(c), (d) blue circles). Ionization chamber measurements of the optimized treatment angles demonstrated dose heterogeneity ranging from 95.4% to 105.2% of prescribed dose (Figure 5.3(d), blue circles), confirming reduction from 24.4% with the original prescribed angles to 9.8% for the Cherenkov-selected optimum treatment angles.

Ionization chamber measurements also confirmed the percent depth-dose curve remained unchanged with the new treatment angles. Figure 5.4 shows both the relative chamber measurements, as well as the calculated percent depth-dose curves, which provide information on how much dose is changing relatively, as well as about the contribution of x-ray contamination (tail of the curve).

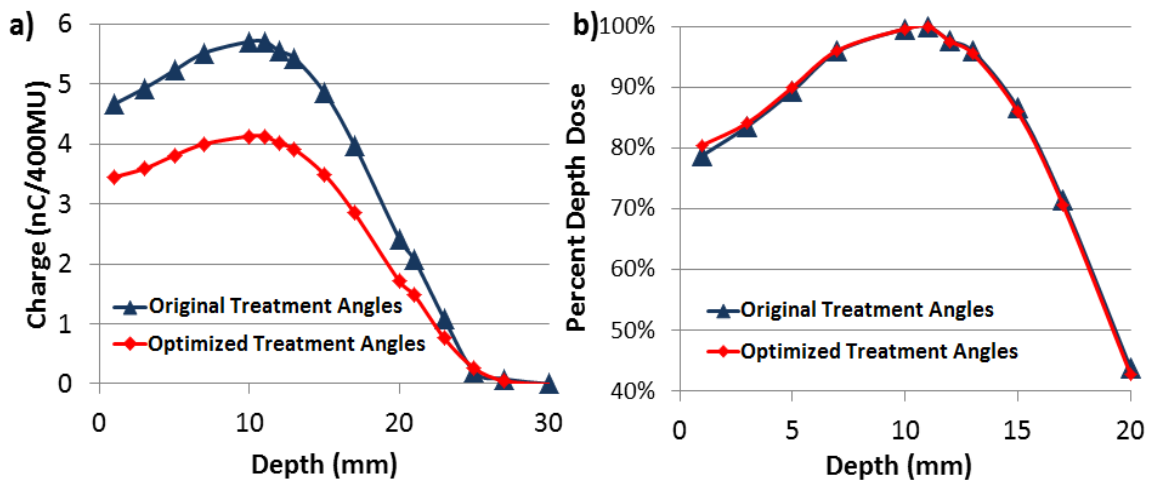


Figure 5.4 (a) Ionization chamber charge measurements for increasing depth of Solid Water between the original treatment angles and the selected optimized treatment angles, demonstrating the decrease in relative dose delivered for the new angles. (b) Normalized percent depth dose between the original treatment angles and the optimized treatment angles.

The calculations were performed following the stopping power values and equations specified in AAPM Report 32. Dose from the ionization chamber is given by:

$$D_{med} = Q_{corr} P_{repl} (\bar{L}/\rho)_{air}^{med} K$$

The percent depth dose curve was then generated by normalizing to the maximum measured dose (dose at d_{max}):

$$\%D(d) = 100\% * \frac{D_{med}(d)}{D_{med}(d_{max})}$$

While the depth of maximum dose did not change with the new angles, evidenced by the two data sets exhibiting a determination coefficient of $R^2=0.998$, the relative absolute dose does decrease. Measurement of the delivered dose per monitor unit, following AAPM TG-51 Worksheet D, can be used to determine the appropriate scaling of monitor units to achieve the same prescription dose on a machine-by-machine basis.

5.3.3 Varying Room Geometry

To extend our findings to treatment rooms with more restrictive space, an equation for SSD-dependent optimal angle spread was identified. Analysis of the composite Cherenkov images of the polyethylene sheet placed at SSDs of 300 cm, 370.5 cm and 441 cm support a linear relationship between angle spread and SSD, as shown in Figure 5.5. Angle spread can be chosen for a given SSD following the empirically-derived equation:

$$Angle\ Spread = 47.5 - 0.028 * SSD$$

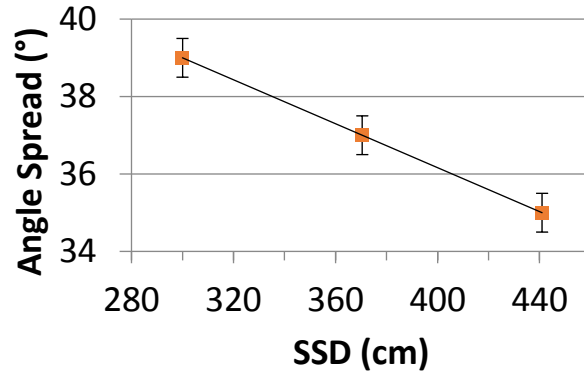


Figure 5.5 Linear dependence of optimal angle spread on the SSD, using symmetric angle pairs. Images were acquired using 1° increments.

5.3.4 In vivo Cherenkov TSET imaging

Initially, 2 patients receiving TSET following the established clinical protocol were imaged with the Cherenkov system. The composite Cherenkov images for both patients in each of the six treatment positions are shown in Figure 5.6 (rows 1 and 2). All twelve images indicated that the torso region exhibited a higher Cherenkov emission intensity compared to the legs and feet.

This observation was further investigated using TLD measurements on patient #1 in a single position (posterior), while dual treatment fields were delivered using the original treatment geometry ($\pm 14.5^\circ$, 29° spread, 255.5° and 284.5°), shown in Figure 5.7. The TLD measurements (Figure 5.7(b)) also indicated a higher surface dose in the torso (95-100% of measured dose normalized to the maximum recorded in the posterior position) compared to the legs and feet (85-91% of the normalized dose). The *in vivo* Cherenkov emission intensities showed an even larger variation, likely due to differences in patient and tissue-specific optical properties, which are still being investigated.



Figure 5.6 Composite Cherenkov images for three patients in the six Stanford technique treatment positions. All images are represented on the same color scale. Patients #1 and #2 were treated with angle spread of 29° at SSD=441 cm, and were wearing cloth shorts. Patient #3 was treated with angle spread of 35° at SSD=441 cm, sitting on a bicycle seat for patient stabilization (no cloth shorts).

All three methods of dose measurement (TLDs, ionization chamber, and Cherenkov intensity) indicated that the original prescribed treatment geometry produced heterogeneous treatment dose that could be reduced to less than 10% with the optimized treatment angles. After extensive verification, the new angle spread of ($\pm 17.5^\circ$, 35° spread, 252.5° and 287.5°), as opposed to ($\pm 14.5^\circ$, 29° spread, 255.5° and 284.5°), at an SSD of 441 cm was adopted clinically, and a third patient was treated using the new angles (Figure 5.6, row 3).

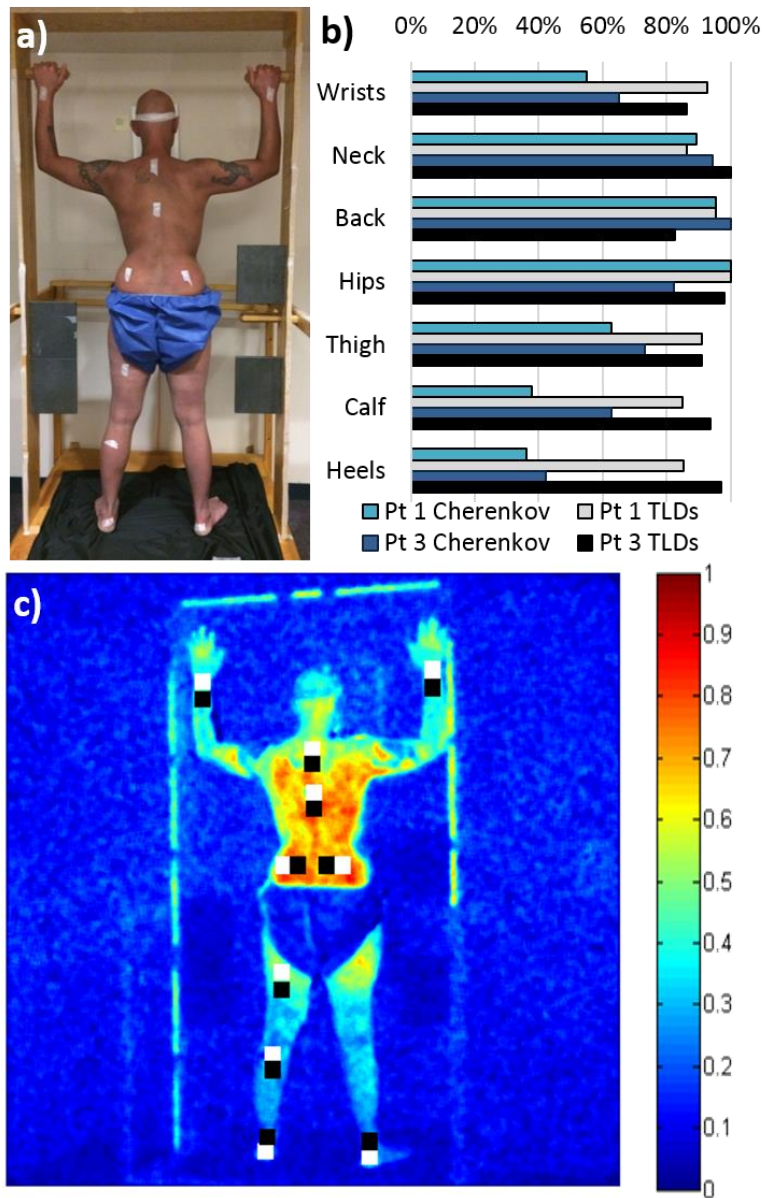


Figure 5.7 (a) Placement of 10 TLDs on Patient #1 (posterior position only). TLDs were also placed on Patient #3 in similar approximate positions. (b) Plot comparing average Cherenkov intensity of ROIs directly on top of the TLD with the measured dose from the TLDs. Each data set is normalized to its respective highest measurement (at the hips). Measurements on opposing wrists and opposing heels are each averaged together for display clarity. Data from Patients #1 and #3 are shown for comparison, although images (a) and (c) correspond to Patient #1 only. (c) The two sets of ten 25x25 pixel regions of interest (ROIs) that were analyzed for average Cherenkov intensity on Patient #1. The white regions are directly on top of the tape affixing the TLDs, and the black regions are offset from the taped regions. There was no statistically significant difference between the mean Cherenkov intensity in the black and white labelled regions; the white labelled regions were used in (b).

The Cherenkov images of the patient treated with the optimized angles is compared to the previously imaged patient who was treated with the original geometry (Figure 5.6). Repeating the TLD measurements made on patient #1, surface dose was measured for the straight-on posterior treatment beam pair for patient #3, using the optimized beam angles. TLDs in 10 positions on patient #3 had a range of 19% of the average dose value, 7% less than the 26% range observed in patient #1 before angle optimization took place, corroborating a more uniform clinical dose distribution.

5.3.5 Improvements during in vivo Imaging

One of the primary directives of patient imaging in the two case studies shown here is to explore the sources of Cherenkov intensity variation, particularly the decreased signal seen in the forearms and legs. Composite Cherenkov images Patient #4 and Patient #5 in the six prescribed treatment poses are shown in Figure 5.8. Patient #4 is shown using the “jet” color scale in the three left columns, and Patient #5 is displayed using a blue color scale in the right three columns. Figure 5.9 shows the first case study on Patient #5, focusing on the legs. Additional imaging sessions were conducted focusing on the torso of TSET Patient #4 (Figure 5.10), with surface-dose verification TLD measurements.

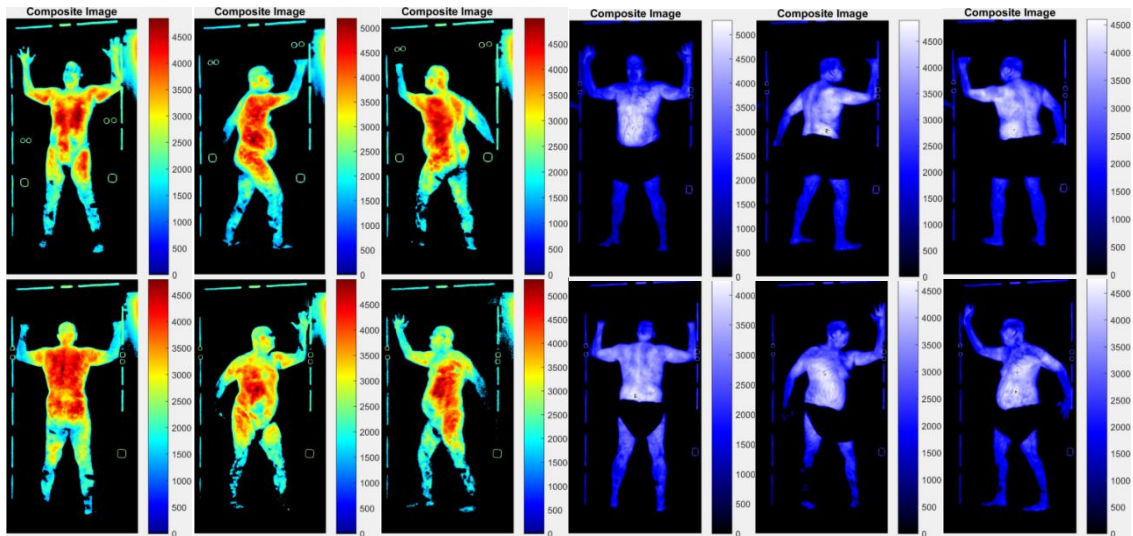


Figure 5.8 Six TSET treatment poses for patients #4 (left, jet) and #5(right, blue).

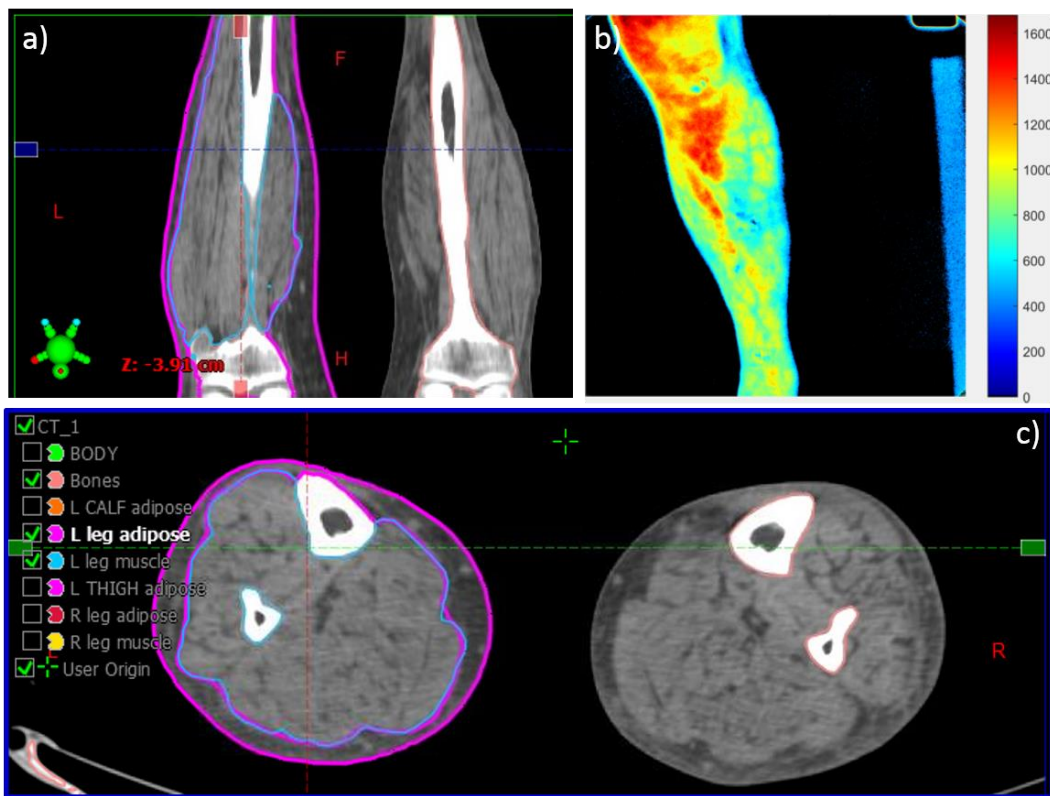


Figure 5.9 Case study of legs of TSET Patient #5. a) Coronal plane view of CT scan with adipose segmented in magenta, and muscle segmented in blue. b) Composite Cherenkov image of Patient #7's left leg for the dual-field AP beam. c) Transverse plane of CT scan of patient's legs, at the blue line indicated in a), using the same color designations for adipose and muscle.

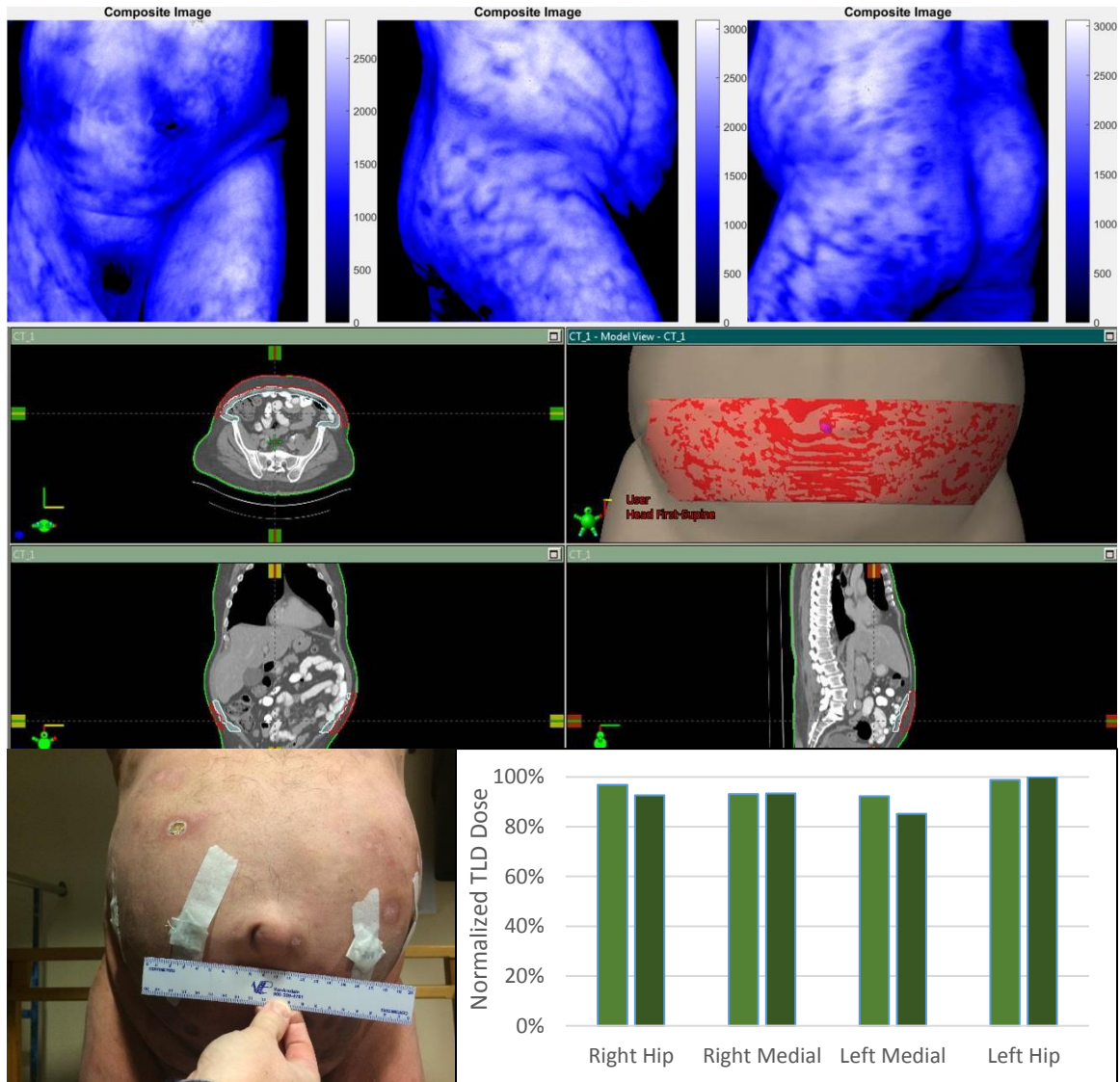


Figure 5.10 Study of TSET Patient #4, comparing the Cherenkov images of the lower torso and groin area (top row), to body tissue composition from diagnostic CT scans (middle rows), and concurrent surface dosimetry TLD data (2 TLDs per position).

5.4 Discussion of Initial Application of Cherenkov Imaging to TSET

5.4.1 Discussion of TSET Geometry Optimization

Cherenkov imaging allows for observation of an optical analog of treatment delivery on a surface as a 2D image. It offers an advantage over other beam imaging technologies, such

as flat panel detectors, which are limited in the scope of the measurement and by the physical size of the detectors themselves. TLDs, diodes and ionization chambers are all useful beam characterization tools, but offer only point measurements with limited implementation for whole body dosimetry. In contrast, Cherenkov imaging uses a camera system to passively capture the data generated by the radiation and the volume being irradiated, and so the field of view and data quality is defined largely by the lens system and camera used. Therefore, this method is capable of observing a large treatment field, as in the case of TSET, by choice of appropriate lens focal length and camera distance.

This also translates into a time advantage by permitting a more rapid and extensive optimization than would be feasible with other modalities, since each pixel in the image can be thought of as an independent measurement provided by a TLD or ionization chamber reading. For example, ionization chambers would require at least 9 point measurements to canvas the entire TSET field at each individual angle tested, thus each beam would need to be repeatedly delivered 9 times to capture a fraction of the information collected from a single beam with Cherenkov imaging.

Similarly, while a set of TLDs could be used to measure many points in the field simultaneously, the time for post-processing makes TLDs too onerous to analyze even a modest subset of gantry angle combinations. Alternatively, there are systems capable of supporting large numbers of diodes to assess similar large fields, however, in addition to much lower measurement resolution (they are still each point detectors), these systems require care in calibration due to angle and energy dependencies.

While a 62° span of gantry angles was considered for completeness in the original study presented here, it would be reasonable to limit future calibration imaging following this method to a smaller subset of possible angles. Both literature⁶⁰ and the results of this study support looking at angles between $\pm 15^\circ$ to $\pm 20^\circ$ (spreads between 30° and 40°).

Past research has demonstrated a strong correlation between Cherenkov intensity and measured surface dose from flat, homogeneous phantoms,⁴⁸ a correlation reinforced by the results presented here. Cherenkov imaging successfully determined the most homogenous combined beam geometry as a function of SSD, and a linear relationship was observed. These measurements are intended to provide general guidance for other institutions, with further verification of the beam field using ionization chamber measurements. While the new treatment angles did not appreciably alter the depth of maximum dose, the increase in angle spread from the previously implemented angles did cause a relative decrease in delivered dose per monitor unit. Either decreasing the SSD and adjusting gantry angles accordingly, or increasing the number of MUs delivered will compensate for the decrease in dose caused by increasing the gantry angle spread.

X-ray or bremsstrahlung contamination is frequently brought up in regards to TSET, because these photons can deposit dose deeper than skin level. While the Cherenkov imaging method does not provide a method to directly measure the contribution of x-ray contamination, it is not regarded as a significant problem at typical TSET energies of 6 MeV and 9 MeV; bremsstrahlung is more extensive in smaller fields at much higher electron energies, such as 20 MeV.^{152, 153} Extensive studies have been conducted by other groups where the electron portion of the beam is magnetically

steered from the main beam path so that only the bremsstrahlung can be measured; these have concluded the dose due to bremsstrahlung photons from 6 MeV TSET beam accounts for less than 1% of the total dose, often on the order of 0.2%, when using a properly designed setup.^{154, 155}

For many institutions, it is more feasible to use the depth-dose measurements from an ionization chamber to acquire a sense of the x-ray contamination for any particular TSET angle pair.¹³⁶ Figure 5.4 clearly shows that the x-ray contamination between the two different treatment geometries compared are nearly the same and less than 1%, which follows suggested guidelines. Since x-ray contamination is most prevalent on the central axis of the beam,¹⁵² following the general rule to choose TSET beam angles where the beam axis does not intersect with the patient is desirable.⁶⁰ The optimized treatment angles selected by the Cherenkov imaging method presented in this paper satisfy that criteria.

5.4.2 Discussion of TSET Patient Imaging

In this chapter, Cherenkov imaging was also used to monitor treatment delivery of five patients receiving TSET (three patients in the initial study, and two additional patients afterwards). Despite the quantitative correlation between phantom images and ionization chamber measurements, localized Cherenkov intensities in patients did not strongly correlate to absolute surface dose as measured by a set of 10 TLDs for the beams treating in the straight-on posterior position only.

However, there was general agreement that the surface dose in the hands and feet was less than the surface dose in the torso between the two methods. In addition,

the TLD measurements from the optimized treatment on Patient #3 had less variation than the TLD measurements from the original treatment setup used on Patient #1, supporting a more homogeneous treatment geometry.

The relationship between dose uniformity in phantom studies as compared to TSET patients is a known issue described in AAPM TG-30 Report 23, which states “the uniformity of dose achieved in phantom studies in the treatment plane cannot be reproduced over the patient... due to variable skin distance, self-shielding, and patient motion.”⁶⁰ This, along with anatomical heterogeneities of the imaged patient volumes, is thought to be the cause of the disparity between the Cherenkov intensity from patients and the measured surface dose. Current work to correct for tissue optical properties is ongoing, which should result in better correlation of Cherenkov emission intensity with absolute surface dose in patients.

Improving delivered dose homogeneity has an important implication for TSET with lower dose schedules, which is a new trend in order to reduce toxicity of the treatment, and to allow repeated delivery of TSET.¹⁵⁶ When treating with these dose-reduced schedules, it seems prudent to verify dose homogeneity to ensure areas of disease are not under-dosed, which could lead to early failures.

Interpreting the Cherenkov images requires understanding of the visualization methods employed. First, processing of patient images was augmented between Patient #3 and Patient #4 to implement a histogram-based thresholding scheme to further reject background noise and isolate the patient habitus in each image. Second, the two color scales adopted in Figure 5.8 are used to highlight distinctive nuances of the Cherenkov

intensity patterns. The “jet” color scale emphasizes the broad variation in intensity across the patient surface. The blue color scale is more adept at drawing attention to localized variation in Cherenkov intensities that arise from more minute details (the skin lesions, plaques, and subdermal vasculature).

As was discussed in previous chapters, one of the most influential factors governing the imaged Cherenkov intensity is the variation of tissue optical properties. This prompted the case studies of Patient #4 (torso) and Patient #5 (leg). The hypothesis here was that the thickness of the superficial adipose layer measured in the diagnostic CT scan would influence the Cherenkov intensity observed, given that adipose tissue is known to have lower blood content than muscle, and therefore less light absorption.

Patient #4 presented with dark patches in the Cherenkov images to the medial region about the umbilicus. Measurements of relative dose from TLDs in the area showed an approximately 15% dose variation. This is reasonable given the calibration of the TLDs is within 10%, and variation in the orientation of the TLDs with respect to the beam position. The hips read the highest dose, as the long physical axis of the TLDs is closer to parallel with the incoming radiation beam because the patient curvature defines the TLD orientation. The TLD results do not corroborate the approximately 50% variation in Cherenkov light intensity observed in the optical images (Figure 5.8 top left, Figure 5.10 top left).

Evaluation of the adipose layer for Patient #4 in the same region did not result in measureable differences of fat thickness when limiting the scope to the superficial 1cm layer of the patient surface; beyond 1cm the tissue composition is ignored, since the

amount of Cherenkov light escaping the tissue after originating at deeper depths is negligible.

This result did not support the stated hypothesis, since the low intensity Cherenkov areas in the images did not have less adipose. Instead, it is thought that the low intensity areas on this patient are a direct result of the skin lesions and plaques of his disease. While these localized regions of dense tissue do not appear on the CT scan, many are easy to see visually on the surface or physically palpate.

Similar examples of visualizing the superficial disease via the Cherenkov images is shown in the top right pictures of Figure 5.10. It is important to note that the low intensity areas on the abdomen of Patient #4 were not observed in the other four patients imaged for this study, which reinforces the notion that these Cherenkov imaging artifacts are from the individual's specific manifestation of the disease.

While the case study of Patient #4 did not support the hypothesis, the results of Patient #5 did lend themselves to the proposition. As seen in Figure 5.9 (c), the interior portion of the lower leg has the most substantial thickness of adipose tissue. This same interior quadrant of the left leg is also the brightest in the Cherenkov image. The closeness of bone and muscle to the remaining portion of the leg reasonably explains the low Cherenkov intensity areas persistent across all imaged patients, in the generally high muscle to fat ratio forearms and lower legs. Therefore, the results of the Patient #5 case study support the hypothesis.

In general, the thickness of the superficial adipose layer does in fact affect the Cherenkov intensity. However, this is only a singular, broad interpretation that does not

take into account the specifics of how the disease manifests in each patient. Therefore, any potential quantitative correction for Cherenkov intensity derived from *a priori* knowledge of superficial adipose thickness will still maintain substantial artifacts from the highly variable distributions of the cutaneous disease. It is thus possible that the Cherenkov images could be used to further inform clinicians of the extent of disease, but it is not clear at this time whether these images would provide any additional information when compared to a traditional physical exam of the patient between radiotherapy sessions.

5.5 Initial TSET Imaging Conclusions

The hypothesis that Cherenkov imaging could be used to verify TSET treatment geometry faster and more extensively than established modalities was supported by the results of this study, and a novel technique for evaluating beam homogeneity for large fields using Cherenkov imaging of phantoms was presented. A linear relationship between angle spread optimized for a homogeneous dual-field and treatment SSD was observed. The angles which produce the most homogenous field can be adopted by other institutions after dose calibration. In addition, TSET patient Cherenkov imaging can be used to verify patient irradiation, but the dosimetric value of this imaging is limited with current techniques.

Chapter 6: Floor Scatter during Total Skin Electron Therapy

This chapter is largely derived from: J.M. Andreozzi et al., “Experimental Investigation of Linac Angles and Floor Scatter Dose Contributions Using Cherenkov Imaging: Improving Total Skin Electron Therapy Treatment Geometries,” *Med. Phys.* (Accepted, April 2018)

Total skin electron therapy (TSET) has long been an accepted form of palliative care to manage the cutaneous T-cell lymphoma known as mycosis fungoides.^{57, 59, 61–63, 142} The goal of the treatment is to deliver homogeneous superficial dose (to a depth of 1-5mm) to the entire patient skin surface, where the disease primarily manifests.⁶⁴ In spite of the intention for dose uniformity, high deviations of *in vivo* dose distributions have been published. Anacak *et al.*⁶⁸ report a mean deviation of $7.7 \pm 7.4\%$ in readings on the trunk, and a mean deviation of $19.7 \pm 17.7\%$ in extratrunk readings using a cohort of 67 TSET patients treated at a single institution, while noting similar deviations in patients treated with and without beam spoilers. While some variation in surface dose readings is expected, the extent of the variation can be minimized by ensuring the planar uniformity of the field before treatment.

Task Group 30 Report 23 (TG30) outlines the current recommendation by the American Association of Physicists in Medicine for commissioning and field dose parameters.⁶⁰ The commonly adopted six position, dual field approach known as the modified Stanford technique places the patient on a raised treatment platform at extended source to surface distances between 3-8m, and irradiates with high dose rate electrons of energies between 4-12 MeV.^{60, 64, 65, 68, 157–160} Using two fields (an upper and

a lower beam) not only helps accommodate the large treatment area, but also aids in the reduction of x-ray contamination at the patient. A beam spoiler is sometimes introduced to degrade the beam energy to better match the required penetration depth at the patient, without affecting dose rate or levels of x-ray contamination,¹⁵⁷ however there is some evidence that beam uniformity suffers.⁶⁸

Typical dose measurement techniques used for TSET commissioning are limited to sparse point measurements using thermoluminescent dosimeters (TLDS), diodes, optically stimulated luminescent dosimeters (OSLDs), ionization chambers, or more regional 2D film measurements.^{150, 151} As a result of this, in conjunction with the large field sizes and extended source to surface distances (SSDs) required for this treatment, there are limited techniques to quickly evaluate the dose distribution in the treatment field as a whole at high resolution.

Previous work introduced a Cherenkov imaging method capable of capturing the full treatment region rapidly and accurately (Cherenkov intensity was linear with ionization chamber measurements with $R^2=0.93$).¹⁶¹ This method utilizes an intensified charge coupled device (ICCD) camera to visualize surface dose on a large polyethylene sheet in the patient treatment plane, in addition to *in vivo* patient imaging during irradiation. The research presented herein aims at expanding the understanding of the TSET dose fields using similar Cherenkov imaging techniques, where the methods of analysis has been further developed and improved to make more extensive conclusions regarding optimal treatment setup.

Two main hypotheses are explored. The first hypothesis states that an asymmetric selection of gantry angles (unequal theta above and below the horizontal) for TSET setup provides a larger, more inclusive 90% isodose area than the recommended symmetric gantry angle pair (equal theta above and below the horizontal). This deviates from the original presentation of the Cherenkov imaging method, which evaluated treatment angle pairs based solely on the coefficient of variation within the test plane.¹⁶¹

In addition, interpretation of the dose distributions during TSET requires some consideration of dose from floor scatter.¹⁶² The second hypothesis states that the remote Cherenkov imaging method will exhibit sensitivity to dose deposited in the treatment plane as a result of the scattering interactions between the ionization radiation beam and the floor, which will be tested by introducing different scattering materials to the field and measuring differences between the collected Cherenkov images.

6.1 Materials and Methods of Floor Scatter Study

For this study, a Cherenkov imaging technique was adopted to image an analog for relative surface dose on a large 1.2m x 2.2m x 1cm white polyethylene sheet at the extended treatment plane used for TSET (SSD=300cm). Following the recommendation of previous publications,^{10, 161} an intensified charge coupled device (ICCD) camera (PIMAX4 1024i, Princeton Instruments, Trenton, NJ, USA), equipped with a 24mm Canon F1.8L lens, was placed approximately 4m away from the polyethylene sheet. No beam spoiler was used between the beam and the treatment plane, consistent with the adopted 6MeV TSET treatment protocol. As shown in Figure 1.a, Black-out fabric

(Thorlabs, Newton, NJ, USA) was affixed to the posterior face of, as well as on the floor in front of, the plastic sheet to eliminate optical reflections on the surface of interest.

Cherenkov image acquisition was triggered to the linac radiation pulses using the current signal out of the high voltage power supply of the linac. A $3\mu\text{s}$ gate delay and a $5\mu\text{s}$ long gate window was used to time synchronize the ICCD acquisition with the radiation pulses. To ensure a strong signal to noise ratio, each image frame consisted of 500 radiation pulses (i.e. on-chip accumulations), which resulted in a readout frame rate of approximately 4 frames per second (fps).

Linac angular reference conventions can vary between models and clinics. In this work, the linac coordinate system used stipulates 0° is the bottom of the gantry arc with the beam pointed towards the ceiling, and progresses counterclockwise so that gantry angle 270° produces a horizontal beam orthogonal to the TSET treatment plane. Gantry angle combinations are listed in reference to the horizontal, 270° ; angles greater than 270° are inclined towards the ceiling (upper treatment beam), and angles less than 270° are slanted towards the floor (lower treatment beam).

6.1.1 TSET Geometry Optimization Experiment Design

Building on the previously published technique in TSET geometry optimization using Cherenkov imaging,¹⁶¹ the ICCD setup described above was used to collect Cherenkov images corresponding to the 2D relative dose profile on the uniform polyethylene sheet placed at $\text{SSD}=300\text{cm}$, for 43 gantry angles (240° - 260° , 270° , and 280° - 300°), where 270° corresponds to the horizontal. The experiment was repeated on two linacs: 1) a Varian 2100CD series linac, and 2) a Varian Clinac iX Trilogy (Varian Medical Systems, Palo Alto,

CA). The former was operated in high dose-rate TSET mode, delivering 6MeV electrons at dose rate 888 monitor units per minute (MU/min) (calibrated at 3cGy/MU), and field size 36cm x 36cm at isocenter. The latter was operated in standard mode, delivering 6MeV electrons at dose rate 1000 MU/min (calibrated at 1cGy/MU), and field size 40cm x 40cm at isocenter.

Through post processing carried out in MATLAB (Mathworks, Natick, MA USA), all unique angle pair combinations were summed into composite images of relative surface dose, then quantitatively analyzed to determine the optimized treatment setup to provide the largest uniform field. The numerical analysis of the composite treatment images consisted of extracting the >90% isodose region of the image. In this context, 100% dose is the maximum intensity in the Cherenkov image, rather than the prescription point at the center of the field. Given that the Cherenkov image provides relative dosimetry, this distinction simplifies the comparison for analysis; any geometry producing a field with the prescription point outside of the 10% tolerance will be rejected after calculating the optimization metric α , to be defined later. The Cherenkov images can be renormalized after analysis to provide the 10% isodose spread about the central prescription point.

The coefficient of variation (CoV , defined as the standard deviation divided by the mean), height (h), width (w), and total area of each >90% isodose region (A_{90}) along the central axes, were each normalized by the best observed value of each measurement. These numbers were then summed into a single optimization metric, α , defined by the equation:

$$\alpha = \frac{CoV_{measured}}{CoV_{min}} + \frac{w_{max}}{w_{measured}} + \frac{h_{max}}{h_{measured}} + \frac{A90_{max}}{A90_{measured}} ,$$

Using this equation, the theoretical “best” treatment geometry would have $\alpha=4$, the minimum possible value. In practice, the angle pair producing the smallest value of α is considered the optimized treatment geometry producing the largest, most uniform dose profile in the flat plane of the TSET setup.

6.1.2 Floor Scatter Experiment Design

To further understand the results of the TSET geometry optimization, an experiment was designed to test the sensitivity of the Cherenkov imaging technique to radiation dose from floor scatter. By imaging the 2D profile of surface dose on the plastic sheet with various materials on the floor at the foot of the polyethylene, the differences in relative dose observed could be inferred as differences in floor scatter.

Because the phantom had homogeneous optical properties, results show no appreciable change in correlation between Cherenkov intensity and surface dose when using the correction method on images of an anthropomorphic solid silicone phantom, as concluded from the plot Figure 4.5. This validates the approach does not unduly alter the Cherenkov intensities, as no change would be expected in a homogeneous phantom. However, the agreement between the Cherenkov and measured dose is not convincingly linear, with R^2 values of 0.58-0.59, which can partially be attributed to the positioning of the TLDs in regions of high gradient dose, as well as tangential with the beam path of TLD position #3 near the apex of the breast phantom.

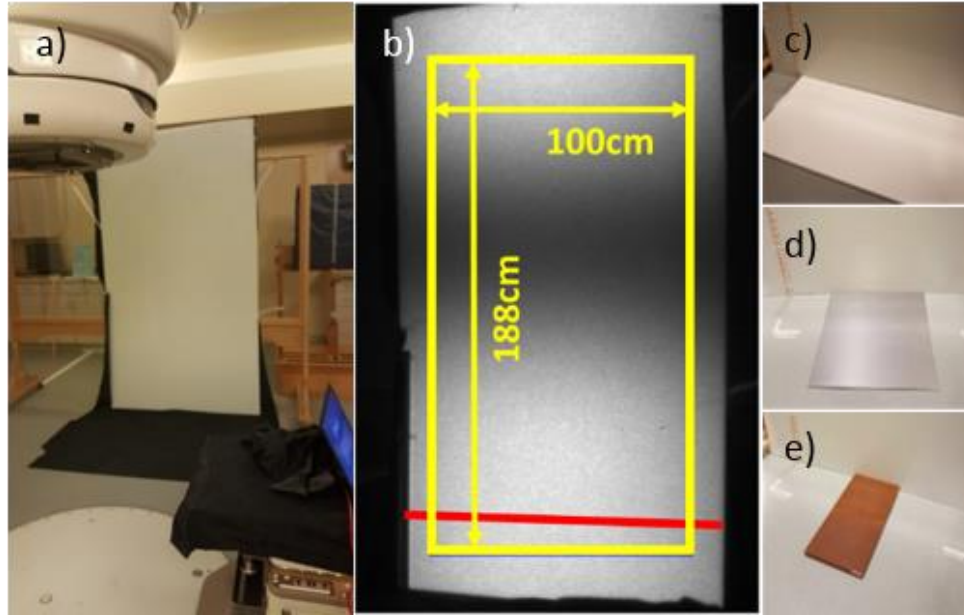


Figure 6.1 a) Experimental setup. b) Test image from camera: yellow box denotes size and shape of analyzed ROI in floor scatter experiment, and red line designates the height (30cm) of the wooden patient support structure used during TSET. c) PVC test material. d) Steel test material. e) Solid water test material. Each test material in c)-e) was covered with blackout fabric prior to Cherenkov imaging.

Table 6.1 List of properties of floor scatter materials tested.

Material	Density (g/cm ³)	R50 (cm)	Length (cm)	Width (cm)	Thickness (cm)
PVC	1.41 ¹⁶⁴	1.6	121.92	60.96	3.81
Solid Water	1.04	2.1	60	30	3
Steel	7.68 ¹⁶⁵	0.3	60.96	60.96	0.318

Post processing of the images was performed in MATLAB. Each test case produced 31 images as a result of the 250 MUs delivered. To eliminate random salt-and-pepper noise caused by stray radiation in the room hitting the camera, a temporal median filter was performed on each set of 5 consecutive images, resulting in a final stack of 27 images for each gantry angle and floor material combination. Background image subtraction was performed on each image to eliminate any influence of ambient light (minimal, given all

images were collected with room lights off and instrumentation lights on the linac and couch were covered). The mean pixel value at each location was then used to generate a single frame of data for each test case. Each image was then normalized to the maximum pixel value observed in all of the data sets combined, so that relative comparison would be possible.

To visualize the changes in radiation floor scatter due to the modification of floor material, residual images were calculated by subtracting the control image (concrete floor covered in blackout fabric) from the experimental image (solid water, PVC, and steel, each covered in blackout fabric). An 11x11 pixel averaging kernel (corresponding to a roughly 2.5cm x 2.5cm area) was then applied to each residual image to smooth the results, and eliminate the influence of noise.

6.2 Results of Floor Scatter Study

6.2.1 TSET Geometry Optimization Results

The numerical TSET optimization described above was performed on the composite Cherenkov images using two criteria. First, limiting the search to symmetric angle pairs that have an equal angle above and below the horizontal gantry position (270°). Second, this restriction was lifted and all possible angle pairs were analyzed.

The two optimized results are shown in Figure 6.2. By adopting an asymmetric angle pair ($270^\circ+23^\circ$ and $270^\circ-17^\circ$), the area of the 90% isodose region shown in Figure 6.2 (b) increased by 16% for the first machine tested (Varian 2100CD), to the area presented in Figure 6.2 (d); at the midline axes, this corresponds to a 90% isodose region that is approximately 3cm wider, and 16 cm taller. The results were even more

pronounced for the second machine (Varian Clinac iX Trilogy); the 90% isodose region grew by approximately 52% by adopting an asymmetric angle pair (Figure 6.2 (h), $270^\circ+25^\circ$ and $270^\circ-17^\circ$) versus a symmetric angle pair (Figure 6.2 (f)), as a result of the 47cm increase in the height at midline, in spite of the 12cm of width lost at midline where the profile exhibits an hourglass shape.

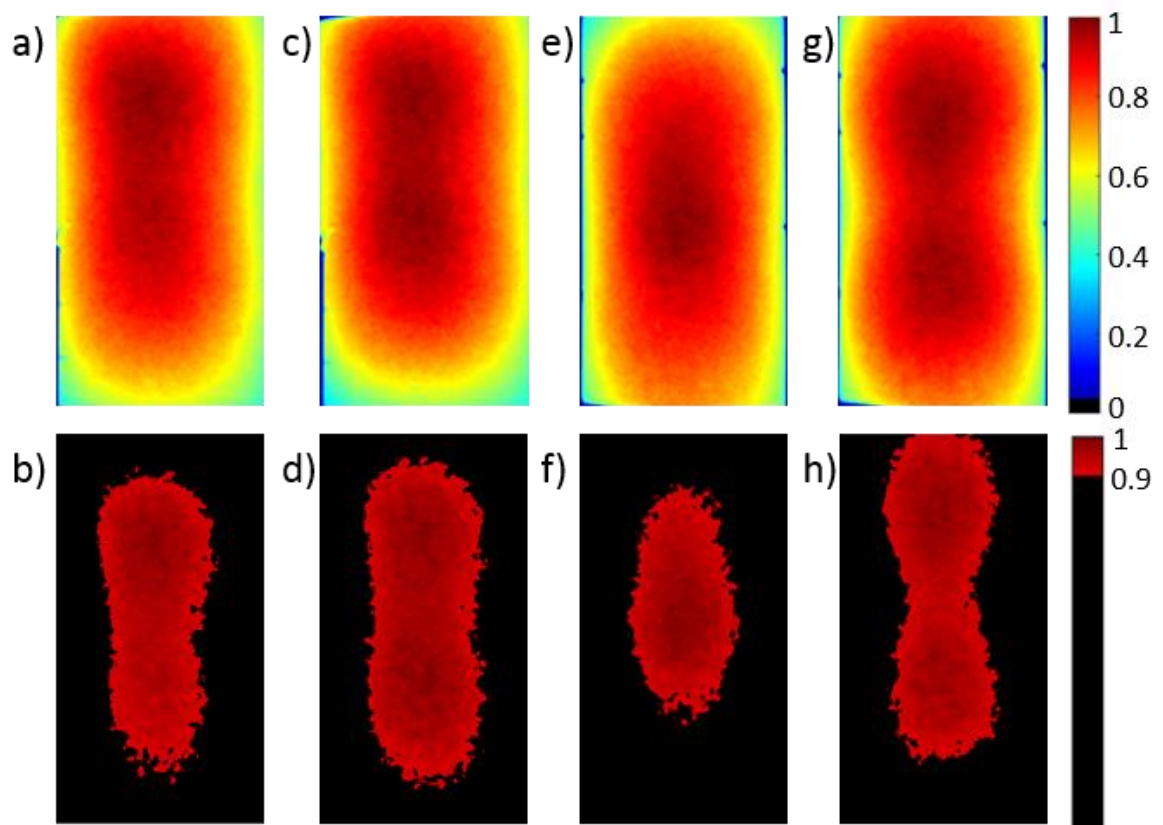


Figure 6.2 Composite images of optimized TSET geometry: a) on linac 1, restrained to symmetric gantry angles ($270^\circ\pm 20^\circ$); b) 90% isodose area of (a); c) on linac 1, asymmetric gantry angles $270^\circ+23^\circ$ and $270^\circ-17^\circ$; d) 90% isodose area of (c); e) on linac 2, restrained to symmetric gantry angles ($270^\circ\pm 20^\circ$); f) 90% isodose area of (e); g) on linac 2, asymmetric gantry angles $270^\circ+25^\circ$ and $270^\circ-17^\circ$; h) 90% isodose area of (g).

6.2.2 Floor Scatter Experiment Results

The results of the floor scatter experiment are shown in Figure 6.3 for visual interpretation. The first row displays the residual images (concrete image control subtracted from the test material image) corresponding to a gantry angle of 270°, where the primary beam is parallel to the floor. The second row contains the residual images for gantry angle 253°, where the field light for the radiation beam is completely on the white polyethylene sheet, but near the floor. The final row shows the residual images for gantry angle 240°, where the field light projects the most appreciably onto the floor. The residual images for each test scatter material are grouped into columns, arranged in order of increasing material density: solid water, PVC, and steel. All images are presented on the same color scale, and were calculated using the same normalization factor.

The box and whisker plots in Figure 6.4 expression present more directly the quantitative characteristics of the residual images in Figure 6.3, but eliminate the spatial information afforded by the 2D plots. The maximum change in percent dose was observed for the case where the primary beam was directed most obliquely at the floor (240°); peak single-pixel differences were +3.3% (maximum), -0.91% (minimum) and -2.3% (minimum) for steel, PVC and solid water, respectively. However, when averaging the changes across the vertical axis (± 10 cm from the central line) as shown in Figure 6.5, the magnitude of the differences decreases to roughly 2.4%, 0% and -1.6%, respectively.

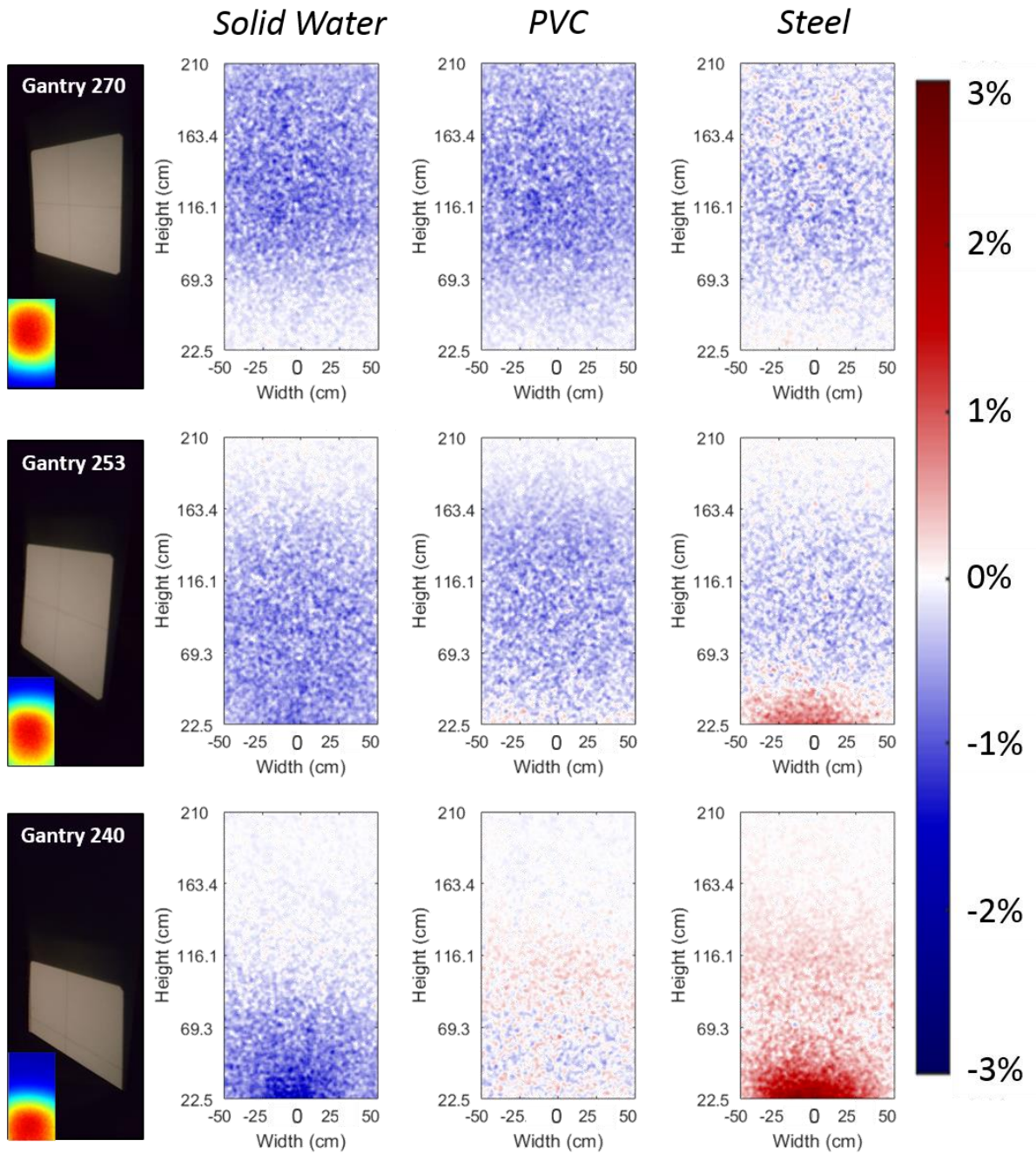


Figure 6.3 Residual images of each test material compared to concrete. The three gantry angles tested are shown in each row of images, with increasing incidence of the primary beam on the floor. The three test materials are grouped into the labeled columns in order of increasing material density (solid water, PVC, steel).

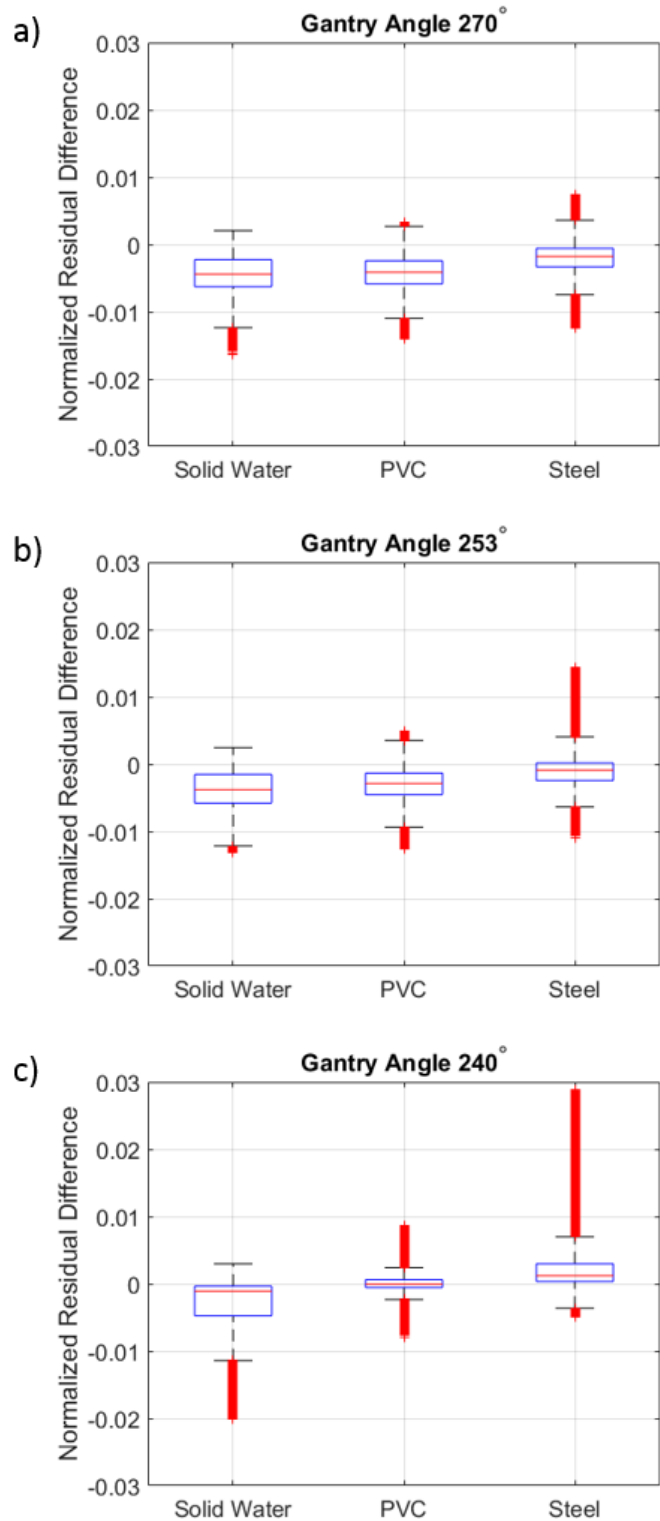


Figure 6.4 Box plots showing distributions of the normalized dose differences from the residual images in Figure 3 for: a) gantry angle 270°; b) gantry angle 253°; c) gantry angle 240°. The whisker lengths correspond to 1.5 times the interquartile range, and outliers, as the primary points of interest, are marked in red.

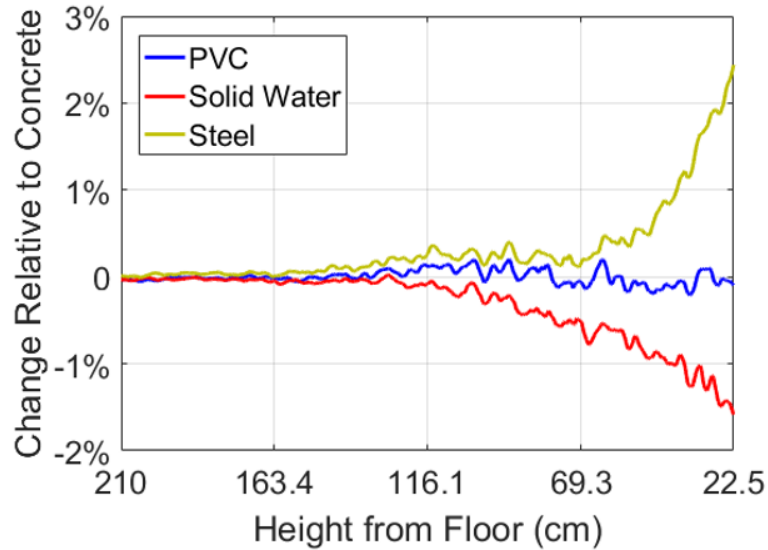


Figure 6.5 Averaged vertical profile of change in relative dose for gantry angle 240°.

6.3 Discussion of Floor Scatter Study

6.3.1 TSET Geometry Optimization Discussion

The accuracy of the Cherenkov-based method for analyzing TSET surface dose has been previously studied and reported as linear with ionization chamber measurements ($R^2=0.93$).¹⁶¹ The innovation of this approach for optimizing TSET geometry lies in calculation of a novel optimization metric, focused on maximizing the 90% isodose area, for quantitative comparison of each field angle pair. Establishing the ROI to the 90% isodose area was intended to draw parallels to the TG-30 TSET commissioning guidelines described briefly below.

Previous work, limited to analyzing coefficient of variation only, came to the conclusion that the homogeneity of the treatment field was approximately the same when optimizing the fields between symmetric gantry angle pair and asymmetric gantry angle pairs.¹⁶¹ This deeper investigation to new data, similarly acquired and corroborated

at a second institution, incorporates the features of the 90% isodose field height, width, and area. Nontrivial gains in the 90% isodose region area were accomplished (16% and 52% for the two linacs at two separate institutions) when adopting an asymmetric gantry angle pair.

When confined to the principle of a symmetric treatment geometry, the results of the expanded Cherenkov image-based TSET optimization method shown in Figure 6.2 agree with the suggested angles for TSET outlined in TG-30: at SSD=300cm, employ angles that are $\pm 20^\circ$ from the horizontal.⁶⁰ However, the new Cherenkov imaging optimization method allows for the rapid measurement of relative treatment field dosimetry from many gantry angle pairs; measuring many pairs of gantry angles using ionization chambers, films, thermoluminescent dosimeters, or diode-based dosimetry devices would be extremely time consuming. Analysis of all gantry angle pairs, irrespective of angle symmetry, supports the hypothesis that an asymmetric treatment geometry provides a larger 90% isodose region than currently adopted symmetric treatment angles; the optimized asymmetric pair increased the area 90% isodose region by over 16% for one machine, and a striking 52% for a second machine.

In practice, TG-30 recommends “a vertical uniformity of $\pm 8\%$ and a horizontal uniformity of $\pm 4\%$ over the central 160 cm x 60 cm area of the treatment plane.”⁶⁰ This means most commissioning takes place by assessing points only along the vertical and horizontal axes about the prescription point at midline; very little is done to investigate the integrated shape of the fields, despite the fact that the patient is treated in all four quadrants beyond these two orthogonal axes. An additional point of concern is that the

defined ROI height is less than the average height of an adult male in the United States (176cm),¹⁶⁶ and the 60cm width scarcely covers the breadth of an average torso, particularly neglecting the wide spread of patient extremities whilst standing in the six positions required of the typical modified Stanford technique.

Often the question arises regarding how a flat treatment plane translates to uniform dose when the realities of curved patient anatomical features come into play. Given that TSET treatment itself is generic, with only clinically managed regional dose boosts prescribed at the physician's discretion, it stands to reason that providing the largest isodose area in the flat treatment plane would translate to the most uniform surface dose to the average patient. This concept is the premise of the TG-30 requirements already quoted above, and is the immediately achievable goal when simulation CT scans or other patient surface information is not considered for patient-specific treatment planning. Methods for rapidly assessing the entire flat treatment plane, such as the Cherenkov-imaging based method used here, could help TSET geometries adopted clinically improve dose homogeneity delivered to patients.

The clinical implications of the hourglass shape in the optimized asymmetric gantry angle pair, particularly on the second linac tested, need further study. The six patient positions during treatment establish a complex aggregate of dose that is influenced by inter-fraction setup variations, and more broadly by disparity in gross anatomy between patients. However, the hourglass isodose region is logically matched to the patient positions where the arms are raised and the legs are spread for even dose coverage. In addition, given that TSET response is clinically managed with compensating

boost fields when necessary, the hourglass shape is not expected to incur negative overall consequences.

A final interpretation of this data, particularly in the notable differences in the 90% isodose field shapes in Figure 6.2 between the two linacs tested, is that the linac models and treatment setups, down to room geometries and construction materials, can affect the ultimate shapes of the composite treatment fields. The flatness and symmetry of beams from of each machine were independently verified through traditional means as well as through Cherenkov imaging, so these differences cannot be written off as irregularities in the machine output. This reinforces the notion that there is not a one-size-fits-all solution, even if translating between two linacs and bunkers within the same clinic. Each commissioned setup must be rigorously tested under the same conditions as patient treatment to ensure the protocol adequately achieves the dosimetric goals of TG-30.

6.3.2 Floor Scatter Experiment Discussion

Definite qualitative changes in the relative dose pattern were observed when the floor material was altered to solid water, PVC or steel for gantry angles 253° and 240°, with minor changes between the three test materials at 270°, as shown in Figure 6.3. The scatter dose from these fields would be the result of inelastic processes with the floor material, producing a spectrum of lower energy electrons deflected towards the treatment plane.

With that in mind, these changes reflect the expectation that the dense, high-Z material of the steel plate would have more near-surface scatter events, and thus

increase scatter in the orthogonally arranged treatment plane. The incoming electrons would stochastically travel deeper into the lower density, low-Z materials solid water and PVC before scattering, and would be more likely to be absorbed after scattering. Figure 6.4 allows for further interpretation to how the materials and angles affect the differences in observed dose, in that the whiskers and outliers to the residual image pixel values follow the expected trends towards hot or cold, depending on scattering material.

The Monte Carlo simulation work of Nevelsky *et al.*¹⁶² reported peak floor scatter contributions at 20cm above the floor to be +3%, -3% and -5% for iron, PVC and water, compared to concrete, given a SSD=400cm and gantry angle 17° above the horizontal. These magnitudes are larger than what was measured with the Cherenkov imaging method (+2.4%, 0.0%, -1.6%), even with a 30° change in gantry angle at the shorter SSD (300cm versus 400cm). This suggests that there is a small amount of scatter dose which is not detected via Cherenkov imaging, most likely due to the energy dependence of the optical emission.

Nevelsky *et al.* stated “the spectrum of the scattered electrons had a distribution which was almost uniform between a few hundred keV to 4 MeV, then decreased linearly to 6 MeV.”¹⁶² While most of these electrons should be above the threshold for Cherenkov light generation, the energy-dependence of the number of photons emitted would deflate the contributions of lower energy scattered electrons. For this reason, the Cherenkov imaging method provides a novel qualitative presentation of scatter dose distribution that follow anticipated and simulated trends, however, the accuracy of the

quantitative results are limited to within a few percent, depending on the material (and subsequently the energy spectrum of the scattered electrons).

It is worth noting that although the Cherenkov imaging method is less sensitive to lower energy electrons, these electrons would be responsible only for very superficial dose (which is the intent of the treatment). Moreover, the simulated scatter doses reported become trivial at a height of 50cm from the floor, and the patient is typically positioned on a wooden platform 20-30cm above the concrete, further diminishing the patients' exposures to the scatter.

Taking into consideration the already broad ranges of dose reported with *in vivo* dosimetry ($\pm 15\%$),⁶⁸ it is not expected that the menial scatter dose magnitudes¹⁶² are the primary cause of heterogeneities in dose received by the patient. Rather, these dose variations could be an indication of a possible weakness in the treatment field setup, in conjunction with patient positioning, which limits the achievement of appropriate dose coverage. Therefore, techniques to optimize the size and uniformity, such as the Cherenkov imaging method described herein, could be useful tools in evaluating and improving current clinical TSET setups.

This work also illustrates the importance of careful consideration of material selection in patient support structure construction. In TSET delivery, whether using a modified Stanford technique or a rotation technique, introducing metal components to the patient support structure could increase scatter dose, as was seen in this work with the steel plate. This also suggests that it would be ideal to perform setup dosimetry

measurements within the confines of the support structure, to ensure scatter dose can be captured in the readings.

6.4 Conclusion of Floor Scatter Study

The results presented support the two tested hypotheses. First, an expanded method of Cherenkov image analysis showed that an asymmetric selection of gantry angles for TSET setup provided an appreciably larger, more inclusive 90% isodose area than the recommended symmetric gantry angle pair ($270^{\circ}\pm 20^{\circ}$). Second, the Cherenkov imaging method was shown to exhibit sensitivity to dose from floor scatter during TSET.

Chapter 7: Quality Assurance of MR-IGRT Systems

This chapter is largely derived from: J.M. Andreozzi et al., “Remote Cherenkov Imaging Based Quality Assurance of a Magnetic Resonance Image Guided Radiotherapy System,” *Med. Phys.* (Accepted, April 2018)

7.1 Introduction to the Co-60 MR-IGRT System

One of the novel areas of research in the scope of this thesis is the adaptation of the Cherenkov-based QA methods briefly described above for use in a Magnetic Resonance Imaging Guided Radiotherapy (MR-IGRT) system, specifically the MRIdian Viewray (Viewray, Inc., Cleveland, OH) at the Siteman Cancer Center at Barnes-Jewish Hospital and Washington University School of Medicine in St. Louis. MR-IGRT has the ability to provide real-time anatomical information during treatment, which is an attractive capability for delivering dose in complex and dynamic scenarios, especially when highly sensitive normal structures are at risk.⁶⁹

Real-time localization of treatment targets has recently become possible with magnetic resonance image-guided radiotherapy (MR-IGRT) systems. The first clinically implemented and commercially available unit was the MRIdian system (ViewRay Inc., Cleveland OH, USA), which integrates three cobalt-60 (Co-60) treatment heads with a split-bore 0.35-T magnetic resonance imaging (MRI) scanner.^{71, 167} Extensive work has also been put into the development of MRI-linac systems that incorporate much stronger magnets (1.5-T),¹⁶⁸ with heavy focus on the effects of the magnetic field not only on beam generation physics, but similarly on dose deposition;^{72, 77, 80, 81, 169, 170} the use of these

systems seems likely to grow extensively in the coming years, because they add the ability to gate the treatment beam to the movement of internal anatomy imaged in real-time.

In the presence of these high magnetic fields, the tools used to measure dose must be carefully constructed, and the perturbations introduced by the fields must be well characterized.¹⁷¹⁻¹⁷⁴ This work describes a novel approach utilizing Cherenkov imaging for quality assurance (QA) testing of physical beam characteristics of the ViewRay system (VRS), which can also feasibly be applied to other integrated MR-IGRT systems. Cherenkov imaging involves detecting the optical photons liberated from irradiated dielectric materials such as water via the Cherenkov effect.²⁻⁴ Cherenkov light intensity has been shown to correlate to deposited dose for monoenergetic beams in homogenous phantoms, as is common for QA measurement setups.^{7, 18, 91, 92, 127}

Because Cherenkov imaging is a passive detection scheme, the sensor can be placed outside of the magnetic field and remain independent of its effects. By aligning a water tank within the bore of MR-IGRT systems, Cherenkov imaging allows for projection imaging of the entire width of tested beams along the optical axis of the camera, so that an integrated 2-D projection image of dose can be used to evaluate beam characteristics. These measurements are put forth as alternatives to more traditionally acquired percent depth dose curves (PDDs) and cross beam profiles (CBPs), and as such will be referred to as projection percent depth dose curves (pPDDs) and projection cross beam profiles (pCBPs).

Quality assurance of beam characteristics in MR-IGRT systems is currently performed using well characterized ionization chambers (ICs), radiographic films, diode

systems such as the ArcCHECK (Sun Nuclear Corporation, Melbourne, FL, USA),^{175, 176} and more experimental polymer gel dosimetry solutions.^{177, 178} While the feasibility of an automated solution has been demonstrated by Smit et al.,¹⁷⁹ there is not yet a commercially available or clinically adopted system that is MR-compatible. Therefore, IC measurements in MR-IGRT systems without access to such prototype solutions are typically acquired by manually translating the detector through the phantom. Additionally, the effects of the magnetic field on the specific ionization chamber or device used must be well characterized, so that proper correction factors can be implemented.¹⁷³

Without an automated system (which was the case for the research institution at the time of this study) each individual measurement from an IC in an MR-IGRT system required repeated entrance and exit to the bunker, as well as repeated movement of the phantom into and out of the bore, with each point measurement requiring additional beam-on events. This time-intensive process, further compounded by the three Co-60 source heads of the VRS that must be analyzed independently, is in direct contrast to the proposed Cherenkov imaging method. The Cherenkov QA metrics proposed herein require a single setup, with only one beam-on event per analyzed beam or source, effectively necessitating merely the time of a single point measurement by an IC-based system.

In this work, projection percent depth dose curves (pPDDs) and projection cross beam profiles (pCBPs) are extracted from the Cherenkov images of a single beam-on event, and compared to predictions of the pPDDs and pCBPs produced by the TPS, as well

as the more laboriously acquired central axis ionization chamber and radiographic film measurements. In addition, real-time Cherenkov imaging of a dynamic intensity modulated radiotherapy (IMRT) commissioning plan delivered by the VRS is shown, and compared to the simulated dose volume of the treatment planning system. These Cherenkov imaging-based measurements are put forth as alternative quality assurance metrics to rapidly assess beam characteristics.

7.2 Materials and Methods with MR-IGRT

All experiments were performed on a commercial MR-IGRT system (Meridian, ViewRay Inc., Cleveland OH, USA).⁷¹ The VRS is equipped with a split-bore 0.35-T whole-body magnetic resonance imaging (MRI) system, and three rotating Co-60 treatment heads placed 120° apart, each with an independent multileaf collimator (MLC). The integrated Monte-Carlo-based treatment planning system (TPS) was used to generate simulation data for the static beams and the intensity modulated radiotherapy (IMRT) plan examined.

Cherenkov images were captured on a commercially available intensified charge-coupled device (ICCD) camera (PIMax4-1024i, Princeton Instruments, Trenton, NJ USA) outfitted with an 135mm f/2 lens (Canon USA Inc., Melville, NY USA). The ICCD was placed at the end of the treatment couch, approximately 4.0 m away from the treatment isocenter, and just outside of the 5-Gauss line of the VRS, as shown in FIG. 1. The VRS alignment lasers were used to ensure the camera was centered and perpendicular to the translational axis of the couch.

A 40cm wide x 30.5cm deep x 37.5cm high standard plastic dosimetry water tank was slightly modified with custom-cut black-out plastic sheets on all sides except for the front imaging face. This was necessary to minimize internal light reflections from the Cherenkov emission during the experiments. Because Cherenkov photon emission is inherently directional,³ observed light at the camera was boosted by doping the tank water at a concentration of 1g/L with isotropically emitting fluorophore quinine sulfate^{8,90} pre-dissolved in HCl and water (0.5-N solution before adding to tank).

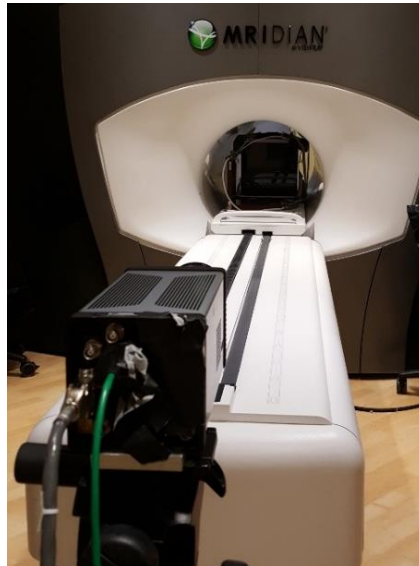


Figure 7.1 Water tank imaging setup with the ICCD looking down the ViewRay bore, set up outside the 5G line.

7.2.1 Establishing Measurement Resolution and Acquisition Settings

The imaging setup was calibrated by submersing a commercial USAF-1951 resolution test target (Thorlabs Inc., Newton, NJ USA) in the center of the tank. The plane of the test target was positioned at the treatment isocenter, and reference images were captured

under full room lights. Post-processing in commercial software (MATLAB, The MathWorks Inc., Natick MA) was implemented to derive the physical pixel size in the treatment plane, which remained constant so long as the camera was not moved.

The technical setup of imaging the Cherenkov emission from the VRS deviated from that described in previous publications using linear accelerators¹⁰ in as much as the radiation source is not electronically pulsed. Because the Co-60 sources are continuously emitting when the treatment heads are open, triggering image acquisition to radiation pulses is not possible. The ICCD acquisition settings had to be tested to ensure optimal data collection in the new imaging environment.

Preliminary Cherenkov images of a 10.5cm x 10.5cm Co-60 beam incident on the water tank were captured under various settings with all room lights turned off (or physically covered in the case of equipment status LEDs around the room). The internal trigger frequency of the ICCD was set to 100 kHz to operate in a quasi-continuous acquisition mode. Stacks of 50 Cherenkov images were acquired using 2 ms, 10 ms, and 20 ms exposure durations. The number of accumulations on chip (AOC) was varied for each exposure time at the intervals of 10, 50, 100, 150, 200, 250, 300, and 500 AOC. If the frame rate dropped much below 1 fps for a given exposure duration, images with increased AOC were not acquired out of practicality.

Post-processing of the preliminary Cherenkov images in MATLAB included a temporal median filter over the stack of 50 images per data set, and background subtraction to remove any remaining room light signal. The test frames were also

normalized to a white-field image to remove the influence of honeycomb patterns introduced by the fiber coupling between intensifier and detector of the ICCD.

Contrast to noise ratio, signal to noise ratio, and average signal intensity of a constant region of interest was calculated and weighed with frame rate to select the most appropriate camera acquisition settings for both static beam and dynamic plan measurements. The SNR was calculated within a static region of interest (ROI) within the beam following the equation:

$$SNR = \frac{\bar{\mu}_{ROI}}{\sigma_{ROI}},$$

where $\bar{\mu}_{ROI}$ is the average intensity in the ROI, and σ_{ROI} is the standard deviation. Likewise, the CBR was calculated using:

$$CBR = \frac{\bar{\mu}_{beam} - \bar{\mu}_{bkg}}{\sigma_{bkg}},$$

where $\bar{\mu}_{beam}$ is the average intensity of an ROI in the radiation beam, $\bar{\mu}_{bkg}$ is the average intensity of an ROI outside of the radiation beam (background), and σ_{bkg} is the standard deviation of that same region.

7.2.2 Projection Cross Beam Profiles and Projection Percent Depth Dose Curves

After the image acquisition settings were determined via the method described above in Section 7.2.1, the projection cross beam profiles (pCBPs) and projection percent depth dose curves (pPDDs) for individual beams were measured simultaneously from a single set of Cherenkov images per beam. The ICCD was set to an internal trigger frequency of 100 kHz, 20 ms exposure, and 50 AOC, which produced a frame rate of 0.929 fps. Fifty

images were captured per Cherenkov data set, and a stack of 50 background images (no radiation) was acquired for the given setup.

With all room lights off or covered, 4.2x4.2 cm², 10.5x10.5 cm², and 14.7x14.7 cm² beams normal to the water surface were imaged in sequence for one treatment head. The VRS has slightly irregular programmable field sizes (for example 10.5cm instead of 10cm squares), due to geometric constraints from matching the isocenter of the MRI system (105-cm source-axial distance bore) with the Co-60 irradiators. The three field sizes were intended to provide a span that fit adequately in the smallest dimension of the water tank used (30.5cm wide). This is necessary to ensure that Cherenkov light is detected solely from the water, and not generated in the acrylic of the tank, which would corrupt the signal of interest. The three beam sizes were repeated with a second treatment head as an additional verification of performance.

Reference central axis PDDs were constructed from ionization chamber (Exradin A18, Standard Imaging, Middleton, WI) measurements of each beam size in a standard water tank. Reference CBPs were acquired from radiographic film (EDR2 Ready Pak, Kodak/Carestream Health, Inc., Rochester NY) digitized (VRX-16, VIDAR Systems Corporation, Herndon, VA, USA) and analyzed using commercial software (RIT113, ver. 7.0 Radiological Imaging Technology, Inc., Colorado Springs, CO, USA); the film was placed at the depth of maximum dose (0.5cm for Co-60 beams) using water equivalent plastic (Solid Water, Gammex, Inc., Middleton, WI) as the attenuating medium. Reference pPDDs and pCBPs were generated by the integrated treatment planning system (TPS) of the VRS.

Post-processing of Cherenkov images was carried out in MATLAB, and again included the white field correction, temporal median filtering, and background image subtraction. A high-pass filter was applied to each resulting image, so that anything below a 4% intensity threshold was forced to zero. This process reduced each beam imaged to a single frame, from which pCBPs and pPDDs were extracted.

The center of the beams in the Cherenkov images were determined by the peak of a Gaussian fit to a horizontal profile. The average intensity of the vertical profile ± 5 pixels (± 1.85 mm) from the center line column was taken as the pPDD; a bilateral filter was applied to smooth out any residual noise. After registration of the Cherenkov pPDD with the TPS pPDD, the location of the depth of maximum dose (d_{max}) in the Cherenkov image was ascertained. The average intensity of the horizontal profile ± 1 pixel (± 0.37 mm) from the d_{max} pixel was taken as the pCBP. Additional pCBPs were obtained from the images at depths of 2.5cm, 5.0cm, 7.5cm and 10cm, and the full width half maximum (FWHM) was used to measure the beam width at each depth, where the maximum was the normalized intensity at the center beam axis.

The Monte Carlo-based simulation from the TPS generated dose volumes for each of the square beams tested, with the magnetic field parameter enabled to model the field effects on dose. Central axis PDDs, as well as pCBPs and pPDDs (analogous for the Cherenkov measurements) were extracted from the dose volumes. The pCBPs were calculated by integrating each dose volume across the centered 6cm, 10.5cm and 15.0cm volumes, to fully contain each of the beam sizes tested. The pPDDs were calculated by integrating the

central 15cm width of each dose volume, to encompass the width of the largest beam. This width is limited by the depth of field of the imaging setup.

Registration of the normalized Cherenkov pPDD to the normalized TPS pPDD was carried out as a two-step process. First, d_{\max} as a single pixel location was determined by a least mean squares (LMS) fitting method along the x-axis (depth direction). With d_{\max} fixed at the same pixel location for each of the three tested beams, the intensities were registered by again performing a least mean squares fit in the y-axis (normalized intensity) direction. This registration was maintained for the comparison between Cherenkov-derived pPDDs to ionization chamber central axis PDDs, as well as for the extraction of the pCBPs at the indicated depths.

7.2.3 System Performance During Active Magnetic Resonance Imaging

It was not practical to test the influence of the primary 0.35T MRI magnet on the Cherenkov imaging, as this would require the expensive and lengthy process of quenching the magnet. However, it was a simple experiment to test the effects of active MR imaging, which introduces additional radiofrequency signals in the vicinity of the Cherenkov imaging camera on the proposed QA. First, to ascertain the independence of camera performance from active MR imaging, a 1cm x 1cm black and white checkerboard pattern was affixed to the front of the water tank. The MR imaging coils were placed above and below the tank, which was then aligned at the treatment isocenter within the magnet bore. The ICCD remained outside of the 5-G line, in the same position previously shown in Figure 7.1.

With room lights on, fifty images of the checkerboard pattern were acquired without active imaging, then fifty images were acquired while the MRI ran a real-time cine-mode T2-T1 ratio balanced steady state free precession (TRUFI) sequence over a 35cm x 35cm field and 0.7 cm slice thickness in the sagittal plane. The ICCD settings were adjusted from Cherenkov imaging settings, to accommodate the increased light levels, to an internal trigger frequency of 100kHz, 1 AOC, and 5 ms exposure, resulting in a 5 fps acquisition rate. Post-processing was again conducted in MATLAB, and the median image of the control frames (no MR imaging) was compared to the median of the experimental images (active MR imaging).

Next, to determine the influence of active MRI on the Cherenkov-image based measurement of PDDs and CBPs, a second experiment was conducted. The checkerboard pattern was removed from the front face of the water tank, still filled to 20cm height with quinine-doped water (1g/L concentration). Fifty Cherenkov images of a single 10.5x10.5 cm² Co-60 beam were captured under the same conditions as described in 7.2.2. An additional 50 Cherenkov image frames were captured during active, real-time MRI. The resulting pPDDs and pCBPs from the two data sets were compared offline following the same post-processing procedure expressed in 7.2.2.

7.2.4 Real-Time Imaging of Commissioning Plan

As a high resolution, real-time imaging modality, Cherenkov imaging was investigated for its potential to supply a novel look at dynamic treatment plans delivered by the VRS. The same experimental setup shown previously in Figure 7.1 was used, with the exception that the water line was increased to 30cm from the bottom of the tank, and additional

quinine was added to accommodate the increased water volume while maintaining the 1g/L dopant concentration. The tank was centered with the treatment isocenter 10 cm below the water surface.

The ICCD settings were chosen following the analysis described in Section 7.2.1 with greater importance being given to frame rate. An internal trigger frequency of 100 kHz, 2 ms exposure, and 200 AOC was selected, which produced a frame rate of 2.09 fps. A commissioning test for intensity modulated radiotherapy (IMRT) plan C4: C-Shape, as described in AAPM TG-119¹⁸⁰ was created for the VRS. Cherenkov imaging during the plan delivery was performed; a separate image stack was saved for each of the five control points to limit file size.

Post-processing in MATLAB required image resizing to 512x512 pixels from the original 1024x1024 pixels to make the file size more manageable. A rolling temporal median filter was applied over each five consecutive frames for the entire 1017 frame stack, background image subtraction, and an 11x11 pixel spatial median filter kernel was applied to remove noise. The processed Cherenkov image stack created a 2.09 fps video of IMRT beam delivery. Another image stack was generated, where each frame was the sum of all previous frames, to depict the aggregate plan dose delivery.

In addition to the IMRT dose delivery videos produced, a single frame of the aggregate dose was produced by summing all of the frames in the real-time video. A central region of interest from this aggregate Cherenkov image was registered with a planar sum of the volume dose simulated by the VRS treatment planning system; this integration was performed over the 12cm width of the imaged C-Shape, to minimize low

signal contributions from the expected out-of-focus regions in the corresponding Cherenkov images. Gamma index analysis comparing the Cherenkov composite intensity to the simulation data was performed in MATLAB.

7.3 Results with MR-IGRT

Post-processing of the initial test images acquired as described in Section 7.2.1 determined the best imaging settings to use with continuously emitting Co-60 sources given an internal ICCD trigger frequency of 100kHz for both static and dynamic beam imaging scenarios.

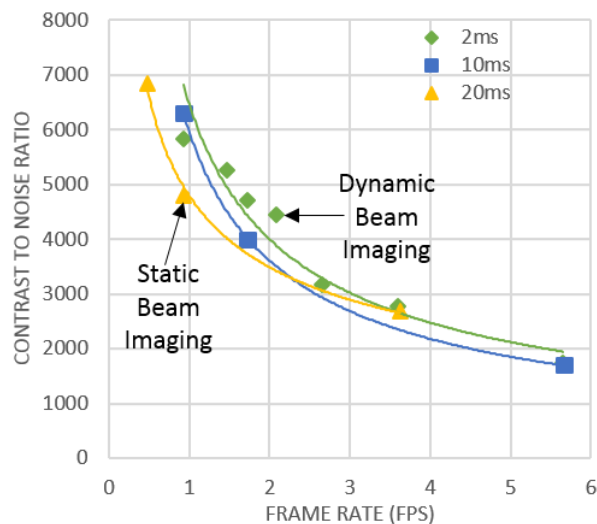


Figure 7.2 Contrast to noise ratio vs. frame rate evaluated from system calibration Cherenkov images. A power curve fit is shown for each tested exposure.

Figure 7.2 shows the trade-off between contrast to noise ratio and data collection frame rate, as calculated from an ROI near d_{max} and the background signal in the processed images. For static imaging, a slower frame rate of 0.929 fps (20 ms exposure, 50 AOC) was deemed the most appropriate to get the highest level of signal. For dynamic

imaging, a higher framerate was desired and therefore settings of 2 ms exposure and 200 accumulations on chip (2.09 fps) were chosen.

7.3.1 Cherenkov-Based Projection Cross Beam Profiles and Projection Percent Depth Dose Curves

The processed, cropped Cherenkov images of the three square beams tested (4.2cm x 4.2cm, 10.5cm x 10.5cm, and 14.7cm x 14.7cm) from a single Co-60 treatment head are shown in Figure 7.3(a)-(c); each column of plots corresponds to the beam size shown in these image titles. The registered TPS and Cherenkov-derived pCBPs from Co-60 Head 1 and Co-60 Head 3 are shown in Figure 7.3 (d)-(f); the beam widths for each curve shown in Figure 7.3 (d)-(f) are presented in the Bland-Altman diagrams¹⁸¹ Figure 7.3 (g)-(i). Next, the pPDDs measured from the Cherenkov images and the TPS dose volume projection calculations are presented in Figure 7.3 (j)-(l), and the residual error between the simulated and measured pPDD are shown in more detail directly below the corresponding beams in Figure 7.3 (m)-(o).

Collectively, the Cherenkov-derived pPDDs exhibited reasonable agreement with their planar projection simulation counterparts from the TPS. This is further summarized in Table 7.1, which lists the statistics of the residual error between the Cherenkov pPDDs and the TPS pPDDs; the percentage differences are with respect to the normalization reference defined as the dose at d_{\max} on the TPS pPDD.

To validate the use of the Cherenkov-derived pPDDs, the TPS derived relationship between the projection PDDs and central axis PDDs was applied as a depth-dependent weighting of the Cherenkov pPDD, so that the Cherenkov data could be directly compared

to ionization chamber measurements collected along the central axis of each beam. As seen in Figure 7.4 (a), the largest deviation between the pPDD and PDD is exhibited by the smallest beam simulated (4.2cm square beam). This predicted ratio was multiplied with the Cherenkov pPDD presented as the dashed blue line in Figure 7.4 (b), to calculate an expected central axis PDD from the Cherenkov data, shown as the solid blue curve. The final result is a Cherenkov-based PDD that exhibits agreement with the discrete IC measurements, plotted in red. Comparison of the weighted Cherenkov PDDs and IC PDDs for all three beam sizes tested are shown in Figure 7.5 (a).

Film CBPs acquired at the depth of maximum dose in solid water are reported alongside the Cherenkov-derived pCBPs in Figure 7.5 (b). The Cherenkov-derived pCBPs matched the film FWHMs accurately, with minor differences in beam width of 0.090 cm (-2.08%), 0.071 cm (-0.679%), and -0.077 cm (-0.531%) for the 4.2-cm, 10.5-cm, and 14.7-cm square beams, respectively. These differences indicate that the Cherenkov image very slightly underreported the beam widths at the depth of maximum dose.

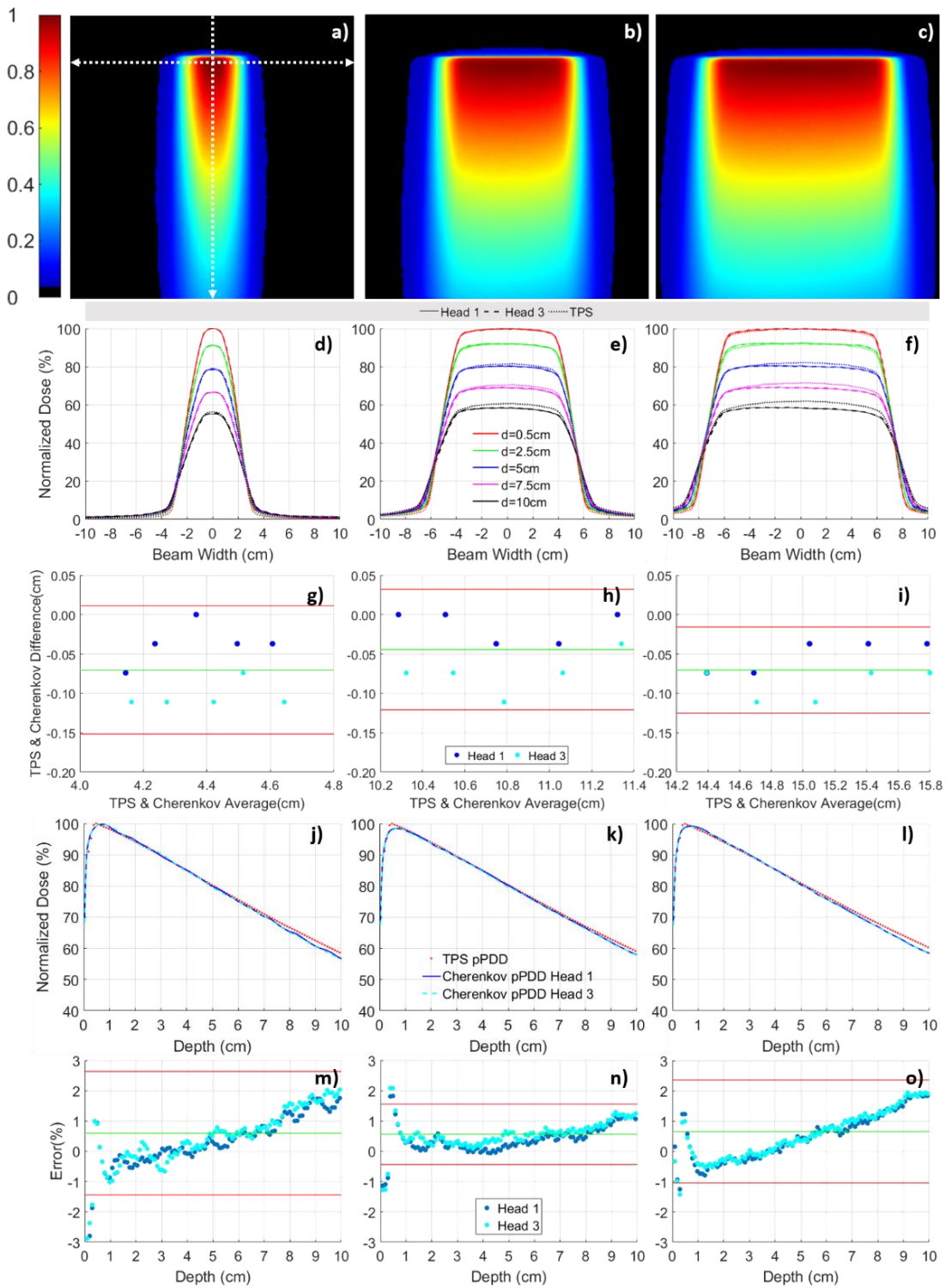


Figure 7.3 Cropped Cherenkov images from one Co-60 source impinging perpendicular to the water surface for square beam sizes: a) 4.2cm; b) 10.5cm; and, c) 14.7cm. The vertical white dotted line in a) designates the location of the Cherenkov pPDD extraction, and the horizontal white dotted line correlates to the Cherenkov pCBP taken at d_{max} . d-f) Cherenkov pCBP curves for the two tested Co-60 sources are compared to projection TPS

results at 5 depths. g)-i) Associated Bland-Altman plots to demonstrate measurement agreement after calculating beam widths for each depth. j)-i) Cherenkov pPDD curves are compared to TPS results. m)-o) Associated error plots between the TPS pPDDs and corresponding Cherenkov pPDDs. The green lines delineate the mean value of the differences ($\bar{\delta}$). The red lines show limits of agreement, two standard deviations above and below the mean ($\bar{\delta} \pm 2\sigma$).

Table 7.1 Measured maximum and average dose differences between normalized Cherenkov and TPS derived pPDDs, at each depth assessed with the TPS simulation.

Beam Size (cm ²)	4.2x4.2	10.5x10.5	14.7x14.7
Maximum Difference	-3.5%	2.1%	2.2%
Average Difference	0.60%	0.56%	0.66%
Repeatability Coefficient (2 s _d)	2.0%	0.99%	1.7%

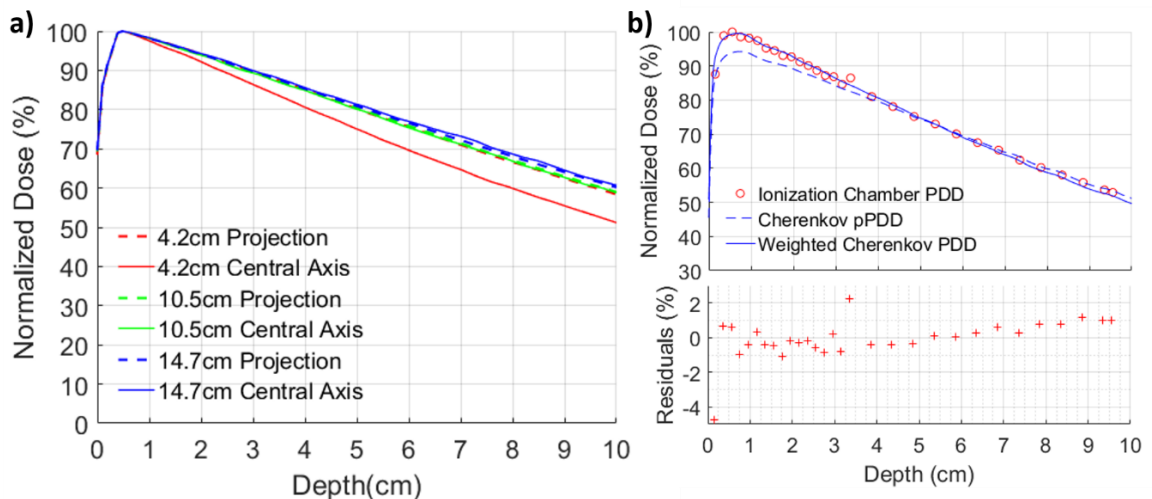


Figure 7.4 a) Simulation comparison from the TPS showing differences between the central axis PDD and the integrated projection PDD for the three square beams tested. b) Ionization chamber PDD acquired along the central axis of a 4.2cm square beam compared to the Cherenkov-based pPDD and Cherenkov-derived PDD, weighted to the ratio of the two 4.2cm curves shown in (a); the residual error difference between the IC and weighted Cherenkov PDD are reported.

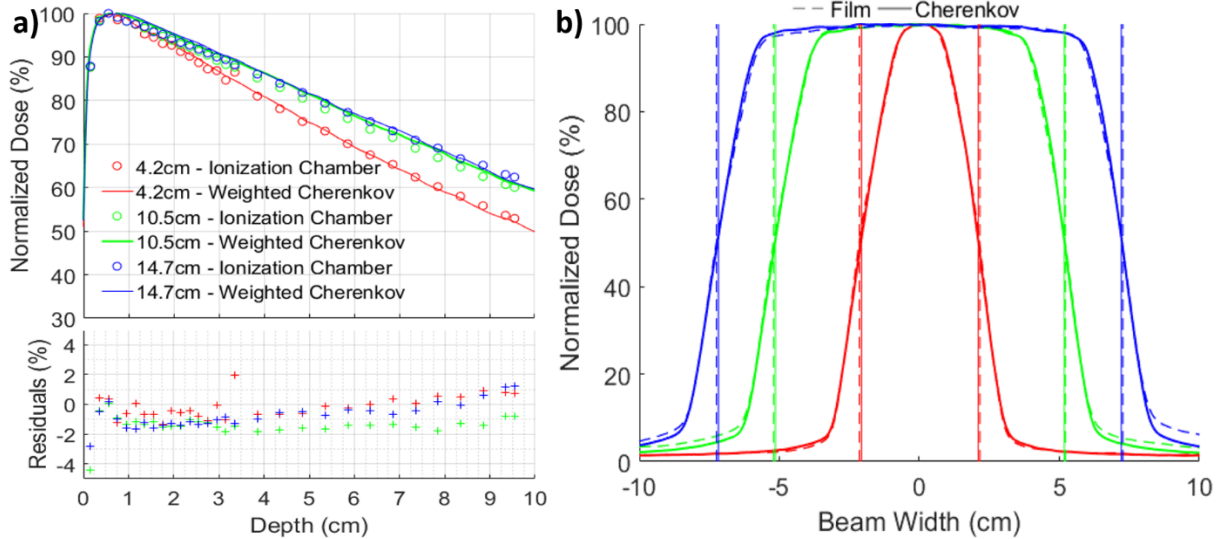


Figure 7.5 a) Simulation weighted Cherenkov PDDs compared to central axis ionization chamber measurements for each beam size (4.2cm, 10.5cm, and 14.7cm). b) Beam widths for three tested beam sizes from one treatment head comparing film central axis (--) and Cherenkov image projection cross beam profile measurements (-).

7.3.2 Cherenkov Measurements Concurrent with Magnetic Resonance Imaging

The ICCD demonstrated independent performance from the additional RF fields introduced during active MRI. As shown in Figure 7.6, there was less than 1% intensity variation on any given pixel in the checkerboard pattern imaged after subtracting the room light images with and without concurrent MRI; this variation was mostly seen in the black areas (low numerical values) of the checkerboard, and ultimately attributed to general electronics readout noise, and not interference from the additional RF fields in the room during active MRI. Inspection of the measured CBP and PDD of a 10.5x10.5 cm² beam with and without active MRI did not produce any meaningful deviations.

Inspection of the Cherenkov images in the presence of the primary magnetic field illustrates beam asymmetry that becomes more pronounced at deeper depths (and

consequently lower overall pixel intensities), as shown in Figure 7.7 for the 14.7-cm square beam. This left-leaning asymmetry is consistent with the direction of the Lorentz forces on the secondary electrons generated in the water.

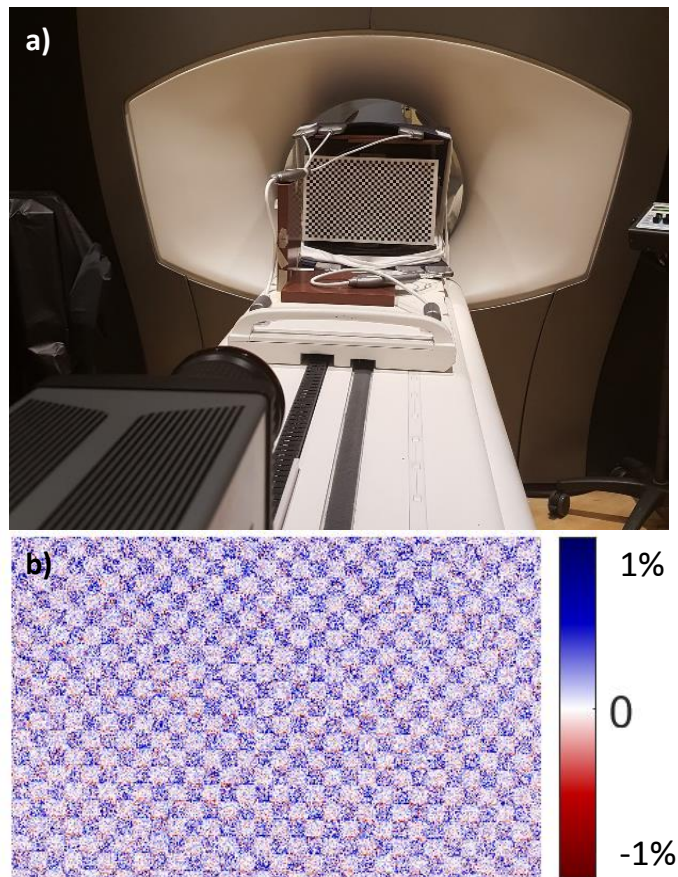


Figure 7.6 a) Checkerboard imaging setup with MRI coils; b) Difference image with and without active MRI imaging.

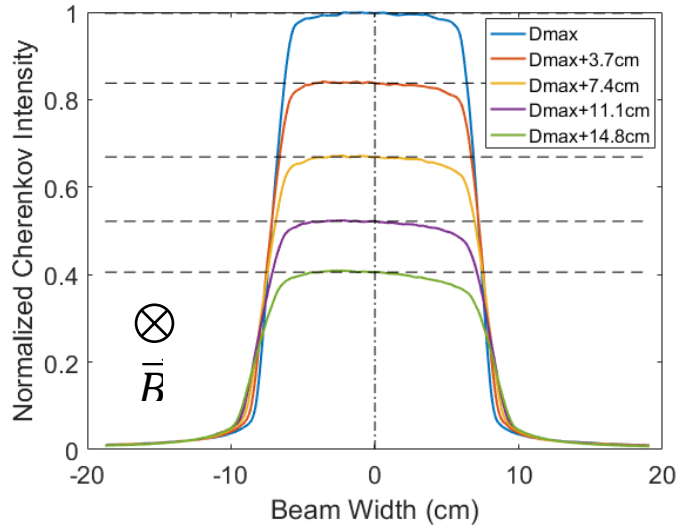


Figure 7.7 Depth-dependent cross-beam profiles from the Cherenkov image of the 14.7-cm square beam illustrating the more pronounced beam asymmetry deeper in the tank.

7.3.3 Real-Time Cherenkov Imaging of IMRT Plan

The ICCD successfully captured real-time video of dose being deposited in the water tank during the delivery of TG-119 C-Shape¹⁸⁰ commissioning test IMRT plan. After post-processing, the beam dynamics can be viewed as instantaneous dose delivery, or as a video of accumulated dose. The latter is shown in the series of video stills presented in Figure 7.8 below.

The linear sum of the frame stack was calculated to form a single frame of aggregate Cherenkov intensity, and compared to the simulated dose volume for the treatment plan. The cropped region of the Cherenkov aggregate image shown in Figure 7.9 (b) was rigidly registered to the projection sum across the 12cm object length of the C-shape object from the dose volume, which is shown in Figure 7.9 (a). The gamma index analysis results using a 3%, 3mm (80.5% passing rate), as well as a 4%, 4mm (95.1% passing rate), distance to agreement criteria are displayed in Figure 7.9 (c) and (d),

respectively. Passing pixels are displayed as red to white in the color scale (gamma index values 0-1), and failing pixels are shown in white to blue shades (gamma index values >1).

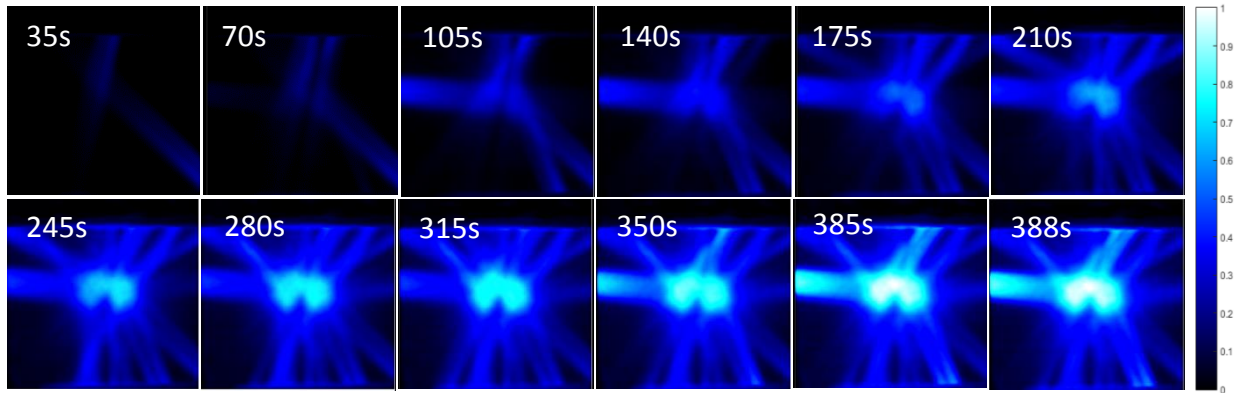


Figure 7.8 Cumulative Cherenkov images of TG-119 C4 IMRT plan in water at 35 second increments during active irradiation (excluding control point interims) until end of plan.

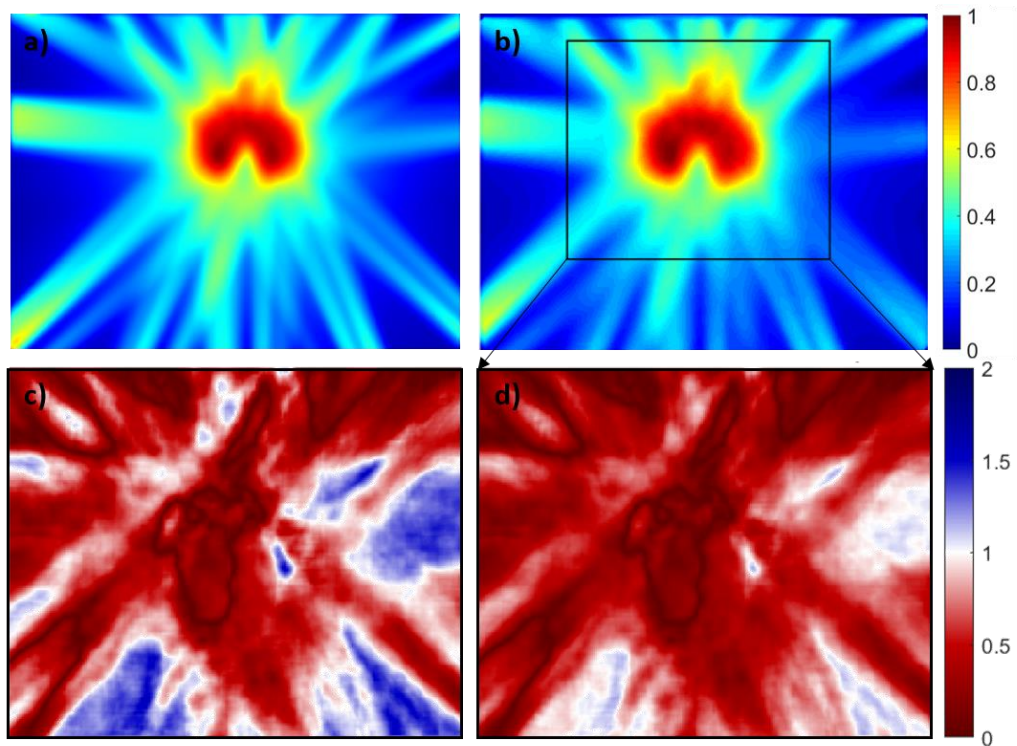


Figure 7.9 a) Cumulative dose from TPS; b) Cumulative Cherenkov intensity of TG-119 C4 IMRT plan in water, where black box denotes region of interest used for gamma analysis; c) Gamma index analysis between (a) and (b) with 3mm/3% criteria and 80.5% pass rate. d) Gamma index analysis between (a) and (b) with 4mm/4% criteria and 95.1% pass rate.

7.4 Discussion of Cherenkov Imaging with MR-IGRT

Cherenkov imaging of radiation from the VRS in a quinine-doped water tank was used to perform basic quality assurance tasks on static treatment beams with new projection-based metrics that were related directly to simulated dose from the TPS, and to provide a novel projection measurement of a dynamic treatment plan for which there is no current competing approach providing the same temporal breadth of detail.

A different image acquisition scheme from previously published work using medical linear accelerators was necessary due to lower beam energies (1.17MV and 1.33MV photons), and the continuous emission nature of the Co-60 radiation sources. This caused overall slower frame rates (1-2fps) to be selected for the given ICCD compared to similar experiments with 6MV linac-produced photons (23.5fps).⁸ However, further experimentation and optimization of the VRS data acquisition process could be performed, or more sensitive imaging hardware could be utilized, to increase the frame rate if it was deemed necessary.

7.4.1 Static Beam Quality Assurance Tests

The Cherenkov-based measurement of pCBPs, including beam width, was demonstrated, and had the added benefit of being acquired at the same time as the pPDDs. The obvious limitation of this technique is that with the described setup, the measurement is limited to a single beam axis normal to the optical axis of the ICCD. In a standard linac, the camera can be moved to view the other dimension of the beam, but the bore of the VRS prevents that approach, as discussed previously.

The Cherenkov pCBP data agreed with the radiographic film CBPs acquired at d_{\max} for each beam size, despite using the central axis values and not the projection-integrated CBP curves from the films. This is because only a single depth is presented for this comparison after normalization, and the projection-correction is depth-dependent.

To more fully explore this concept, the Cherenkov pCBPs were compared to TPS-derived pCBPs at five discrete depths: 0.5cm (d_{\max}), 2.5cm, 5.0cm, 7.5cm, and 10cm. For the smallest beam, there was excellent agreement in the shapes of each pCBP between the TPS and Cherenkov measurements. The larger beams appear to be slightly under-responding at the deeper depths; the worst case shown accounts for a 3.7% difference for the 14.7cm square beam at depth of 10cm along the central axis. This is thought to be due to the depth of field of the camera system being shallower than the width of the two larger beams. Future iterations of these measurements must be taken with the depth of field matched to the tank width to minimize this source of error.

The depth of field is determined by the focal length of the lens, the distance to the imaged object, the physical size of a pixel on the camera chip, and the size of the aperture opening. Therefore, it is important to note that the imaging optimization method described in Section 7.2.1 would need to be performed after any such changes were made, particularly since decreasing the aperture to increase the depth of field would also decrease light intensity. However, once the appropriate imaging settings are determined for given equipment and setup with these considerations in mind, they would remain stable.

The Cherenkov pCBPs also show a distinct left-leaning asymmetry, which is hypothesized to be an effect of the primary magnetic field on the dose distribution, which is discussed further in Section 7.4.2. This asymmetry is not echoed by the TPS pCBPs, however, so further investigations are necessary to determine the accuracy of the Cherenkov images in this regard. Despite the slight intensity disagreements for the larger beams, the beam widths as measured using the FWHM of the Cherenkov pCBPs and the TPS pCBPs were on average accurate within less than 1mm, as shown in Figure 7.3 (g)-(i).

Cherenkov-based pPDD measurements were acquired from the same dataset as the pCBPs, which contributes to the major benefit of the proposed methods given the rapid acquisition time. Furthermore, the imaging process only requires a single beam-on event as opposed to repeated measurements with an ionization chamber (IC) at different depths, it took substantially less time to acquire the Cherenkov data.

While there have been successful MR-compatible automated scanning water phantoms reported in research,¹⁷⁹ these systems are not yet available commercially. Such scanning systems remove the time required to manually translate the detector, but the IC requires a discrete amount of time to acquire each point measurement and scanning speed is limited by acceptable amounts of water disruption caused by the moving parts.

Although the Cherenkov-based projection metrics presented here cannot provide the degree of direct dose-localization as IC measurements along the imaging axis (MRI bore axis), they still have the potential to offer a time advantage, in that all of the data is captured from a single beam-on event without the need to wait for the physical movement of any devices. Previous studies have shown tomographic reconstruction of

Cherenkov images can provide accurate, projection-deconvolved measurement of dose in water tanks,⁹⁰ however the physical constraint of the MRI bore prevent similar techniques from being possible in MR-IGRT systems.

One possible solution to this issue is to place a mirror to the side of the tank at a 45° angle, and focus the camera on the mirror to capture a second projection image. This is rather complicated to implement, especially considering the limited amount of physical space available in the bore, but it would provide a more complete measurement than the single projection image. It is feasible that a reconstruction algorithm similar to that implemented in the work of Brůža et al.⁹⁹ could be adapted to construct a 3D dose volume from only Cherenkov images.

Overall, the agreement between the Cherenkov-derived pPDDs and the TPS pPDDs is strong, with each of the three beams exhibiting an average error of less than 1% (Table 7.1). The maximum error was observed in the build-up region near the water surface. This error in the Cherenkov images can be attributed to the slight surface reflections from an imperfect alignment of the camera imaging axis with the water line, combined with the meniscus of the water in the tank causing slight distortions in the water level across the entire projection. Given these effects are repeatable and explainable, they do not present a problem in the possible adaptation of Cherenkov-based measurements for quick QA measurements to ensure beam characteristics remain unchanged.

The remaining error in the pPDDs is attributed to mismatch between the optical depth of field employed in the imaging setup and the width of the water tank, as discussed

previously. It is thought that some of the Cherenkov signal near the edges of the water tank is slightly out of focus in the data presented here, causing the slight drift in error with increasing depth shown in Figure 7.3(m)-(o). This source of error can be eliminated in future iterations of the setup by ensuring the optical depth of field matches the full width of the water tank. This reinforces the necessity of constancy in imaging setup parameters (particularly the lens aperture size and imaging distance), should this method be employed for QA measurements on a weekly or monthly basis.

The tightest limits of agreement as well as the closest to zero difference mean was observed for the 10.5 cm beam, as illustrated by the error plot diagrams in Figure 7.3 (m)-(o). This is a reassuring result, considering PDD_{10} is a recommended QA metric.¹⁸² The average error of these measurements was well below the repeatability coefficient for all three cases, and only a select few outliers were observed. With properly calibrated hardware, changes in detected Cherenkov intensities from week to week could be used to alert the user of possible issues in beam output that would require a more in-depth investigation using ICs or film. For the case of Co-60, this would mean issues with the beam shaping or source position, while for the upcoming linac version of the VRS, Cherenkov testing would potentially catch issues with the beam energy, as well.

The original agreement between the Cherenkov-derived pPDDs and the IC PDDs, before weighting due to the projection-based nature of the Cherenkov data, was not found to be robust, especially for small beam sizes, as illustrated by the data presented in Figure 7.4 (b). This was determined to be a result of a mismatch between measurement modalities, where the IC measures strictly dose at the central axis, and the Cherenkov

imaging method images an integration of the dose projected across the camera optical axis.

To support this argument for the cause of the discrepancy, it was demonstrated that the known relationship between the projection and central axis dose measurements from the TPS could be applied to the Cherenkov pPDDs, in order to validate the Cherenkov measurements with well understood experimental measurements from the IC. The average error between the Cherenkov pPDD and the IC PDD for the 4.2cm square beam was 2.0%, which decreased to a mere 0.09% after applying the central axis weighting correction. For the purposes of QA in the clinic, this extra step is redundant and unnecessary, since it is more direct to compare Cherenkov data directly with the TPS or previously acquired Cherenkov data.

There is one physical advantage offered by the bi-energetic Co-60 gamma rays (1.17 and 1.33MV), when compared to higher energy linac-generated spectral photon beams (6-18MV peaks) previously reported. Simulation studies of Cherenkov photon generation (*not* detection) from the latter have shown a depth-dependence of Cherenkov photon production attributed to beam hardening, necessitating the introduction of a beam-hardening correction.^{8, 90} This effect is not an issue with characteristic Co-60 gamma rays, meaning the primary consideration is how efficiently the generated photons can make it to the detector as a function of proximity to the water's surface.

Small field dosimetry (beams $\leq 1\text{cm}$) using the Cherenkov method is technically feasible, however much consideration needs to be given to the camera settings used to acquire the data. For this study, the camera optimization (with focus on signal to noise

ratio (SNR) and signal intensity) was carried out for a 10.5cm x 10.5cm beam. Small fields produce much less light with respect to the entire tank volume, with the added factor that the integration of the light as it is projected along the optical axis occurs over much smaller distances. This resulted in a 1.05cm x 1.05cm beam (not shown) manifesting with poor overall intensities and low SNR, not adequate for repeatable measurement. Therefore the limit on beam size with the described setup is reached between 1.05cm and 4.2cm.

Carrying out the described optimization process for a small field specifically would be necessary to improve the quality of the measurements. A more in-depth look at small field dosimetry using these techniques is planned for a state-of-the-art MR-linac, where the imaging settings can not only be optimized, but the Cherenkov acquisition can also be triggered to the radiation pulses to more substantially reject background light.

7.4.2 Magnetic Field Effects on Camera System

A supplementary question was proposed as to whether active MRI would affect static beam measurements due to proximity of the ICCD electronics to the added radiofrequency (RF) noise in the room. The fixed-pattern imaging experiment (Figure 7.6) showed that the camera was not affected by the RF fields, with a very modest error within $\pm 1\%$.

The spatial information about the error is an important point of presenting this figure as a difference image. The checkerboard pattern is clearly visible in the image, and the areas of the highest error correlate to the black checkerboard boxes, which have lower numerical values in terms of intensity than the white box counterparts. Since the

magnitude of error is presented as a percentage, it makes sense that the black boxes would manifest the bulk of the error. In addition to the fixed pattern test, supplementary measurements of the pPDDs and pCBPs were indistinguishable with and without active MRI (not pictured to avoid redundancy).

It was not possible to repeat these measurements in the absence of the 0.35-T primary magnetic field for direct comparison, but the imaging results did exhibit the expected deviations in beam dose asymmetry, following the known directions of the Lorentz forces within the MRI bore. Simulation studies by Raaijmakers *et al.*⁷⁷ identified two effects of the magnetic field on dose deposition. First is the altered point spread kernel, which causes an asymmetrical beam penumbra. This is what we believe is observed in the experimental results presented in Figure 7.7; the effect is more pronounced with increasing depth and the associated decreasing secondary electron fluence.

The second, more prominent influence is the electron return effect (ERE), by which Lorentz forces push secondary electrons back into tissue at tissue-air boundaries. Overall, Raaijmakers *et al.*⁷⁷ concluded that minimal ERE effects were observed in the 0.2-T simulations (closest tested field strength to the 0.35-T VRS magnet). Cherenkov imaging has the potential to uniquely image these effects for systems, especially for those with stronger magnets than the VRS, given that dose deposition effects from magnetic fields become stronger with increasing field strengths.^{77, 80, 81, 169, 183} Further experiments to image ERE using the 0.35-T of the VRS available might be possible if a large air cavity were introduced in the center of the water tank.⁷⁷

7.4.3 Novel Views of IMRT Plans

One of the most interesting capabilities afforded by Cherenkov imaging is that it provides a real-time, high spatial resolution look at treatment delivery. Previous applications of this technique to imaging the TG-119 C-Shape IMRT and VMAT plans on a traditional medical linear accelerator resulted in a >95% passing rate for gamma index analysis with 3%/3mm distance to agreement (DTA) criteria.⁸ This approach could be adopted to complement patient-specific QA methods already implemented in clinical practice.¹⁷⁵

The VRS achieved an 80.5% passing rate for the typically accepted 3%/3mm DTA. The primary cause for the passing rate not meeting the 90% benchmark is thought to be a mismatch between the depth of field of the camera system used in the data acquisition to the tank width. Depth of field was lost in a trade off with light intensity, since opening the camera aperture to allow more light to reach the detector decreases the length along the imaging axis that is in direct focus without blur. Future iterations of this technique should take care to ensure the camera system setting optimization is performed with an aperture setting and imaging distance that allows for the entire projection width of the tank to remain in focus.

It is noticeable that the majority of the pixels that fail gamma analysis for the VRS are in regions of <40% total dose, generally in areas of smaller diameter beams, and in beams that must first travel through the thick treatment couch before entering the water tank, suggesting a combination of these three factors may have also influenced Cherenkov intensity to predicted dose accuracy. Variation in treatment planning

techniques between the linac plans imaged by Glaser *et al.*⁸ versus the VRS-specific plans imaged in this study influence the prevalence of error from the first two factors.

In addition, the optimization of camera settings at the beginning the experiment was conducted with a 10.5cm x 10.5cm beam, and not for small beam sizes employed by the IMRT plan. Because small beams produce much less Cherenkov light overall, the imaging settings would have to be adjusted to adequately capture the small beam information with acceptable signal to noise ratio. Overall, the results presented here serve as a demonstrator of future applications on newer MR-linac systems, where the Cherenkov acquisition can be easily triggered by the radiation pulses to achieve better signal to noise ratios, particularly for small beams.

To increase the accuracy of the Cherenkov measurements, it would be feasible to implement a lens projection correction factor, since the data was acquired as an optical “cone beam,” whereas the planar dose integration is performed as a linear summation. This correction would be highly dependent on the lens, camera, and physical imaging geometry used during acquisition, and follow the same framework as the algorithm described by Glaser *et al.*⁹¹ or Brůža *et al.*⁹⁹ Such a correction was not performed in the presented data, due to the known issues regarding the imperfect depth of field to tank width mismatch.

It is noteworthy that the Cherenkov imaging technique provides novel information regarding the temporal aspect of dose delivery in a treatment plan. This could facilitate the identification of *when* a particular plan fails QA, in addition to simply *where*, and is a key defining feature of the method that makes it stand out compared to competing novel

modalities such as 3D chemical dosimeters. While radiochromic plastic (PRESAGE®), radiochromic gel (FOX), and polymer gel (BANG™) have been shown to be independent of magnetic field effects for dosimetry purposes,^{184, 185} they are limited to reporting temporally integrated dose, with laborious preparation times, storage requirements, and read-out procedures.

However, as with static beam imaging, the gantry and bore of the VRS prevents adjustment of the camera vantage point, meaning the Cherenkov imaging technique is limited to the transverse plane, and detailed information in the sagittal direction is lost. Implementing an optical system with mirrors, as discussed briefly in the previous section, may allow for this data to be collected. With the current physical geometry of the VRS, tomographic capture and subsequent reconstruction of the MR-IGRT system beams, as demonstrated previously on standard medical linacs,⁹⁰ is not feasible.

7.5 Conclusion of Cherenkov Imaging with MR-IGRT

We have shown for the first time Cherenkov-imaging based quality assurance measurements performed on an MR-IGRT Co-60 system, and gauged the influence of the 0.35-T magnetic field on the imaging device to be inconsequential at the extended imaging distance behind the 5-Gauss line. Because commercialized automated QA systems are not yet MRI compatible, Cherenkov imaging in water tanks is offered as an alternative measurement system capable of generating 2D beam characteristic information from a single beam-on event, with minimal error, making it a time-saving procedure.

Analysis of the Cherenkov images allows for extraction of *projection* measurements (projection percent depth dose curves and projection cross beam profiles), because dosimetric information from the entire beam width is integrated along the optical axis. These measurements were within acceptable levels of accuracy for beams ranging in size from 4.2cm-14.7cm, however small field dosimetry requires further study. These techniques would feasibly extend to newer MRI-linac systems in development with much stronger magnets.

The Cherenkov imaging setup also makes it possible to acquire completely novel information on the temporal dose delivery of dynamic treatment plans, which can be summed to compare with the simulated dose volume generated by the treatment planning system. Further understanding of the influence of low dose Cherenkov intensity accuracy and beam size effects at Co-60 beam energies is required for small field dosimetry.

Chapter 8: Expanding to MR-Linacs

It is a natural extension to apply the principles and findings of Cherenkov-based quality assurance on the MR-cobalt-60 system to the newer MR-linac systems that are already replacing them. With this in mind, a study was designed to evaluate the accuracy of Cherenkov-based projection percent depth dose curves (pPDDs) and projection cross beam profiles (pCBPs) acquired in a water tank for a 6MV flattening filter free (FFF) beam from an MR-linac for the first time.

The proposed method can capture data for many subsequent beams without need to alter the setup or move the water tank out of the bore, making it a time-saving approach independent of the magnetic field. This study also offers an in-depth analysis of the merits and limits of using this optical imaging technique for small field dosimetry, with beams ranging from 2mmx4mm (smallest possible from machine) to 16mmx16mm.

8.1 Imaging Methods Adapted to an MR-Linac

An intensified CMOS camera (DoseOptics LLC., Hanover, NH) was placed at the foot of an MR-linac (ViewRay Inc., Cleveland, OH) treatment couch, 4.25m from the radiotherapy isocenter, as shown in Figure 8.1 (a). A Canon 135mm focal length lens was used, set to F#4 to match the imaging depth of field to the depth of the water tank. A 40cm x 30.5cm x 38cm high water tank was filled with water to a height of 18.8cm, to coincide with an SSD of 90cm (bore isocenter), and doped with 1g/1L of fluorophore quinine sulfate dissolved in HCl and water (0.5-N solution); optical Cherenkov-excited fluorescence was imaged.

With the tank water line and transverse center of the tank at treatment isocenter, it was irradiated with four large field beams (200MUs), and three small field beams (1000MUs). Large field beam sizes were 24.07cm x 27.20cm (largest possible out of the machine), 14.94cm x 14.94cm, 9.96cm x 9.96cm, and 4.98cm x 4.98cm. The three small beam sizes were 1.6cm x 1.6cm, 0.8cm x 0.8cm, and 0.2cm x 0.4cm (smallest possible out of the machine). The non-integer beam sizes are a result of the shortened source to axis distance within the MRI bore of 90cm, compared to the conventional 100cm.

Experimental Cherenkov-induced fluorescence images of small beams being analyzed to determine the beam size limits of the proposed method; a) 2mm x 4mm beam (smallest possible from machine); b) 8mm x 8mm beam; c) 16mm x 16mm 6MV FFF beam from MR-linac. ending with the smallest (0.2cm x 0.415cm beam).

A novel remote triggering device was used to synchronize image acquisition to the radiation pulses without a physical interface. This device detects stray radiation in the room, and signals the camera acquisition to begin. This triggering method deviates from other experiments documented thus far, which have predominantly relied on a cable connection to with the target current signal from the linac console. This also diverges from the previous cobalt-60 system experiments, which required extensive testing to optimize the quasi-steady state image acquisition using an internal triggering mechanism, since the cobalt-60 source is a continuous and not pulsed emitter of radiation.

Images were post-processed in MATLAB, and pPDDs and pCBPs were extracted and compared to summed projection images of dose from the treatment planning system (TPS). The image processing and profile extraction methods were already described in

Chapter 7; and use a least means squared registration method in first the x direction then the y direction to compare the experimental to the simulated curves. All curves used the same position in x as the water line, which remained unchanged during the experiment.

8.2 MR-Linac Dosimetry Results

8.2.1 Large Field Dosimetry

Characteristic Cherenkov images and the associated TPS-generated dose predictions are shown in Figure 8.1 (b-e) for two of the four large field beams imaged in this study. The pPPDs for each Cherenkov and TPS image was extracted along the central axis of each beam (illustrated in Figure 8.1 (e)), and plotted in Figure 8.2. No beam hardening corrections were deemed necessary, as the average errors between the optical pPDDs and TPS pPDDs were less than 0.5% for all cases, as summarized in Table 8.1. Note that the first 3mm of data points within the buildup region were excluded from these statistics.

Likewise, the pCBPs for each image were extracted along the lateral axis at the depth of maximum dose (illustrated in Figure 8.1 (c)), and are presented in Figure 8.3. Since FFF beams are being measured, there is a pronounced apex and penumbra to the pCBPs, in contrast to the lower energy, more homogeneous cobalt-60 beam pCBPs reported in Chapter 7.

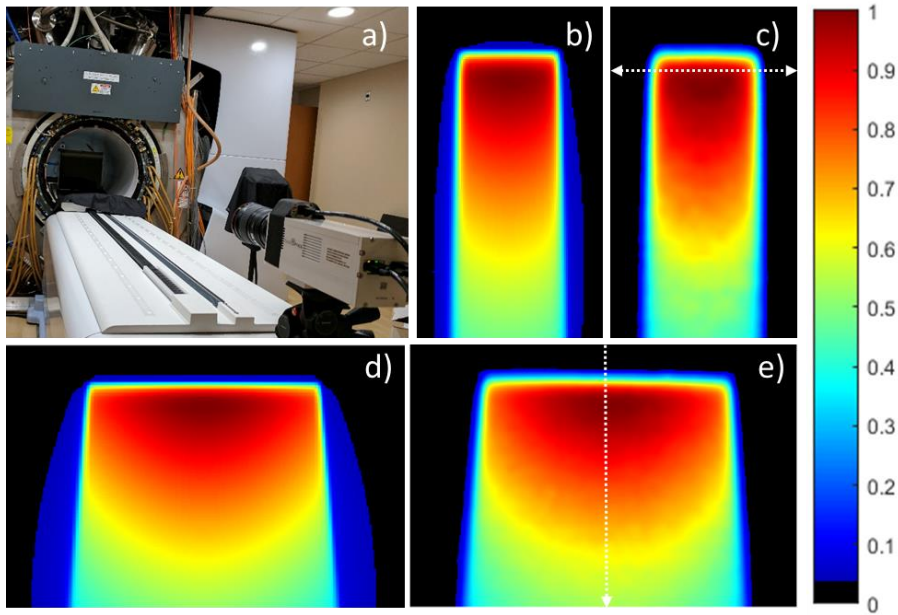


Figure 8.1 a) Experimental setup, with ICMOS at foot of the couch looking down MR-linac bore; b) TPS projection dose image of 4.98cmx4.98cm beam; c) experimentally acquired Cherenkov image of beam in b); white dashed line denotes extraction of pCBP; d) TPS projection dose image of 14.94cmx14.94cm beam; e) experimentally acquired Cherenkov image of beam in d); dashed white line shows extraction of pPDD.

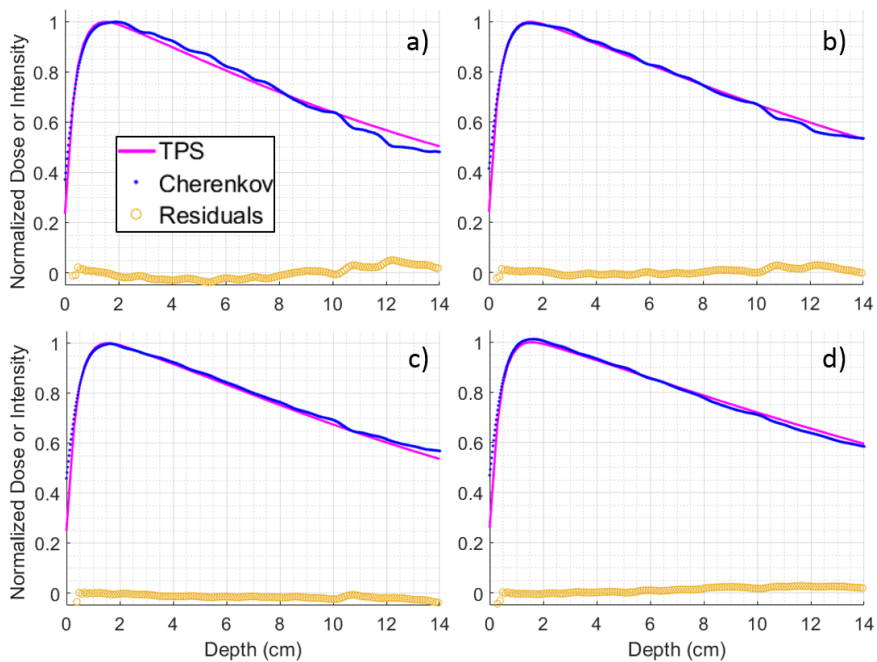


Figure 8.2 a) Projection PDDs of 4.98cm x 4.98cm beam; b) pPDDs of 9.96cm x 9.96cm beam; c) pPDDs of 14.94cm x 14.94cm beam; d) pPDDs of 24.07cm x 27.20cm beam (largest deliverable).

Table 8.1 Statistics calculated from the residual errors between the Cherenkov-based and TPS pPDDs for the four beam sizes shown, omitting the first 3mm of buildup region.

Error Metric	Beam Size			
	4.98cm x 4.98cm	9.96cm x 9.96cm	14.94cm x 14.94cm	24.07cm x 27.20cm
Average	0.08%	0.35%	0.18%	0.36%
Minimum	-3.47%	-2.28%	-2.92%	-5.17%
Maximum	5.30%	2.93%	1.71%	1.95%
Standard Deviation	2.35%	1.14%	0.66%	1.23%

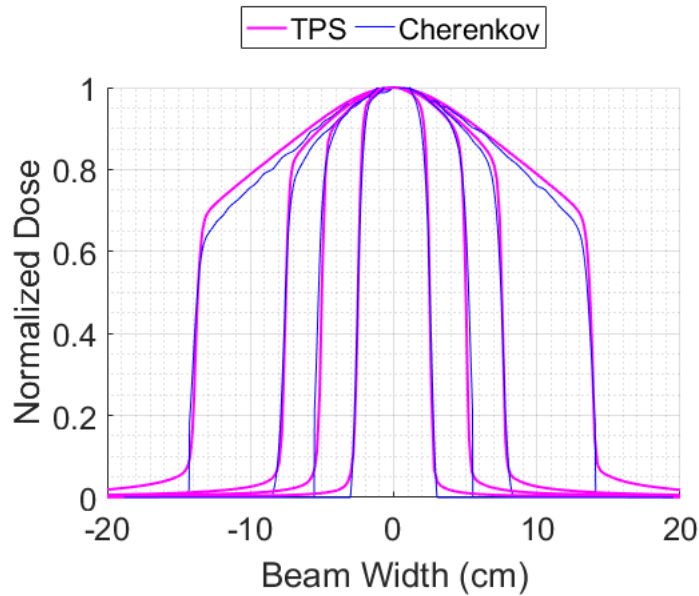


Figure 8.3 The pCBPs extracted from the TPS (magenta) and Cherenkov fluorescence images (blue) for the 4.98cmx4.98cm, 9.96cmx9.96cm, 14.94cmx14.94cm, and 24.07cm x 27.20cm beams.

8.2.2 Small Field Dosimetry

To evaluate the limits of beam size on the proposed Cherenkov imaging method, three small beams were also studied. The optical images of the 2mm x 4mm beam, 8mm x 8mm beam, and 16mm x 16mm beam are shown in Figure 8.4, and associated pPDDs plotted

in Figure 8.5. The error statistics are presented in Table 8.2. While all images are shown on a normalized scale, the ratio of the pixel intensities at depth of maximum dose between the small fields and the 24.07cm x 27.20cm large field beam were 0.850%, 6.32%, and 18.7%.

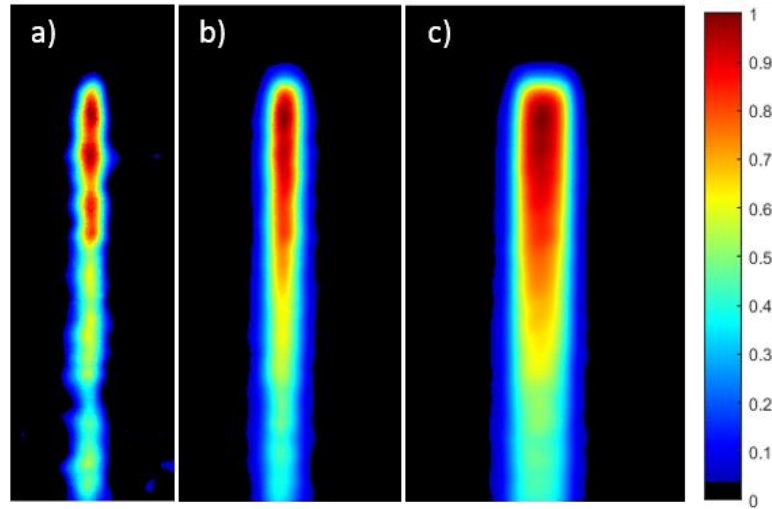


Figure 8.4 Experimental Cherenkov-induced fluorescence images of small beams being analyzed to determine the beam size limits of the proposed method; a) 2mm x 4mm beam (smallest possible from machine); b) 8mm x 8mm beam; c) 16mm x 16mm 6MV FFF beam from MR-linac.

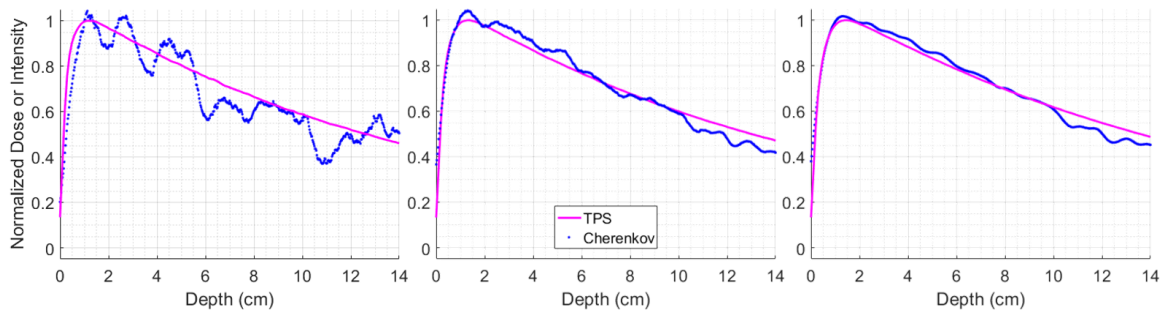


Figure 8.5 Small field TPS and optical pPDDs for a) 2mm x 4mm, b) 8mm x 8mm, and c) 16mm x 16mm beams.

Table 8.2 Statistics calculated from the residual errors between the Cherenkov-based and TPS pPDDs for the three small beam sizes shown, omitting the first 3mm of buildup region.

Error Metric	Beam Size		
	2mm x 4mm	8mm x 8mm	16mm x 16mm
Average	3.66%	0.31%	0.44%
Minimum	-9.91%	-6.18%	-3.57%
Maximum	21.27%	7.43%	7.27%
Standard Deviation	7.61%	3.58%	2.96%

8.3 MR-Linac Dosimetry Discussion

The same concepts demonstrated in Chapter 7 on the cobalt-60 MR-IGRT were translated to an MR-linac with comparable primary magnet. The large field results are both qualitatively and quantitatively compelling. Despite previous experiences in imaging linac beams in water tanks,⁸ the error between the Cherenkov-based and TPS pPDDs was minimal enough to not require a beam hardening correction factor. This is attributed to the increased dose fluence in FFF beams, which in turn generates more optical photons for improved signal to noise ratio (SNR) across through the depth of interest. This is further illustrated by the expected and observed peaked shapes of the pCBPs from the MR-linac compared to the cobalt-60 beams.

Small field dosimetry has long been a challenge for Cherenkov methods.⁹⁰ The small beam sizes mean there is less projection depth along the optical axis over which the optical signal can integrate, leading to poor SNRs. This is moderately compensated for by increasing the dose delivered to the water tank, which allowed for the images in Figure

8.4 to be produced; dose delivered to the tank was increased from 200MUs for the large fields to 1000MUs for the small fields.

In spite of the dose escalation, the amount of optical signal measured by the camera system was inadequate to produce convincing pPDDs for the 2mm x 4mm (Figure 8.5 (a)) and 8mm x 8mm (Figure 8.5 (b)) beams using the given imaging setup. This is seen qualitatively in the noise of the pPDD plots, and quantitatively in the observation of the small ratios of pixel intensities at the depth of maximum dose when comparing each small field to the largest field size image. Given the large field images comprise 5 times less dose (and subsequently 5 times fewer frames summed together into the composite image), this speaks to the very poor SNRs in each individual image in the stack before integration. The 16mm x 16mm pPDD falls on the edge of acceptable noise and quality.

Because the camera system must remain behind the 5-Gauss line of the MR system, it is not possible to move the camera closer to the radiotherapy beam to compensate for the expected $1/r^2$ losses in optical signal. It is, however, possible to improve the imaging equipment, particularly the lens used for data collection.

In this experiment, the aperture was set using an F#4, so that the optical depth of field matched the entire width of the tank. This was necessary for the large beams imaged, and is thought to be another contributing factor in the improved pPDD measurements collected on the MR-linac when compared to the cobalt-60 system for large fields.

While this F# performed well for large fields, for very small beam sizes, increasing the aperture to even F#2 would theoretically quadruple the light intensity collected by

the camera. Although it would be shallower than in the F#4 case, the depth of field with the larger aperture would still be more than sufficient for the very small beam sizes.

It can be extrapolated from the relative imaged intensities that the 2mm x 4mm beam would only exhibit a ratio of 3.40% when comparing the pixel intensity at d_{max} in the small field image to the 2 if the signal was theoretically quadrupled; the same ratio would be 25.3% for the 8mm x 8mm beam, which is greater than that shown experimentally here for the 16mm x 16mm beam. This suggests that under more ideal imaging conditions, the minimum field size limit of the proposed Cherenkov-based pPDD modality would be somewhere between a 2mm x 4mm and a 8mm x 8mm beam.

8.4 MR-Linac Dosimetry Conclusion

Optical dosimetry from Cherenkov excited fluorescence in water tanks has been demonstrated on an MR-linac with 6MV FFF photon beams for the first time. Large field results (4.98cm x 4.98cm to 27.20cm x 24.07cm beam sizes) produced accurate pCBPs and pPDDs. The pPDDs did not need to be corrected for beam hardening effects, most likely due to the increased dose fluence from the FFF beams mitigating intensity losses, but also due to proper matching of the imaging depth of field to the water tank width.

Small fields were also measured with escalated dose and number of acquired frames. The 16mm x 16mm beam performed acceptably, but the two smallest beams (2mm x 4mm and 8mm x 8mm) were inundated with noise. This can be mitigated in the future by increasing the aperture on the imaging lens, thereby implying the theoretical smallest beam size for the proposed method would be somewhere between a 4 to 8mm square beam.

Chapter 9: The Electron Return Effect in MR-Linacs

9.1 Introduction to the Electron Return Effect in MR-Linacs

The field of radiotherapy has long sought the ability to visualize internal anatomy in real time during irradiation in order to validate targeting, shrink treatment margins, and enable precise dose escalation. This has recently proven possible using integrated magnetic resonance image guided radiotherapy (MR-IGRT) systems, now adopted clinically at several institutions worldwide. There are both MR systems combined with Co-60 radioactive sources, and more advanced systems incorporated with medical linear accelerators (MR-linacs).^{69, 71, 75, 167, 168, 186, 187}

One of the primary technical challenges of MR-IGRT systems is the presence of a strong transverse magnetic field, which in the case of MR-linacs can affect the electronic generation of x-rays, and in both cases affect the behavior of dose-depositing secondary electrons. These effects have been extensively studied throughout the development and implementation of MR-IGRT systems through Monte Carlo (MC) simulations.^{72, 80, 169, 170, 188} It is also understood that for instances of highly contrasting physical density interfaces, such as tissue-air boundaries, the electron return effect (ERE) will generate localized areas of escalated and reduced dose.^{169, 188} However, experimental validation of these studies proves challenging due to magnetic field effects and resolution limits on many currently accessible detectors.

Diodes have been shown to produce incorrect dose profiles in the presence of a magnetic field.^{76, 189} Ionization chambers can be characterized and corrected with respect to magnetic field strength,^{172, 173, 179, 190} but are inherently point measurements that lack

spatial resolution required to characterize bulk dose field effects such as those introduced by the ERE.

Two-dimensional dose distributions can be measured with GafChromic and radiochromic films with reasonable accuracy, but require strict physical and temporal protocols for irradiation and readout; both have been used to measure ERE in limited scenarios.^{171, 191, 192} Gel-based 3-D dosimeters, such as PRESAGE® radiochromic plastic and FOX gels, have been demonstrated to not be influenced significantly by magnetic field effects.^{184, 185, 193} However, they are not generally regarded as user-friendly, utilize toxic materials,¹⁷⁸ and limited literature is available in regards to using them to quantify ERE with respect to commissioned MR-IGRT treatment planning system (TPS) data.¹⁹⁴

To be prudent in clinical treatment with MR-IGRT systems, rigorous validation of simulated ERE results is necessary. This study aims to employ a novel method of observing and quantifying ERE through optical imaging of scintillation and Cherenkov emission. The experimental results are compared to TPS and radiochromic film results in an attempt to substantiate the predicted scope and severity of dose variation due to the ERE.

9.2 Materials and Methods

9.2.1 MR-Linac and TPS

The Viewray MRIdian (Viewray, Cleveland, OH) MR-linac and its commissioned treatment planning system (TPS) were studied. All irradiations from the Viewray were 6MV flattening filter free (FFF) beams, delivered with set dose rate of 650MU/min, for a total of 200Mus; the only exception is the film Phantom B, which was delivered 400MUs. The primary magnetic field of the system was measured to be 0.345T.

Each phantom was scanned in a CT simulator at a resolution of 0.9004mm x0.9004mm pixels with 0.8mm slice width. Individual treatment plans were created for each irradiation scheme using the Viewray TPS, and the associated dose volume dicom files were exported for analysis in MATLAB (Mathworks Inc., Natick, MA).

9.2.2 Phantom Design

The three phantoms shown in Figure 9.1 were fabricated with air cavities of varying sizes to illicit the ERE to different intensities, where the larger cavities are expected to be more severely affected. Acrylic was chosen as the material for two of the phantoms for the comparability of its density to water, the ease of machining air cavities in the solid material, and optical transparency. Irradiated acrylic emits optical signal as a result of predominantly scintillation, with additional light contributions from the Cherenkov Effect. Both light sources are known to be linear in proportion to deposited dose, although Cherenkov emission exhibits more energy-dependence.^{7, 90, 195}

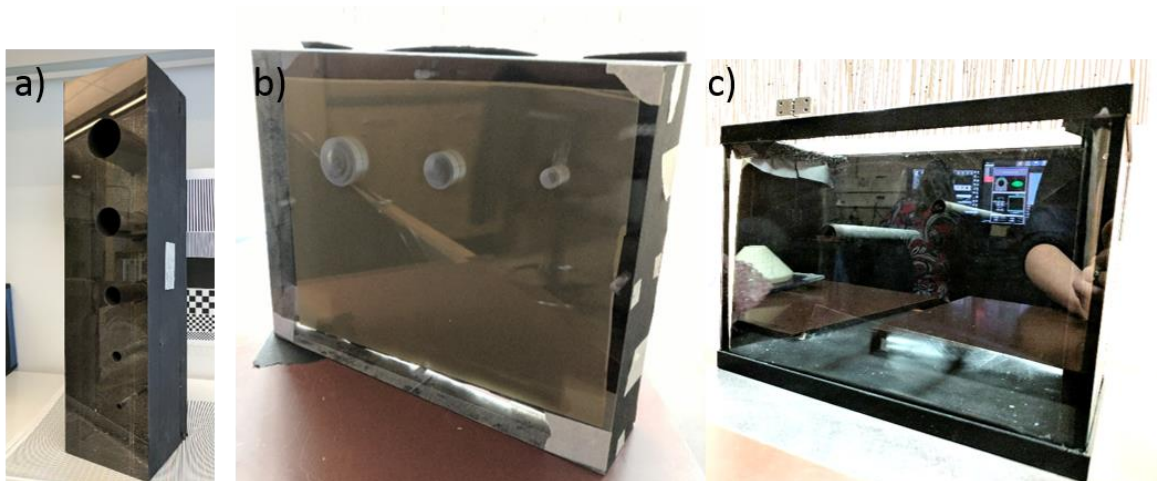


Figure 9.1 a) Phantom A: 5 cavities in acrylic; b) Phantom B: 3 cavities and film in acrylic; c) Phantom C: 2 cavities in water.

9.2.3 Phantom A: Five Cavity Phantom

The first phantom studied was a 40cm x 10cm x 10cm block of clear acrylic milled with 5 holes of increasing diameter (0.5cm, 1cm, 2cm, 3cm, and 4cm), shown in Figure 9.1(a). The top apex of each circular cavity was aligned 3cm below the surface, so that the beam attenuation would be equivalent in each case before reaching the hole. The interiors of all cavities were painted black to eliminate optical reflections or light tunneling effects. All faces, except the front face being imaged by the IC MOS camera, were covered in optical blackout tape.

The air cavities were spaced so that each could be independently irradiated by an 8.3cm x 8.3cm beam, with the top face of the phantom set to SSD=95cm. The inner 3 cavities were individually aligned so that the center of the circular holes were coincident with the lateral treatment isocenter. Due to the physical constraints of the MRI bore, the outer two cavities (4cm and 0.5cm diameter) could not be coincident with the treatment isocenter, so the couch was used to shift in either direction as much as possible, while the MLCs were utilized to center the beam on the off-center cavities.

9.2.4 Phantom B: Three Cavity Phantom with Film

The second phantom studied was a smaller acrylic block with 3 milled circular cavities (3cm, 2cm, and 1cm), that was split into two opposing blocks so that a piece of radiochromic film could be inserted. The film was situated in the transverse plane of the MRI bore, perpendicular to the optical axis of the camera, so that it produced an image of dose in the same plane as the optical imaging system. A single 24cm x 4.15cm beam was used to irradiate all three cavities simultaneously. The top apex of each cavity was

5cm below the acrylic surface for this phantom, compared to the 3cm depth of the cavities in Phantom A.

9.2.5 Phantom C: Two Cavity Water Tank

A final phantom was constructed from a 30.5cm x 15.2cm x 20.3cm water tank, shown in Figure 9.1(c). Black rubber sheets were affixed to the interiors of the bottom, rear, and side faces of the tank. Two polycarbonate tubes with outer diameters of 0.95cm and 1.6cm, and plastic wall thicknesses of 1.6mm were painted black. Black neoprene washers were used to create a water tight seal between the tubes and the clear front face of the water tank, while the black rubber covering of the back face provided a seal on the opposite end. A digital level was used to align the tubes parallel to the water surface.

The water tank was filled with water, and doped with a 1g/L concentration of fluorophore quinine sulfate. The fluorophore was introduced to redistribute the highly directional Cherenkov emission to isotropically emitted Cherenkov-excited fluorescence (CEF).⁷ Phantom C was used to evaluate the differences of observed optical signal between the predominantly scintillation emissions from acrylic Phantoms A and B with the CEF signal of Phantom C, and to perform similar measurements in a water phantom, and not the approximately water-equivalent acrylic (density 1.18 g/cm³).

The water tank was placed on the treatment couch between the MRI coils, and first imaged in the treatment position to ensure the alignment and water-tight seal in the air cavities. The top coil was then removed from the tank, and optical images were collected while the phantom was irradiated with a single 9.96cm x 20cm wide beam.

9.2.6 Camera System and Imaging Setup

As shown in Figure 9.2 (a), a 1200x1600 pixel intensified complementary metal-oxide-semiconductor (ICMOS) camera system (DoseOptics LLC., Hanover, NH, USA) with an attached Canon 135mm lens set to f/4 was aligned at the foot of the treatment couch, just behind the 5-G line of the MRI, approximately 4.25m away from treatment isocenter. The camera height was adjusted so that the height of the optical axis was the same as the height of the treatment isocenter with respect to the floor. All room lights were turned off or covered during acquisition to diminish background signal and eliminate any possible effects of glare.

C-Dose Research Software (DoseOptics LLC., Hanover, NH, USA) was used to acquire the image data. A remote trigger device that detects the presence of radiation in the room was used to synchronize the optical image acquisition to the radiation pulses, without the need for a physical interface with the Viewray linac components, using a 6 μ s exposure duration per detected radiation pulse. Background images were acquired using the same settings with an internal trigger module, without the presence of the radiation. The internal camera hardware was set to perform a temporal median filter across 5 subsequent images during readout. This approach removes most of the stray radiation noise that manifests in the images as sporadic hot spots.

The physical resolution of the experimental setup was measured using a custom test target with known feature sizes positioned at the treatment isocenter, shown in the right half of the components in Figure 9.2(b). To ensure the depth of field matched the sizes of the imaged phantoms, this test target was also imaged at 5cm increments to

range -15cm to +15cm. An additional test of depth of field was performed using the high frequency pattern in the left most portion of Figure 9.2 (b). The pattern was aligned at a 45° angle with respect to the treatment couch, to span a 14cm depth along the optical axis, and analyzed for changes in light and dark contrast between line pairs to indicate level of focus in the imaging field along the optical axis.

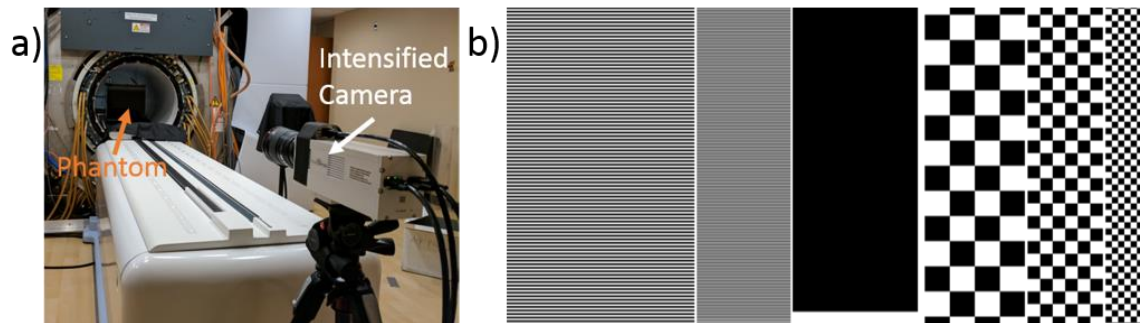


Figure 9.2 a) Experimental setup with ICMOS at foot of treatment couch, looking down the MR-linac bore to the phantom; b) cropped and scaled resolution and depth of field test target.

9.2.7 Control Experiment Imaging

To validate the approach, Phantom A was also irradiated and imaged on a Varian TrueBeam linac (Varian Medical Systems, Palo Alto, CA, USA) with 6MV FFF beams and dose rate of 600 MU/min to mimic the MR-linac beam without the presence of the magnetic field. The same ICMOS, lens and acquisition setup described in Section 9.2.6 was used, placed at the foot of the treatment couch approximately 3m away from treatment isocenter.

The 3cm, 2cm, and 1cm diameter cavities were aligned to the treatment isocenter, with the top surface of the phantom at SSD=95cm. The phantom was irradiated with 200MUs of a 8.3cm x 8.3cm beam. The phantom was then aligned so that the beam

was directly between the 3cm diameter and 2cm diameter holes, and irradiated and imaged with an 8.3cm x 8.3cm beam. Eclipse (Varian Medical Systems, Palo Alto, CA, USA) TPS was used to generate volume dose dicoms for both scenarios using the Acuros XB dose calculation algorithm, and the optical images were compared to the simulation results through post-processing in MATLAB. The Acuros XB algorithm was chosen over the Anisotropic Analytical Algorithm (AAA) due to the established superior dosimetric performance in literature, particularly when air gaps are included in the irradiated volume.¹⁹⁶

9.2.8 Image Post Processing

MATLAB was used for all post-processing of optical images and TPS data. Each test setup of 200MU delivery produced stacks of approximately 175 frames. A minimum intensity filter was used over every fifth frame to remove any residual stray radiation noise. The stack of images was then summed into one composite image, and normalized to a flat field image of the camera response under uniform illumination. An edge-preserving bilateral filter with Gaussian half-width of 11 pixels was applied to each composite image to smooth remaining noise.

The average intensity calculated in a 6x6 pixel region of interest at the depth of maximum dose ($d_{\max}=1.5\text{cm}$) was used to determine the normalization factor for each image. Likewise, the volume dose dicoms from the TPS were imported into MATLAB, and all slices were summed into a single image along the optical axis for comparison to the optical images, and the central axis slice was used for comparison to the film in the case

of Phantom B. The dose at the d_{max} was identified, and used as a normalization factor in all images independently.

9.3 ERE Imaging Results

9.3.1 Control Imaging of Phantom A

Both the TPS (Eclipse, Acuros algorithm) generated integrated dose images, and the experimentally measured optical images for the four control cases of Phantom A irradiation on the Varian TrueBeam linac, without magnetic field present, are shown in Figure 9.3. Note the TPS models the dose in air, while the experimental images are insensitive to air dose.

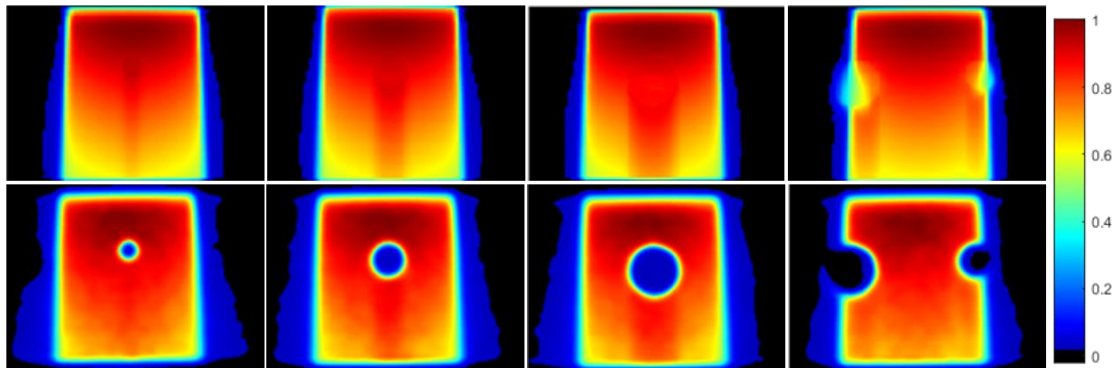


Figure 9.3 Top row: Eclipse TPS integrated dose images (Acuros algorithm); Bottom row: optical images for each test case of the control experiment without magnetic field. All images are independently normalized to the dose at d_{max} .

The projection percent depth dose curves (pPDDs) were extracted from each image by taking the intensity profiles along the central vertical axis down the height of the phantom. In addition, the pPDD tangent to each cavity at a 5mm lateral shift from each cavity edge was plotted and compared for each case; when the area between two

cavities was irradiated, this plot reflects a lateral shift 1cm from the central pPDD axis. Finally, the projection cross beam profiles (pCBPs) at the depth of maximum dose (d_{max}) were obtained from each image by taking a horizontal line plot. These plots are presented in Figure 9.4

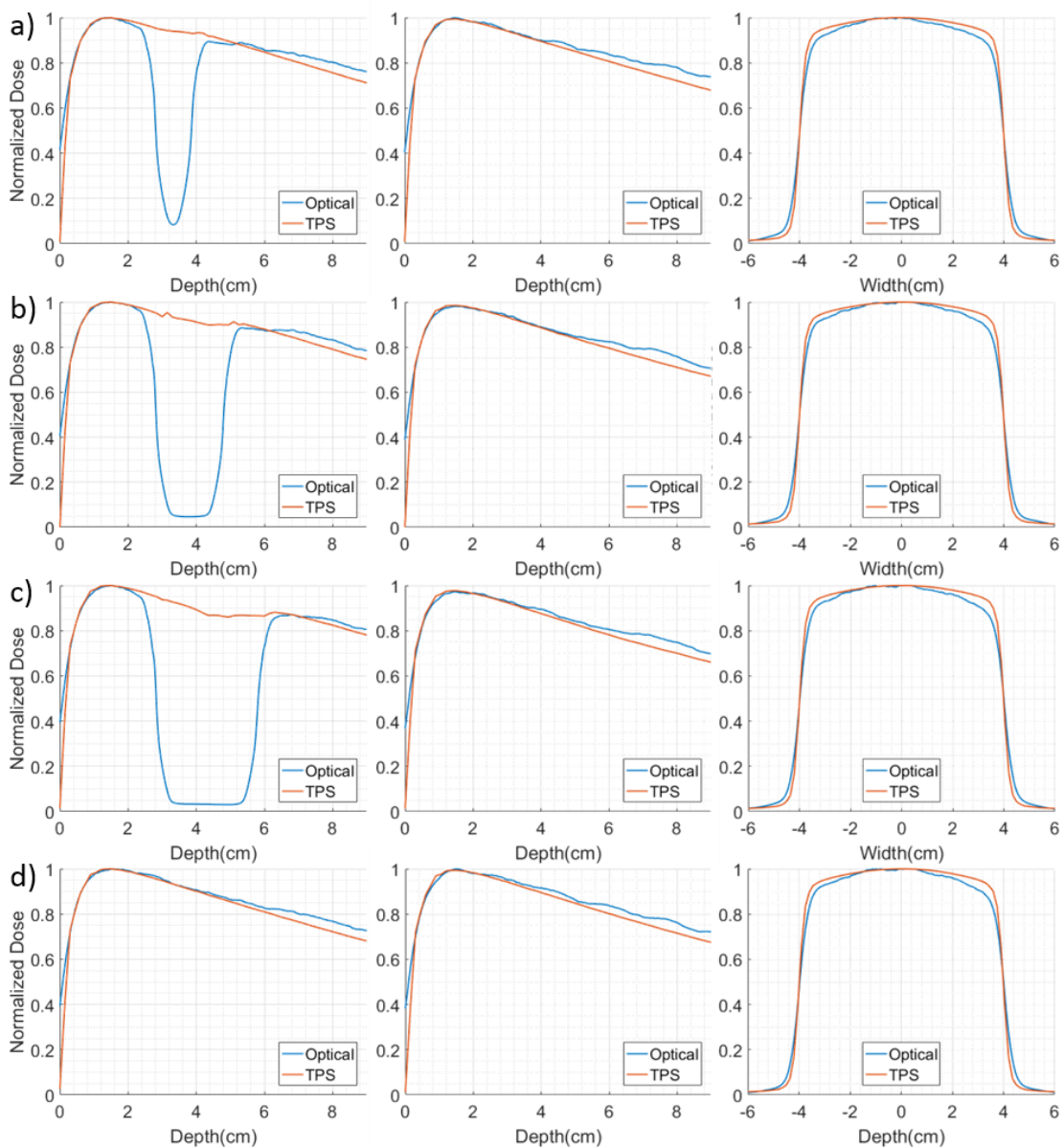


Figure 9.4 Control experiment line plots for the same sized beam impinging the: a)1cm cavity, b)2cm cavity, c)3cm cavity, and d)the solid area between the 3cm and 2cm cavity. Column 1 presents the pPDDs through the center of each beam. Column 2 shows the pPDDs taken 5mm to the left of each cavity in a)-c), and 1cm to the left of the central axis in d). Column 3 contains the pCBPs at the d_{max} .

Given the expected variation between the TPS and optical pPPDs at the location of the air cavity, error was predominantly studied for the fourth case, where the phantom was irradiated in the solid area between the 3cm and 2cm diameter cavities. This error plot is presented in Figure 9.5, with error statistics summarized in Table 9.1.

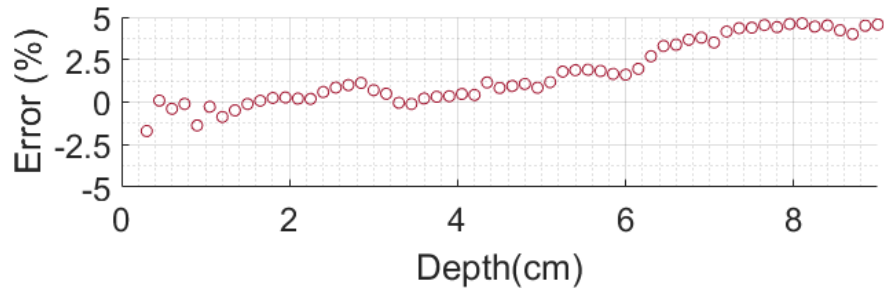


Figure 9.5 Percent error between the optical and TPS pPPDs in Figure 9.4 (d) for depth 3-90mm.

Table 9.1 Statistical summary of errors plotted in Figure 9.5.

Depth Span	Error (%)			Standard Deviation
	Average	Maximum	Minimum	
3-60mm	0.48	1.90	-1.70	0.85
3-90mm	1.67	4.63	-1.70	-1.85

9.3.2 Phantom A Results

To observe the ERE, Phantom A was irradiated on the Viewray system by a 6MV FFF beam in the presence of the 0.345-T primary magnetic field of the MR-linac. The TPS simulation projection dose images for the 1cm, 2cm and 3cm cavity cases are shown in Figure 9.6 (a), and the respective experimental optical images are shown in Figure 9.6 (b). Each image is normalized to the dose or light intensity at the depth of maximum dose.

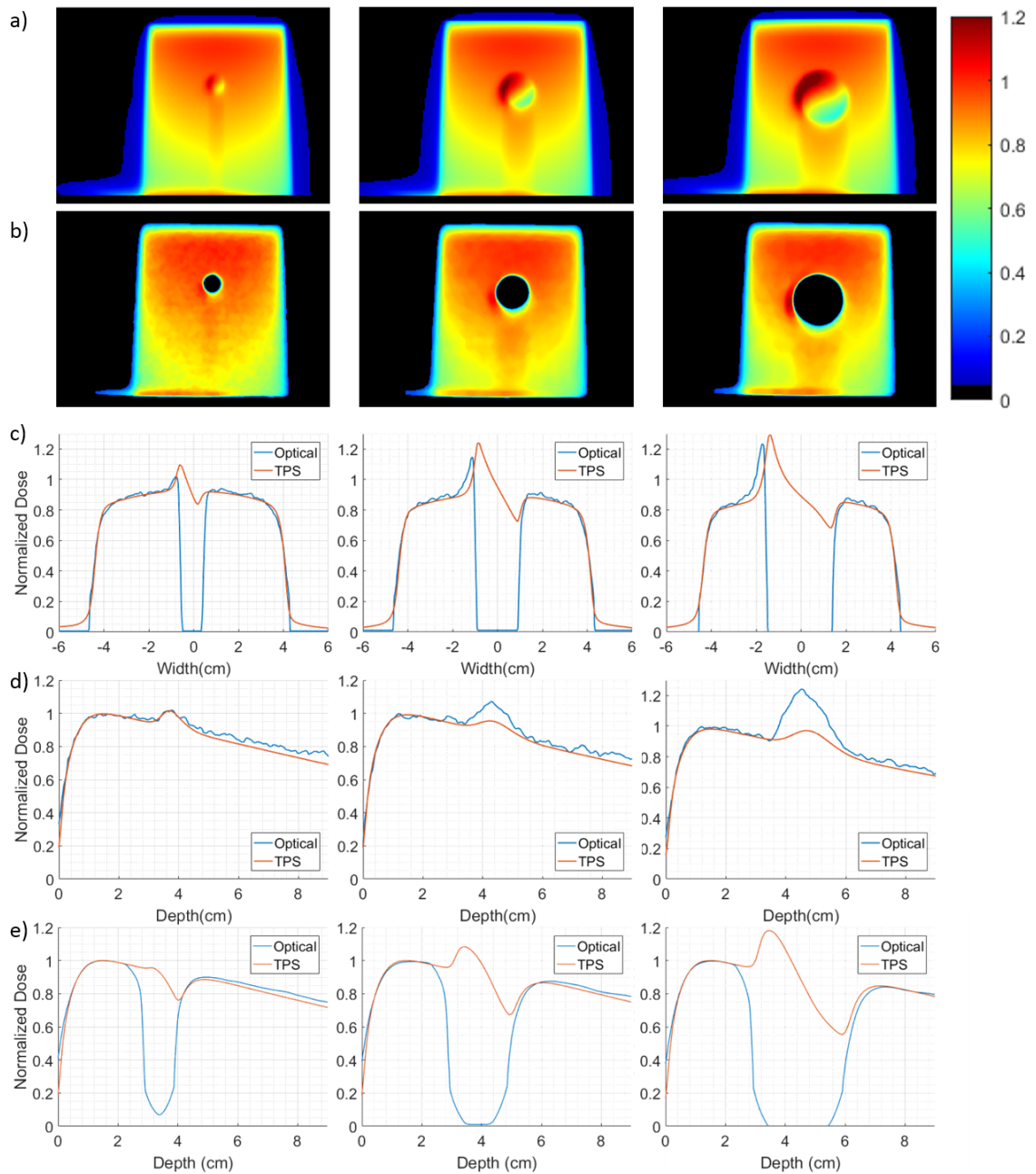


Figure 9.6 a) Projection sum images of TPS dose predictions of ERE resulting from 1cm, 2cm, and 3cm cavities in Phantom A, normalized to the dose at d_{max} ; b) associated optical images for each respective cavity irradiation in the presence of the magnetic field, normalized to the dose at d_{max} ; c) pCBPs through the center of each cavity comparing a) and b) for each cavity size; d) cavity-tangent pPDDs, or the vertical dose profiles set to a 2mm lateral shift from the left cavity boundary comparing a) and b); e) central axis pPDDs containing d_{max} comparing a) and b).

Again, the TPS models the dose in air, while the proposed imaging method, as expected, cannot detect dose within the cavity. Unfortunately, the size of the bore with respect to the size of the phantom prohibited direct, isocenter-aligned irradiation of the 0.5cm and 4cm cavities; these data sets are not shown.

Line profiles at three areas of interest were compared to evaluate the differences between the TPS and experimental data sets. First, the pCBPs for each cavity, drawn as the horizontal profile containing the center of each cavity, are shown in Figure 9.6 (c). Next, the pPDD curves were drawn in an area of expected dose escalation due to the ERE, 2mm to the left of each cavity; these profiles are shown in Figure 9.6 (d). Finally, the pPDDs taken as the vertical profiles through the centers of the beams and cavities are presented in Figure 9.6 (e).

9.3.3 Phantom B Results

The second acrylic phantom, Phantom B, was irradiated on the MR-linac with a piece of radiochromic film sandwiched between the two halves to produce a film reading (Figure 9.7(b)) in the same plane as the optical image (Figure 9.7 (c)). The optical image was acquired during a second irradiation with the same setup and beam, without the film in place. The results are compared to the TPS generated image of the central axis planar dose (Figure 9.7 (a)) below. Each of the three figures are independently normalized; the TPS and optical images are normalized to the intensity at the depth of maximum dose. However, the physical size of the film was smaller than the full phantom, and the film had to be placed between the four metal securing pins that hold the two components

sandwiched together. This means that the film data begins near depth 1.6cm, and thus was normalized to the maximum intensity observed in the first 1cm of film depth.

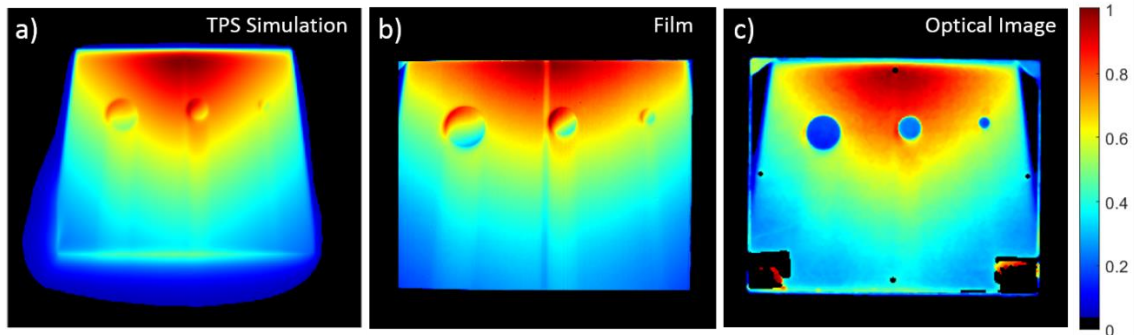


Figure 9.7 a) TPS planar dose simulation; b) readout of radiochromic film irradiated while within phantom; c) optical dose measurement (film was not inside the phantom at the time of optical acquisition). Dark artifacts in the optical image are the result of the tape (bottom corners) and metal pins used to secure the phantom pieces together.

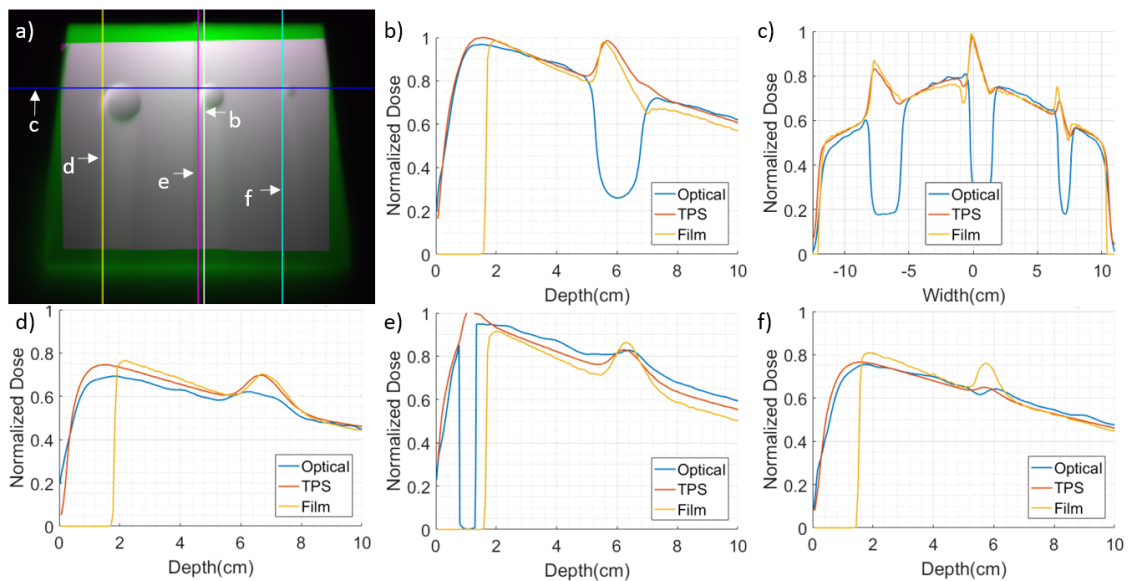


Figure 9.8 PDD and CBP plots comparing the results of the three modalities, optical imaging, TPS dose prediction, and film measurement. a) Registered film (gray) and TPS (green) dose images, with colored line plots designating the physical locations of the subsequent plots (b-f); b) PDDs directly to the right of the metal phantom alignment pin (white line); c) CBPs intersecting all three cavities (blue horizontal line); d) PDDs 2mm to the left of the 3cm cavity (yellow line); e) PDDs 2mm to the left of the 2cm cavity, intersecting the metal pin (magenta line); f) PDDs 2mm to the right of the 1cm cavity (cyan line).

Figure 9.8 compares the three modalities (TPS simulation, radiochromic film, and the proposed optical imaging technique. Figure 9.8 (a) shows the registration between the film and the TPS image, with drawn lines to designate the locations of the four subsequent PDD line plots and singular CBP plot. Note that the film and TPS data are planar and not projection data.

9.3.4 Phantom C Results

The final phantom, water tank Phantom C, produced the TPS-generated integrated dose image shown in Figure 9.9 (a). This is juxtaposed with the Cherenkov-excited fluorescence image of optical light captured from the quinine-doped water tank (Figure 9.9 (b)). Again, each image was normalized to the intensity at the depth of maximum dose for the 6MV photon beam (1.5cm). Misalignment of the beam with respect to the water tank in the TPS dose simulation prevents more quantitative comparison of these two images, however the data will be rectified and analyzed in future studies.

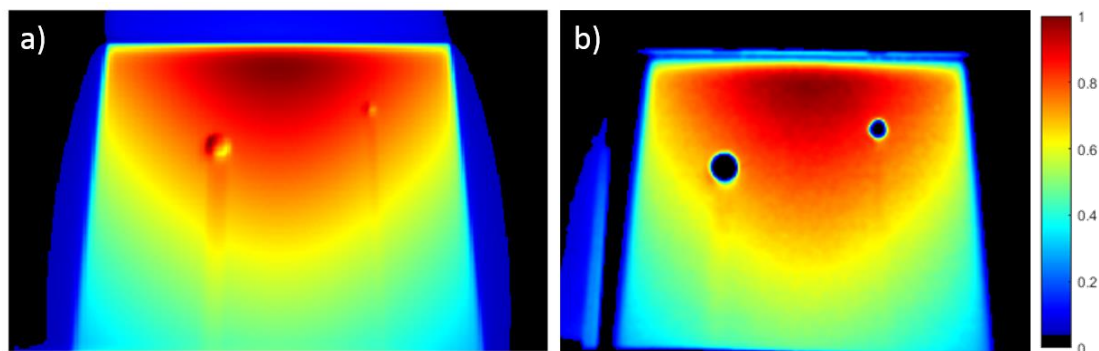


Figure 9.9 integrated dose image of water tank Phantom C from a) TPS simulation, and b) optical image measurement.

9.4 ERE Imaging Discussion

ERE has traditionally been a difficult phenomenon to measure, because it is of most interest at solid-gas interfaces, where the electrons are permitted to move and be manipulated by the magnetic field after they are liberated from the solid medium and ejected into a gas medium. Surveying the entire area with point measurements is fundamentally challenging, because any solid-gas phantom arrangement would restrict the possibilities of physical placement of a point detector with its own inherent footprint. This has limited the ability to rigorously, quantitatively validate the simulation results modeling magnetic field effects on radiation dose deposition.

Optical imaging of scintillation or Cherenkov excited fluorescence to observe the ERE is the novel idea proposed here, with the attractive asset that the irradiated medium itself is the generator of the detected signal, measured remotely in real time. The optical images were compared to the TPS simulation results, and in one case, the reported dose from radiochromic film, to assess the strengths and limitations of the proposed method.

The control experiment was conducted on Phantom A to evaluate the accuracy of scintillation as a surrogate for dose in the given experimental setup without the magnetic field effects, where TPS dose simulations are inherently trusted. As expected, given the fact that the TPS is able to model dose deposited in air while the intensity of scintillation in air is much too low to be detected in the given scheme,¹³² the major deviation between the two results occurs within the air cavities (Figure 9.3 and Figure 9.4). The air cavity dose must therefore be disregarded in the TPS images when comparing to optical images.

The interesting result here is the trending drift of increased error with depth. The error plot shown in Figure 9.5. While the average error is still relatively low over the entire depth (1.65%), it becomes more pronounced after depth of 6cm. In fact, over the first 6cm, the average error is only 0.48%, spanning +/-2%. There are two possible reasons for this depth-deviation which will be investigated further: 1) beam hardening, or 2) edge reflections from the bottom of the phantom.

Beam hardening is the more likely cause of the discrepancy at larger depths, since the phantom is coated on the outside with optically black tape and paint. The results here reinforce the beam hardening conclusion, given the depth-dependent errors manifest as larger in the scenarios where more acrylic is in place to filter the radiation beam (i.e. the no/small cavity cases); the error is more minimal for the large cavity cases, where less beam energy filtering is occurring since more of the beam is passing through air. In the given setup, this suggests the dosimetric confidence of the proposed method in this phantom is the highest for the first 6cm. To this end, the cavities of Phantom A were placed 3cm below the surface, and end at or before the 6cm mark. Phantom B did not have this design flexibility, and the cavities are 5cm below the top surface, and therefore results from this phantom must be considered accordingly.

The final note about the control experiment is the low intensity ring in the immediate vicinity of the solid-air interface. This is thought to be an optical artifact originating from the inner surfaces of the holes, which were painted black and therefore absorbing some of the generated light. This causes the holes to appear slightly larger in the pPDD plots than the known physical size of the cavity, but otherwise can be

acknowledged and disregarded. This, combined with the known issue of accuracy at larger depths, prompts the primary focus of this study to be the areas of escalated dose localized near the superior edges of the cavities, and not the mirrored areas of decreased dose concentrated on the inferior sides of the cavities.

The ERE results of dose measurement in the presence of the magnetic field are qualitatively convincing for all three phantoms. The between the optical and TPS images for Phantom A (Figure 9.6) suggests that it is possible the TPS is under-reporting the extent of dose escalation due to ERE, as well as the localization of the dose escalation. This is particularly true for the larger cavities. The pPPDs measured 2mm to the left of each cavity (Figure 9.6 (d)) show that while the 1cm cavity results between the TPS and optical imaging technique largely agree, the dose escalation differs by 10% and 20% for the 2cm and 3cm cavities respectively.

Likewise, the pCBPs presented in Figure 9.6 (c) also reinforce this observation. The TPS dose simulations model similar magnitudes of dose escalation, however it is localized within the air cavity, which logically starts where the optical and TPS curves intersect at the two points closest to the center of the beam (0cm point). The dose most pertinent to clinical implementation, however, is the dose deposited within the solid. The optical images suggest that this dose is instead localized in the solid rather than the air, raising concern that the TPS may be misrepresenting the actual dose to tissue in clinical cases.

Further quantitative analysis of these images, along with the data for Phantoms B and C, must be conducted to more completely establish the differences between the TPS and experimentally measured intensities to assess their validity. However, the

preliminary results of this study suggest that the localization and intensity predictions of increased dose to tissue due to the ERE might not be accurate.

9.5 ERE Imaging Conclusion

In this work, ERE was measured for the first time in an MR-linac using a novel optical method (scintillation and Cherenkov excited fluorescence) in phantoms. This method allows for 2-D measurement of dose distributions without the need to perturb the beam and solid-air interface with a detector. There are some observed artifacts that can be accounted for, such as the inability of the optical method to measure the dose within the air cavities. Regardless, the method is promising to provide dosimetric value to quantifying the ERE, and additional work is forthcoming regarding the ultimate utility and limitations of the approach.

Chapter 10: Optical Imaging Prototype for MR-RT Alignment

10.1 Introduction to Alignment Problem

Magnetic resonance image guided radiotherapy (MR-IGRT) is an exceptional technology that allows clinicians to escalate dose prescriptions based on the premise of increased precision in disease targeting.¹⁶⁸ This is because the MRI provides real-time information of internal tumor motion that can be used to gate radiotherapy beam delivery. Therefore, it is logical that the known coincidence of the MR generated images and the position of the radiotherapy beam must be well characterized.

Commissioning of integrated MRI radiotherapy machines requires precise alignment between MRI and radiation treatment (RT) isocenters, which is a nontrivial task.¹⁹⁷ Other imaging modalities common in radiotherapy, such as on board cone-beam CT and portal imaging, rely on radiation sources, sometimes the treatment source itself, to generate image data. This intrinsic similarity allows for straightforward registration between collected images and the RT source. MRI, on the other hand, is completely non-reliant on any type of radiation source, and as such, the phantoms suitable for MR alignment are not inherently adaptable to also discern the placement of the RT isocenter.

With this in mind, an optical measurement system and novel phantom was devised with the potential to quantify the displacement of the MRI isocenter with respect to the optically imaged RT isocenter. When placed in a water tank, the proposed device and method is a novel approach to simplify the process of measuring the coincidence between the MRI isocenter and RT isocenter. This measurement is intended to provide a quantitative answer to the magnitude of the 3D shifts required to co-align the two

independent isocenters, in first the Z direction (axis of the MRI bore), and then the X-Y direction (transverse plane within the MRI bore).

This methodology relies on predominantly the optical scintillation generated by the plastic upon irradiation, which can be captured using the same camera systems developed for *in vivo* and quality assurance applications of Cherenkov emission imaging described in this thesis. This remote approach to scintillation imaging of choice plastics has already been demonstrated to have some dosimetric value in the clinic,¹⁹⁵ however for this application, quantitative dosimetry is not required.

10.2 Prototype Phantom and Methods

10.2.1 Prototype Phantom Design and Optical Imaging Setup

A novel conical frustum-shaped phantom was designed and drafted in computer aided design (CAD) software package SolidWorks (Dassault Systèmes, Vélizy-Villacoublay, France). The phantom (CAD drawing shown in Figure 10.1) had base radius=7cm, and top face radius=2cm, with cone half-angle of 45 degrees. The CAD drawing was sent to rapid prototyping company Proto Labs Inc. (Maple Plain, MN) to be machined out of natural colored ABS plastic.

For proof of principle, the phantom was mounted in air and irradiated using a Varian TrueBeam linac capable of delivering 6MV flattening filter free (FFF) beams, also employed by the ViewRay MR-linac. An intensified complementary metal oxide semiconductor (ICMOS) camera (DoseOptics LLC., Hanover, NH) was placed at the foot of the treatment couch, so that the optical axis was parallel to the conical axis, as indicated in Figure 10.2 (a). A 135mm Canon lens set to F#4 was affixed to the ICMOS body, so that

the focal depth of field matched the size of the phantom. The phantom shown previously in Figure 9.2 (b) was aligned and imaged to measure the physical dimension of each pixel.

Image acquisition was synchronized to the radiation pulses of the linac through a physical connection to the current on the linac photon target (Targ1); room lights were turned off during phantom imaging. The IC MOS was set to perform on-board temporal median filtering between 5 subsequent frames, and on-board spatial median filtering with a [3,3] pixel kernel. These allowed for rejection of the bulk of the salt and pepper noise originating from stray radiation hitting the camera, and eliminated the necessity of performing these operations during post processing of the images.

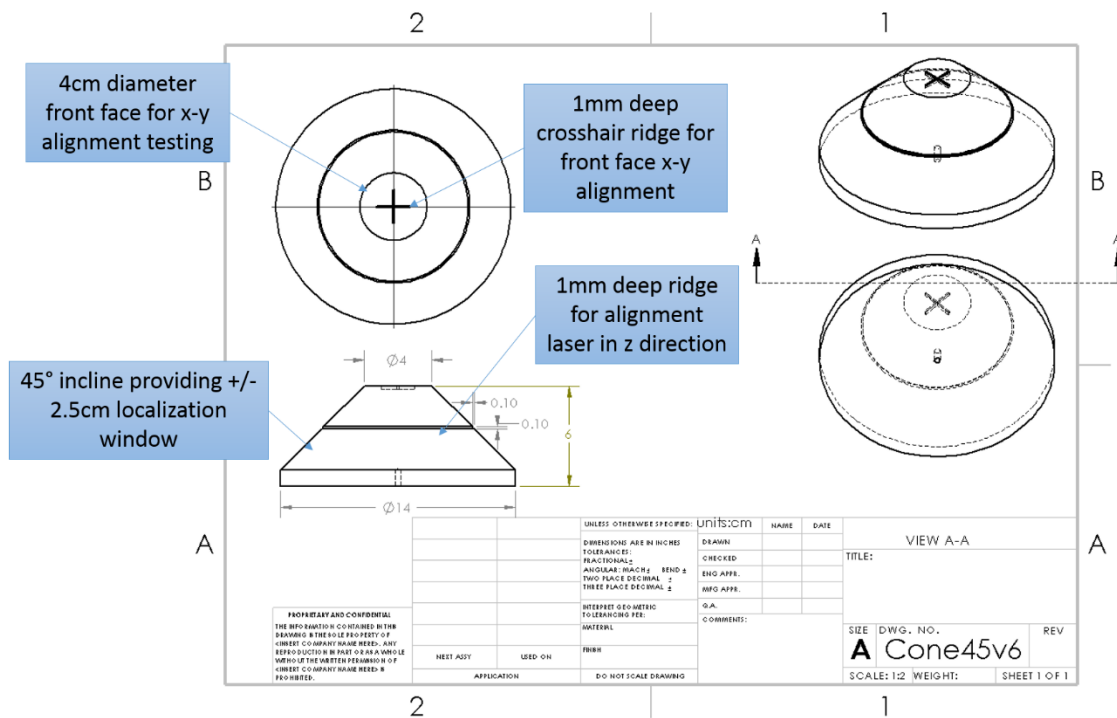


Figure 10.1 CAD drawing of prototype MR-RT alignment phantom.

10.2.2 Method for Measuring Z-Axis Alignment

Two 20cm long and 1cm wide 6MV FFF sheet beams (gantry at 270° and 90°) at dose rate of 600 MU/min were delivered to the phantom at iterative positions along the z-axis, and

the optical emission of the plastic was imaged for each beam. The irradiation scheme is illustrated in Figure 10.2 (c). The TrueBeam treatment couch, commissioned to submillimeter precision, was used to translate the phantom along the z-axis to simulate varying magnitudes of isocenter misalignment with respect to the lasers.

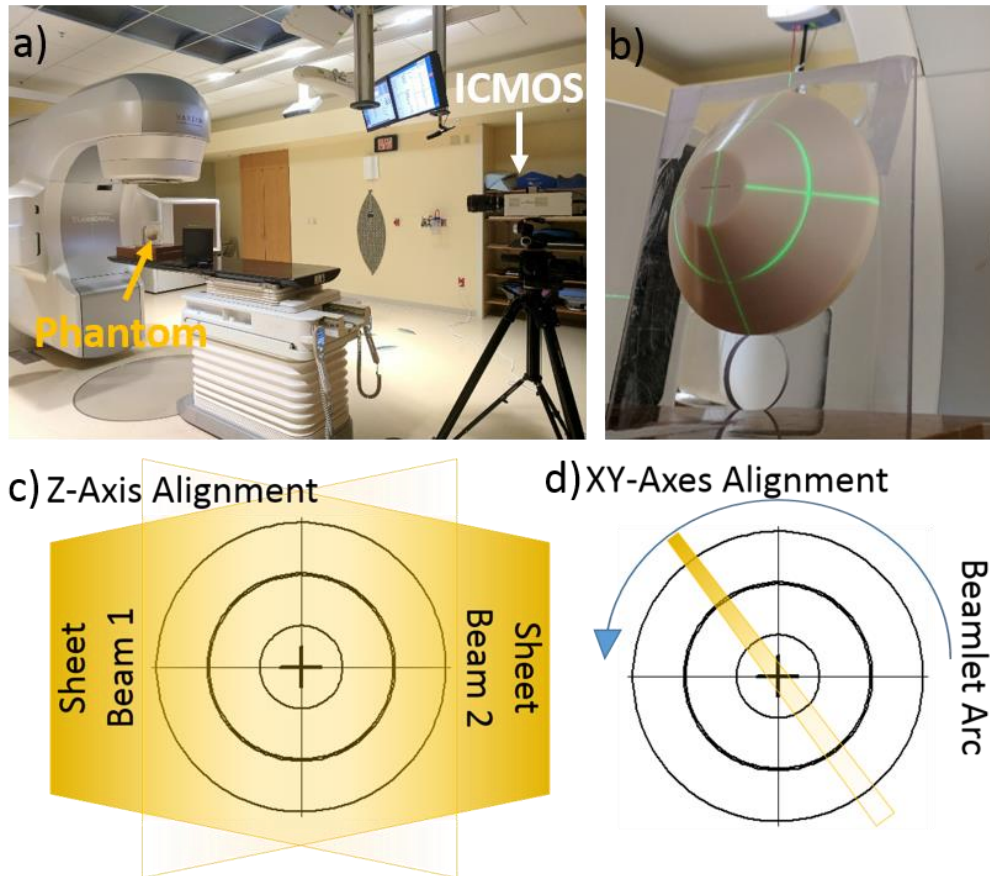


Figure 10.2 a) Imaging setup of prototype phantom on TrueBeam linac with ICMOS camera at foot of treatment couch; b) close up of prototype phantom aligned using treatment room lasers; c) schematic of irradiation scheme for z-axis alignment; d) schematic of irradiation scheme for x-y axes alignment.

The phantom was first aligned using the treatment room lasers to the front face crosshairs and the inscribed alignment ring 2.5cm posterior to the front face, as shown in Figure 10.2 (b). The phantom was then translated in the positive z-direction by 10mm

(couch moving towards the gantry, and the phantom moving further away from the camera). This technique allowed for translation in a single direction between image acquisitions, to minimize error resulting from the mechanical motion of the couch.

The phantom was irradiated and imaged with the two described sheet beams at phantom isocenter +10mm, then translated in the negative z-direction for the remaining couch positions, specified with respect to original alignment with the inscribed ring (+8mm, +4mm, +2mm, +1mm, phantom isocenter, -1mm, -2mm, -5mm, -10mm, -15mm, -20mm); dual sheet beam irradiation and imaging was repeated at each position. A stack of 50 background images was collected at each phantom position along z.

The resulting images were post-processed in MATLAB (Mathworks Inc., Natick, MA). Each image was background subtracted, and then all images associated with the two sheet beams were summed into a single composite image for each gantry position, depicting rings of illumination of increasing diameter on the phantom surface. A minimal bilateral filter was applied to the composite images to smooth out noise while preserving edges. Two-dimensional plots corresponding to the horizontal and vertical ring diameters were extracted from the images, and the intensity maximums were used to pin-point the radiation beam. The ring diameters measured in this method were correlated with the known shifts in the z direction, since the 45 degree cone angle allows for direct translation of the ring diameter to the z-axis shift.

10.2.3 Method for Measuring XY-Alignment

While the premise of the Z-direction localization was predicated by the change in ring diameter as the radiation beams vary on the slanted surface of the cone phantom, the xy-

alignment was designed to be measured through tomographic localization, similar to start shot methods of measuring isocenter coincidence between RT systems and the room lasers. The phantom was again aligned to its inherent isocenter using the crosshairs and inscribed alignment ring, then the treatment couch was used to translate the phantom +20mm, so that the front face of the phantom was in closer proximity to the radiation isocenter.

A 1cmx1cm 6MV FFF beam was imaged delivering 800 MUs of dose over a partial 180° arc over the superior portion of the phantom. The ICMOS was set to perform real-time, on board background subtraction between alternating Cherenkov emission and Cherenkov-free frames at a 1:1 acquisition ratio, where an increased delay from the trigger signal allowed for programmed acquisition of the latter. This is the same principle that was first utilized in Section 4.3 for *in vivo* VMAT patient imaging,⁸⁸ and is necessary to minimize the artifacts introduced by the changing light levels in the room given the dynamic motion of the linac gantry, even with room lights turned off.

Irradiation and imaging were performed in five positions beginning with the xy-alignment origin: (0mm,0mm). The couch was used to translate the phantom to the following positions, where shifts in x are lateral, and shifts in y are vertical: (1mm, 0mm); (1mm,1mm); (0mm,1mm); (0mm,10mm).

Like the z-alignment images, the acquired stacks of xy-alignment images were summed for each position, to form a single composite image for analysis, in post-processing conducted in MATLAB. Each composite image was again smoothed using a minimal bilateral filter. The 2D images were then summed into two 1D plots

corresponding to the rows (to measure vertical or y shift) and to the columns (to measure the lateral or x shift).

For this proof of concept, the intensity peaks for the composite image with the phantom at the alignment origin were used as the measurement reference points to which the pixel locations of the peaks in the subsequent alignment coordinates were compared. Knowledge of the physical pixel resolution, as calculated from the resolution test target image, was used to translate the number of pixels to mm values for an evaluation of technique accuracy.

10.3 Prototype Phantom Results

Analysis of the resolution test target concluded that a single pixel in the optical images represented a 0.17mm x 0.17mm square in physical space at the RT isocenter. The checkerboard in the test target was used to repeatedly calculate the resolution between 40 sample points with known spacing, producing a standard deviation of 0.0007mm and a range of 0.167mm to 0.170mm, indicating high confidence in the measurement.

10.3.1 Results of Z-Axis Alignment Test

The optical images generated at each of the twelve tested translational positions are shown in Figure 10.3. The horizontal and vertical ring diameters measured optically had a strong linear correlation to the known translation distance in the z direction, which is reflected in the two plots of Figure 10.4. The calculated correlation coefficients were $R^2=0.999$ and $R^2=0.998$, respectively, with resolution down to 1mm shifts in z.

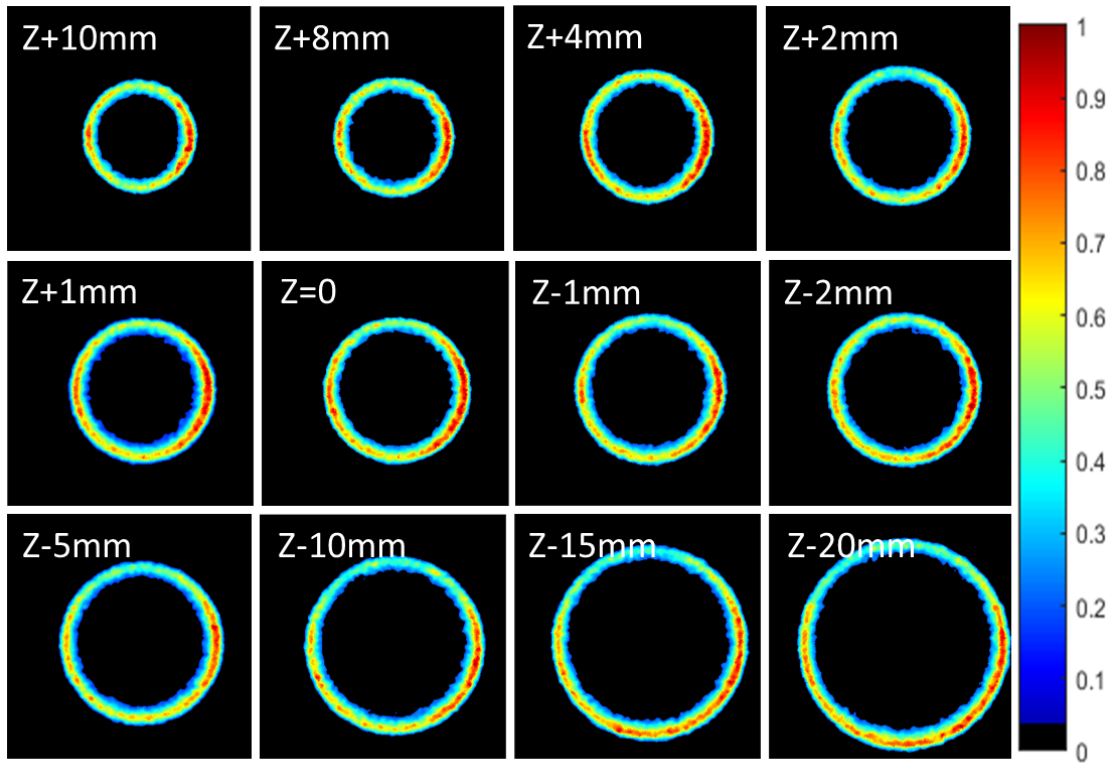


Figure 10.3 Integrated optical images of the prototype phantom irradiated by two tangential sheet beams in each tested position for the z-axis alignment test.

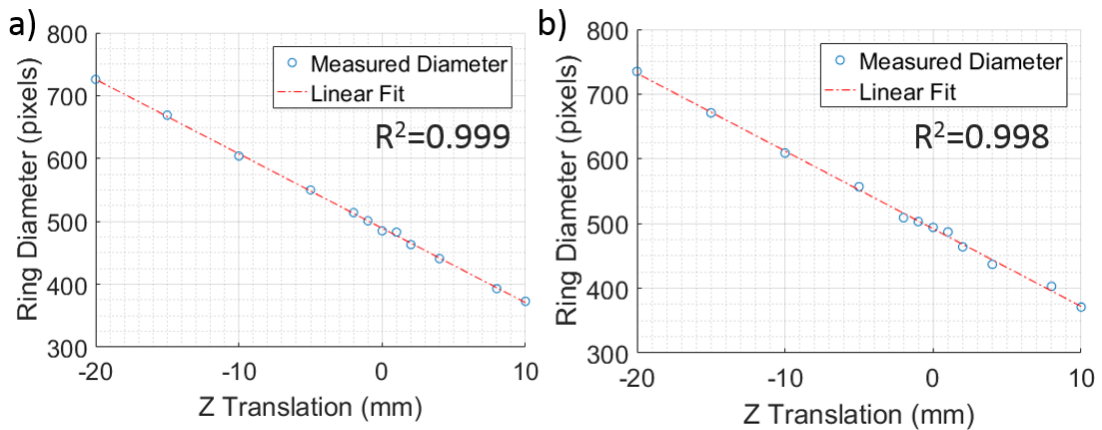


Figure 10.4 Correlation between optically measured ring diameter and known z translation of the phantom measured using the a) horizontal 1D line profiles, and b) vertical 1D line profiles containing the circle centroid.

10.3.2 Results of XY-Alignment Test

The integrated optical images used for the measurement of the radiotherapy isocenter with respect to the phantom geometry are presented in Figure 10.5. The subsequent 1-D integrations of the image intensity across each plane (rows to measure vertical y displacement, columns to measure lateral x displacement) are presented in Figure 10.6.

The maxima of the plots in Figure 10.6 were used to calculate the displacements in x and y. The pixel locations of the maxima when the phantom was positioned at the initial alignment position (Figure 10.5 (e)) were used as the origin from which the shifts in the remaining four imaged positions were calculated. These measurements are summarized in Table 10.1. The observed error in alignment was on average -0.02mm in for the vertical displacement, and -0.03mm in the lateral direction.

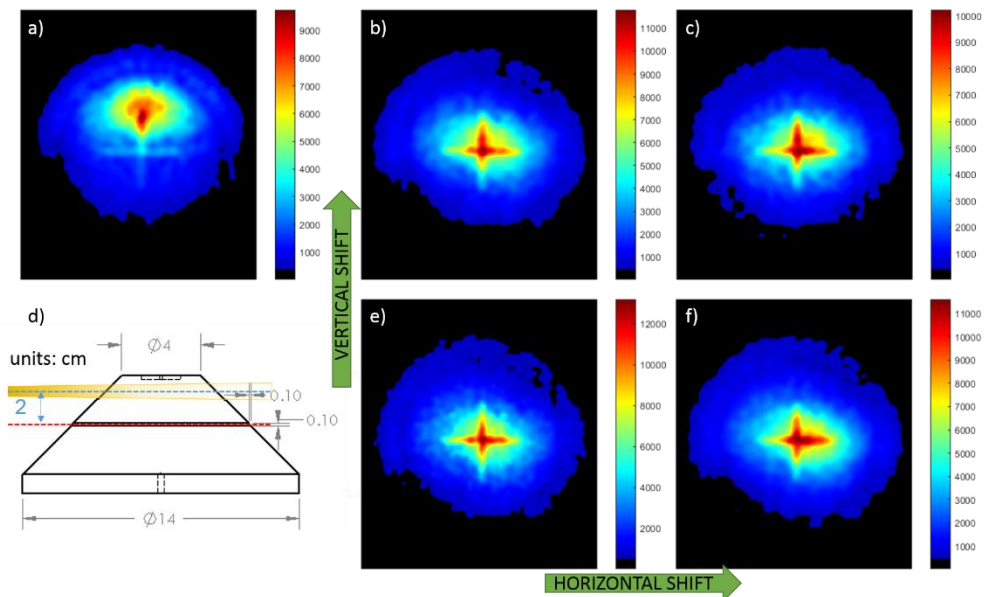


Figure 10.5 Integrated optical images of the beamlet arc across the 180° superior portion of the phantom near its front face for x-y localization. The position of the beamlet with respect to the known phantom geometry is shown in d). a) Image at (0mm,10mm); b) image at (0mm,1mm); c) image at (1mm,1mm); e) image at (0mm,0mm); f) image at (1mm,0mm).

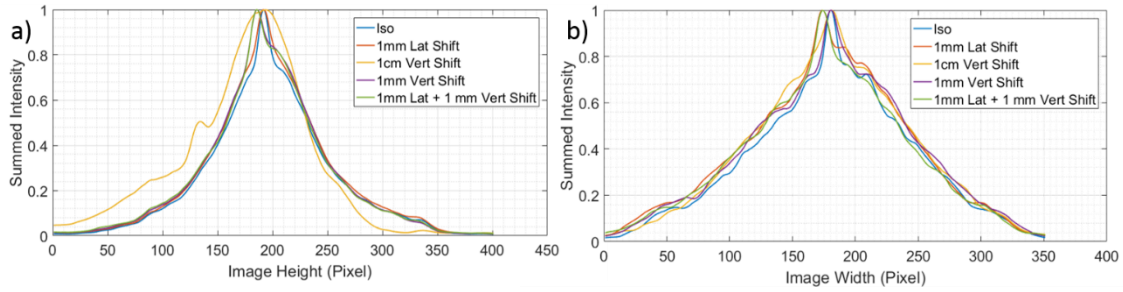


Figure 10.6 Integrated 1D plots of optical image intensity a) along the image rows to measure vertical y displacement, and b) down the image columns to measure lateral x displacement.

Table 10.1 Known and optically measured shifts in the vertical y direction (left) and lateral x direction (right).

Known Vertical Shift (mm)	Measured Vertical Shift (mm)	Error (mm)	Known Horizontal Shift (mm)	Measured Horizontal Shift (mm)	Error (mm)
0.00	0.00	-	0.00	0.00	-
0.00	0.00	0.00	1.00	1.02	0.02
1.00	1.02	0.02	0.00	0.00	0.00
1.00	1.02	0.02	1.00	1.02	0.02
10.00	9.86, 10.02*	-0.14, 0.02*	0.00	-0.17	-0.17

The asterisk marked values in the final row of the table of measured vertical shifts corresponds to using the secondary maxima in the singular 1-D plot for the case of the 10mm vertical shift (yellow plot in Figure 10.6 (a)), as opposed to the (0mm,0mm) reference point. This peak occurs due to the light aggregating at the center of the inscribed alignment crosshairs on the front face on the phantom, which is visible in the associated image Figure 10.5 (a).

10.4 Prototype Phantom Discussion

The results presented in this chapter are the first illustration of the potential of an optical imaging phantom and method for measuring the placement of an RT isocenter with respect to known phantom geometry. Both the z-axis, as well as the x-y alignment methods allow for accurate positioning the of RT isocenter with respect to the central axis of the phantom on at least 1 millimeter level. This is clinically relevant for MR-IGRT applications, where the resolution of the MR images is 1.5mm.

These results also indicate improvements can be made to the methodology, as well. In the z-axis alignment, two tangential sheet beams were used to illuminate the phantom from the left and right. Irradiating at two additional angles originating at the superior and inferior sides of the phantom could further improve accuracy in the vertical measurement of the ring diameter.

The primary improvement to the x-y alignment protocol arises from the placement of the 1cm x 1cm beamlet with respect to the proximal face of the phantom. In the method implemented here, the center of the beam was 0.5cm behind the proximal phantom face. It is possible that increased signal to noise ratio (SNR) in each optical image would be achieved if the center of the beam was aligned directly to the proximal face of the phantom, especially considering the use of FFF beams.

An additional improvement to the setup would be to use a full 360° arc about the phantom, rather than the 180° arc used here. The half-arc accounts for the preferential distribution of the signal in the images shown in Figure 10.5, as the top half of the phantom was the only portion directly irradiated. The 360° arc would require careful

consideration of the placement and positioning apparatus used to secure the plastic phantom, so that the beam is approximately equally attenuated when it reaches the plastic of the phantom. It is important to note, however, that the results as they are for the x-y alignment test correspond to an error of less than a single pixel in the optical images; average errors were only -0.02mm and -0.03mm in each direction, while a single pixel spans 0.17mm.

Overall, these results also only establish the technique for accuracy in measuring the RT isocenter. Further experiments are required to illustrate the phantom accuracy in measuring the position of the MRI isocenter. This will require suspension of the phantom in a water bath to provide an MR detectable media, and the plastic phantom would appear in the negative space of the image volume. Ease of MR localization will be enhanced by hollowing out the phantom from the distal side in a conical fashion leading to a point at the phantom isocenter. This would be easily accomplished by modifying the CAD drawing again capitalizing on the accuracy and precision of CNC milling systems.

Experience imaging both the optical emissions from the Cherenkov Effect that dominate in water, compared to optical scintillation which dominates in plastics, suggest that there will be no problems in achieving adequate SNR between the surrounding water and plastic phantom once the device is placed in a water bath and the irradiations are repeated. Once the phantom design and imaging protocol is finalized, rigorous testing of setup repeatability will be necessary to evaluate system precision.

Finally, the vessel containing the water bath and phantom must be designed to allow for ease in placement of the MRI RF coils above and below the system, while

maintaining visualization of the phantom within the tank. This is a trivial issue to overcome that only requires deliberate forethought to the practicality of the design before final fabrication of the water tank-plastic phantom unit as a whole.

10.5 Prototype Phantom Conclusion

A novel conical phantom was designed, fabricated from ABS plastic, and tested for its potential to measure offsets in the actual versus expected radiotherapy treatment isocenter. This utilized optical imaging techniques, where an IC MOS camera system was placed remotely at the foot of a traditional linac treatment couch to acquire the scintillation signal generated in the plastic phantom upon irradiation with either static sheet beams or an arcing beamlet.

First the z-axis alignment was measured, and the observed illuminated ring diameter correlated strongly with the known translations in z ($R^2 > 0.99$). Likewise, the x-y alignment test produced convincing measurement of the translation of the isocenter within the x-y-plane, with accuracy within 1 pixel in the optical image (0.17mm). Overall, this technique has strong promise to be adapted to the final intended application of easily identifying and quantifying the 3-dimensional physical offsets between the MRI and RT isocenter in state of the art MR-IGRT systems.

Chapter 11: Conclusions and Future Directions

The work presented in this thesis documents novel applications of Cherenkov and optical imaging during radiotherapy. These applications span three main areas: 1) *in vivo* Cherenkov imaging during whole breast irradiation (WBI), 2) *in vivo* and phantom Cherenkov imaging for total skin electron therapy (TSET), and 3) quality assurance Cherenkov imaging for magnetic resonance image guided radiotherapy (MR-IGRT) systems. The wide scope of these applications speaks to the continued promising utility of Cherenkov imaging techniques in the radiotherapy clinic as a whole, and maintains its potential to accomplish niche functions of which other modalities have yet been able to realize.

The innovation that made most of these findings possible was the synchronization of optical image acquisition to the pulsed radiation sources via an image intensifier. This is critical in a patient treatment setting where very controlled radiation doses are being monitored, as opposed to pre-treatment quality assurance situations where dose can be escalated indefinitely, within the time constraints of the operator him or herself. Given this synchronization, patients can be imaged with modest levels of ambient room light with no major detriment to image quality. Regardless, it is still recommended that ambient light levels are minimized as severely as reasonably possible when imaging non-living targets that do not require visual monitoring throughout irradiation, such as in the case of water tank imaging.

Cherenkov imaging, like any other modality, has inherent strengths and weaknesses. First and foremost, the strengths of Cherenkov imaging stem from the fact

that it is the singular known mechanism for visualizing an otherwise invisible ionizing beam interacting directly on the patient surface when entering or exiting the tissue.

The only somewhat comparable modality in this capacity is the electronic portal imaging device (EPID), which captures the transmitted radiation beam after exiting the patient. However, use of the EPID is limited to situations where the additional panel does not present a collision hazard, and it cannot be intrinsically registered to the patient surface the way a Cherenkov image can be, since the same detector is used to capture white light images of the patient during treatment as the radiation deposition images.

Another strength of Cherenkov imaging is that the detector itself is remote, and does not have to perturb the beam or patient to gather the measurement. This allows remarkable flexibility to adapt the technique to capture large fields, small fields, irregular setups such as TSET, and be deemed MR-compatible (since the camera can remain behind the 5-G line of the magnetic field, given a low or well-shielded field). This is augmented by the high resolution of the images acquired (1024 x 1024 pixels or 1200 x 1600 pixels in cameras used for this work). The physical size of each pixel in a Cherenkov image will relate to the experimental imaging setup, particularly the distance between the camera and the subject, the specific camera lens, and post-processing techniques applied to the images; representative values range from 0.17 mm/pixel – 0.35 mm/pixel.

The last general strength of Cherenkov imaging is that at conventional therapeutic radiotherapy beam energies, the optical signal will always be present in tissue, water, and plastics (albeit plastics are dominated by optical scintillation). This means there is not an essential disposable device, applique, or patient-specific cost-driving resource required

outside of general camera maintenance. The Cherenkov imaging system can operate like a fly on the wall, without the need to alter patient treatments in any way to acquiesce its utility.

The weaknesses that arise from Cherenkov imaging center predominantly on the efficiencies in collecting the generated optical photons. While the number of Cherenkov photons generated has unequivocally been demonstrated as linearly proportional to deposited dose, the number of optical photons that make it to the detector from any given point in space is reliant on several known factors: 1) the tissue optical properties of any materials those photons must traverse, which is typically not uniform, 2) the directionality of the photons when they are generated (and whether there is a scattering medium present), and 3) the curvature of the emitting surface with respect to the position of the optical axis.

There are also intrinsic factors of the irradiation setup that will impact the observed Cherenkov intensities that should be known for proper interpretations of Cherenkov images. Namely, these are: 1) the beam energies used, since higher energies produce more Cherenkov photons, and 2) the orientation of the radiation beam with respect to the optical imaging axis, to discern the variations in intensity consequent of the ionizing radiation entering or exiting tissue. It can be noted, however, that energy and directional dependence of radiation detectors is not a disadvantage unique to Cherenkov imaging; film, diodes, and even ionization chambers can be influenced by effects of beam energy and orientation.

The final encountered weakness of Cherenkov imaging is the variability of the quantitative data between imaging geometries and image processing approaches. Consistency of response between experiments, researchers, and one day clinicians, will require rigid protocols and frequent quality control practices. In terms of image processing, clinically adopted conventions should be tested for repeatability, while research efforts can be more open to investigative methods of filtering, smoothing, and noise reduction.

The work of this thesis strove to develop methods that exploited the strengths of Cherenkov imaging and minimized the impact of its weaknesses. These endeavors have culminated in the following observations and recommendations for future work, arranged with respect to the three primary categories of application.

11.1 *In vivo* Cherenkov Imaging of Primarily Whole Breast Irradiation

The bulk of patients imaged and studied in this thesis exploring the potential of *in vivo* Cherenkov imaging were undergoing WBI. This was because of the design of the internal review board-approved clinical study protocol, based on the fact that there is a large throughput of patients in this category receiving relatively similar treatments. However, the basic concepts elucidated by this research are applicable to most other conventional treatments in external beam therapy.

Complications can arise when bolus materials or patient positioning devices are within the beam path, but this predominantly affects the observed optical intensities (thereby dosimetric potential), and not the ability to capture the beam footprint. The work documented in Section 4.3 concerning the imaging two head and neck VMAT

patients, both restrained with plastic face masks, successfully produced the first ever real-time VMAT patient imaging videos on both the patient skin and the restraining masks, despite the obstruction.

Given the strength of Cherenkov imaging as a real-time beam-monitoring modality, the most immediately achievable, realistic application of the technology is treatment verification, for which is a clinical product being actively pursued. The more distant goal, not currently attainable, is *in vivo* relative or absolute surface dosimetry (with the former being more pragmatic than the latter). However, future work in this area may make this objective realizable.

The dominant obstacle in surface dosimetry is tissue optical property variation in the very non-homogeneous, very non-flat, living subjects. Methods of approximating superficial tissue optical properties using IR reflectance images were explored in this work, but ultimately deemed inadequate for patient imaging. The more promising technique is the use of structured light imaging to measure and approximate surface tissue optical properties, so that a spatially resolved correction map can be constructed that translates the detected Cherenkov intensity to relative dose. Once this approach is more thoroughly vetted, and a method to take into account the intensity differences between entrance and exit dose captured in a single image from a ceiling mounted camera is realized, comparisons between different patients can be computed to determine the viability of absolute *in vivo* surface dosimetry.

11.2 *In vivo* and Phantom Cherenkov Imaging for Total Skin Electron Therapy

Just as was the case for the WBI and VMAT patients documented above, *in vivo* Cherenkov imaging of patients undergoing TSET is mostly valuable as a treatment verification tool. The combination of gross variations in subdermal tissue optical properties which result from the bulk distributions of adipose, muscle, bone and vasculature under the skin surface, along with the very superficial lesions and areas of disease, make surface dosimetry based purely on the Cherenkov images, or even Cherenkov images in combination with diagnostic CT scan information, impractical.

Nevertheless, in the research context, a qualitative evaluation of patient images in the clinic where the study was conducted did lead to the subsequent realization that the prescribed TSET protocol was not optimized to provide the most homogeneous dose distribution possible. The TSET geometry optimization technique described in this thesis is an acute example of the flexibility of the technique, where relative dosimetry was possible on the flat, homogeneous phantom spanning the entire 1m x 2m treatment region. This application is perhaps a hallmark role for Cherenkov imaging as a technology, since no other current methods can accomplish this goal with the same resolution and time efficiency.

Cherenkov imaging of TSET patients has also paved the way towards remote scintillator-based optical dosimetry using the same imaging systems. This technique uses small, thin discs of known scintillator material (without the complication of heterogeneous optical properties) that can be affixed gently to the patient skin and imaged to report dose in real-time. Unlike currently adopted methods of surface

dosimetry, this process eliminates the need for cumbersome wires, lengthy read-out protocols, and meticulous detector tracking that could lead to the inadvertent loss of data.

11.3 Quality Assurance Optical Imaging for MRI Integrated Radiotherapy Systems

Once again exploiting the remote, real-time acquisition of the optical signals generated by radiotherapy beams, rapid quality assurance (QA) tests of MR-IGRT systems is a distinctive application of Cherenkov imaging. Optical imaging has been demonstrated as independent of the primary magnetic field, as well as the associated RF noise requisite of the MRI. Even so, it is able to capture information regarding the effects of the magnetic field on dose deposition within water and plastics.

The initial application of Cherenkov imaging to MR-IGRT systems sought to generate optical-signal based percent depth dose curves (PDDs) and cross beam profiles (CBPs). These have been successfully measured with the caveat that they represent the integrated projection of these values along the optical axis, through the width of the water tank. For this reason, it is suggested that Cherenkov projection PDDs and projection CBPs be compared to the simulated dose of the treatment planning system, and not simply point measurement-based PDDs like those generated from ionization chamber measurements.

As such, Cherenkov imaging will not be able to replace conventional QA methods completely. It has still only been demonstrated in the capacity of relative dosimetry, and uncertainty in the interpretation of the position of the water line requires registration to the conventional or simulated curves to solidify depth information in the Cherenkov

emission-based curves. It can, however, offer an enticing alternative to baseline-comparison QA tests performed weekly or monthly, which present as much more time consuming on MR-IGRT systems with limited MR-compatible techniques and tools.

Further studies should be conducted to prove that the Cherenkov imaging method is capable of discerning the problems of primary concern from these QA tests (for example, fluctuating beam energy spectra in linac-based RT systems). This would augment the documentations to date, which only establish the feasibility and premise in commissioned, maintained, QA-passing scenarios.

An additional application of optical imaging was devised with the intent to simplify the problem of identifying the coincidence of both the MRI and RT isocenters in combined systems. While the preliminary proof of concept study has thus far only been conducted on a conventional medical linac, the results are encouraging. Both the resolution and technical feasibility of the method has been established, and further fine tuning could result in a useful, thoughtfully engineered phantom and protocol. The growing interest and activity in commissioning of MR-IGRT systems worldwide advocates the continued development of such devices that can easily translate to the clinic and fulfil a relevant need to simplify currently extensive endeavors.

In fact, since dosimetric information is not a goal of this process (purely localization is required), careful choice of a highly scintillating material, as opposed to ABS plastic, for the phantom construction could allow for adequate imaging from much cheaper, non-intensified CCD or CMOS cameras. This would drive down the cost significantly, and make the method accessible to more clinics.

Expanding the application of Cherenkov imaging to *in vivo* imaging of patients undergoing treatment on MR-linacs is not as straightforward as patient imaging on traditional linacs. First, the view of the patient is physically limited by the bore of the MRI, meaning mirrors or imaging fibers would have to be used to relay the optical image to a camera outside the bore. In addition, the requisite use of the large, padded RF coils above and below the patient implies much of the patient surface of interest would be physically covered, and limit the practicality of the approach. Therefore, applications in QA hold more merit with current capabilities and restrictions.

11.4 Final Remarks

The radiotherapy clinic is an extraordinary paragon of physics applied to biology that inevitably compels and promotes highly translational research opportunities. Cherenkov imaging is poised to become a prime example of the bench-to-bedside research model as the applications described herein are perfected and expanded. This was already observed locally, where the results of the Cherenkov imaging-based TSET optimization study were used to inform the adopted clinical treatment protocol.

The medical field is a very human-driven arena. Exceptional patient care and improved prognoses are undeniable motivators for those that find themselves in any aspect of the discipline. However, unintentional human error is a harsh reality of patient treatment, and tools with the potential to mitigate such problems should be scrutinized. Treatment verification with Cherenkov imaging is a relatively straightforward process that has the promise to help identify and interrupt errors in delivery, both human-derived and technical.

Even ignoring the dosimetric potential of optical imaging techniques, the ability to verify ionizing radiation beam placement on patient surfaces using only a remote camera system to capture essentially free information should be regarded as highly valuable. When this technology becomes more widely adopted in the clinic, it will be possible to more confidently report the incidence and implications of radiotherapy dose delivery errors, and subsequently bolster trust of practitioners in the field.

Appendix

The utility of Cherenkov imaging techniques is inherently dependent on the ability to extract meaningful information from the raw image data. This necessitates the application of several image-processing techniques, which for this work, have largely been applied through post-processing in MATLAB (Mathworks Inc., Natick, MA, USA). This appendix is intended to document the generic image-processing workflow, and show examples of the implementations in MATLAB.

A.1 Salt-and-Pepper Noise Removal

Stray radiation hitting the red and near-infrared sensitive ICCD camera system produces random, speckled, high intensity salt-and-pepper noise within each image frame. Removal of this noise is typically the first step in image processing. The most basic application is applying a temporal median filter over the entire, static-beam image stack. In cases where the dynamic or dosimetric features need to be preserved, this is more aptly achieved using a rolling temporal median filter over 5-15 subsequent frames. Smaller groups of frames are used for data acquired with slower frame rates (<10 frames per second, or fps), and larger groups of frames are sometimes needed for high frame-rate data, where the noise spots persist across more frames in sequence, as there are more frames per set time interval.

The following function *rollmed.m* can be used to perform the rolling median filter and concurrent background subtraction and flatfield image correction on an image stack. The flatfield image is acquired under uniform illumination of the camera sensor, to correct for the heterogeneities in sensitivity of the camera system on a pixel-by-pixel basis.

```

function [ sumCh, filstack ] = rollmed( Chkin, bkg, window,
flatfieldim )
%Takes in stack of raw Cherenkov images, performs rolling
temporal median filter of size window, and returns the
background subtracted, flatfield-corrected sum and image
stack

%Input variables:
%      Chkin: Input stack of raw Cherenkov images
%      bkg: Single frame of background for subtraction
%      window: Number of concurrent frames over which
%              to perform the operation
%      flatfieldim: flatfield image under uniform
%                    sensor illumination to correct for sensor
%Output variable:
%      sumCh: Singular, salt-and-pepper noise-removed,
%              background subtracted, integrated Cherenkov image
%      filstack: Filtered stack of noise-removed,
%                 background subtracted Cherenkov images

for ii=1:(size(Chkin,3)-window)
    filstack(:, :, ii)=(median(Chkin(:, :, ii:ii+window), 3)-
bkg)./flatfieldim;
end
sumCh=(sum(filstack, 3));

end

```

A.2 Shot Noise Removal and Image Smoothing

In most cases, additional image filtering is necessary to remove the fluctuations in intensity attributed to shot noise, given the relatively low Cherenkov photon count involved in this type of imaging. This can be accomplished through smoothing with a simple spatial median filter, using the built in MATLAB function $imOut = medfilt2(imInput, [m,n])$. This function takes the input image $imInput$, and a given kernel size $[m,n]$, and performs the spatial median filter. Typical kernel sizes vary between $[3,3]$ to $[11,11]$, with smaller kernels being preferred for this type of smoothing.

When edge-data is of importance, in the case of finding beam edges or beam energy features such as the build-up region of a percent depth dose curve, a bilateral filter is recommended over a large kernel ($m, n > 3$) spatial median filter. The implementation of the bilateral filter used in this research was acquired from the MATLAB file exchange: `imOut = bfilter2(imInput, W, [SIGMA_spatial, SIGMA_intensity])`.¹⁹⁸ A 2D bilateral filter is applied to the normalized, grayscale input image *imInput*, with Gaussian half-size window *W*, and standard deviations in space and intensity defined by input variables *SIGMA_spatial* and *SIGMA_intensity*. A conservative bilateral filter in this application was implemented using the following inputs: `imOut=bfilter2(imInput,3,[3 .1])`; a more aggressive bilateral filter was implemented in some cases with the following inputs: `imOut=bfilter2(imInput,11,[11 ..3])`. If the input image is not normalized, larger filter parameters would be suitable.

A.3 TSET Optimization Code

```
%05/11/2016 - Jacqueline Andreozzi

%This code analyzes images of a large polyethylene sheet
set in the TSET treatment plane, to determine the angle
pair which produces the least amount of dose variation.
Data acquired on 5/10/2016 at WashU on a Varian Trilogy
linac. 6MeV and 9MeV beams were imaged, with and without
1cm thick transparent spoiler, at SSD=300cm. The 6MeV beam
was also imaged at SSD=340cm, as well as with a collimator
rotation of 45 degrees.
%~~~~~
~~~~~
close all
clear
map=jet;
map(1,:)=[0,0,0];
%Read in image of beam at 270 as reference image
im270=median(double(readSPE('6MeV_270.spe')),3);
```

```

bkg270=median(double(readSPE('bkg_270.spe')),3);
refim=im270-bkg270;
refim=medfilt2(refim,[11,11]);
refthr=refim/max(refim(:));
levelref=find(refthr<.5);
refthr(levelref)=0;
figure
imagesc(refthr)
colormap(map)
axis image
axis off
%Average 20 lines near center column to get vertical
profile
vertline=mean(refim(:,450:470,1),2);
f=fit([1:1024]',vertline,'gauss1');
vertcent=round(f.b1);
%Use location of maximum on vertical profile as horizontal
treat midline
midline=mean(refim(vertcent-10:vertcent+10, :, 1), 1);
x=[1:1024]';
exclude1=x<250;
exclude1(665:end)=1;
fm=fit(x,midline','gauss1','Exclude',exclude1);

halfmax=fm.a1/2; %Half of profile midline for FWHM
diff=abs(midline-halfmax); %Take absolute value on
horizontal midline minus the half max value.
leftbound=round(find(diff(1:512)==min(diff(1:512)))));
%First minimum (0 crossing) is first boundary
rightbound=round(511+find(diff(512:1024)==min(diff(512:1024
))))); %second minimum (0 crossing) is second boundary
wid=rightbound-leftbound; %Width for plotting rectangle on
image

len=850; %Choose how many pixels to use in vertical
direction
topbound=round(vertcent-len/2); %Choose ROI to span +/- the
midline;
botbound=round(vertcent+len/2);

%Set up array of angle designations
ind1=linspace(240,260,21);
ind2=linspace(300,280,21);
ind=[ind1 ind2];
spreads=(ind2-ind1);
imOut=zeros(1024,1024,size(ind,2));
%Read in all Cherenkov images
for n=1:size(ind,2)

```

```

    %Clear previous im and bkg to save memory
    clear im
    clear bkg
    %Read in data from each angle, take temporal median,
and subtract bkg
    im=median(double(readSPE(['6MeV_' num2str(ind(n))
'.spe'])),3);
    bkg=median(double(readSPE(['bkg_' num2str(ind(n))
'.spe'])),3);
    imOut(:, :, n)=im-bkg;
    imOut(:, :, n)=medfilt2(imOut(:, :, n), [11,11]);
end

sta=size(ind,2);
count=1;
for n=1:(sta/2)
    for m=1:sta
        clear roi
        imadd(:, :, 1, count)=imOut(:, :, n)+imOut(:, :, m);

        roi=imadd(topbound:botbound, leftbound:rightbound, cou
nt);
        roithr=roi/max(roi(:));
        level=find(roithr<.9);
        roithr(level)=0;
        roit(:, :, 1, count)=roithr;
        roi2=roit(:, :, 1, count);
        roi3=roit(find(roit>0));
        avgroi(count)=[mean(roi(:))];
        stdroi(count)=[std(roi(:))];
        cov(count)=[stdroi(count)/avgroi(count)];
        ref(count,1)=ind(n);
        ref(count,2)=ind(m);
        ref(count,3)=cov(count);
        ref(count,4)=abs(ref(count,1)-ref(count,2));
        cov2(count)=[std(roi2(:))/mean(roi2(:))];
        cov3(count)=[std(roi3(:))/mean(roi3(:))];
        ref2(count,1)=ind(n);
        ref2(count,2)=ind(m);
        ref2(count,3)=cov2(count);
        ref2(count,4)=cov3(count);
        count=count+1;
    end
end

for n=1:length(cov)
    ref(n,4)=abs(ref(n,1)-ref(n,2));

```

```

end
locofmin=find(cov==min(cov(:)));
locofmin2=find(cov2==min(cov2(:)));
[ref3, indexref]=sortrows(ref2,3);
smallest=indexref(1:24);

figure(2)
suptitle('Vertical Profile (midline)')
figure(3)
suptitle('Horizontal Profile (midline)')

for ii=1:length(smallest)
    clear pks locs fh invrt locw oh
    smallestadd(:, :, 1, ii)=imadd(:, :, 1, smallest(ii));
    smallestthresh(:, :, 1, ii)=roifit(:, :, 1, smallest(ii));
    smallestvert(:, ii)=mean(smallestthresh(:, round(fm.b1)-
leftbound-10:round(fm.b1)-leftbound+10, 1, ii), 2);
    figure(1)
    plot(smallestvert(:, ii))
    [locs, pks]=ginput(2);
    locs=round(locs);
    smheight(ii)=locs(2)-locs(1);

    flatnessvert(ii)=100*(max(smallestvert(locs(1)+10:locs(2)-
10, ii))-min(smallestvert(locs(1)+10:locs(2)-
10, ii)))/(max(smallestvert(locs(1)+10:locs(2)-
10, ii))+min(smallestvert(locs(1)+10:locs(2)-10, ii)));

    maxvarvert(ii)=100*(max(smallestvert(locs(1)+10:locs(2)-
10, ii))-min(smallestvert(locs(1)+10:locs(2)-
10, ii)))/(max(smallestvert(locs(1)+10:locs(2)-10, ii)));
    smallesthor(:, ii)=mean(smallestthresh(round(f.b1)-
topbound-10:round(f.b1)-topbound+10, :, 1, ii), 1);
    fh=smallesthor(:, ii)-max(smallesthor(:, ii))/2;
    [locw, ph]=find(fh>0);
    smwid(ii)=length(locw);

    flatnesshor(ii)=100*(max(smallesthor(locw(1)+10:locw(end)-
10, ii))-min(smallesthor(locw(1)+10:locw(end)-
10, ii)))/(max(smallesthor(locw(1)+10:locw(end)-
10, ii))+min(smallesthor(locw(1)+10:locw(end)-10, ii)));

    maxvarhor(ii)=100*(max(smallesthor(locw(1)+10:locw(end)-
10, ii))-min(smallesthor(locw(1)+10:locw(end)-
10, ii)))/(max(smallesthor(locw(1)+10:locw(end)-10, ii)));
    figure(2)
    %suptitle('Vertical Profile (midline)')
    subplot(5, 5, ii)

```

```

    plot(smallestvert(:,ii))
    title([num2str(ref3(ii,1)) '^{\circ} & '
num2str(ref3(ii,2)) '^{\circ}'])

    figure(3)
    %suptitle('Horizontal Profile (midline)')
    subplot(5,5,ii)
    plot(smallesthor(:,ii))
    title([num2str(ref3(ii,1)) '^{\circ} & '
num2str(ref3(ii,2)) '^{\circ}'])

end

figure
scatter(smwid,smheight)
xlabel('Beam Width at Midline (pixels)')
ylabel('Beam Height at Midline (pixels)')
a = [1:size(smallest,1)]'; b = num2str(a); c = cellstr(b);
dx = 0.5; dy = 0.5; % displacement so the text does not
overlay the data points
text(smwid+dx, smheight+dy, c);
title('Beam Height vs. Beam Width at Midline')

figure
scatter(flatnesshor,flatnessvert)
xlabel('Flatness of Horizontal Midline (%)')
ylabel('Flatness of Vertical Midline (%)')
dx = 0.01; dy = 0.01; % displacement so the text does not
overlay the data points
text(flatnesshor+dx, flatnessvert+dy, c);
title('Height Flatness vs. Width Flatness at Midline')

figure
montage(smallestthresh,'Size',[5,5])
colormap(map)
figure
montage(smallestadd,'DisplayRange',[[]])
colormap(map)

figure
hold on
h1=scatter(cov,avgroi,30,'o','b','filled',
'HandleVisibility','off')
xlabel('Coefficient of Variation','FontSize',16)
ylabel('Mean Cherenkov Intensity (A.U.)','FontSize',16)
xlim([0.08 0.2])

```

```

figure
plot(midline)
xlim([0 1024])
ylim([0 max(midline)])
xlabel('Position')
ylabel('Cherenkov Intensity (A.U.)')
line([leftbound leftbound],[0 max(midline)], 'Color','r')
line([rightbound rightbound],[0 max(midline)], 'Color','r')

figure
plot(vertline)
xlim([0 1024])
ylim([0 max(vertline)])
xlabel('Position')
ylabel('Cherenkov Intensity (A.U.)')
line([vertcent vertcent],[0 max(vertline)], 'Color','r')

figure
hold on
scatter(ref(:,4),cov)
ax=gca;
ax.XTick=linspace(20,60,21);
title({'Coefficeint of Variation vs Angle Spread'; '6MeV, No Spoiler'})
xlabel('Angle Spread (degrees)')
ylabel('CoV (unitless)')

% Grouping all variables of interest into one matrix; used
% for calculation of the optimization metric for each case
allvar=cat(2,ref3(1:24,:),flatnesshor',flatnessvert',maxvarhor',maxvarvert',smwid',smheight');

```

A.4 Registration of Quality Assurance Curves

The nature of the quality assurance data provided by Cherenkov imaging is not yet absolute, but relative. With current acquisition and analysis techniques, the data does not provide a clear indication of the singular pixel where the depth of maximum dose is reached, nor the pixel location of physical feature of the water line due to ambiguity in viewing the meniscus. As such, the projection percent depth dose curves (pPPDs) and

projection cross beam profiles (pCBPs) require registration to known data, typically from the treatment planning system (TPS) or a previous iteration of the Cherenkov imaging method, to evaluate likeness.

Registration of the data occurs in two main steps after the data is processed and normalized. First, registration in the x-direction occurs using the entire pPDD curve produced in the image. The function below named *msshift3()* completes this task by translating the Cherenkov pPDD with respect to the TPS pPDD, and computing the mean square error for each iteration; the least mean square error case is then used to identify the rows of pixels constituting the water line and the depth of maximum dose. For a bulk dataset with many beam sizes imaged in the same experimental setup, this step should return the same “start” pixel between setups.

Similarly, the second step is registration in the y-direction. In situations where beam hardening can be ignored, such as the case with bi-energetic cobalt-60 radiation sources, the registration process can focus on minimizing error at extended depths (4+ cm), as opposed to the more error-prone, high-gradient buildup region. Otherwise, the least mean square error over the entire curve (starting at the pixel identified in the x-registration process above) can be iteratively calculated. This is accomplished in the function below *msshifty3()*, by applying increasing, percentage-based shifts in the y-direction and calculating the mean square error.

```

function [ out] = msshift3( tps,tpsx, Chpdd,pddstartin,
res, fignum )
%This function performs iterative calculations of mean
square and chi-squared error metrics between x-direction
moving Cherenkov PDD curve with respect to the target TPS
PDD.
% Input Variables:
%   tps: PDD data from the treatment planning system
(static data)
%   tpsx: x axis for the TPS PDD, in cm
%   Chpdd: 1-D PDD plot extracted from the Cherenkov image
%   pddstartin: initial guess at the starting pixel/row for
the water line in the Chpdd
%   res: Cherenkov pixel resolution, in cm
%   fignum: figure number to display results
%Output variables:
%   out:[9,3] output containing each iterative pdd start
pixel (first column),
%   calculated mean square error (second column), and chi-
squared error (third column) for that case

av=10;
count=1;

for ii=pddstartin:pddstartin+8
    pddstart=ii;
    pddtest=(Chpdd(pddstart:1024));
    xaxpdd=res*[0:1:length(pddtest)-1]; %res in cm
    npddtest=pddtest/max(pddtest(:));
    figure(fignum)
    hold on
    subplot(3,3,count)
    hold on
    plot(tpsx,tps, '.', 'Color', 'm')
    plot(xaxpdd,npddtest, 'Color', 'b')
    xlabel('Depth (cm)')
    ylabel('Normalized Dose/Intensity')
    title(['Pddstart = ' num2str(pddstart)])
    xlim([0 20])
    grid on
    for nn=1:(size(tpsx,1))
        val(nn) = tpsx(nn); %depth to find
        tmp = abs(xaxpdd-val(nn));
        [idx loc] = min(tmp); %index of closest depth value
        closest(nn) = loc; %closest depth value
        clear idx tmp
    end
    resid=(tps-npddtest(closest));

```

```

scatter(tpsx,resid,'o')
diffsq=resid.^2;
chisq=sum((diffsq(2:end-1)./tps(2:end-1)));
ms=sum(diffsq)/(size(diffsq,1));
out(count,1)=pddstart;
out(count,2)=ms;
out(count,3)=chisq;
count=count+1;

```

end

```

function [ out, resid ] = msshifty3( tps,tpsx, Chpdd,
Chxax, fignum )
%This function performs iterative calculations of mean
square and chi-squared error metrics between y-direction
moving Cherenkov PDD curve with respect to the tartget TPS
PDD.
% Input Variables:
% tps: PDD data from the treatment planning system
(static data)
% tpsx: x axis for the TPS PDD, in cm
% Chpdd: 1-D PDD plot extracted from the Cherenkov image,
already
% registered in the x direction to the TPS PDD
% Chxax: x axis for the Cherenkov PDD, in cm
% fignum: figure number to display results
%Output variables:
% out:[9,2] output containing each iterative pdd start
pixel (first column),
% and calculated mean square error (second column) for
that case
% resid: [aa,9] matrix containing all of the residual
error values for
% the given iteration, where aa is the length of the TPS
PDD vector

av=10;
count=1;
percshift=-.0025; %In decimal format
for ii=0:8
pddstart=ii;
pddtest=(Chpdd);
pddtest=pddtest-percshift*ii; %Step vertical by certain
percentage
xaxpdd=Chxax; %res in cm
figure(fignum)

```

```

hold on
subplot(3,3,count)
hold on
plot(tpsx,tps, '.', 'Color', 'm')
plot(xaxpdd,pddtest, 'Color', 'b')
%axis([0,100,-.3,1])
xlabel('Depth (cm)')
ylabel('Normalized Dose/Intensity')
title(['Percent of Vertical Shift = '
num2str(ii*percshift*100) '%'])
xlim([0 14])
ylim([-0.05 1.05])
grid on
for nn=1:(size(tps,1))
    val(nn) = tpsx(nn); %depth to find
    tmp = abs(xaxpdd-val(nn));
    [idx loc] = min(tmp); %index of closest depth value
    closest(nn) = loc; %closest depth value
    clear idx tmp
end
resid(:,count)=(tps-pddtest(closest));
scatter(tpsx,resid(:,count), 'o')
diffsq=resid(:,count).^2;
chisq=sum((diffsq(2:end-1) ./ tps(2:end-1)));
ms=sum(diffsq) / (size(diffsq,1));
out(count,1)=ii*percshift*100;
out(count,2)=ms;
count=count+1;

end

```

A.5 Image Registration and Gamma Index Analysis

Performing 2-D gamma index analysis on the Cherenkov data first requires image registration between two or more imaging modalities. Only rigid registration transformations were permitted (scaling, translation, and rotation), and the Cherenkov image was always treated as the moving image; the TPS dose projection image was the typical target image. Rigid, intensity-based registration was performed using the following MATLAB function, included in the image processing toolbox:

```
moving_reg = imregister(moving,fixed,transformType,optimizer,metric),
```

where *moving_reg* is the output, registered Cherenkov image, given the input Cherenkov image *moving*, and TPS dose image *fixed*. The variable *transformType* is set to 'similarity' to allow the operations of scaling, translation, and rotation, and the following are typical starting-point declarations of the *optimizer* and *metric* parameters, which can then be adjusted if the function does not converge to an acceptable answer:

```
[optimizer, metric] = imregconfig('multimodal');  
optimizer.MaximumIterations=750;  
optimizer.InitialRadius = 0.009;  
optimizer.Epsilon = 1.5e-4;  
optimizer.GrowthFactor = 1.1;
```

Once the two images are registered, gamma index analysis could be performed.

This was carried out using an implementation of the formalism originally described by Low et al.,¹⁹⁹ available freely in an online repository authored by M. Geurts as a function called *CalcGamma()*.²⁰⁰ An example of the implementation of this function is provided below. Note that if the images are already registered and the same size, *widA=widB*.

```
reference.width=[widA widA]; %Ref image pixel size (mm)  
reference.start=[0 0];%Ref image pixel start designation  
reference.data=TPS_image; %Ref image data  
target.width=[widB widB]; %Target image pixel size (mm)  
target.start=[0 0];%Target image pixel start designation  
target.data=Chk_image; %Target image data  
percent=3; %Gamma index percent qualifier (3%/3mm)  
dta=3; %Distance to agreement (mm)  
local=0;  
gamma = CalcGamma(reference, target, percent, dta);
```

References

- ¹ R. Baskar, J. Dai, N. Wenlong, R. Yeo, and K.-W. Yeoh, "Biological response of cancer cells to radiation treatment.," *Front. Mol. Biosci.* **1**(November), 24 (2014).
- ² P.A. Cerenkov, "Visible radiation produced by electrons moving in a medium with velocities exceeding that of light," *Phys. Rev.* **52**(4), 378–379 (1937).
- ³ I.M. Frank and I. Tamm, "Coherent visible radiation of fast electrons passing through matter," *C. R. Acad. Sci. URSS* **14**, 109–114 (1937).
- ⁴ J. Jelley, *Cerenkov radiation and its applications* (Pergamon Press LTD., London, 1958).
- ⁵ R. Zhang, J.M.J.M. Andreozzi, D.J.D.J. Gladstone, *et al.*, "Cherenkov based patient positioning validation and movement tracking during post-lumpectomy whole breast radiation therapy.," *Phys. Med. Biol.* **60**(1), L1–L14 (2015).
- ⁶ P.A. Cerenkov, "Visible light from pure liquids under the impact of γ -rays," *C. R. Acad. Sci. URSS* **2**, 451–457 (1934).
- ⁷ A.K. Glaser, R. Zhang, D.J. Gladstone, and B.W. Pogue, "Optical dosimetry of radiotherapy beams using Cherenkov radiation: the relationship between light emission and dose.," *Phys. Med. Biol.* **59**(14), 3789–811 (2014).
- ⁸ A.K. Glaser, J.M. Andreozzi, S.C. Davis, *et al.*, "Video-rate optical dosimetry and dynamic visualization of IMRT and VMAT treatment plans in water using Cherenkov radiation.," *Med. Phys.* **41**(6), 062102 (9 pp.) (2014).
- ⁹ R. Zhang, A.K. Glaser, J. Andreozzi, *et al.*, "Beam and tissue factors affecting Cherenkov image intensity for quantitative entrance and exit dosimetry on human tissue," *J. Biophotonics* **10**(August), 645–656 (2016).
- ¹⁰ J.M.J.M. Andreozzi, R. Zhang, A.K.A.K. Glaser, L.A.L.A. Jarvis, B.W.B.W. Pogue, and D.J.D.J. Gladstone, "Camera selection for real-time in vivo radiation treatment verification systems using Cherenkov imaging," *Med. Phys.* **42**(2), 994–1004 (2015).
- ¹¹ S.L. Jacques, "Optical properties of biological tissues: a review.," *Phys. Med. Biol.* **58**(11), R37-61 (2013).
- ¹² R. Zhang, *Cherenkov Imaging and Biochemical Sensing in vivo During Radiation Therapy* (2015).
- ¹³ I. V. Meglinski and S.J. Matcher, "Quantitative assessment of skin layers absorption and skin reflectance spectra simulation in the visible and near-infrared

- spectral regions,” *Physiol. Meas.* **23**(4), 741–753 (2002).
- ¹⁴ S. Agostinelli, J. Allison, K. Amako, *et al.*, “Geant4—a simulation toolkit,” *Nucl. Instruments Methods Phys. Res. Sect. A Accel. Spectrometers, Detect. Assoc. Equip.* **506**(3), 250–303 (2003).
- ¹⁵ D. Shu, X. Tang, C. Geng, C. Gong, and D. Chen, “Determination of the relationship between dose deposition and Cerenkov photons in homogeneous and heterogeneous phantoms during radiotherapy using Monte Carlo method,” *J. Radioanal. Nucl. Chem.* (2015).
- ¹⁶ P. Arce, P. Rato, M. Cafiadas, and J.I. Lagares, “GAMOS : a GEANT4-based easy and flexible framework for nuclear medicine applications,” in *IEEE Nucl. Sci. Symp.*(2008), pp. 3162–3168.
- ¹⁷ S. Jan, G. Santin, D. Strul, *et al.*, “GATE: a simulation toolkit for PET and SPECT,” *Phys. Med. Biol.* **49**(19), 4543–4561 (2004).
- ¹⁸ A.K. Glaser, S.C. Kanick, R. Zhang, P. Arce, and B.W. Pogue, “A GAMOS plug-in for GEANT4 based Monte Carlo simulation of radiation-induced light transport in biological media.,” *Biomed. Opt. Express* **4**(5), 741–59 (2013).
- ¹⁹ J. Axelsson, S.C. Davis, D.J. Gladstone, and B.W. Pogue, “Cerenkov emission induced by external beam radiation stimulates molecular fluorescence,” *Med. Phys.* **38**(7), 4127 (2011).
- ²⁰ J. Axelsson, A.K. Glaser, D.J. Gladstone, and B.W. Pogue, “Quantitative Cherenkov emission spectroscopy for tissue oxygenation assessment.,” *Opt. Express* **20**(5), 5133–42 (2012).
- ²¹ E.J. Hall, *Radiobiology for the radiologist*, 6th ed. (Harper & Row, Hagerstown, Md, 1973).
- ²² S.M. Bentzen, “Preventing or reducing late side effects of radiation therapy: Radiobiology meets molecular pathology,” *Nat. Rev. Cancer* **6**(9), 702–713 (2006).
- ²³ B. Mijnheer, S. Beddar, J. Izewska, and C. Reft, “In vivo dosimetry in external beam radiotherapy.,” *Med. Phys.* **40**(7), 070903 (19 pp.) (2013).
- ²⁴ X. Mei, J.A. Rowlands, and G. Pang, “Electronic portal imaging based on cerenkov radiation: a new approach and its feasibility,” *Med Phys* **33**(11), 4258–4270 (2006).
- ²⁵ I.C. Silva and G. Pang, “Electronic portal imaging using Cherenkov radiation,” *Proc. SPIE* **6913**, 69130A (2008).

- 26 G.G. Pang and J.A. Rowlands, *Cerenkov X-Ray Detector for Portal Imaging*, 2007.
- 27 A. Teymurazyan and G. Pang, "Megavoltage X-ray imaging based on Cerenkov effect: A new application of optical fibres to radiation therapy," *Int. J. Opt.* **2012**(1), (2012).
- 28 K.W. Jang, W.J. Yoo, S.H. Shin, D. Shin, and B. Lee, "Fiber-optic Cerenkov radiation sensor for proton therapy dosimetry.," *Opt. Express* **20**(13), 13907–14 (2012).
- 29 R. Gaza, S.W.S. McKeever, M.S. Akselrod, *et al.*, "A fiber-dosimetry method based on OSL from Al₂O₃:C for radiotherapy applications," *Radiat. Meas.* **38**(4–6), 809–812 (2004).
- 30 K.W. Jang, T. Yagi, C.H. Pyeon, *et al.*, "Application of Cerenkov radiation generated in plastic optical fibers for therapeutic photon beam dosimetry.," *J. Biomed. Opt.* **18**(2), 27001 (2013).
- 31 E.J. Bloemen-van Gurp, B.J. Mijnheer, T.A.M. Verschueren, and P. Lambin, "Total body irradiation, toward optimal individual delivery: dose evaluation with metal oxide field effect transistors, thermoluminescence detectors, and a treatment planning system.," *Int. J. Radiat. Oncol. Biol. Phys.* **69**(4), 1297–304 (2007).
- 32 L.G. Pacyna, M. Darby, and K. Prado, "Use of thermoluminescent dosimetry to verify dose compensation in total body irradiation.," *Med. Dosim.* **22**(4), 319–24 (1997).
- 33 M. Amor Duch, M. Ginjaume, H. Chakkor, X. Ortega, N. Jornet, and M. Ribas, "Thermoluminescence dosimetry applied to in vivo dose measurements for total body irradiation techniques.," *Radiother. Oncol.* **47**(3), 319–24 (1998).
- 34 F. Sánchez-Doblado, J.A. Terrón, B. Sánchez-Nieto, *et al.*, "Verification of an on line in vivo semiconductor dosimetry system for TBI with two TLD procedures.," *Radiother. Oncol.* **34**(1), 73–7 (1995).
- 35 P. Mangili, C. Fiorino, a Rosso, *et al.*, "In-vivo dosimetry by diode semiconductors in combination with portal films during TBI: reporting a 5-year clinical experience.," *Radiother. Oncol.* **52**(3), 269–76 (1999).
- 36 R. Weaver, B. Gerbi, and K. Dusenbery, "Evaluation of dose variation during total skin electron irradiation using thermoluminescent dosimeters," *Int. J. Radiat. ...* **33**(2), 475–478 (1995).
- 37 S.J. Blake, A.L. McNamara, S. Deshpande, *et al.*, "Characterization of a novel EPID designed for simultaneous imaging and dose verification in radiotherapy.," *Med. Phys.* **40**(9), 091902 (11 pp.) (2013).

- 38 K. Chytky-Praznik, E. van Uytven, T.A. van Beek, P.B. Greer, and B.M.C. McCurdy, "Model-based prediction of portal dose images during patient treatment.," *Med. Phys.* **40**(3), 031713 (11 pp.) (2013).
- 39 T. Fuangrod, H.C. Woodruff, E. van Uytven, *et al.*, "A system for EPID-based real-time treatment delivery verification during dynamic IMRT treatment.," *Med. Phys.* **40**(9), 091907 (11 pp.) (2013).
- 40 M.-H. Lin, J. Li, L. Wang, *et al.*, "4D patient dose reconstruction using online measured EPID cine images for lung SBRT treatment validation.," *Med. Phys.* **39**(10), 5949–58 (2012).
- 41 N. Naiyanet, S. Oonsiri, C. Lertbutsayanukul, and S. Suriyapee, "Measurements of patient's setup variation in intensity-modulated radiation therapy of head and neck cancer using electronic portal imaging device.," *Biomed. Imaging Interv. J.* **3**(1), e30 (2007).
- 42 R.L. Smith, M.L. Taylor, L.N. McDermott, A. Haworth, J.L. Millar, and R.D. Franich, "Source position verification and dosimetry in HDR brachytherapy using an EPID.," *Med. Phys.* **40**(11), 111706 (12 pp.) (2013).
- 43 S. Steciw, B. Warkentin, S. Rathee, and B.G. Fallone, "Three-dimensional IMRT verification with a flat-panel EPID," *Med. Phys.* **32**(2), 600 (2005).
- 44 W. van Elmpt, L. McDermott, S. Nijsten, M. Wendling, P. Lambin, and B. Mijnheer, "A literature review of electronic portal imaging for radiotherapy dosimetry.," *Radiother. Oncol.* **88**(3), 289–309 (2008).
- 45 H. Wang, "Development of a portal imager and of tools for radiation treatment verification," *Med. Phys.* **24**(8), 1334 (1997).
- 46 H.C. Woodruff, T. Fuangrod, P. Rowshanfarzad, B.M.C. McCurdy, and P.B. Greer, "Gantry-angle resolved VMAT pretreatment verification using EPID image prediction.," *Med. Phys.* **40**(8), 081715 (9 pp.) (2013).
- 47 S.L. Berry, C. Polvorosa, S. Cheng, I. Deutsch, K.S.C. Chao, and C.-S. Wu, "Initial clinical experience performing patient treatment verification with an electronic portal imaging device transit dosimeter.," *Int. J. Radiat. Oncol. Biol. Phys.* **88**(1), 204–9 (2014).
- 48 R. Zhang, A.K. Glaser, D.J. Gladstone, C.J. Fox, and B.W. Pogue, "Superficial dosimetry imaging based on Čerenkov emission for external beam radiotherapy with megavoltage x-ray beam.," *Med. Phys.* **40**(10), 101914 (12 pp.) (2013).
- 49 L.A. Jarvis, R. Zhang, D.J. Gladstone, *et al.*, "Cherenkov Video Imaging Allows for the First Visualization of Radiation Therapy in Real Time," *Int. J. Radiat. Oncol.*

89(3), 615–22 (2014).

- 50 R. Zhang, D.J. Gladstone, L.A. Jarvis, *et al.*, “Real-time in vivo Cherenkovscopy imaging during external beam radiation therapy.,” *J. Biomed. Opt.* **18(11)**, 110504 (2013).
- 51 C.E. Desch, K.K. McNiff, E.C. Schneider, *et al.*, “American Society of Clinical Oncology/National Comprehensive Cancer Network quality measures,” *J. Clin. Oncol.* **26(21)**, 3631–3637 (2008).
- 52 B.D. Smith, S.M. Bentzen, C.R. Correa, *et al.*, “Fractionation for whole breast irradiation: an American Society for Radiation Oncology (ASTRO) evidence-based guideline.,” *Int. J. Radiat. Oncol. Biol. Phys.* **81(1)**, 59–68 (2011).
- 53 S. Darby, P. McGale, C. Correa, *et al.*, “Effect of radiotherapy after breast-conserving surgery on 10-year recurrence and 15-year breast cancer death: meta-analysis of individual patient data for 10,801 women in 17 randomised trials.,” *Lancet* **378(9804)**, 1707–16 (2011).
- 54 J.P. Pignol, B.M. Keller, and A. Ravi, “Doses to internal organs for various breast radiation techniques - implications on the risk of secondary cancers and cardiomyopathy,” *Radiat. Oncol.* **6(1)**, 5 (2011).
- 55 K.A. Reardon, P.W. Read, M.M. Morris, M.A. Reardon, C. Geesey, and K. Wijesooriya, “A comparative analysis of 3D conformal deep inspiratory-breath hold and free-breathing intensity-modulated radiation therapy for left-sided breast cancer,” *Med. Dosim.* **38(2)**, 190–195 (2013).
- 56 K. Hwan Shin, K. Su Kim, N. Choi, and S.-W. Lee, “Hypofractionated whole breast irradiation: new standard in early breast cancer after breast-conserving surgery,” *Radiat Oncol J* **34(2)**, 81–87 (2016).
- 57 F.Y. De Moraes, H.D.A. Carvalho, S.A. Hanna, J.L.F. Da Silva, and G.N. Marta, “Literature review of clinical results of total skin electron irradiation (TSEBT) of mycosis fungoides in adults,” *Reports Pract. Oncol. Radiother.* **19(2)**, 92–98 (2014).
- 58 E.M. Farber, H.M. Schneidman, and J. Llerena, “The natural history of mycosis fungoides.,” *Calif. Med.* **87(4)**, 225–30 (1957).
- 59 M.A. Bagshaw, H.M. Schneidman, E.M. Farber, and H.S. Kaplan, “Electron beam therapy of mycosis fungoides.,” *Calif. Med.* **95(5)**, 292–297 (1961).
- 60 C.J. Karzmark, J. Anderson, A. Buffa, *et al.*, *Total Skin Electron Therapy: Technique and Dosimetry, Report of the American Association of Physicists in Medicine (AAPM) Task Group 30* (Medical Physics Publishing, Madison, WI, AAPM Report

No. 23, 1987).

- 61 P. Maingon, G. Truc, S. Dalac, *et al.*, "Radiotherapy of advanced mycosis fungoides: indications and results of total skin electron beam and photon beam irradiation.," *Radiother. Oncol.* **54**, 73–78 (2000).
- 62 T.C. Lo, F. a Salzman, S.L. Moschella, E.L. Tolman, and K. a Wright, "Whole body surface electron irradiation in the treatment of mycosis fungoides. An evaluation of 200 patients.," *Radiology* **130**(October 1978), 453–457 (1979).
- 63 K. Desai, R. Pezner, J. Lipsett, *et al.*, "Total skin electron irradiation for mycosis fungoides: relationship between acute toxicities and measured dose at different anatomic sites," *Journal of Radiat. Oncol. Biol.* **15**(April), 641–645 (1988).
- 64 G.W. Jones, B.M. Kacinski, L.D. Wilson, *et al.*, "Total skin electron radiation in the management of mycosis fungoides: Consensus of the European Organization for Research and Treatment of Cancer (EORTC) Cutaneous Lymphoma Project Group," *J. Am. Acad. Dermatol.* **47**(3), 364–370 (2002).
- 65 T. Piotrowski, P. Milecki, M. Skórska, and D. Fundowicz, "Total skin electron irradiation techniques: A review," *Postep. Dermatologii i Alergol.* **30**(1), 50–55 (2013).
- 66 S. Diamantopoulos, K. Platoni, M. Dilvoij, *et al.*, "Clinical implementation of total skin electron beam (TSEB) therapy: A review of the relevant literature," *Phys. Medica* **27**(2), 62–68 (2011).
- 67 N.-R. Azam, M.T. Gillin, R. Komaki, R.W. Kline, and D.F. Grimm, "Dose distribution in total skin electron beam irradiation using the six-field technique," *Int. J. Radiat. Oncol.* **12**, (1986).
- 68 Y. Anacak, Z. Arican, R. Bar-Deroma, A. Tamir, and A. Kuten, "Total skin electron irradiation: Evaluation of dose uniformity throughout the skin surface," *Med. Dosim.* **28**(1), 31–34 (2003).
- 69 P. Kupelian and J.J. Sonke, "Magnetic Resonance-Guided Adaptive Radiotherapy: A Solution to the Future," *Semin. Radiat. Oncol.* **24**(3), 227–232 (2014).
- 70 A. Choudhury, G. Budgell, R. MacKay, *et al.*, "The Future of Image-guided Radiotherapy," *Clin. Oncol.* **29**(10), 662–666 (2017).
- 71 S. Mutic and J.F. Dempsey, "The ViewRay System: Magnetic Resonance-Guided and Controlled Radiotherapy," *Semin. Radiat. Oncol.* **24**(3), 196–199 (2014).
- 72 A.J.E. Raaijmakers, B.W. Raaymakers, S. van der Meer, J.J.W. Lagendijk, S. van der Meer, and J.J.W. Lagendijk, "Integrating a MRI scanner with a 6 MV radiotherapy

accelerator: impact of the surface orientation on the entrance and exit dose due to the transverse magnetic field.," *Phys. Med. Biol.* **52**(4), 929–39 (2007).

- 73 ViewRay, *ViewRay Announces World's First Patients Treated Using MRI- Guided Radiation Therapy*, www.prnewswire.com 2–3 (2014).
- 74 ViewRay, *First Patients Treated with ViewRay's MRIdian Linac System at Henry Ford Health System*, www.prnewswire.com 1–2 (2017).
- 75 B.W. Raaymakers, I.M. Jürgenliemk-Schulz, G.H. Bol, *et al.*, "First patients treated with a 1.5T MRI-Linac: clinical proof of concept of a high-precision, high-field MRI guided radiotherapy treatment," *Phys. Med. Biol.* (62 L41), (2017).
- 76 D.J. O'Brien, J. Dolan, S. Pencea, N. Schupp, and G.O. Sawakuchi, "Relative dosimetry with an MR-linac: Response of ion chambers, diamond, and diode detectors for off-axis, depth dose, and output factor measurements: Response," *Med. Phys.* **45**(2), 884–897 (2018).
- 77 A.J.E. Raaijmakers, B.W. Raaymakers, and J.J.W. Lagendijk, "Magnetic-field-induced dose effects in MR-guided radiotherapy systems: dependence on the magnetic field strength.," *Phys. Med. Biol.* **53**(4), 909–923 (2008).
- 78 B.W. Raaymakers, A.J.E. Raaijmakers, A.N.T.J. Kotte, D. Jette, and J.J.W. Lagendijk, "Integrating a MRI scanner with a 6 MV radiotherapy accelerator: Dose deposition in a transverse magnetic field," *Phys. Med. Biol.* **49**(17), 4109–4118 (2004).
- 79 A.J.E. Raaijmakers, B.W. Raaymakers, and J.J.W. Lagendijk, "Magnetic-field-induced dose effects in MR-guided radiotherapy systems: Dependence on the magnetic field strength," *Phys. Med. Biol.* **53**(4), 909–923 (2008).
- 80 A.J.E. Raaijmakers, B.W. Raaymakers, and J.J.W. Lagendijk, "Experimental verification of magnetic field dose effects for the MRI-accelerator.," *Phys. Med. Biol.* **52**(14), 4283–4291 (2007).
- 81 A.J.E. Raaijmakers, B. Hårdemark, B.W. Raaymakers, C.P.J. Raaijmakers, and J.J.W. Lagendijk, "Dose optimization for the MRI-accelerator: IMRT in the presence of a magnetic field.," *Phys. Med. Biol.* **52**(23), 7045–7054 (2007).
- 82 A.J.E. Raaijmakers, B.W. Raaymakers, and J.J.W. Lagendijk, "Integrating a MRI scanner with a 6 MV radiotherapy accelerator: Dose increase at tissue-air interfaces in a lateral magnetic field due to returning electrons," *Phys. Med. Biol.* **50**(7), 1363–1376 (2005).
- 83 S. Rudra, N. Jiang, S.A. Rosenberg, *et al.*, "High Dose Adaptive MRI Guided Radiation Therapy Improves Overall Survival of Inoperable Pancreatic Cancer,"

- Int. J. Radiat. Oncol. **99**(2), E184 (2017).
- 84 L. Henke, R. Kashani, C. Robinson, *et al.*, "Phase I trial of stereotactic MR-guided online adaptive radiation therapy (SMART) for the treatment of oligometastatic or unresectable primary malignancies of the abdomen," *Radiother. Oncol.* **126**(3), 519–526 (2017).
- 85 L.E. Henke, R. Kashani, D. Przybysz, *et al.*, "In Silico Trial of MR-Guided Mid-Treatment Adaptive Planning for Hypofractionated Stereotactic Radiotherapy in Centrally Located Thoracic Tumors," *Int. J. Radiat. Oncol.* **98**(2), E3–E4 (2017).
- 86 K. Otto, "Volumetric modulated arc therapy: IMRT in a single gantry arc.," *Med. Phys.* **35**(1), 310–317 (2008).
- 87 M. Teoh, C.H. Clark, K. Wood, S. Whitaker, and A. Nisbet, "Volumetric modulated arc therapy: a review of current literature and clinical use in practice.," *Br. J. Radiol.* **84**(1007), 967–96 (2011).
- 88 J.M. Andreozzi, R. Zhang, A.K. Glaser, D.J. Gladstone, L.A. Jarvis, and B.W. Pogue, "Cherenkov imaging during volumetric modulated arc therapy for real-time radiation beam tracking and treatment response monitoring," in *Prog. Biomed. Opt. Imaging - Proc. SPIE*, edited by A. Wax and V. Backman (2016), p. 971905.
- 89 Y. Helo, A. Kacperek, I. Rosenberg, G. Royle, and A.P. Gibson, "The physics of Čerenkov light production during proton therapy," *Phys. Med. Biol.* **59**(23), 7107–7123 (2014).
- 90 A.K.A.K. Glaser, J.M.J.M. Andreozzi, R. Zhang, B.W.B.W. Pogue, and D.J.D.J. Gladstone, "Optical cone beam tomography of Čerenkov-mediated signals for fast 3D dosimetry of x-ray photon beams in water.," *Med. Phys.* **42**(7), 4127–4136 (2015).
- 91 A.K. Glaser, S.C. Davis, D.M. McClatchy, R. Zhang, B.W. Pogue, and D.J. Gladstone, "Projection imaging of photon beams by the Čerenkov effect.," *Med. Phys.* **40**(1), 12101 (2013).
- 92 A.K. Glaser, W.H.A. Voigt, S.C. Davis, R. Zhang, D.J. Gladstone, and B.W. Pogue, "Three-dimensional Čerenkov tomography of energy deposition from ionizing radiation beams.," *Opt. Lett.* **38**(5), 634–6 (2013).
- 93 M.H. Lin, S. Koren, I. Veltchev, *et al.*, "Measurement comparison and Monte Carlo analysis for volumetric-modulated arc therapy (VMAT) delivery verification using the ArcCHECK dosimetry system.," *J. Appl. Clin. Med. Phys.* **14**(2), 3929 (2013).
- 94 A. Van Esch, T. Depuydt, and D.P. Huyskens, "The use of an aSi-based EPID for routine absolute dosimetric pre-treatment verification of dynamic IMRT fields,"

- Radiother. Oncol. **71**(2), 223–234 (2004).
- 95 D.W. Bailey, L. Kumaraswamy, M. Bakhtiari, H.K. Malhotra, and M.B. Podgorsak, “EPID dosimetry for pretreatment quality assurance with two commercial systems.,” *J. Appl. Clin. Med. Phys.* **13**(4), 3736 (2012).
- 96 M.G. Herman, J.M. Balter, D. a Jaffray, *et al.*, “Clinical use of electronic portal imaging: report of AAPM Radiation Therapy Committee Task Group 58.,” *Med. Phys.* **28**(5), 712–737 (2001).
- 97 M. Wendling, L.N. McDermott, A. Mans, J.-J. Sonke, M. van Herk, and B.J. Mijnheer, “A simple backprojection algorithm for 3D *in vivo* EPID dosimetry of IMRT treatments.,” *Med. Phys.* **36**(7), 3310–3321 (2009).
- 98 A. Mans, P. Remeijer, I. Olaciregui-Ruiz, *et al.*, “3D Dosimetric verification of volumetric-modulated arc therapy by portal dosimetry,” *Radiother. Oncol.* **94**(2), 181–187 (2010).
- 99 P. Bruza, J.M. Andreozzi, D.J. Gladstone, L.A. Jarvis, J. Rottmann, and B.W. Pogue, “Online combination of EPID & Cherenkov imaging for 3D dosimetry in a liquid phantom,” *IEEE Trans. Med. Imaging* **PP**(99), (2017).
- 100 J.S. Cho, R. Taschereau, S. Olma, *et al.*, “Cerenkov radiation imaging as a method for quantitative measurements of beta particles in a microfluidic chip,” *Phys. Med. Biol.* **54**(22), 6757–6771 (2009).
- 101 R. Robertson, M.S. Germanos, C. Li, G.S. Mitchell, S.R. Cherry, and M.D. Silva, “Optical imaging of Cerenkov light generation from positron-emitting radiotracers.,” *Phys. Med. Biol.* **54**(16), N355-65 (2009).
- 102 A.E. Spinelli, D. D’Ambrosio, L. Calderan, M. Marengo, A. Sbarbati, and F. Boschi, “Cerenkov radiation allows *in vivo* optical imaging of positron emitting radiotracers,” *Phys. Med. Biol.* **55**(2), 483–495 (2010).
- 103 Y. Xu, H. Liu, and Z. Cheng, “Harnessing the Power of Radionuclides for Optical Imaging: Cerenkov Luminescence Imaging,” *J. Nucl. Med.* **52**, 2009–2018 (2011).
- 104 G. Lucignani, “Čerenkov Radioactive Optical Imaging: a Promising New Strategy,” *Eur. J. Nucl. Med. Mol. Imaging* **38**(3), 592–595 (2011).
- 105 T.F. Massoud, T.F. Massoud, S.S. Gambhir, and S.S. Gambhir, “Molecular imaging in living subjects: seeing fundamental biological processes in a new light,” *Genes Dev.* 545–580 (2003).
- 106 A. Ruggiero, J.P. Holland, J.S. Lewis, and J. Grimm, “Cerenkov luminescence imaging of medical isotopes.,” *J. Nucl. Med.* **51**(7), 1123–30 (2010).

- 107 D.H. Kim, Y.S. Choe, J.Y. Choi, K.-H. Lee, and B.-T. Kim, "Binding of 2-[18F]fluoro-CP-118,954 to mouse acetylcholinesterase: microPET and ex vivo Cerenkov luminescence imaging studies," *Nucl. Med. Biol.* **38**(4), 541–7 (2011).
- 108 T.A. Aweda, V. Eskandari, D.L. Kukis, *et al.*, "New covalent capture probes for imaging and therapy, based on a combination of binding affinity and disulfide bond formation," *Bioconjug. Chem.* **22**(8), 1479–1483 (2011).
- 109 J.P. Holland, G. Normand, A. Ruggiero, J.S. Lewis, and J. Grimm, "Intraoperative Imaging of Positron Emission Tomographic Radiotracers Using Cerenkov Luminescence Emissions," *Mol. Imaging* **10**(3), 177–186 (2011).
- 110 J.C. Park, G. Il An, S.-I. Park, *et al.*, "Luminescence imaging using radionuclides: a potential application in molecular imaging," *Nucl. Med. Biol.* **38**(3), 321–9 (2011).
- 111 W. Yang, W. Qin, Z. Hu, *et al.*, "Comparison of Cerenkov luminescence imaging (CLI) and gamma camera imaging for visualization of let-7 expression in lung adenocarcinoma A549 Cells," *Nucl. Med. Biol.* **39**(7), 948–53 (2012).
- 112 X. Zhang, C. Kuo, A. Moore, and R. Chongzhao, "Cerenkov Luminescence Imaging of Interscapular Brown Adipose Tissue," *J. Vis. Exp.* **92**, e51790 (2014).
- 113 Y. Wang, Y. Liu, H. Luehmann, *et al.*, "Radioluminescent gold nanocages with controlled radioactivity for real-time in vivo imaging," *Nano Lett.* **13**(2), 581–585 (2013).
- 114 A. Natarajan, F. Habte, H. Liu, *et al.*, "Evaluation of 89Zr-rituximab tracer by Cerenkov luminescence imaging and correlation with PET in a humanized transgenic mouse model to image NHL," *Mol. Imaging Biol.* **15**(4), 468–75 (2013).
- 115 A.E. Spinelli, M. Ferdeghini, C. Cavedon, *et al.*, "First human Cerenkography," *J. Biomed. Opt.* **18**(2), 20502 (2013).
- 116 D.L.J. Thorek, C.C. Riedl, and J. Grimm, "Clinical Cerenkov luminescence imaging of (18)F-FDG," *J. Nucl. Med.* **55**(1), 95–8 (2014).
- 117 H. Hu, X. Cao, F. Kang, *et al.*, "Feasibility study of novel endoscopic Cerenkov luminescence imaging system in detecting and quantifying gastrointestinal disease: first human results," *Eur. Radiol.* **25**, 1814–1822 (2015).
- 118 X. Zhang, C. Kuo, A. Moore, and C. Ran, "In Vivo Optical Imaging of Interscapular Brown Adipose Tissue with 18F-FDG via Cerenkov Luminescence Imaging," *PLoS One* **8**(4), e62007 (2013).
- 119 C. Li, G.S. Mitchell, and S.R. Cherry, "Cerenkov Luminescence Tomography for Small Animal Imaging," *Opt. Lett.* **35**(7), 1199–1216 (2010).

- 120 Z. Hu, W. Yang, X. Ma, *et al.*, “Cerenkov Luminescence Tomography of Aminopeptidase N (APN/CD13) Expression in Mice Bearing HT1080 Tumors,” *Mol. Imaging* **12**(3), 173–181 (2013).
- 121 H. Liu, X. Yang, T. Song, *et al.*, “Multispectral hybrid Cerenkov luminescence tomography based on the finite element SPn method,” *J. Biomed. Opt.* **20**(8), 86007 (2015).
- 122 X. Ma, J. Wang, and Z. Cheng, “Cerenkov radiation: a multi-functional approach for biological sciences,” *Front. Phys.* **2**(February), 1–14 (2014).
- 123 Y. Bernhard, B. Collin, and R. a. Decréau, “Inter/intramolecular Cerenkov radiation energy transfer (CRET) from a fluorophore with a built-in radionuclide,” *Chem. Commun.* 6711–6714 (2014).
- 124 R. Zhang, S.C. Davis, J.-L.H. Demers, *et al.*, “Oxygen tomography by Čerenkov-excited phosphorescence during external beam irradiation.,” *J. Biomed. Opt.* **18**(5), 50503 (2013).
- 125 J. Czupryna, a. V. Kachur, E. Blankemeyer, *et al.*, “Cerenkov-Specific Contrast Agents for Detection of pH In Vivo,” *J. Nucl. Med.* **56**(3), 483–488 (2015).
- 126 R. Zhang, A. V. D’souza, J.R. Gunn, *et al.*, “Cerenkov-excited luminescence scanned imaging,” *Opt. Lett.* **40**(5), 827–830 (2015).
- 127 A.K. Glaser, R. Zhang, S.C. Davis, D.J. Gladstone, and B.W. Pogue, “Time-gated Cerenkov emission spectroscopy from linear accelerator irradiation of tissue phantoms.,” *Opt. Lett.* **37**(7), 1193–5 (2012).
- 128 J. Sandell and T. Zhu, “A review of in vivo optical properties of human tissues and its impact on PDT,” *J. Biophotonics* **4**(11–12), 773–787 (2011).
- 129 R. Zhang, A. Glaser, T. V Esipova, *et al.*, “Čerenkov radiation emission and excited luminescence (CREL) sensitivity during external beam radiation therapy: Monte Carlo and tissue oxygenation phantom studies.,” *Biomed. Opt. Express* **3**(10), 2381–94 (2012).
- 130 L. Archambault, T.M. Briere, and S. Beddar, “Transient noise characterization and filtration in CCD cameras exposed to stray radiation from a medical linear accelerator,” *Med. Phys.* **35**(10), 4342–4351 (2008).
- 131 A. Rose, *Vision: Human and Electronic* (Plenum Press, New York-London, 1974).
- 132 B. Fahimian, A. Ceballos, S. Türkcan, D.S. Kapp, and G. Pratz, “Seeing the invisible: direct visualization of therapeutic radiation beams using air scintillation.,” *Med. Phys.* **41**(1), 010702 (6 pp.) (2014).

- 133 Y. Helo, I. Rosenberg, D. D'Souza, *et al.*, "Imaging Cerenkov emission as a quality assurance tool in electron radiotherapy.," *Phys. Med. Biol.* **59**(8), 1963–78 (2014).
- 134 S.L. Jacques, "Corrigendum: Optical properties of biological tissues: a review," *Phys. Med. Biol.* **58**(14), 5007–5008 (2013).
- 135 C. Snyder, B.W. Pogue, M. Jermyn, *et al.*, "Algorithm development for intrafraction radiotherapy beam edge verification from Cherenkov imaging," *J. Med. Imaging* **5**(1), 1 (2018).
- 136 F.M. Kahn and P. Gibbons, John, *The Physics of Radiation Therapy* (Lippincott Williams and Wilkins, Philadelphia, 2014).
- 137 J.M. Andreozzi, R. Zhang, A.K. Glaser, D.J. Gladstone, L.A. Jarvis, and B.W. Pogue, "Using a reflectance-based correction on Cherenkov images to strengthen in vivo correlation with surface dose in whole-breast radiotherapy patients," *SPIE Photonics West BIOS* **9689**, 9689–147 (2016).
- 138 V. Krishnaswamy, J.T. Elliott, D.M. McClatchy, *et al.*, "Structured light scatterometry scatterometry," *J. Biomed. Opt.* **19**(7), 70504–1 (2014).
- 139 S.D. Konecky, A. Mazhar, D. Cuccia, A.J. Durkin, J.C. Schotland, and B.J. Tromberg, "Quantitative optical tomography of sub-surface heterogeneities using spatially modulated structured light," *Opt. Express* **17**(17), 14780 (2009).
- 140 J.R. Weber, D.J. Cuccia, A.J. Durkin, and B.J. Tromberg, "Noncontact imaging of absorption and scattering in layered tissue using spatially modulated structured light," *J. Appl. Phys.* **105**(10), (2009).
- 141 D.M. McClatchy, E.J. Rizzo, W.A. Wells, *et al.*, "Wide-field quantitative imaging of tissue microstructure using sub-diffuse spatial frequency domain imaging," *Optica* **3**(6), 613 (2016).
- 142 D. Navi, N. Riaz, Y.S. Levin, N.C. Sullivan, Y.H. Kim, and R.T. Hoppe, "The Stanford University experience with conventional-dose, total skin electron-beam therapy in the treatment of generalized patch or plaque (T2) and tumor (T3) mycosis fungoides.," *Arch. Dermatol.* **147**(5), 561–567 (2011).
- 143 B. Micaily, E.C. Vonderheid, L.W. Brady, and C. Andrews, "Beam and total nodal irradiation for T-Cell lymphoma," *Int. J. Radiat. Oncol. Biol. Phys.* **11**(January), 1111–1115 (1985).
- 144 T.H. Kim, C. Pla, M. Pla, and E.B. Podgorsak, "Clinical aspects of a rotational total skin electron irradiation," *Br. J. Radiol.* **57**(1983), 501–506 (1984).
- 145 C.J. Karzmark, R. Loevinger, R.E. Steele, and M. Weissbluth, "A technique for

- large-field, superficial electron therapy.," *Radiology* **74**, 633–644 (1960).
- 146 Z. Chen, A.G. Agostinelli, L.D. Wilson, and R. Nath, "Matching the dosimetry characteristics of a dual-field Stanford technique to a customized single-field Stanford technique for total skin electron therapy," *Int. J. Radiat. Oncol. Biol. Phys.* **59**(3), 872–885 (2004).
- 147 H. Fuse, K. Suzuki, K. Shida, *et al.*, "Total skin electron beam therapy using an inclinable couch on motorized table and a compensating filter.," *Rev. Sci. Instrum.* **85**(6), 64301 (2014).
- 148 T. Piotrowski and J. Malicki, "The rotary dual technique for total skin irradiation in the treatment of mycosis fungoides – a description of the applied method," *Reports Pract. Oncol. Radiother.* **11**(1), 29–37 (2006).
- 149 P. Schiapparelli, D. Zefiro, F. Massone, and G. Taccini, "Total skin electron therapy (TSET): a reimplementation using radiochromic films and IAEA TRS-398 code of practice.," *Med. Phys.* **37**(2010), 3510–3517 (2010).
- 150 L.M. Gamble, T.J. Farrell, G.W. Jones, and J.E. Hayward, "Two-dimensional mapping of underdosed areas using radiochromic film for patients undergoing total skin electron beam radiotherapy," *Int. J. Radiat. Oncol. Biol. Phys.* **62**(3), 920–924 (2005).
- 151 G. Guidi, G. Gottardi, P. Ceroni, and T. Costi, "Review of the results of the in vivo dosimetry during total skin electron beam therapy.," *Reports Pract. Oncol. Radiother. J. Gt. Cancer Cent. Poznań Polish Soc. Radiat. Oncol.* **19**(2), 144–50 (2014).
- 152 J.G. Holt, "Some physical considerations in whole skin electron beam therapy," *Med. Phys.* **9**(5), 769–776 (1982).
- 153 D. Gur, "Photon contamination in 8–20-MeV electron beams from a linear accelerator," *Med. Phys.* **6**(2), 145–146 (1999).
- 154 J.E. Morgan, D. Ph, and A.H. Dowdy, "Some Problems Peculiar to Electron Therapy'," *Radiology* **81**(February), 317–319 (1963).
- 155 J.H. Grollman Jr., S.M. Bierman, J.E. Morgan, and R.E. Ottoman, "X-Ray Contamination in Total-Skin Electron Therapy of Lymphoma Cutis and Exfoliative Dermatitis !," *Radiology* **85**, 356–360 (1964).
- 156 R.T. Hoppe, C. Harrison, M. Tavallaee, *et al.*, "Low-dose total skin electron beam therapy as an effective modality to reduce disease burden in patients with mycosis fungoides: Results of a pooled analysis from 3 phase-II clinical trials," *J. Am. Acad. Dermatol.* **72**(2), 286–292 (2015).

- 157 V. Peters and S. Jaywant, "Implementation of Total Skin Electron Therapy Using an Optional High Dose Rate Mode on a Conventional Linear Accelerator," *Med. Dosim.* **20**(2), 99–104 (1995).
- 158 M.D.C. Evans, C. Hudon, E.B. Podgorsak, and C.R. Freeman, "Institutional experience with a rotational total skin electron irradiation (RTSEI) technique-A three decade review (1981-2012)," *Reports Pract. Oncol. Radiother.* **19**(2), 120–134 (2014).
- 159 F.W. Hensley, G. Major, C. Edel, H. Hauswald, and M. Bischof, "Technical and dosimetric aspects of the total skin electron beam technique implemented at Heidelberg University Hospital," *Reports Pract. Oncol. Radiother.* **19**(2), 135–143 (2014).
- 160 K. Platoni, S. Diamantopoulos, G. Panayiotakis, *et al.*, "First application of total skin electron beam irradiation in Greece: Setup, measurements and dosimetry," *Phys. Medica* **28**(2), 174–182 (2012).
- 161 J.M.J.M. Andreozzi, R. Zhang, D.J.D.J. Gladstone, *et al.*, "Cherenkov imaging method for rapid optimization of clinical treatment geometry in total skin electron beam therapy," *Med. Phys.* **43**(2), 993–1002 (2016).
- 162 A. Nevelsky, E. Borzov, and S. Daniel, "Room scatter effects in Total Skin Electron Irradiation : Monte Carlo simulation study," *J. Appl. Clin. Med. Phys.* **18**, 196–201 (2017).
- 163 E.B. Podgorsak, "Radiation Oncology Physics: A Handbook for Teachers and Students," *Med. Phys.* **33**(6), (2006).
- 164 I. Boedeker *Plastics, PVC (PolyVinyl Chloride) & CPVC (Chlorinated PolyVinyl Chloride) Specifications*, (2017).
- 165 W.E. Luecke, J.D. McColskey, C.N. McCowan, *et al.*, *Mechanical Properties of Structural Steels* (2005).
- 166 N.C. for H.S. Centers for Disease Control and Prevention, *Measured average height, weight, and waist circumference for adults ages 20 years and over*, (2017).
- 167 S. Acharya, B.W. Fischer-Valuck, R. Kashani, *et al.*, "Online Magnetic Resonance Image Guided Adaptive Radiation Therapy: First Clinical Applications," *Int. J. Radiat. Oncol. Biol. Phys.* **94**(2), 394–403 (2016).
- 168 L.G.W. Kerkmeijer, C.D. Fuller, H.M. Verkooijen, *et al.*, "The MRI-Linear Accelerator Consortium: Evidence-Based Clinical Introduction of an Innovation in Radiation Oncology Connecting Researchers, Methodology, Data Collection, Quality Assurance, and Technical Development.," *Front. Oncol.* **6**(October), 215

(2016).

- 169 A.J.E. Raaijmakers, B.W. Raaymakers, and J.J.W. Lagendijk, "Integrating a MRI scanner with a 6 MV radiotherapy accelerator: Dose increase at tissue-air interfaces in a lateral magnetic field due to returning electrons," *Phys. Med. Biol.* **50**(7), 1363–1376 (2005).
- 170 B.W. Raaymakers, A.J.E. Raaijmakers, A.N.T.J. Kotte, D. Jette, and J.J.W. Lagendijk, "Integrating a MRI scanner with a 6 MV radiotherapy accelerator: Dose deposition in a transverse magnetic field," *Phys. Med. Biol.* **49**(17), 4109–4118 (2004).
- 171 M.L. Reyhan, T. Chen, and M. Zhang, "Characterization of the effect of MRI on Gafchromic film dosimetry," *J. Appl. Clin. Med. Phys.* **16**(6), 5743 (2015).
- 172 I. Meijsing, B.W. Raaymakers, A.J.E. Raaijmakers, *et al.*, "Dosimetry for the MRI accelerator: the impact of a magnetic field on the response of a Farmer NE2571 ionization chamber," *Phys. Med. Biol.* **54**(10), 2993–3002 (2009).
- 173 D.J. O'Brien, D.A. Roberts, G.S. Ibbott, and G.O. Sawakuchi, "Reference dosimetry in magnetic fields: formalism and ionization chamber correction factors," *Med. Phys.* **43**(8), 4915–4927 (2016).
- 174 D.J. O'Brien and G.O. Sawakuchi, "Monte Carlo study of the chamber-phantom air gap effect in a magnetic field," *Med. Phys.* **44**(4), (2017).
- 175 H.H. Li, V.L. Rodriguez, O.L. Green, *et al.*, "Patient-specific quality assurance for the delivery of ⁶⁰Co intensity modulated radiation therapy subject to a 0.35-T lateral magnetic field," *Int. J. Radiat. Oncol. Biol. Phys.* **91**(1), 65–72 (2015).
- 176 H.O. Wooten, V. Rodriguez, O. Green, *et al.*, "Benchmark IMRT evaluation of a Co-60 MRI-guided radiation therapy system," *Radiother. Oncol.* **114**(3), 402–405 (2015).
- 177 Y. Roed, Y. Ding, Z. Wen, J. Wang, L. Pinsky, and G. Ibbott, "The potential of polymer gel dosimeters for 3D MR-IGRT quality assurance," *J. Phys. Conf. Ser.* **847**(1), 12059 (2017).
- 178 C. Baldock, Y. De Deene, S. Doran, *et al.*, "Topical Review: Polymer gel dosimetry," *Phys. Med. Biol.* **55**(5), 1–87 (2010).
- 179 K. Smit, B. van Asselen, J.G.M. Kok, a H.L. Aalbers, J.J.W. Lagendijk, and B.W. Raaymakers, "Towards reference dosimetry for the MR-linac: magnetic field correction of the ionization chamber reading.," *Phys. Med. Biol.* **58**(17), 5945–57 (2013).

- 180 AAPM, *TG-119 IMRT Commissioning Tests Instructions for Planning, Measurement, and Analysis* (2009).
- 181 J. Bland, D.D. Altman, J. Martin Bland, and D.D. Altman, "Statistical methods for assessing agreement between two methods of clinical measurement," *Lancet* **327**(8476), 307–310 (1986).
- 182 E.E. Klein, J. Hanley, J. Bayouth, *et al.*, "Task Group 142 report: Quality assurance of medical accelerators," *Med. Phys.* **36**(9), 4197 (2009).
- 183 A.E. Rubinstein, Z. Liao, A.D. Melancon, *et al.*, "Technical Note: A Monte Carlo study of magnetic-field-induced radiation dose effects in mice," *Med. Phys.* **42**(9), 5510–5516 (2015).
- 184 H.J. Lee, Y. Roed, S. Venkataraman, M. Carroll, and G.S. Ibbott, "Investigation of magnetic field effects on the dose–response of 3D dosimeters for magnetic resonance – image guided radiation therapy applications," *Radiother. Oncol.* **In Press**(3), 426–432 (2017).
- 185 L.J. Rankine, S. Mein, B. Cai, *et al.*, "Three-Dimensional Dosimetric Validation of a Magnetic Resonance Guided Intensity Modulated Radiation Therapy System," *Int. J. Radiat. Oncol.* **97**(5), 1095–1104 (2017).
- 186 C. A.M., H. S., L. J., *et al.*, "MRI-guided radiotherapy for head and neck cancer: initial clinical experience," *Clin. Transl. Oncol.* **20**(2), 1–9 (2017).
- 187 J.J.W. Lagendijk, M. van Vulpen, and B.W. Raaymakers, "The development of the MRI linac system for online MRI-guided radiotherapy: a clinical update," *J. Intern. Med.* **280**(2), 203–208 (2016).
- 188 A.J.E.E. Raaijmakers, B.W. Raaymakers, and J.J.W.W. Lagendijk, "Magnetic-field-induced dose effects in MR-guided radiotherapy systems: dependence on the magnetic field strength," *Phys. Med. Biol.* **53**(4), 909–923 (2008).
- 189 S.T. Ellefson, W.S. Culberson, B.P. Bednarz, L.A. DeWerd, and J.E. Bayouth, "An analysis of the ArcCHECK-MR diode array's performance for ViewRay quality assurance," *J. Appl. Clin. Med. Phys.* **18**(4), 161–171 (2017).
- 190 K. Smit, J. Sjöholm, J.G.M. Kok, J.J.W. Lagendijk, and B.W. Raaymakers, "Relative dosimetry in a 1.5 T magnetic field: an MR-linac compatible prototype scanning water phantom," *Phys. Med. Biol.* **59**(15), 4099–4109 (2014).
- 191 B. Delfs, A.A. Schoenfeld, D. Poppinga, *et al.*, "Magnetic fields are causing small, but significant changes of the radiochromic EBT3 film response to 6 MV photons," *Phys. Med. Biol.* **63**(3), (2018).

- 192 H. Wooten, O. Green, H. Li, V. Rodriguez, and S. Mutic, "WE-G-17A-04: Measurements of the Electron-Return-Effect in a Commercial Magnetic Resonance Image Guided Radiation Therapy (MR-IGRT) System," *Med. Phys.* **41**(6Part30), 524–525 (2014).
- 193 H.J. Lee, M. Kadbi, G. Bosco, and G.S. Ibbot, "Real-time volumetric relative dosimetry for magnetic resonance – image- guided radiation therapy (MR-IGRT)," *Phys. Med. Biol.* 0–6 (2018).
- 194 H.J. Lee, G. Won Choi, M. Alqathami, M. Kadbi, and G. Ibbott, "Using 3D dosimetry to quantify the Electron Return Effect (ERE) for MR-image-guided radiation therapy (MR-IGRT) applications," *J. Phys. Conf. Ser.* **847**(1), (2017).
- 195 P. Bruza, S.L. Gollub, J.M. Andreozzi, *et al.*, "Time-gated scintillator imaging for real-time optical surface dosimetry in total skin electron therapy," *Phys. Med. Biol.* Accepted for Publication (2018).
- 196 S. Rana and K. Rogers, "Dosimetric evaluation of Acuros XB dose calculation algorithm with measurements in predicting doses beyond different air gap thickness for smaller and larger field sizes," *J. Med. Phys.* **38**(1), 9 (2013).
- 197 T. Stanescu, T. Tadic, and D.A. Jaffray, "Commissioning of an MR-Guided Radiation Therapy System," *Int. J. Radiat. Oncol.* **90**(1), S94–S95 (2014).
- 198 D. Lanman, *Bilateral Filtering*, (2006).
- 199 D. a Low, W.B. Harms, S. Mutic, and J. a Purdy, "A technique for the quantitative evaluation of dose distributions.," *Med. Phys.* **25**(1998), 656–661 (1998).
- 200 M. Geurts, *CalcGamma()*, (2015).